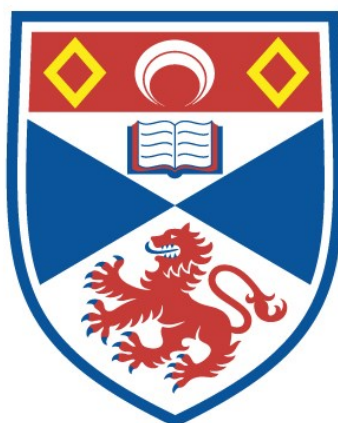# EXPLORING AZETIDINIUM AS THE A-SITE IN ORGANICINORGANIC HYBRID PEROVSKITES

Jiyu Tian

A Thesis Submitted for the Degree of PhD
at the
University of St Andrews

2021

Exploring azetidinium as the A-site in organic-inorganic hybrid perovskites
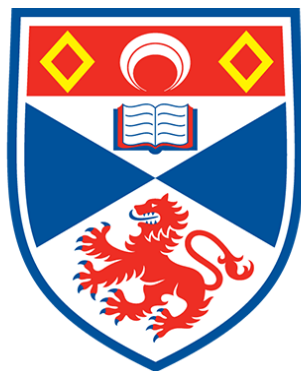
Jiyu Tian

University of
St Andrews

This thesis is submitted in partial fulfilment for the degree of

Doctor of Philosophy (PhD)

at the University of St Andrews

May 2021

Candidate's declaration

I, Jiyu Tian, do hereby certify that this thesis, submitted for the degree of PhD, which is approximately 31,000 words in length, has been written by me, and that it is the record of work carried out by me, or principally by myself in collaboration with others as acknowledged, and that it has not been submitted in any previous application for any degree. I confirm that any appendices included in my thesis contain only material permitted by the 'Assessment of Postgraduate Research Students' policy.

I was admitted as a research student at the University of St Andrews in August 2016.

I received funding from an organisation or institution and have acknowledged the funder(s) in the full text of my thesis.

Date   20.05.2021   Signature of candidate

Supervisor's declaration

I hereby certify that the candidate has fulfilled the conditions of the Resolution and Regulations appropriate for the degree of PhD in the University of St Andrews and that the candidate is qualified to submit this thesis in application for that degree. I confirm that any appendices included in the thesis contain only material permitted by the 'Assessment of Postgraduate Research Students' policy.

Date   21/05/2021   Signature of supervisor

Date   21/05/2021   Signature of supervisor

Permission for publication

In submitting this thesis to the University of St Andrews we understand that we are giving permission for it to be made available for use in accordance with the regulations of the University Library for the time being in force, subject to any copyright vested in the work not being affected thereby. We also understand, unless exempt by an award of an embargo as requested below, that the title and the abstract will be published, and that a copy of the work may be made and supplied to any bona fide library or research worker, that this thesis will be electronically accessible for personal or research use and that the library has the right to migrate this thesis into new electronic forms as required to ensure continued access to the thesis.

I, Jiyu Tian, confirm that my thesis does not contain any third-party material that requires copyright clearance.

The following is an agreed request by candidate and supervisor regarding the publication of this thesis:

Printed copy

Embargo on all of print copy for a period of 1 year on the following ground(s):

- Publication would preclude future publication

Supporting statement for printed embargo request

Not all the material in this thesis has been published at the current stage.

Electronic copy

Embargo on all of electronic copy for a period of 1 year on the following ground(s):

- Publication would preclude future publication

Supporting statement for electronic embargo request

Not all the material in this thesis has been published at the current stage.

Title and Abstract

- I agree to the title and abstract being published.

20.05.2021

Date   Signature of candidate

Date   21/05/2021   Signature of supervisor

Date   21/05/2021   Signature of supervisor

Underpinning Research Data or Digital Outputs

Candidate's declaration

I, Jiyu Tian, understand that by declaring that I have original research data or digital outputs, I should make every effort in meeting the University's and research funders' requirements on the deposit and sharing of research data or research digital outputs.

Date   20.05.2021   Signature of candidate

Permission for publication of underpinning research data or digital outputs

We understand that for any original research data or digital outputs which are deposited, we are giving permission for them to be made available for use in accordance with the requirements of the University and research funders, for the time being in force.

We also understand that the title and the description will be published, and that the underpinning research data or digital outputs will be electronically accessible for use in accordance with the license specified at the point of deposit, unless exempt by award of an embargo as requested below.
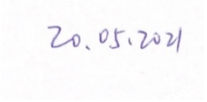
The following is an agreed request by candidate and supervisor regarding the publication of underpinning research data or digital outputs:

Embargo on all of electronic files for a period of 1 year on the following ground(s):

- Publication would preclude future publication

Supporting statement for embargo request

Not all the material in this thesis has been published at the current stage.

Date   20.05.2021   Signature of candidate

Date   21/05/2021   Signature of supervisor

Date   21/05/2021   Signature of supervisor

Abstract

Organic inorganic hybrid perovskites (OIHPs) have appealing optoelectronic properties. As sample preparation is relatively straightforward, there are opportunities to investigate novel compositions and structures. This thesis concerns the synthesis, structure and optoelectrical properties of OIHPs with azetidinium as an A-site cation.

Azetidinium [$(CH_2)_3NH_2^+$, Az] is a four-member ring ammonium, and its size is calculated to be promising as an A-cation for OIHPs. A stable 6H hexagonal perovskite $AzPbBr_3$ was synthesised and analysed, and its bandgap was determined to be 2.81 eV. On cooling, $AzPbBr_3$ undergoes a symmetry lowering distortion which was identified by variable temperature PXRD and dielectric spectroscopy. An anisotropic change in lattice parameters on cooling marked a phase transition likely driven by the Pb$^{...}$Pb repulsion in the face sharing octahedra.

Compositional and structural analyses were performed on precipitation synthesised and mechanosynthesised OIHPs $Az_{1-x}FA_xPbBr_3$ and $Az_{1-x}MA_xPbBr_3$ ($0 \leq x \leq 1$). For samples obtained from precipitation synthesis, the actual FA% or MA% in the precipitate was found to be less than the nominal composition in the reaction solution. No such mismatch was found for mechanosynthesised samples. PXRD indicated partial solid solution formation for Az-rich and MA- or FA-rich compositions, separated by an intermediate two-phase region. The result suggests the extent of the solid solution of halide perovskites is dependent only on the average A-cation size; the size mismatch is less of an influence. This is in contrast to solid solution formation observed in oxide perovskites.

A tuneable bandgap was achieved ranging from 2.00 eV ($AzPbI_3$) to 3.41 eV ($AzPbCl_3$) for the mixed halide perovskite $AzPbBr_{3-x}X_x$ (X = Cl or I, $0 \leq x \leq 3$). The structural analyses revealed a complete 6H solid solution for $AzPbBr_{3-x}Cl_x$ in comparison to the structural progression from 6H, 4H to 9R polytypes, when varying the halide composition from Br ($x = 0$) to I ($x = 3$) in $AzPbBr_{3-x}I_x$. A linear variation in unit cell volume as a function of anion average radius was observed not only within the solid solution of each polytype (following Vegard's law) but continuously across all three polytypes.

Preliminary results on the synthesis and structural analysis indicate that Az_2PbBr_4 adopts the $n = 1$ Ruddlesden-Popper structure while azetidinium bismuth bromide has a 1D chain structure. Detailed structural and optical analysis are planned in future projects.

Declaration

I acknowledge that the work presented in this thesis is my own. The research was carried out during my PhD studies under the supervisor of Prof Eli Zysman-Colman and Dr Finlay Morrison, University of St Andrews. Moreover, the research is interdisciplinary with contributions from collaborators and co-authors. Contributions to each chapter are listed below:

Chapter 1: I am the primary author of the text.

Chapter 2: I am the primary author of the text.

Chapter 3: I am the primary author of the text. Synthesis, characterisation and spectroscopy described in this chapter were carried out by me. Single crystals were grown by me while the diffraction data collection and structure solving were performed by Dr David B. Cordes (University of St Andrews). Density functional theory (DFT) calculations and analysis were performed by Dr Claudio Quarti and Prof David Beljonne (University of Mons). Variable temperature capillary PXRD were collected by me while the detailed variable temperature PXRD were collected by Tim van de Goor (University of Cambridge). Some of the work in this chapter has been published:

> Tian, J.; Cordes, D. B.; Quarti, C.; Beljonne, D.; Slawin, A. M. Z.; Zysman-Colman, E.; Morrison, F. D., Stable 6H Organic-Inorganic Hybrid Lead Perovskite and Competitive Formation of 6H and 3C Perovskite Structure with Mixed A Cations. *ACS Appl. Energy Mater.* **2019**, *2* (8), 5427–5437.

Chapter 4: I am the primary author of the text. Synthesis, characterisation and spectroscopy described in this chapter were carried out by me. The work in this chapter has been published:

> Tian, J.; Zysman-Colman, E.; Morrison, F. D. Compositional Variation in Hybrid Organic–Inorganic Lead Halide Perovskites: Kinetically versus Thermodynamically Controlled Synthesis. *Chem. Mater.* **2021**, acs.chemmater.1c00470.

Chapter 5: I am the primary author of the text. Synthesis, characterisation and spectroscopy analysis described in this chapter were carried out by me. Single crystals were grown by me while the diffraction data collection and structure solving were

performed by Dr David B Cordes (University of St Andrews). The work in this chapter has been submitted to ChemRxiv and is under peer review:

Tian, J.; Cordes, D.; Slawin, A.; Zysman-Colman, E.; Morrison, F. Progressive Polytypism and Bandgap Tuning in Azetidinium Lead Halide Perovskites. *ChemRxiv. Prepr.* **2021**. https://doi.org/10.26434/chemrxiv.14502372.v1.

Chapter 6: I am the primary author of the text. Synthesis, materials and optical characterisation described in this chapter were carried out by me. Single crystals were grown by me while the single crystal diffraction data collection and structure solving were performed by Dr David B. Cordes (University of St Andrews).

Acknowledgements

I would like to thank many people for their support during my time studying in the UK.

First and foremost, I would like to convey my gratitude to Prof Eli Zysman-Colman and Dr Finlay Morrison for their support and guidance through my entire time in the UK. Eli is a wise man with vision, and he does a fantastic job at group management. I will always remember how meticulous Finlay is, and he is a hands-on mentor who made my study as a foreign student much easier.

I would like to thank all of the staff at the school of Chemistry, St Andrews. My special gratitude to Dr David B. Cordes and Prof Alexandra M.Z. Slawin for X-ray crystallography. I would like to thank all collaborators: Claudio Quarti and Dr David Beljonne for DFT calculation on $AzPbBr_3$; Dr Karuna Kara Mishra for Raman measurements on $AzPbBr_3$. In addition, I would like to thank all the others for their professional advice and aid on samples analysis: Prof James Scott, Prof Phil Lightfoot, Mr Tim van de Goor, Dr Sian Dutton.

I would like to thank all the group members from EZC and FDM. It is their companionship and help that made this five-year journey joyful and fruitful. Among them, I would particularly like to thank Chenfei, Dianming, Jason and Jonathan for their professional guidance and support on my study. Grant, Kerry, David and Tom brought so much laughter and joy to the lab.

I would like to thank the Chinese Scholarship Council and the University of St Andrews for the PhD studentship support and the chance to experience a whole new way of life. I would like to thank all ELT staff for their help with English language, and for involving me in local culture from the beginning.

I would like to thank my parents - Li Li and Guihui Tian for their support and care throughout my life. I would like to thank my lovely partner Calum for dragging me out of house for air and being the reason I smile.

Funding

Research Data

Research data underpinning this thesis are available at https://doi.org/10.17630/f1f27a88-f5a0-4a56-ba2a-33bc37a0f640

Contents

List of Abbreviations

Abbreviations	Expansion
Az	Azetidinium
BA	Butylammonium
BDA	1,4-benzene diammonium
CBM	Conduction band minimum
CPE	Constant phase element
DCM	Dichloromethane
DFT	Density functional theory
DMA	Dimethylammonium
DMF	Dimethyl formamide
DMSO	Dimethyl sulfoxide
EDX	Energy dispersive X-ray microscopy
FA	Formamidinium
GBL	γ-Butyrolactone
LARP	Ligand-assisted reprecipitation
LED	Light-emitting diode
MA	Methylammonium
NPA	1-Naphthylammonium
OIHP	Organic-inorganic hybrid perovskite
PBE	Perdew-Burke-Ernzerhof
PEA	2-Phenylethylammonium
PMA	Phenylmethylammonium
PXRD	Powder X-ray diffraction
R-P	Ruddlesden-Popper

SCXRD	Single crystal X-ray diffraction
SEM	Scanning electron microscopy
TGA	Thermogravimetric analysis
TMA	Trimethylammonium
TOC	Table of content
VBM	Valence band maximum
XPS	X-ray photoelectron spectroscopy

Chapter 1

Background and Introduction

1.1 Perovskite

Perovskite was discovered by Russian geologist Gustav Rose in 1839.[1] The term was initially used to describe the mineral calcium titanate ($CaTiO_3$) but was soon applied to other compounds which have the same crystal structure. Perovskites share a general formula AMX_3, where A is typically an alkali metal, alkaline earth metal, lanthanoid or organic cation, M is a transition metal or post-transition metal, and X is an anion. In the perovskite structure, M-X octahedra are connected through corner sharing and result in the formation of a three-dimensional framework, while the A-site element occupies the cuboctahedral cavities[2] (Figure **1.1**).
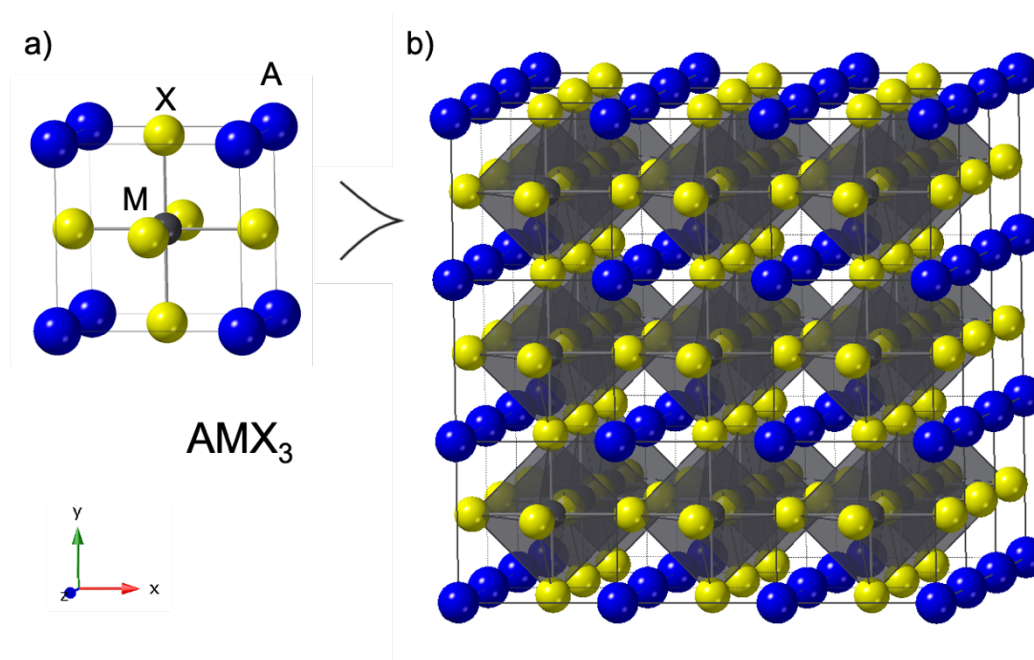
Figure 1.1. (a) A typical model of the AMX_3 perovskite unit cell (b) polyhedral representation of how perovskite structure extends in three dimensions, adapted from Ref. 2 with permission from The Royal Society of Chemistry.

In 1912, the application of X-ray diffraction in studying matter brought a prosperous period of perovskite study. Many oxide perovskites such as $PbTiO_3$ and $BaTiO_3$ were discovered and are still used in industry.[3] In 1893, halide perovskites were first studied by Wells, who discovered the synthesis and structure of all-inorganic halide perovskites $CsPbX_3$ (X = Cl or Br).[4] The simple solution synthesis protocol inspired trials of organic cation replacement at the A-site. In 1978, Weber *et al.* managed to synthesise the first organic-inorganic hybrid perovskite (OIHP) structure using the organic cation methylammonium (MA) $CH_3NH_3^+$ on the A-site, and the crystal structures of $MAPbX_3$ (X = Cl, Br, I)[5] and $MASnBr_xI_{3-x}$ [6] were analysed.

To identify potential A-site elements for corresponding M and X combinations, the Goldschmidt tolerance factor t was introduced to predict the formation of oxide perovskites, with ideal cubic perovskites having the value of $t = 1$. The ionic radii of A, M and X are taken into account in the tolerance factor, but the stability of M-X octahedra is not. The octahedral factor μ is used to examine the coordination of M by six X anions, and a combination of t and μ shows a classification accuracy of 85% for 576 AMX_3 compounds for $0.83 < t < 1.06$ and $0.43 < \mu < 0.78$.[7] Goldschmidt tolerance factor t, and octahedral factor μ, are defined as:

$$t = \frac{r_A + r_X}{\sqrt{2}(r_M + r_X)} \qquad \text{(Equation 1.1)}$$

$$\mu = \frac{r_M}{r_X} \qquad \text{(Equation 1.2)}$$

where r_A, r_M and r_X are the Shannon ionic radii[8] of A, M and X elements in their corresponding valence and coordination states. The concept of tolerance factor can be extended to predict the formation of halide perovskites, although the accuracy is not satisfactory (reported as 74% in 2019 for > 1000 reported halide perovskite compounds[7]). Recently, there have been several attempts to better predict the formation of halide perovskites.[9,10] Christopher *et al.*[7] introduced a new tolerance factor, which combined the octahedral factor into their equation and improved the prediction accuracy of the original tolerance factor from 74% to 91%.

Goldschmidt's group made and analysed the very first series of synthetic perovskites, such as $SrTiO_3$ and $BaTiO_3$ in 1924-26.[11] Since Goldschmidt introduced the principle of the tolerance factor, many perovskite compounds have been synthesised and added to the

perovskite family. The popularity of perovskite materials is highly dependent on their related properties (Figure **1.2**).[12] Perovskite materials have been intensively studied recently due to a combination of their ease of preparation and appealing photochemical properties. This recent boom was inspired by the study of Tsutomu and co-workers on the triiodide perovskite $CH_3NH_3PbI_3$ in 2009, in which they reported a power conversion efficiency of 3.8% using the OIHP material as the key absorber layer in solar cells.[13] From 2009 to 2020, the power conversion efficiency of perovskite solar cells has steadily increased from 3.8% to 25.5%;[14–18] the same improvement in conversion efficiency for Si cells took 25 years to achieve.[19] The use of OIHP materials has since diversified beyond high-efficiency solar cells to photodetectors,[20,21] light-emitting diodes (LEDs)[22,23] and optically pumped lasers[24,25] while the photophysical properties underpinning these applications has been investigated.[26,27] Illustrating the interest in this field, the number of halide perovskite related publications has risen from 34 in 2009 to more than 2900 in 2020,[28] with more than 6,800 indexed citations in 2020 alone.
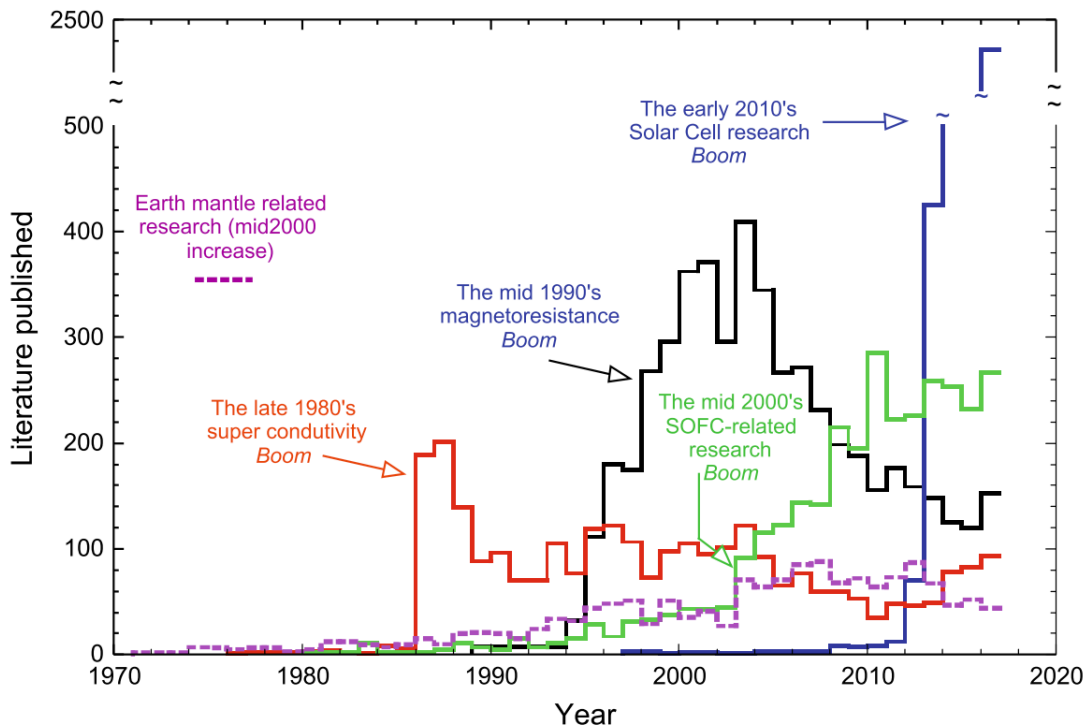
Figure 1.2. Volume of literature published from 1970 to 2017 on perovskite-related research fields, reproduced from Ref. 12 with permission.

1.1.1 Hexagonal perovskite polytypes

Polytypism represents a subset of polymorphism in which the structure of crystalline is the same along two dimensions but differs in three dimensions. Except the typical $CaTiO_3$ cubic perovskite, hexagonal perovskite polytypes share the same molecular formular AMX_3 while the stacking sequence of AX_3 layers alters. There are two basic ways to stack successive closely packed atomic layers – hexagonal packing (h-, ABAB…) and cubic packing (c-, ABCABC…), which are shown in Figure **1.3a**. By altering the ratio of h- and c- stacking of AX_3 layers, different perovskite polytypes such as 2H (h-),[29,30] 9R (hhc-),[31,32] 4H (hc-)[33] and 6H (hcc-)[34,35] etc, can be achieved. These are commonly known as "hexagonal perovskites", the representations of which are shown in Figure **1.3b**. Ramsdell notation is commonly used to describe these perovskite polytypes,[36,37] and takes the form nY, where n denotes the number of stacking layers in the cell and Y indicates the lattice type (R for rhombohedral, H for hexagonal and C for cubic). The great number of stacking possibilities results in potential new structures with diverse physical properties associated with octahedral connectivity, particularly the band structure. The studies in oxide and halide perovskites indicate that hexagonal polytypes normally occur in the case of tolerance factor $t > 1$ (Equation **1.1**), which involves a relatively large A-cation with the same combination of M and X compared to the cubic analogue. Due to the change of connectivity of the metal-halide octahedra (specifically the M-X-M bond angles and M-X bond length in the AMX_3 perovskite), the bandgap of hexagonal perovskites is usually larger than that of the cubic perovskite.[35,38]

1.1.2 Ruddlesden-Popper phases and other perovskite-related structures

Ruddlesden-Popper (R-P) phases are described as a layered structure with alternating layers of AMX_3 perovskite and AX rock-salt along c-axis with general formula $A_{n+1}M_nX_{3n+1}$ or $A'_2A''_{n-1}M_nX_{3n+1}$, where n represents the number of octahedral layers, n = 1, 2, 3… which are separated by additional 'A-cation excess' rock-salt layers. The basic structure of R-P phases with varying n in $A_{n+1}B_nO_{3n+1}$ are shown in Figure **1.4a**. In 1955, Balz and Plieth reported the first R-P phase layered structure K_2NiF_4 (n = 1).[39] In 1957-58, Ruddlesden and Popper found a series of layered structures in oxides.[40] Nowadays, the R-P phase is more commonly used to represent this type of layered perovskite
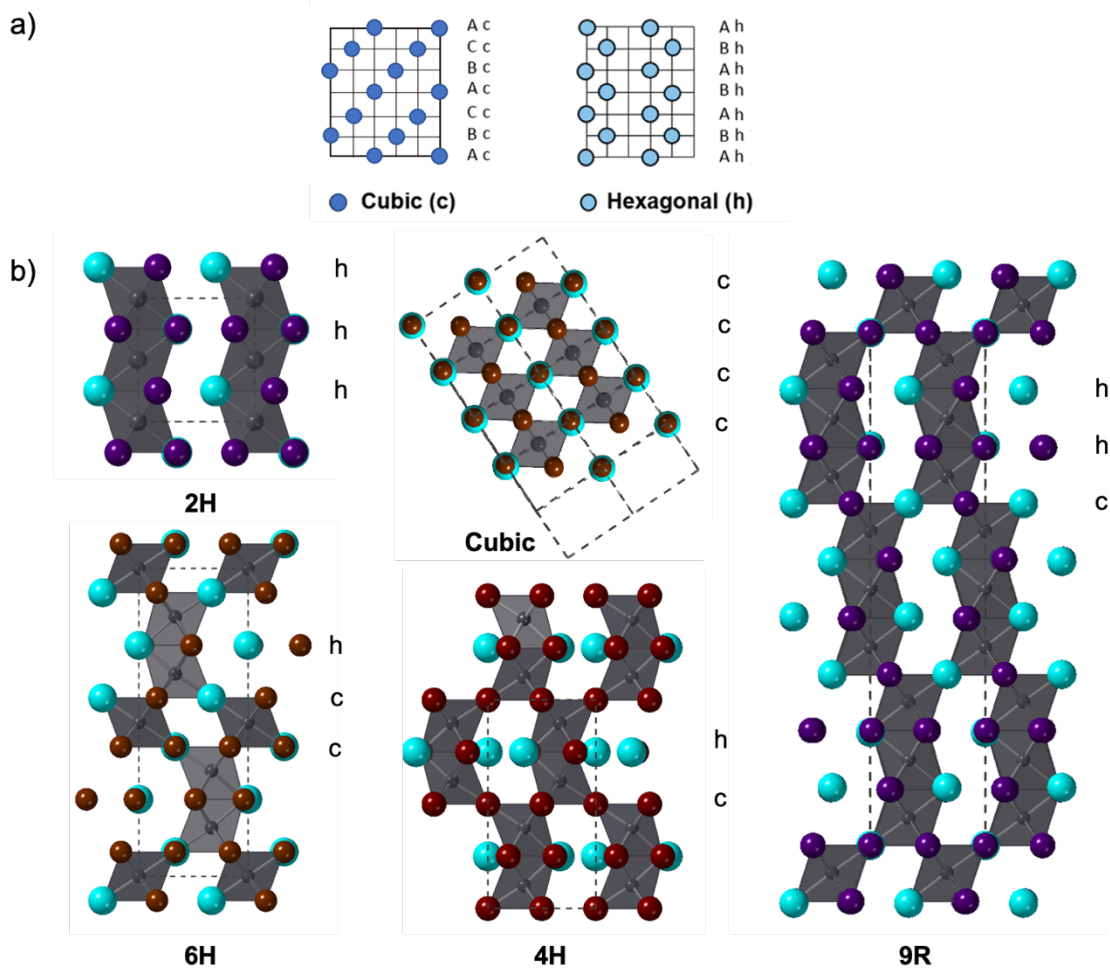
Figure 1.3. (a) Comparison of AX_3 stacking sequence: cubic stacking (*c*-) and hexagonal stacking (*h*-), adapted from Ref. 35 with permission. Copyright (2017) American Chemical Society. (b) Representation of perovskite structures of cubic and hexagonal polytypes with 2H(*h*-), 9R(*hhc*-), 4H(*hc*-) and 6H(*hcc*-) stacking of AX_3 layers.

structure. In the studies on R-P phases, researchers found that tolerance factor failed to give a good prediction of R-P phase stability. In 1979, Ganguli reported an empirical rule that formation of R-P phases (especially for *n* = 1) is associated with the ratio of A-site and metal cation radius - r_A/r_M in the range of 1.7 to 2.4.[41] Since then, a number of R-P phase layered perovskite structures have been synthesised and studied as ferromagnetics,[42] LEDs[43] and solar cells,[44] amongst other applications.

Several families of layered OIHPs containing alternating layers of AMX_3 perovskite and organic cations with structures similar to R-P phases, have been discovered (Figure **1.4b**).
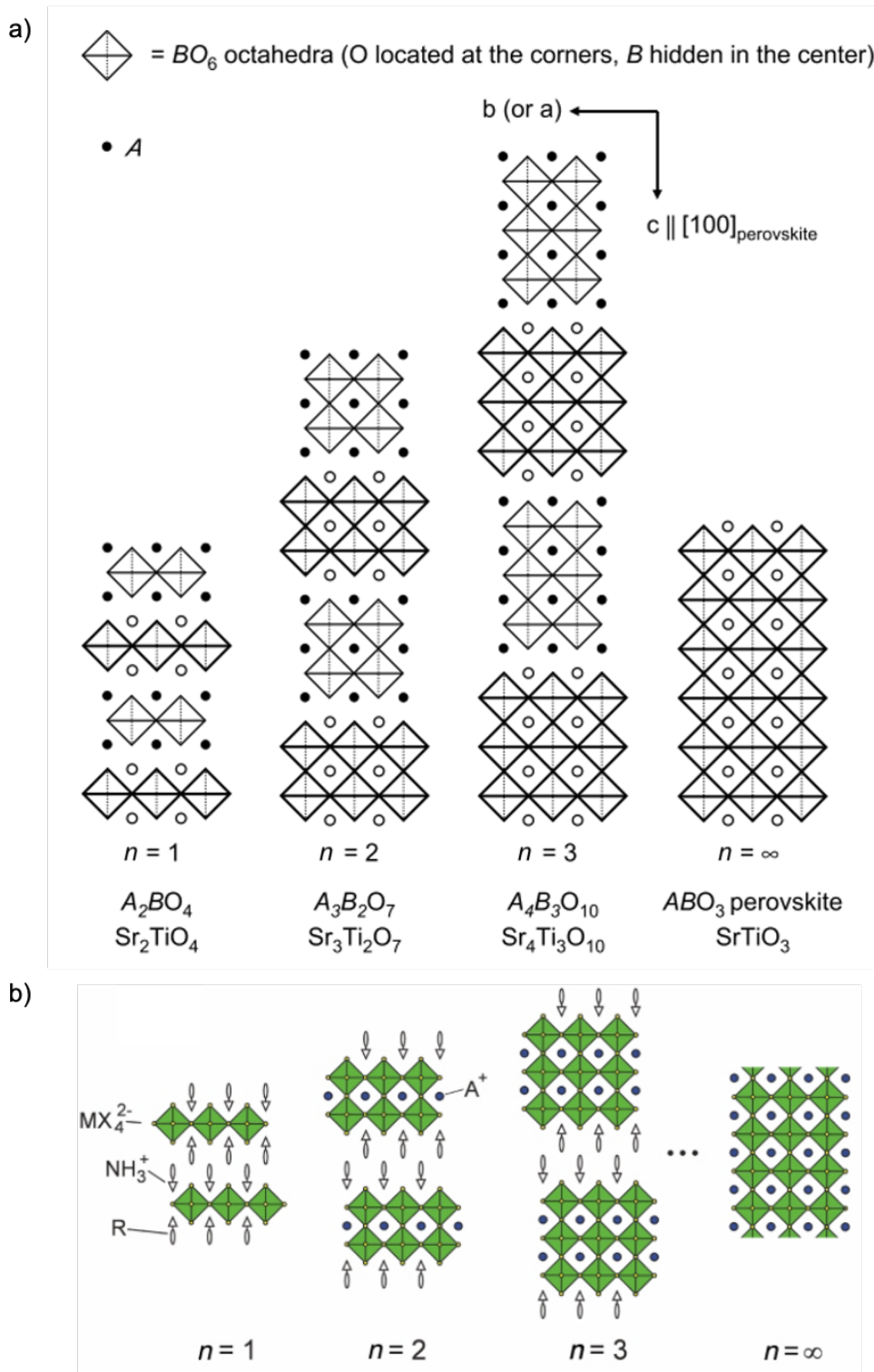
Figure 1.4. (a) Idealised structures of R-P phases $A_{n+1}B_nO_{3n+1}$ (n = 1, 2, 3 and ∞) projected along a- or b- axis. The compositional examples are from Sr(II)-Ti(IV)-O systems, adapted from Ref. 45 with permission. (b) Representation of organic-inorganic hybrid layered structure $(R-NH_3)_2A_{n-1}M_nX_{3n+1}$, reproduced from Ref. 2 with permission from The Royal Society of Chemistry.

Such examples of layered organic-inorganic hybrid structures include BA_2PbI_4 (BA = $C_4H_9NH_3$)[46] and PEA_2PbX_4 (PEA = $C_8H_{12}N$, X = Cl, Br, I),[47,48] in which the organic cations are too big to be accommodated in the cuboctahedral cavities of the 3D MX_6 framework. In addition, by mixing large organic cations, such as those mentioned above, and small organic cations such as MA, organic-inorganic hybrid materials with the general formular $A_2MA_{n-1}Pb_nX_{3n+1}$ can be prepared. They show good bandgap tunability by modifying the number of layers (n) of AMX_3.[46,49] Stoumpos et $al.$[46] reported orthorhombic crystal structures of $BA_2MA_{n-1}Pb_nX_{3n+1}$ (X = Br, I) with bandgaps changing progressively from 2.43 eV (n = 1) to 1.50 eV (n = ∞) with intermediate values of 2.17 eV (n = 2), 2.03 eV (n = 3) and 1.91 eV (n = 4). The thickness of $(BA)_2(MA)_{n-1}Pb_nI_{3n+1}$ can be reasonably controlled by modifying the ratio of BA/MA cations in the precursor solutions.

Other than the 2D perovskite-related structures mentioned above, '1D' organic-inorganic hybrid materials have also been reported where the 1D simply refers to the dimensionality of octahedral connectivity. For example, 1D zigzag chains were observed in $H_2AETHBiI_5$ (H_2AETH = $H_3NC_{18}H_{24}S_2NH_3$),[50] which contain corner-sharing distorted BiI_6 octahedra (Figure **1.5a**). In addition, edge-sharing chain structures were also reported for $NPABiI_4$ (NPA = $C_{10}H_7NH_3$)[51] and $BDAPbI4$ (BDA = $H_3NC_6H_4NH_3$)[52]. The crystal structure of $NPABiI_4$ is shown in Figure **1.5b**. The cations used in these '1D' chain organic-inorganic hybrid materials are summarised in the next section.
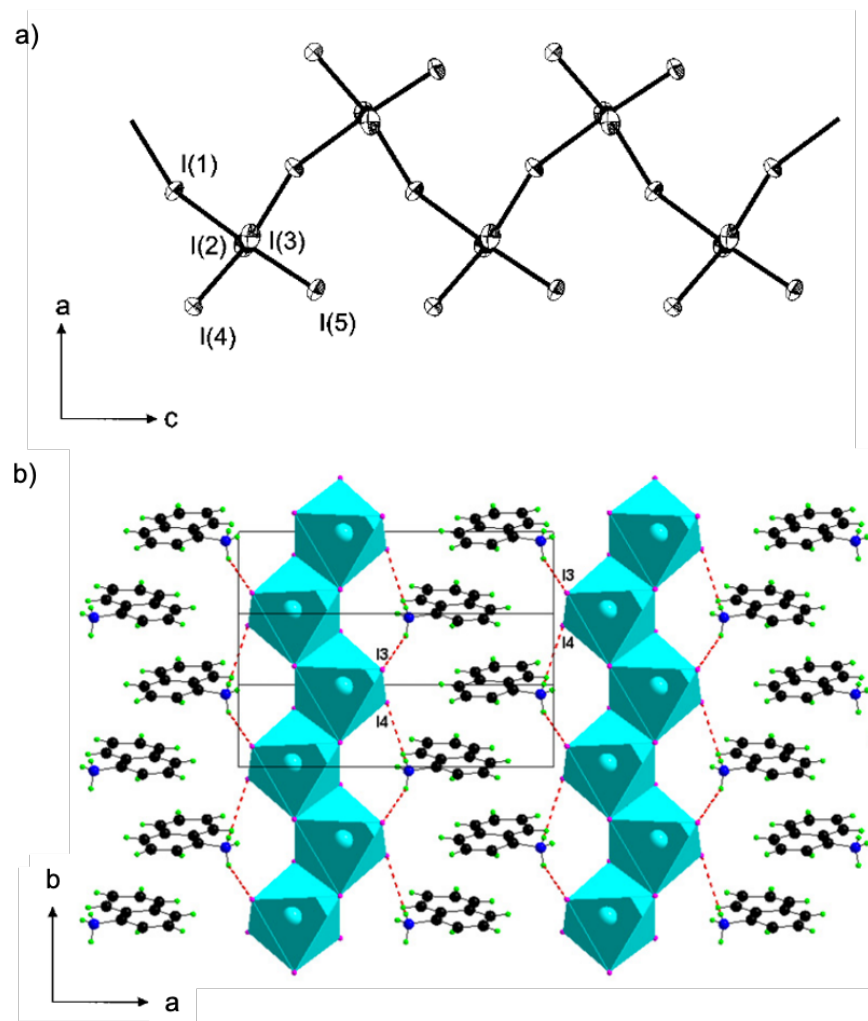
Figure 1.5. (a) The corner-sharing BiI_6 chain structure for $H_2AETHBiI_5$ viewed along the *b*-axis, reproduced from Ref. 50 with permission. Copyright (2001) American Chemistry Society. (b) The crystal packing of $NPABiI_4$ with edge-sharing BiI_6 chain structure viewed along the *c*-axis, reproduced from Ref. 51 with permission.

1.1.3 Organic cations used in perovskites and perovskite-like structures

The use of a wide range of organic cations can provide numerous perovskite and other perovskite-like structures. The recent boom in studies of OIHPs inevitably demands clarity about what kind of structures can be called 'perovskite' structure. Some conservative views suggest[45] that only AMX_3 compounds with structures formed from AX_3 closed packing and octahedrally coordinated M-cations can accurately be termed perovskite, while other more liberal views would use the term 'perovskite' for all structures containing MX_6 octahedra, even if the octahedra are not connected; the latter

have been referred to as '0D perovskite'.[53,54] In this thesis, the only structures termed perovskite are those based on AX_3 closed packing with octahedral M-cations, regardless of how octahedra are connected (corner-sharing, face-sharing or edge-sharing, including hexagonal polytypes). A summary of some of the most common organic cations that form OIHPs or perovskite-related 2D layered and 1D organic-inorganic hybrid structures is shown in Table **1.1**. The structural data included in the table are recorded at room temperature. All OIHPs and perovskite-related low dimensional structures mentioned in the table are synthesised with protonated ammonium cations, except some 1D chain structures which can be obtained with $(CH_3)_3S^+$. Although it is reported that organic cations do not contribute to the valence band or conduction band of the materials,[55] the colour and bandgap change of OIHPs with A-cation size indicates that organic cations can indirectly change the band structure by altering the structure of the materials. Generally, small ammonium cations form (pseudo-) cubic structures with Pb. When the size of the cation gets bigger (Figure **1.6**), other polytypes or perovskite-related structures such as hexagonal, 2D layered or 1D chain structures are expected. It is also reported that perovskites with larger cations exhibit improved humidity resistance due to their hydrophobic properties that result from the aliphatic organic parts.[56]

Table 1.1. Organic cations used in compounds reported as OIHPs, and 2D layered or 1D chained perovskite-like structures with crystallographic information, tolerance factor (t), optical appearance and bandgap.

Cation used	Compound	Structure	Space group	t	Colour	Bandgap / eV	Ref
CH_3NH_3	$CH_3NH_3PbI_3$	Tetragonal	$I4/mcm$	0.91(2)	Black	1.58	[57]
CH_3NH_3	$CH_3NH_3PbBr_3$	Cubic	$Pm\bar{3}m$	0.92(7)	Orange	2.20	[20]
CH_3NH_3	$CH_3NH_3PbCl_3$	Cubic	$Pm\bar{3}m$	0.93(8)	White	2.97	[58]
CH_3NH_3	$CH_3NH_3SnI_3$	Tetragonal	$P4mm$	0.91(4)	Black	1.20	[59]
$HC(NH_2)_2$	α-$HC(NH_2)_2PbI_3$	Cubic	$Pm\bar{3}m$	0.98(7)	Black	1.47	[60]
$HC(NH_2)_2$	δ-$HC(NH_2)_2PbI_3$	Hexagonal	$P6_3mc$	0.98(7)	Yellow		[60]
$HC(NH_2)_2$	$HC(NH_2)_2PbBr_3$	Cubic	$Pm\bar{3}m$	1.00(8)	Orange	2.26	[61]
$HC(NH_2)_2$	$HC(NH_2)_2PbCl_3$	Cubic	$Pm\bar{3}m$	1.02(3)	White	3.35	[62]
$C_2H_5NH_3$	$C_2H_5NH_3SnI_3$	Hexagonal	$P6_3mc$	1.02(1)	Dark red	1.90	[63]
$NH_2(CH_3)_2$	$NH_2(CH_3)_2PbI_3$	2H	$P6_3/mmc$	1.02(2)		2.39	[64]
$NH_2(CH_3)_2$	$NH_2(CH_3)_2PbBr_3$	4H	$P6_3/mmc$	1.05(2)	Colourless	3.03	[65]
$C_3H_6NH_2$	$C_3H_6NH_2PbI_3$	9R	$R\bar{3}m$	0.98(1)	Orange	1.97	[66]

Cation used	Compound	Structure	Space group	t	Colour	Bandgap / eV	Ref
$C_3H_7NH_3$	$(C_3H_7NH_3)_3Sn_2I_7$	2D	$Ac2a$		Red	2.10	63
$C_4H_9NH_3$	$(C_4H_9NH_3)_2PbI_4$	2D	$Pbca$		Orange		67
$C_4H_9NH_3$	$(C_4H_9NH_3)_2SnI_4$	2D	$Pbca$		Dark red	1.9	63
$C_5H_{11}NH_3$	$(C_5H_{11}NH_3)_2PbI_4$	2D	$Pbca$		Red		67
$C_6H_{13}NH_3$	$(C_6H_{13}NH_3)_2PbI_4$	2D	$Pbca$		Orange		67
$NH(CH_3)_3$	$NH(CH_3)_3PbI_3$	2H	$P6_3/mmc$	1.07(2)		2.81	64
$NH(CH_3)_3$	$NH(CH_3)_3PbBr_3$	2H	$P6_3/mmc$	1.10(2)		3.45	64
$NH(CH_3)_3$	$NH(CH_3)_3SnI_3$	Trigonal	$R3c$	1.07(5)	Pale yellow	2.55	63
$CH(NH_2)_3$	$CH(NH_2)_3SnI_3$	Hexagonal	$P6_3/m$	1.03(1)	Dark red	1.90	63
$H_3CCH(NH_2)_2$	$H_3CCH(NH_2)_2\ SnI_3$	4H	$P6_3mc$		Orange	2.15	63
$N(CH_3)_4$	$N(CH_3)_4PbI_3$	2H	$P6_3/m$				68
$N(CH_3)_4$	$N(CH_3)_4SnI_3$	2H	$P6_3/m$	1.06(1)	Pale yellow		63
$N(CH_3)_4$	$[N(CH_3)_4]_3Sb_2Cl_9$	Hexagonal	$P6_3/mmc$		Colourless		69
$C_3H_{12}N_2$	$(C_3H_{12}N_2)PbBr_4$	2D	$P2_12_12_1$		Colourless	3.8	70

Cation used	Compound	Structure	Space group	t	Colour	Bandgap / eV	Ref
$C_7H_{10}N$	$(C_7H_{10}N)_2PbI_4$	2D	*Pbca*		Red		47
$C_8H_{12}N$	$(C_8H_{12}N)_2PbI_4$	2D	*P$\bar{1}$*		Red		47
$C_8H_{12}N$	$(C_8H_{12}N)_2PbBr_4$	2D	*P$\bar{1}$*		Colourless		48
$C_8H_{12}N$	$(C_8H_{12}N)_2PbCl_4$	2D	*P$\bar{1}$*		Colourless		48
$(CH_3)_3S$	$(C_3H_9S)_2SnCl_6$	1D	*Pa$\bar{3}$*		White	4.1	71
$(CH_3)_3S$	$(C_3H_9S)_2SnBr_6$	1D	*Pa$\bar{3}$*		Yellow	2.9	71
$(CH_3)_3S$	$(C_3H_9S)_2SnI_6$	1D	*Pa$\bar{3}$*		Black	1.4	71
$C_2H_{14}N_2$	$(C_2H_{14}N_2)PbBr_4$	1D	*Imma*		Colourless	3.27	72
$H_3NC_6H_4NH_3$	$(C_6H_{10}N_2)PbI_4$	1D	*Pnnm*			2.58	52
$H_3NC_6H_{12}NH_3$	$(C_6H_{18}N_2)BiI_5$	1D				2.29	50,73
$C_{10}H_7NH_3$	$(C_{10}H_{10}N)BiI_4$	1D	*Pbca*		Dark red	2.33	51
$H_3NC_{12}H_{24}NH_3$	$(C_{12}H_{30}N_2)BiI_5$	1D	*Ibam*			2.41	50
$H_3NC_{18}H_{24}S_2NH_3$	$(C_{18}H_{30}S_2N_2)BiI_5$	1D	*Aba*2			2.53	50

(Pseudo-)cubic

Methylammonium
CH_3NH_3

Formamidinium
$HC(NH_2)_2$

Hexagonal or 2D layered

Ethylammonium
$C_2H_5NH_3$

Dimethylammonium
$NH_2(CH_3)_2$

Azetidinium
$C_3H_6NH_2$

Isopropylammonium
$C_3H_7NH_3$

Trimethylammonium
$NH(CH_3)_3$

Guanidinium
$CH(NH_2)_3$

Acetamidinium
$H_3CCH(NH_2)_2$

Tetramethylammonium
$N(CH_3)_4$

N^1-methylethane-1,2-diammonium
$C_2H_{12}N_2$

Butylammonium
$C_4H_9NH_3$

Pentylammonium
$C_5H_{11}NH_3$

Hexylammonium
$C_6H_{13}NH_3$

Phenylmethylammonium
$C_7H_{10}N$

2-Phenylethylammonium
$C_8H_{12}N$

Trimethyl sulfonium
$(CH_3)_3S$

N,N′-Dimethylethylenediammonium
$C_2H_{14}N_2$

1,4-Benzene diammonium
$H_3NC_6H_4NH_3$

1-Naphthylammonium
$C_{10}H_7NH_3$

1D chained

Figure 1.6. Structural formulae of the organic cations mentioned in Table **1.1**.

13

1.1.4 Octahedral distortion and cation dynamics

Understanding the nature of the photochemical properties of halide perovskites is the key to enhancing the performance of materials and designing novel structures for optoelectronics. A potential clue lies in the lattice instability of these systems in phase space; symmetry-lowering distortion of the group 14 divalent cation containing octahedra occurs while altering composition, pressure, strain and temperature (Figure **1.7**). This instability is influenced by the electronegativity of the coordination X site, the size and shape of A-site cation and the stability of the lone pair carrying metal cation. Metal cations with lone pair s^2p^0 valence state (e.g. Pb^{2+}, Sn^{2+}, Tl^+, Bi^{3+}) are inclined to symmetry-lowering distortion, which is related to second-order or pseudo-Jahn-Teller effects.[74,75] Douglas *et al.*[76] reported a lone pair-driven Sn^{2+} off-centring displacement in CsSnBr$_3$ from 300 K to 420 K. Laurita *et al.*[77] compared AMX$_3$ systems (A = MA, formamidinium (FA); M = Pb^{2+}, Sn^{2+}; X = Br^-, I^-) and found that the magnitude of M-cation dynamic displacement increased with the exchange of a larger A-site cation (FA for MA) and a more electronegative anion (Br^- for I^-).
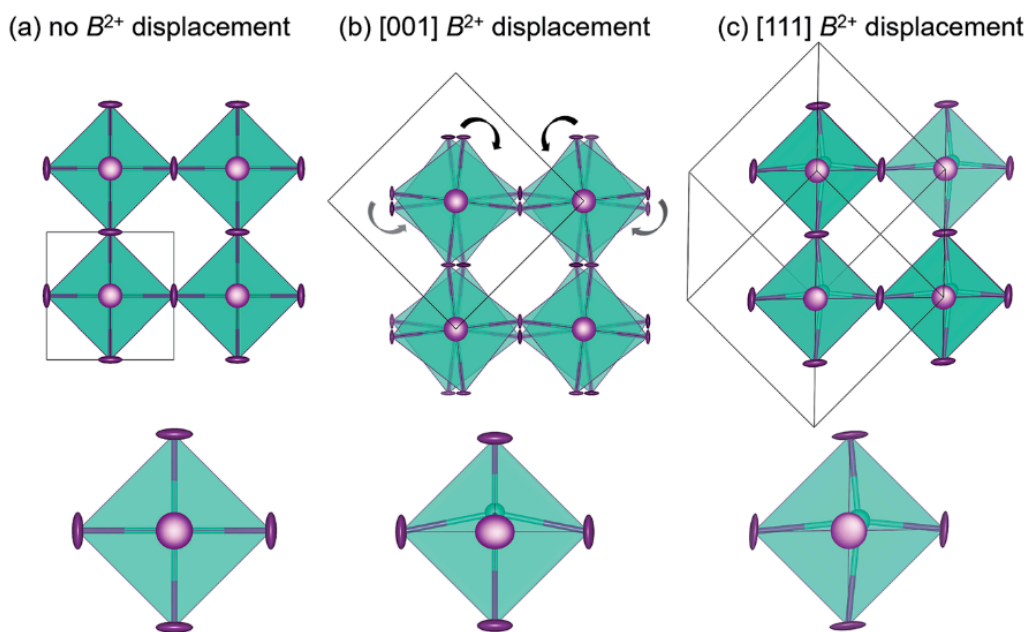
Figure 1.7. (a) No M-site off-centering or octahedral rotation (b) M-site off-centering and static octahedral rotation (c) M-site off-centering and no octahedral rotation. Reproduced from Ref. 77 with permission from The Royal Society of Chemistry.

The most common type of distortion driven by the size of the A-cation is octahedral tilting, which affects the B-X orbital overlap and hence the optical bandgap.[59] The crystallographic information in Table **1.1** indicates that the symmetry and packing configuration of OIHPs or other perovskite-related low dimensional structures is associated with the A-cation in addition to the choice of metal and halide. The role of the A-cation in OIHPs is closely related to the diverse steric constraints enforced by these cations (e.g. disparity in shape, length, degree of flexibility and rotation), the interactions between the organic cations and the inorganic framework (e.g. hydrogen bonding and ionic forces between the halides and ammonium end groups), and forces between the organic cations themselves (e.g. Van der Waals forces or aromatic interaction).[50,78,79] MAPbI$_3$ is an example of this - MAPbI$_3$ goes through phase transitions from cubic to tetragonal to orthorhombic at ca. 330 K and 160 K, respectively (Figure **1.8**). Neutron and synchrotron XRD indicate MA cations are fully disordered (dynamically rotating), partially ordered and fully ordered (static) in the cubic, tetragonal and orthorhombic crystal structures, respectively.[80] Molecular dynamic simulations indicate that the dipole-dipole interaction between MA ions is essential to the formation of ordered domains, in which the MA dipoles take positions in energetically favoured, ordered structures, especially in the low temperature orthorhombic structure.[81]
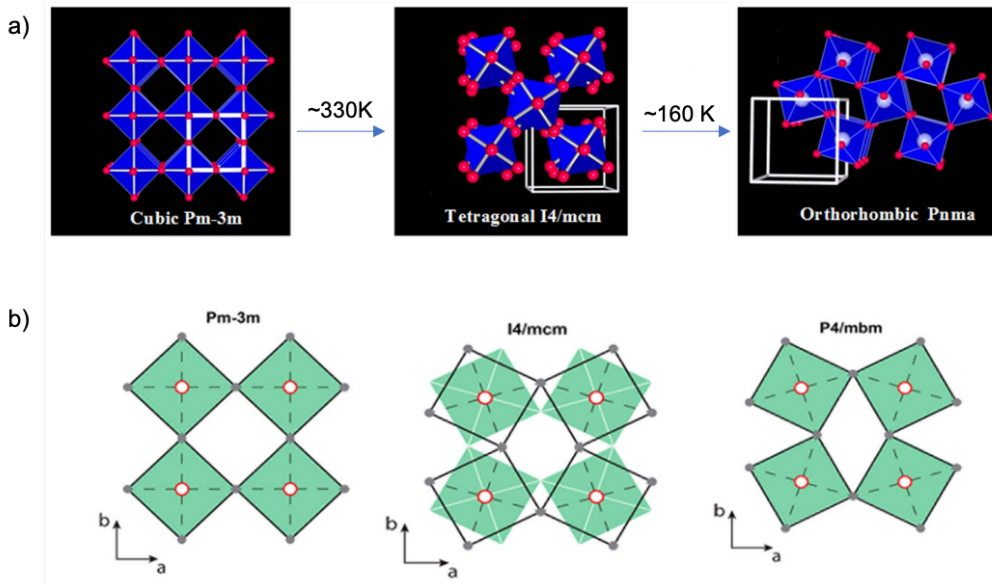
Figure 1.8. (a) Crystal structure of MAPbI$_3$ going through phase transition from cubic to tetragonal to orthorhombic at ca. 330 K and 160 K. (b) Relative rotation of adjacent PbI$_6$ octahedra viewed along *c*-axis. Adapted from Ref. 81 and Ref. 80 with permission.

The formation of domains leads to the phase transitions in OIHPs, which are induced by the joint interactions between dipole-dipole interactions of MA cations and interactions between MA cations and Pb-I lattice. The process is combined with the deformation of the Pb-I lattice which supports the transition from free rotating dipoles to ordered domains.

1.1.5 Phase transitions

Generally, phase transitions are the physical procedures of transition between different states of matter: gas, liquid and solid. The concept of order of phase transition was suggested by Ehrenfest[82] as the order of lowest differential of Gibbs Energy (G), which appeared to be discontinuous at a certain temperature.[83] This temperature point is the phase transition temperature or critical temperature, T_C. Gibbs Energy, first differential of Gibbs Energy and the gradient of entropy can be defined as:

$$G = H + TS \qquad \text{(Equation 1.3)}$$

$$dG = -SdT + Vdp \qquad \text{(Equation 1.4)}$$

$$dS = C_p \frac{dT}{T} \qquad \text{(Equation 1.5)}$$

where H, T, S, V, p, C_p are enthalpy, temperature, entropy, volume, pressure and heat capacity, respectively. With the equations above, expression of volume and heat capacity can be denoted as $V = \left(\frac{dG}{dp}\right)_T$ and $C_p = (\frac{d^2G}{dT^2})_p$. In other words, volume and heat capacity represent the first and second differential of G with appropriate constraint (constant T or p). Thus, for a first-order phase transition, the volume (V) displays a discontinuity (Figure 1.9a) while heat capacity (C_p) would display a discontinuity for a second-order phase transition (Figure 1.9b).

In addition to the Ehrenfest classification, one type of phase transition in thermodynamics includes the idea of symmetry breaking. Symmetry breaking during the phase transition is often measured with the dielectric response of the matter or by XRD. The dielectric response, with variations such as temperature and frequency of the applied field, represents the polarisation change during the transition (see further discussion in Section 2.1.6). XRD can identify the phase transition with additional diffraction peaks associated

16

with the symmetry change of the materials, in addition to continuous or discontinuous changes in volume (see further discussion in Section **2.1.1**).
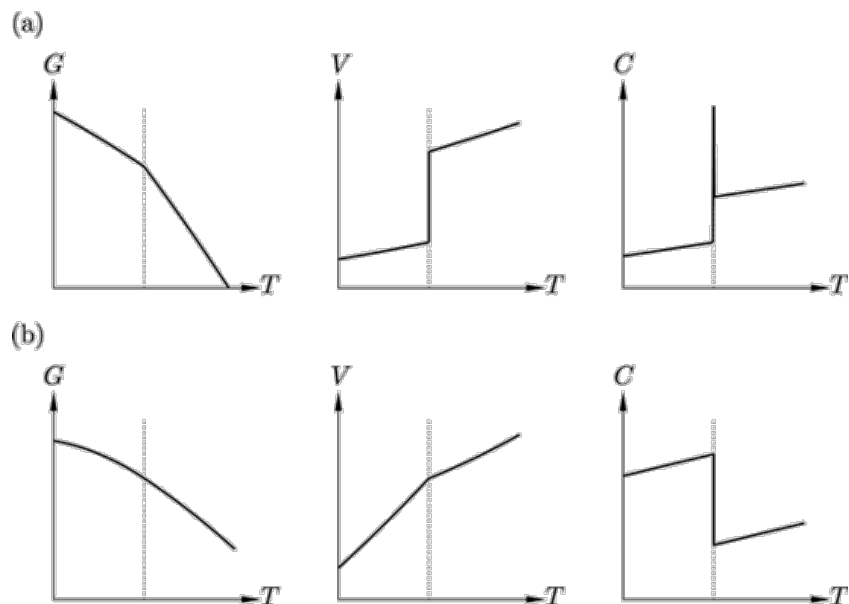
Figure 1.9. Order of phase transition defined by Ehrenfest: (a) first-order phase transition (b) second-order phase transition. G, V, C, T are Gibbs Energy, volume of the matter, heat capacity and temperature, respectively. The phase transition temperatures T_C are marked by vertical dotted lines. Reproduced from Ref. 83 with permission.

1.1.6 Band structure of perovskites

The cubic aristotype is one of the most common crystal systems for OIHPs. The band structure diagram of one example of cubic OIHP (MAPbI$_3$) is shown in Figure **1.10**. From this diagram we can see that the MAPbI$_3$ perovskite is a direct bandgap material. The valence band maximum (VBM) has most contribution from the hybridisation of the I 5p orbitals and Pb 6s orbitals, and the conduction band minimum (CBM) from the Pb 6p orbitals. This suggests that the organic cations do not contribute directly to the bandgap of OIHPs. It is reported that the role played by the organic A-cations is simply to stabilise the perovskite structure by their cation ionic size and the hydrogen bonding between the metal-halide framework.[2,84] The size of the A-cation will also determine the degree (if any) of octahedral tilting, and so the M-X orbital overlap. However, this cannot fully

address the question of why perovskites with the same elemental composition[63,85] are stable as different structures - for example, $CH_3C(NH_2)_2SnI_3$ can adopt both $4H\text{-}BaRuO_3$ and $9R\text{-}BaRuO_3$ structures. More evidence is needed to determine how the organic molecules affect the structure and properties of these materials.
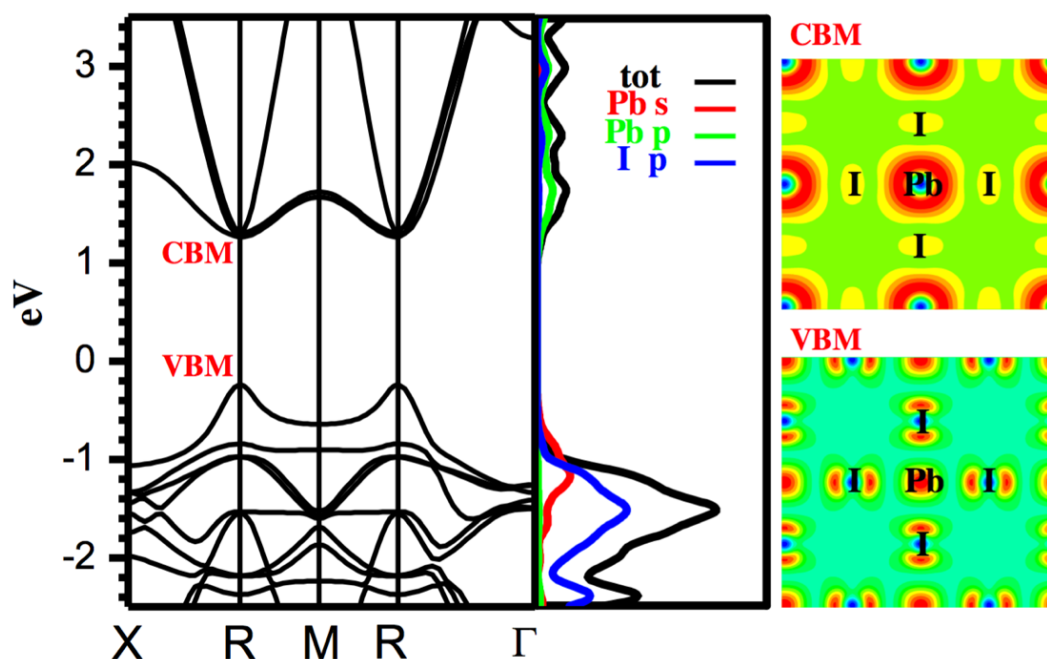
Figure 1.10. Band structure of $MAPbI_3$ perovskite, reproduced from Ref. 86 with permission.

1.2 Synthesis of OIHPs

Solution precipitation, vapor-assisted solution crystallisation and mechanosynthesis are typically used to obtain polycrystalline or single crystal perovskite materials. Other methods such as vapor deposition[87] are less common which would not be discussed in detail in this section.

1.2.1 Solution precipitation

Perovskite thin films are the key functional layers for perovskite photovoltaics and LEDs. Such films are typically made in one[13,88–90] or two[91] steps from precursor solutions (PbX_2 and MAX or FAX). Commonly used solvents include DMF, DMSO and GBL for the relatively good solubility of both lead and organic salt precursors in them, and their high boiling point which enables slow crystal nucleation. Kojima et $al.$[13] reported preparing $MAPbI_3$ perovskite films by one step deposition of a precursor solution of MAI and PbI_2 in DMF on TiO_2 substrates. Antisolvent assisted deposition,[88] blade-coating,[89] and gas and vacuum pumping[90] are all utilised to aid the uniformity of perovskite thin films. In two-step deposition (Figure **1.11a**), solutions containing PbX_2 are deposited on the substrate first and then dried, leaving PbX_2 as the nucleation centre for the perovskite. The solutions of organic cation salts are then spin-coated and annealed, typically at 100 °C.[91]

Other than thin films, perovskite single crystals can be obtained with solution crystallisation. Inverse temperature crystallisation is a common method which is reported to obtain millimetre sized crystals (Figure **1.11b**).[20,58] This method is possible due to the retrograde solubility of $APbX_3$ (A = FA or MA and X = Br or I) in DMF and GBL.[92] For instance, two-inch-sized single crystals of $MAPbX_3$ (X = Cl, Br, I) can be obtained by increasing the temperature of precursor solution in the range of 80 to 100 °C.[58] Cooling HX-based precursor solutions is another common method to obtain single crystalline perovskite which was first reported by Poglitsch and Weber in 1987.[93] This method is based on the reduced perovskite solubility in the HX based aqueous solvent with a lower temperature. For examples, cooling concentrated aqueous solution of HX acid, MA^+ and Pb^{2+} from ca. 100 to 20-40 °C allows $MAPbX_3$ (X = Cl, Br, I) crystal growth.[59]

Ligand-assisted reprecipitation (LARP) is commonly used to obtain OIHP nanostructures, such as nanoplatelets, nanowires and quantum dots.[94] In the presence of assisting ligands, the precursor solution in good solvent (e.g. DMF, DMSO) is added dropwise into a poor solvent (e.g. toluene, hexane). Assisting ligands reported in the literature are typically alkyl amines (e.g. octylamine, dodecyl amine, hexadecyl amine) and carboxylic acids (e.g. oleic acid, octanoic acid).[94,95] After the precursor solutions are added to the poor solvent, an emulsion forms with the help of the assisting ligands. The subsequent addition of de-

emulsifiers (e.g. tert-butanol or acetone) triggers recrystallisation, and perovskite nanocrystals are obtained. Huang *et al.*[96] reported a study on the emulsion synthesis of colloidal halide perovskite MAPbBr$_3$ with a quantum yield up to 92 %.
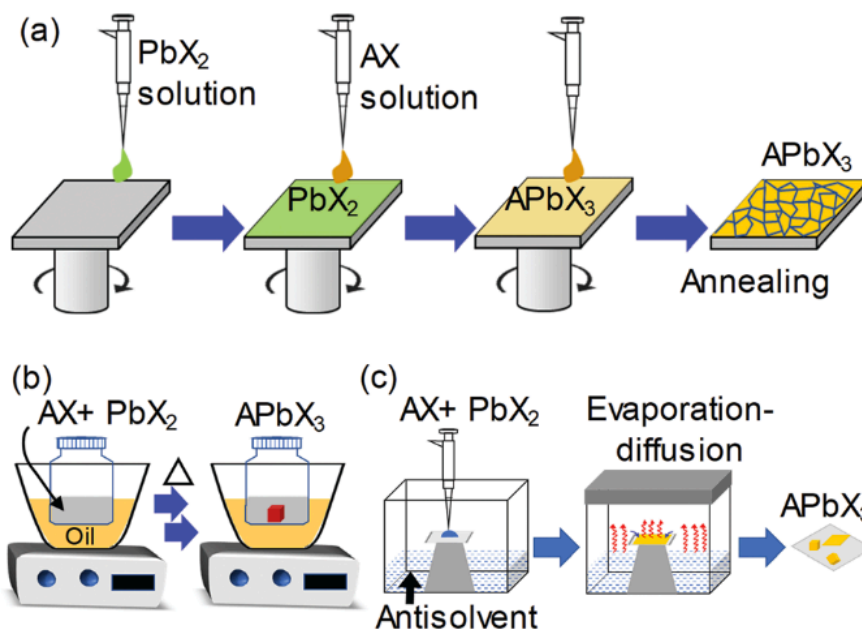
Figure 1.11. Schematics of perovskite synthesis: (a) two-step solution deposition (b) inverse temperature crystallisation (c) antisolvent vapor-assisted crystallisation. Reproduced from Ref. 94 with permission from The Royal Society of Chemistry.

1.2.2 Vapor-assisted solution crystallisation

Antisolvent vapor-assisted solution crystallisation is another commonly used technique to obtain single crystals (Figure **1.12**). Precursor solutions in an open vial are put in a sealed chamber with a low boiling point antisolvent (e.g. DCM, chloroform, ethyl acetate). Perovskite single crystals are obtained by slow diffusion of the antisolvent into the perovskite precursor solutions. By using this method, Shi *et al.*[16] reported high quality and low trap-state density single crystals of MAPbX$_3$ (X = Br, I).

Other than the antisolvent vapor-assisted solution crystallisation, a two-step vapor deposition method is reported to synthesise perovskite nanocrystals.[97] This method uses a first step similar to the two-step solution precipitation detailed above - the PbX$_2$

20

solutions are deposited and dried on the substrate (Figure **1.12**). Instead of using solution in the second step, MX vapor flow passes the PbX$_2$-containing substrate and forms perovskite nanocrystals such as nanowires and nanosheets. The advantage of this two-step vapor-assisted solution method is to produce high-quality crystalline materials for highly efficient photovoltaics.[97] The challenges remaining for this method are to improve the stability of materials, and to reduce the cost and time involved in synthesis. Liu *et al.*[98] reported the synthesis of nanosheets of MAPbI$_3$ which are as thin as a single unit cell (ca. 1.3 nm) and can be used as photodetectors.
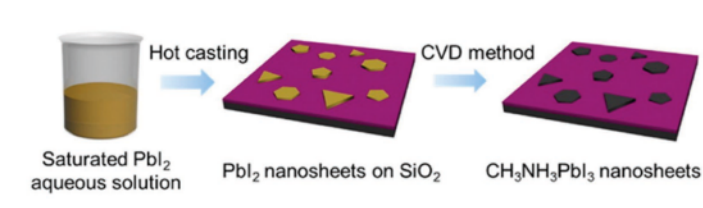
Figure 1.12. Schematics of a two-step vapor deposition method to synthesise MAPbI$_3$, adapted from Ref. 98 with permission. Copyright (2016) American Chemical Society.

1.2.3 Mechanosynthesis

Mechanosynthesis has been reported as a simple and effective way to obtain OIHPs. In addition, grinding is an environmentally friendly (solvent free) approach and can reduce the particle size of the samples by mechanical force. Different kinds of milling equipment such as planetary ball mills, shaker mills and attritor mills are utilised to synthesise perovskite.[99] The mechanosynthesis technique was first reported to synthesise OIHPs by Stoumpos *et al.*[59] In their study, they used hand grinding in an agate mortar to synthesise MAPbI$_3$ and they noted that a subsequent thermal annealing in the vacuum was essential to obtain the pure phase products. After that, many following studies show that electrically powered ball milling is sufficient to synthesise single phase perovskite.[100,101] Hong *et al.*[102] reported a successful solvent-free large scale mechanosynthesis of around 250 g of CsSnX$_3$ (X = I, Br or Cl) and FAPbI$_3$. It has been reported that when using solution precipitation, the stoichiometry of precipitation products does not always match that of the reaction solution.[103–106] This does not occur in mechanosynthesis. Thus, the

latter method is used to synthesise mixed A-cation,[107] mixed metal[108] and mixed halide perovskites[109] with more carefully controlled composition. Chen *et al.*[109] reported a mechanosynthesis of mixed halide perovskite $APbX_3$ (A = MA and FA, X = Cl, Br and I) which yielded full-spectral emissions with a maximal photoluminescence quantum yield up to 92 % (Figure **1.13**).

Despite the advantages of large-scale processing and being environmentally friendly, grinding is not as common a method of OIHP synthesis as solution synthesis. The solution synthesis is preferred when manufacturing devices because solution can be easily processed into thin films by spin-coating and blade-coating methods compared to bulk powder.[110] Single crystals are important when studying the structure of OIHPs, and in terms of single crystal growth, solution or vapor-assisted solution methods are preferred as grinding methods cannot obtain single crystals. Both methods are proven to obtain pure phase OIHPs and have no obvious impact on the stability of compounds.[111]
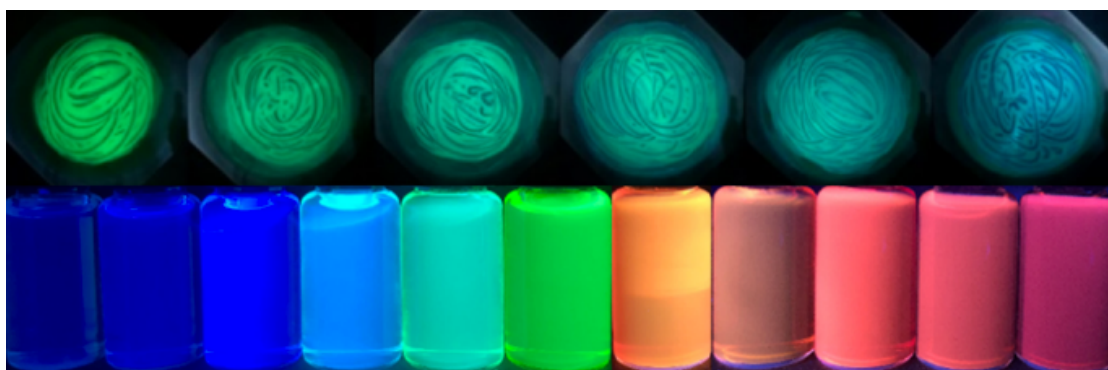
Figure 1.13. Photos showing luminescence under a UV lamp of mixed halide $FAPbX_3$ (X = Cl/Br, Br/I) perovskite nanocrystals in mortar pestle (top) and in toluene suspension (bottom), reproduced from Ref. 109 with permission. Copyright (2019) American Chemical Society.

1.3 Compositional variations of perovskites

OIHPs are currently one of the fastest-growing areas of solid-state/condensed matter science. However, many OIHP compounds are unstable in air due to moisture-induced decomposition and phase changes, which hinders the light-harvesting and electron/hole

transportation.[59,112] This is an adverse feature in their use in photovoltaics. To address this stability issue, different material design strategies such as mixed cations,[113–115] mixed halides,[116–119] nanostructuring[120] and contact passivation[121] have been explored.

The compositional variations among A, M and X result in a diverse range of structures with distinct chemical and physical properties. Here, a brief review of doping on A, M and X sites of halide perovskites is given as a background to this thesis.

1.3.1 Mixed A-site perovskite

Based on the concept of tolerance factor, the choice of ideal A-cations for a certain combination of M and X to form the cubic perovskite structure is rather limited. Other than the ideal cases, AMX_3 compounds usually adapt structural distortion - the most common type of distortion driven by the size of the A-cation is octahedral tilting which affects the B-X orbital overlap and hence the optical bandgap.[59] The pioneering work in halide perovskites used MA^+ as the A-site cation to produce a cubic 3D-perovskite structure,[13] with FA^+ also adopting the cubic structure.[122] Generally, these metal halide perovskites suffer from lack of resistance to moisture, especially for $MAPbI_3$, which decomposes to PbI_2 in the presence of water.[123,124] Doping A-site cations has been reported as an effective method to improve the moisture resistance and thus improve the stability of the materials; Prochowicz et al.[107] obtained a mixed A-cation solid solution system $MA_xFA_{1-x}PbI_3$ by mechano-synthesis to stabilise the α-$FAPbI_3$ cubic phase in air, which is a key absorber layer in highly efficient solar cells.[15,125]

Moreover, doping a relatively larger cation such as BA, PEA or pentylammonium and so on, could result in two-dimensional (2D) layered structures, which form by cutting the framework of the 3D perovskite into precise 2D slabs. 2D perovskite-like structure have been reported to be more tolerant to moisture than the 3D analogues and display bandgap tunability.[49] Stoumpos et al.[46] reported a study of layered perovskite-like structures by doping BA into $MAPbI_3$, the bandgap of which can be tuned from 2.43 eV to 1.50 eV by changing the composition of $BA_2MA_{n-1}Pb_nI_{3n+1}$ (n = 1, 2, 3, …). Hassan et al.[126] reported $(C_{18}H_{35}NH_3)_2MA_{n-1}Pb_nI_{3n+1}$ (n = 1, 2, 3) with absorption peaks maxima at 505 nm (2.45 eV), 565 nm (2.19 eV), and 593 nm (2.09 eV) (Figure **1.14**). Bandgaps of these 2D

layered structures vary with the number of layers as the absorption is mainly ascribed to the electronic transitions within the inorganic layers. Other advantages of A-cation doping include improved power conversion efficiency of photovoltaic devices[17,127] and reduced trap states in the fabrication of solar cells.[56,128] Saliba *et al.*[17] achieved high efficiency solar cells up to 21.6% with a mixed A-cation composition $(Rb,Cs,MA,FA)PbI_3$, which retained 95% power conversion efficiency after 500 hours at 85 °C.
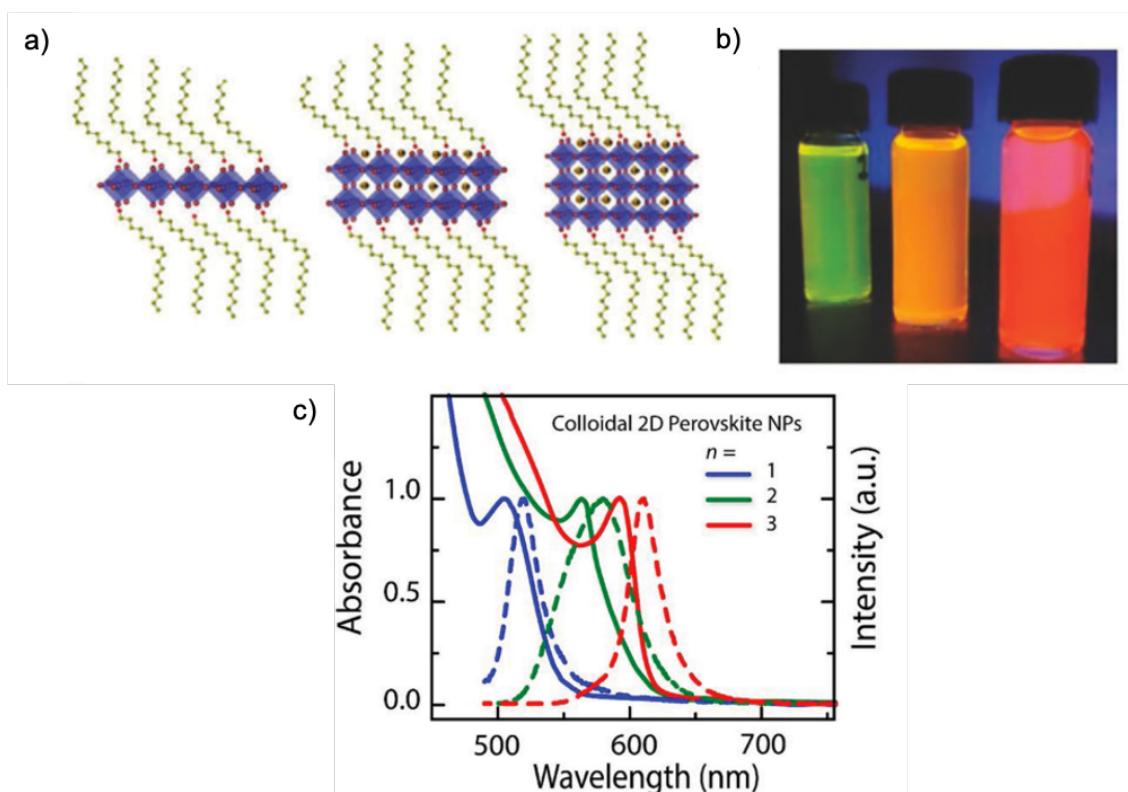
Figure 1.14. (a) Schematic structure of the 2D layered structures $(C_{18}H_{35}NH_3)_2MA_{n-1}Pb_nI_{3n+1}$ (n = 1, 2, 3) (b) Photo of 2D organo-lead perovskite-like nanocrystals solution in toluene (left to right, n = 1, 2, 3) (c) Absorption spectra and steady-state photoluminescence of $(C_{18}H_{35}NH_3)_2MA_{n-1}Pb_nI_{3n+1}$. Reproduced from Ref. 126 with permission.

1.3.2 Mixed metal perovskite

Although lead halide perovskites have drawn extensive attention due to their distinct optoelectrical properties, lead toxicity remains a problem in the commercialisation of the

materials. To replace lead, doping isovalent (e.g. Sn^{2+}, Mn^{2+}, etc)[116–118] and heterovalent (e.g. Bi^{3+}, In^{3+}, etc)[119,129] metal ions has been studied. For example, $CsPb_xMn_{1-x}Cl_3$ quantum dots have been reported with a maximum photoluminescent quantum yield up to 54% with tuneable emission from 569 to 587 nm.[118] Mn-doping in halide perovskites results in no change to the original crystal structure, and the absorption spectra indicate a small effect on the electronic structure. (Figure **1.15a**). Notably, sensitized Mn luminescence (ca. 600 nm) from *d-d* transitions was found, which results from the efficient energy transfer from the excitons of the perovskite host (Figure **1.15b**). Furthermore, Mn-doping in the nanocrystals in turn improved the photoluminescence of the perovskite host.[116] In addition to Mn-doping, Bi-doped $CsPbBr_3$ crystals exhibit much broader absorption spectra compared to undoped $CsPbBr_3$, and the colour of Bi-doped crystals changes from orange to deep red with a higher percentage of Bi in the composition.[119] This bandgap narrowing arises from the interaction between the electrons and positively charged dopants (Bi^{3+}). Double perovskites with general formula $A^I_2M^IM^{III}X_6$ ($A^I = Cs^+$, MA, $M^I = Ag^+$, Cu^+ and $M^{III} = Bi^{3+}$, In^{3+}, Sb^{3+} etc) were reported as replacements of lead perovskites.[86,130,131] $Cs_2AgBiBr_6$ and $Cs_2AgBiCl_6$ were reported to be stable in air with an indirect bandgap of 2.19 eV and 2.77 eV respectively.[130] Compared to $CsPbBr_3$ (2.22 eV) and $CsPbCl_3$ (2.99 eV), which have direct bandgaps, the source of indirect bandgap in double perovskites is the altered electronic structure of both valance band and conduction band.[132]
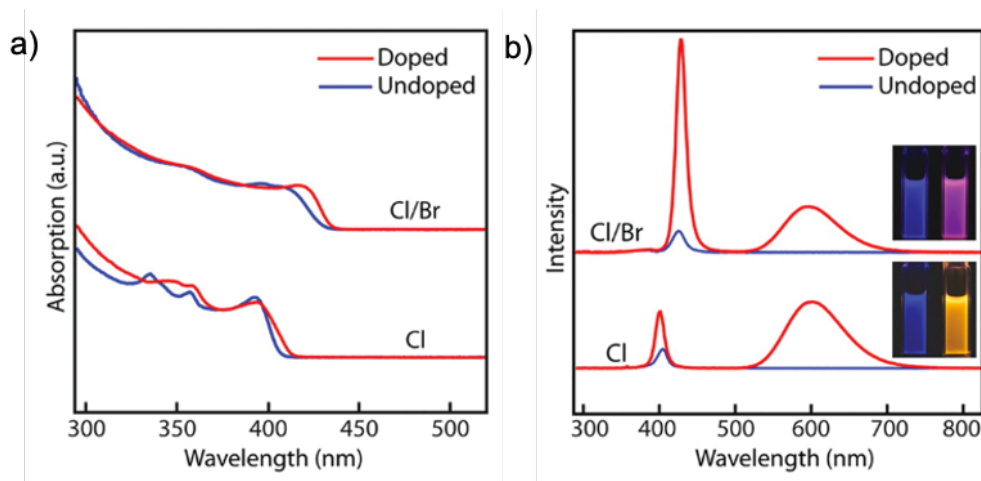
Figure 1.15. (a) absorption spectra and (b) photoluminescence of Mn-doped and undoped $CsPbX_3$ (X = Cl, Br) nanocrystals. Reproduced from Ref. 116 with permission. Copyright (2016) American Chemical Society.

Despite the attention paid to the lead-free perovskites, there is still a performance gap between them and the lead-containing perovskite materials.

1.3.3 Mixed halide perovskite

As the band structure of OIHPs has a strong dependence on halide orbitals and Pb-X orbital interaction, varying the halide, X, is a common method to realise bandgap tunability for halide perovskites. [35,109,133] Yuiga *et al.*[133] showed that the bandgap of MAPbBr$_x$I$_{3-x}$ varied quadratically with Br content from 1.65 to 2.38 eV while the structure changed from tetragonal to cubic. Jang *et al.*[134] reported the synthesis of MAPbBr$_{3-x}$Cl$_x$ and MAPbBr$_{3-x}$I$_x$ nanocrystals by halide exchange reactions of MAPbBr$_3$ with MACl and MAI, respectively (Figure **1.16a**). Both absorption onset and photoluminescence peaks of MAPbBr$_{3-x}$Cl$_x$ and MAPbBr$_{3-x}$I$_x$ films showed systematic shifting with composition as shown in Figure **1.16b.** Corresponding bandgap calculations indicate a wide range of tuneable bandgap from 1.6 to 3.0 eV. Levchuk *et al.*[122] reported nanocrystals of FAPbBr$_{3-x}$Cl$_x$ and FAPbBr$_{3-x}$I$_x$, the photoluminance energy of which was found to change from 1.68 eV to 2.98 eV(Figure **1.16c**). Bandgap-composition relationships of MAPbX$_3$ and FAPbX$_3$ indicate their band structure has a strong dependence on the energy of Cl, Br or I orbitals and Pb-X orbital interaction.

Other benefits of mixed halide perovskites include improving solar cell power conversion efficiency and the stability of the perovskite materials.[14,135] Jun *et al.*[135] reported that mixing 15-20% Br in MAPbI$_3$ resulted in solar cells which could keep 95% efficiency for more than 15 days after exposure to humidity, while the efficiency of triiodide cells dropped below 50% after the same exposure. The authors explained that mixing MAPbI$_3$ with Br leads to a stable and compact structure, as the partial substitution of larger I with smaller Br results in the reduction of lattice constant and a transition from tetragonal to cubic phase. Cl doping in OIHPs has been reported to improve the carrier mobility, which is crucial in achieving competitive photovoltaic efficiency.[127,136] Madjet *et al.*[137] performed molecular dynamics simulations and found that incorporation of 3% - 4% Cl in MAPbI$_3$ can slow down the carriers relaxation dynamics due to the structural distortion caused by Cl doping. As a result, the lifetime of excitons is increased, which gives a better chance of charge separation, and improves the carrier mobility.
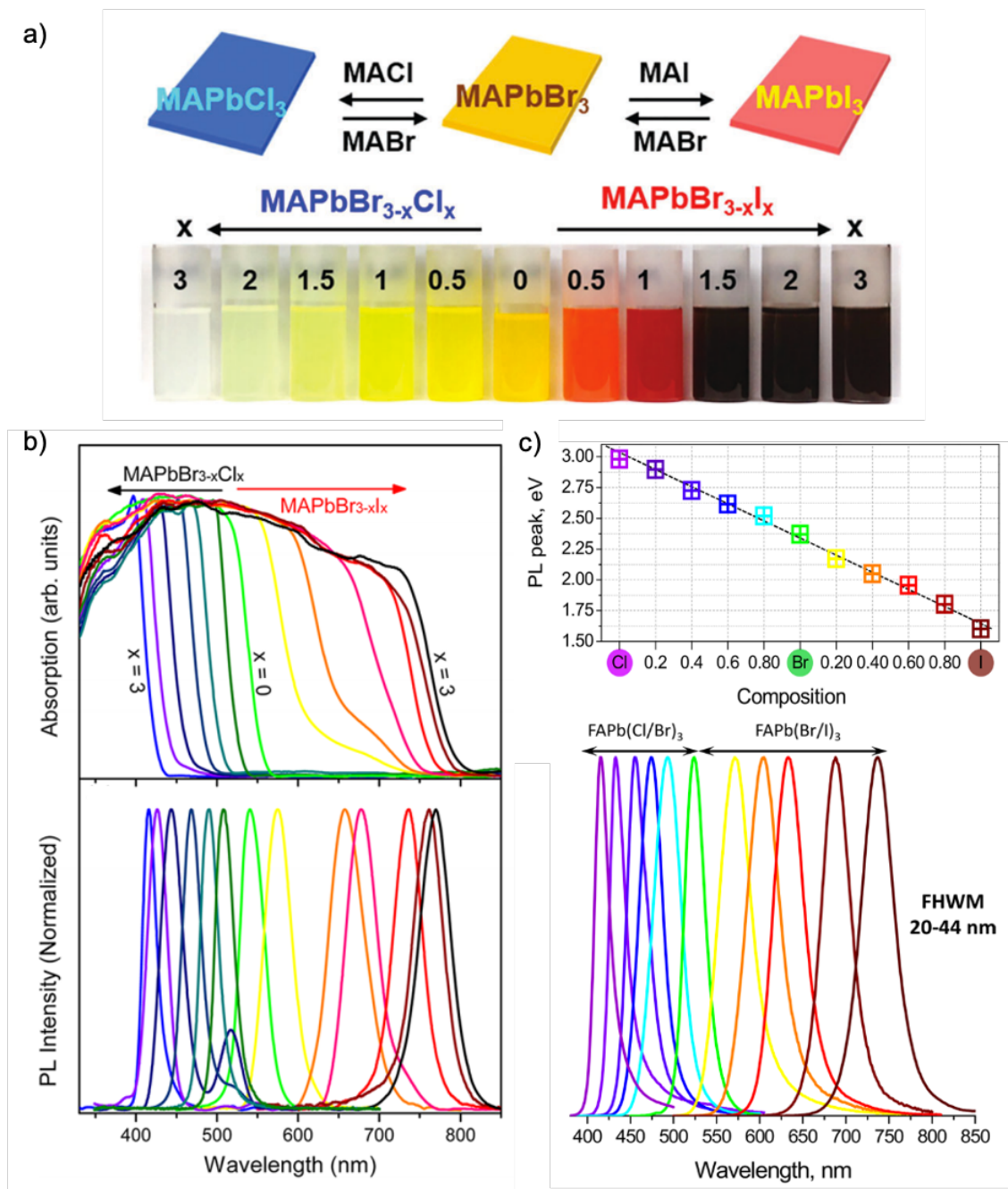
Figure 1.16. (a) Photo of MAPbBr$_{3-x}$Cl$_x$ and MAPbBr$_{3-x}$I$_x$ colloidal solutions, where $x = 0, 0.5, 1, 1.5, 2,$ and 3 (b) Absorption and photoluminescence spectra of MAPbBr$_{3-x}$Cl$_x$ and MAPbBr$_{3-x}$I$_x$ films. Figures (a, b) reproduced from Ref. 134 with permission. Copyright (2015) American Chemical Society. (c) Photoluminescence peaks plotted with composition and photoluminescence spectra of FAPbBr$_{3-x}$Cl$_x$ and FAPbBr$_{3-x}$I$_x$ nanocrystals, adapted from Ref. 122 with permission. Copyright (2017) American Chemical Society.

27

1.4 Summary

This chapter provides a brief overview of perovskite and compositional variations introduced by doping. The family of AMX_3 crystals with perovskite structure is typified by a 3D framework made up of MX_6 octahedra. Although many structural types of oxide perovskite are well-studied, the field of halide OIHPs is relatively new. The recent research boom concerning halide perovskite and perovskite-like layered structures with organic A-cations opens up opportunities for using these materials in numerous applications such as solar cells and LEDs. These optoelectronic applications are closely related to the band structure of halide perovskite which is mainly affected by the MX_6 octahedra framework. Thus, it is necessary to study the behaviour of MX_6 octahedra such as octahedral distortions and related phase transitions. Unwanted phase transitions or decomposition has been reported as a major challenge for the commercialisation of perovskite materials and doping at the A- or X-site has been reported as an approach to overcoming this challenge.

1.5 Thesis Overview

This thesis explores the synthesis, structure and optoelectrical properties of OIHPs with azetidinium as the A-site cation. The aim is to study a series of new perovskite structures and to investigate the relationship between structure and bandgap.

Experimental techniques and synthesis details are given in Chapter 2. Structural analysis techniques such as PXRD and SCXRD, and subsequent methods of analysis are discussed. Equipment details of other characterisation techniques including SEM, absorption spectroscopy, NMR spectroscopy, impedance spectroscopy and TGA are given in Chapter 2. The synthesis of precursors and perovskites are given as the last part of the chapter.

Chapter 3 discusses a stable 6H hexagonal OIHP $AzPbBr_3$. PXRD and SCXRD are used to determine the structure of $AzPbBr_3$. Two suspected phase transitions in $AzPbBr_3$ at low temperature are investigated using variable temperature PXRD which is supported by the data of impedance spectroscopy. In addition, the octahedral distortion of $AzPbBr_3$

is investigated using variable temperature SCXRD data. DFT calculations and absorption spectroscopy are explored to understand the band structure of $AzPbBr_3$.

Chapter 4 explores two mixed A-cation perovskites by combining Az with either MA or FA. Two common synthetic methods, precipitation synthesis and mechanosynthesis, are used for both $Az_{1-x}FA_xPbBr_3$ and $Az_{1-x}MA_xPbBr_3$ ($0 \leq x \leq 1$). The A-site cation composition in both $Az_{1-x}FA_xPbBr_3$ and $Az_{1-x}MA_xPbBr_3$ is systematically studied using NMR spectra. For samples obtained from the precipitation synthesis, the actual FA% or MA% in the precipitate is found to be less than the nominal composition in the reaction solution. Such composition mismatch is not found for mechanosynthesised samples. The lattice parameters of all samples are studied with PXRD and Rietveld refinement, and analysed as a function of the actual composition as determined by NMR spectroscopy. The optical properties of the mixed A-cation perovskites are studied with absorption spectroscopy.

In Chapter 5, the influence of halides is explored with mixed halide perovskite $AzPbBr_{3-x}X_x$ (X = Cl or I, $0 \leq x \leq 3$) prepared by mechanosynthesis. PXRD and Rietveld refinement are used to analyse the structure of the mixed halide perovskite solid solutions. Structure progression from 6H to 4H to 9R polytypes is determined in conjunction with varying halide composition from Cl to I in $AzPbBr_{3-x}X_x$ samples. Using PXRD, $AzPbX_3$ (X = Cl, Br or I) samples are shown to be stable in ambient air with no decomposition. The bandgap of mixed halide perovskites is studied with absorption spectroscopy.

In Chapter 6, a $n = 1$ Ruddlesden-Popper phase Az_2PbBr_4, and a 1D chain structure azetidinium bismuth bromide are briefly explored using PXRD, SCXRD and Rietveld refinement. The bandgaps of both compounds are studied with absorption spectroscopy.

References

(1)   Rose, G. Beschreibung Einiger Neuen Mineralien Des Urals. *Ann. der Phys. und Chemie* **1839**, *124* (12), 551–573.

(2)   Mitzi, D. B. Templating and Structural Engineering in Organic–Inorganic Perovskites. *J. Chem. Soc. Dalt. Trans.* **2001**, No. 1, 1–12.

(3)   Bhalla, A. S.; Guo, R.; Roy, R. The Perovskite Structure - A Review of Its Role in Ceramic Science and Technology. *Mater. Res. Innov.* **2000**, *4* (1), 3–26.

(4)   Wells, H. L. Über Die Cäsium- Und Kalium-Bleihalogenide. *Zeitschrift für Anorg. Chemie* **1893**, *3* (1), 195–210.

(5)   Weber, D. CH3NH3PbX3, Ein Pb(II)-System Mit Kubischer Perowskitstruktur. *Zeitschrift fur Naturforsch. - Sect. B J. Chem. Sci.* **1978**, *33* (12), 1443–1445.

(6)   Weber, D. CH3NH3SnBrxI3-x (x = 0-3), Ein Sn(II)-System Mit Kubischer Perowskitstruktur / CH3NH3SnBrxI3-x(x = 0-3), a Sn(II)-System with Cubic Perovskite Structure. *Zeitschrift für Naturforsch. B* **1978**, *33* (8), 862–865.

(7)   Bartel, C. J.; Sutton, C.; Goldsmith, B. R.; Ouyang, R.; Musgrave, C. B.; Ghiringhelli, L. M.; Scheffler, M. New Tolerance Factor to Predict the Stability of Perovskite Oxides and Halides. *Sci. Adv.* **2019**, *5* (2), eaav0693.

(8)   Shannon, R. D. Revised Effective Ionic Radii and Systematic Studies of Interatomic Distances in Halides and Chalcogenides. *Acta Crystallogr. Sect. A* **1976**, *32* (5), 751–767.

(9)   Kieslich, G.; Sun, S.; Cheetham, A. K. An Extended Tolerance Factor Approach for Organic–Inorganic Perovskites. *Chem. Sci.* **2015**, *6* (6), 3430–3433.

(10)   Travis, W.; Glover, E. N. K.; Bronstein, H.; Scanlon, D. O.; Palgrave, R. G. On the Application of the Tolerance Factor to Inorganic and Hybrid Halide Perovskites: A Revised System. *Chem. Sci.* **2016**, *7* (7), 4548–4556.

(11)   Beskow, G. V. M. Goldschmidt: Geochemische Verteilungsgesetze Der Elemente. *Geol. Föreningen i Stock. Förhandlingar* **1924**, *46* (6–7), 738–743.

(12)   Ortega-San-Martin, L. Introduction to Perovskites: A Historical Perspective. In *Revolution of Perovskite: Synthesis, Properties and Applications*; Arul, N. S., Nithya, V. D., Eds.; Springer Singapore: Singapore, 2020; pp 1–41.

(13)   Kojima, A.; Teshima, K.; Shirai, Y.; Miyasaka, T. Organometal Halide Perovskites as Visible-Light Sensitizers for Photovoltaic Cells. *J. Am. Chem. Soc.* **2009**, *131*

(17), 6050–6051.

(14) Yang, W. S.; Park, B.-W.; Jung, E. H.; Jeon, N. J.; Kim, Y. C.; Lee, D. U.; Shin, S. S.; Seo, J.; Kim, E. K.; Noh, J. H.; et al. Iodide Management in Formamidinium-Lead-Halide Based Perovskite Layers for Efficient Solar Cells. *Science (80-.).* **2017**, *356* (6345), 1376–1379.

(15) Mei, A.; Li, X.; Liu, L.; Ku, Z.; Liu, T.; Rong, Y.; Xu, M. M.; Hu, M.; Chen, J.; Yang, Y.; et al. A Hole-Conductor-Free, Fully Printable Mesoscopic Perovskite Solar Cell with High Stability. *Science (80-.).* **2014**, *345* (6194), 295–298.

(16) Shi, D.; Adinolfi, V.; Comin, R.; Yuan, M.; Alarousu, E.; Buin, A.; Chen, Y.; Hoogland, S.; Rothenberger, A.; Katsiev, K.; et al. Solar Cells. Low Trap-State Density and Long Carrier Diffusion in Organolead Trihalide Perovskite Single Crystals. *Science* **2015**, *347* (6221), 519–522.

(17) Saliba, M.; Matsui, T.; Domanski, K.; Seo, J.-Y.; Ummadisingu, A.; Zakeeruddin, S. M.; Correa-Baena, J.-P.; Tress, W. R.; Abate, A.; Hagfeldt, A.; et al. Incorporation of Rubidium Cations into Perovskite Solar Cells Improves Photovoltaic Performance. *Science (80-.).* **2016**, *354* (6309), 206–209.

(18) Kim, G.; Min, H.; Lee, K. S.; Lee, D. Y.; Yoon, S. M.; Seok, S. Il. Impact of Strain Relaxation on Performance of A-Formamidinium Lead Iodide Perovskite Solar Cells. *Science (80-.).* **2020**, *370* (6512), 108–112.

(19) https://www.nrel.gov/pv/cell-efficiency.html. Accessed 25 Jul. 2021.

(20) Cao, M.; Tian, J.; Cai, Z.; Peng, L.; Yang, L.; Wei, D. Perovskite Heterojunction Based on CH3NH3PbBr3 Single Crystal for High-Sensitive Self-Powered Photodetector. *Appl. Phys. Lett.* **2016**, *109* (23), 233303.

(21) Zhou, H.; Song, Z.; Grice, C. R.; Chen, C.; Yang, X.; Wang, H.; Yan, Y. Pressure-Assisted Annealing Strategy for High-Performance Self-Powered All-Inorganic Perovskite Microcrystal Photodetectors. *J. Phys. Chem. Lett.* **2018**, *9* (16), 4714–4719.

(22) Veldhuis, S. A.; Boix, P. P.; Yantara, N.; Li, M.; Sum, T. C.; Mathews, N.; Mhaisalkar, S. G. Perovskite Materials for Light-Emitting Diodes and Lasers. *Adv. Mater.* **2016**, *28* (32), 6804–6834.

(23) Zhao, B.; Bai, S.; Kim, V.; Lamboll, R.; Shivanna, R.; Auras, F.; Richter, J. M.; Yang, L.; Dai, L.; Alsari, M.; et al. High-Efficiency Perovskite–Polymer Bulk

Heterostructure Light-Emitting Diodes. *Nat. Photonics* **2018**, *12* (12), 783–789.

(24) Zhu, H.; Fu, Y.; Meng, F.; Wu, X.; Gong, Z.; Ding, Q.; Gustafsson, M. V.; Trinh, M. T.; Jin, S.; Zhu, X. Y. Lead Halide Perovskite Nanowire Lasers with Low Lasing Thresholds and High Quality Factors. *Nat. Mater.* **2015**, *14* (6), 636–642.

(25) Jia, Y.; Kerner, R. A.; Grede, A. J.; Rand, B. P.; Giebink, N. C. Continuous-Wave Lasing in an Organic–Inorganic Lead Halide Perovskite Semiconductor. *Nat. Photonics* **2017**, *11* (12), 784–788.

(26) Yang, Z.; Surrente, A.; Galkowski, K.; Bruyant, N.; Maude, D. K.; Haghighirad, A. A.; Snaith, H. J.; Plochocka, P.; Nicholas, R. J. Unraveling the Exciton Binding Energy and the Dielectric Constant in Single-Crystal Methylammonium Lead Triiodide Perovskite. *J. Phys. Chem. Lett.* **2017**, *8* (8), 1851–1855.

(27) Herz, L. M. Charge-Carrier Mobilities in Metal Halide Perovskites: Fundamental Mechanisms and Limits. *ACS Energy Lett.* **2017**, *2* (7), 1539–1548.

(28) Web of Science. Accessed 28 Jan. 2021. Search Query: (TS=(Hybrid Perovskite OR Perovskite Halide) NOT TS=(Er3* OR Yb3* OR SrT* OR Calcium* OR Magnate* OR Titanate OR Oxi* OR Ceramic)) AND DOCUMENT TYPES: (Article).

(29) Geselle, M.; Fuess, H. Crystal Structure of Tetrakis(Ethylammonium) Decachlorotriplumbate(II), (C2H5NH3)4Pb3Cl10. *Zeitschrift fur Krist.* **1997**, *212* (1), 241–242.

(30) Almond, D. P.; Rayne, J. A. Ultrasonic Determination of the Phase Diagram in CsNiCl3. *Phys. Lett. A* **1975**, *55* (2), 137–138.

(31) Jin, C. Q.; Zhou, J. S.; Goodenough, J. B.; Liu, Q. Q.; Zhao, J. G.; Yang, L. X.; Yu, Y.; Yu, R. C.; Katsura, T.; Shatskiy, A.; et al. High-Pressure Synthesis of the Cubic Perovskite BaRuO3 and Evolution of Ferromagnetism in ARuO3 (A = Ca, Sr, Ba) Ruthenates. *Proc. Natl. Acad. Sci. U. S. A.* **2008**, *105* (20), 7115–7119.

(32) Zalkin, A.; Lee, K.; Templeton, D. H. Crystal Structure of CsMnF3. *J. Chem. Phys.* **1962**, *37* (4), 697–699.

(33) Zaleski, J.; Pietraszko, A. Structure at 200 and 298 K and X-Ray Investigations of the Phase Transition at 242 K of [NH2(CH3)2]3Sb2Cl9(DMACA). *Acta Crystallogr. Sect. B Struct. Sci.* **1996**, *52* (2), 287–295.

(34) Ling, C. D.; Rowda, B.; Avdeev, M.; Pullar, R. Structures, Phase Transitions and

Microwave Dielectric Properties of the 6H Perovskites Ba3BSb2O9, B=Mg, Ca, Sr, Ba. *J. Solid State Chem.* **2009**, *182* (3), 479–483.

(35) Gratia, P.; Zimmermann, I.; Schouwink, P.; Yum, J.-H.; Audinot, J.-N.; Sivula, K.; Wirtz, T.; Nazeeruddin, M. K. The Many Faces of Mixed Ion Perovskites: Unraveling and Understanding the Crystallization Process. *ACS Energy Lett.* **2017**, *2* (12), 2686–2693.

(36) Stein, F.; Palm, M.; Sauthoff, G. Structure and Stability of Laves Phases. Part I. Critical Assessment of Factors Controlling Laves Phase Stability. *Intermetallics* **2004**, *12* (7–9), 713–720.

(37) Patrick, L. Inequivalent Sites and Multiple Donor and Acceptor Levels in SiC Polytypes. *Phys. Rev.* **1962**, *127* (6), 1878–1880.

(38) Kamminga, M. E.; De Wijs, G. A.; Havenith, R. W. A.; Blake, G. R.; Palstra, T. T. M. The Role of Connectivity on Electronic Properties of Lead Iodide Perovskite-Derived Compounds. *Inorg. Chem.* **2017**, *56* (14), 8408–8414.

(39) Balz, D.; Plieth, K. Die Struktur Des Kaliumnickelfluorids, K2NiF. *Zeitschrift für Elektrochemie, Berichte der Bunsengesellschaft für Phys. Chemie* **1955**, *59* (6), 545–551.

(40) Ruddlesden, S. N.; Popper, P. New Compounds of the K 2 NIF 4 Type. *Acta Crystallogr.* **1957**, *10* (8), 538–539.

(41) Ganguli, D. Cationic Radius Ratio and Formation of K2NiF4-Type Compounds. *J. Solid State Chem.* **1979**, *30* (3), 353–356.

(42) Mao, H.; Wei, Y.; Gui, H.; Li, X.; Zhao, Z.; Xie, W. First-Principle Investigations of K2NiF4-Type Double Perovskite Oxides La4B′B″O8 (B′B″ = Fe, Co, Ni). *J. Appl. Phys.* **2014**, *115* (21), 213910.

(43) Tsai, H.; Nie, W.; Blancon, J.-C.; Stoumpos, C. C.; Soe, C. M. M.; Yoo, J.; Crochet, J.; Tretiak, S.; Even, J.; Sadhanala, A.; et al. Stable Light-Emitting Diodes Using Phase-Pure Ruddlesden-Popper Layered Perovskites. *Adv. Mater.* **2018**, *30* (6), 1704217.

(44) Tsai, H.; Nie, W.; Blancon, J. C.; Stoumpos, C. C.; Asadpour, R.; Harutyunyan, B.; Neukirch, A. J.; Verduzco, R.; Crochet, J. J.; Tretiak, S.; et al. High-Efficiency Two-Dimensional Ruddlesden-Popper Perovskite Solar Cells. *Nature* **2016**, *536* (7616), 312–317.

(45) Lichtenberg, F.; Herrnberger, A.; Wiedenmann, K. Synthesis, Structural, Magnetic and Transport Properties of Layered Perovskite-Related Titanates, Niobates and Tantalates of the Type AnBnO3n+2, A′Ak-1BkO3k+1 and AmBm-1O3m. *Prog. Solid State Chem.* **2008**, *36* (4), 253–387.

(46) Stoumpos, C. C.; Cao, D. H.; Clark, D. J.; Young, J.; Rondinelli, J. M.; Jang, J. I.; Hupp, J. T.; Kanatzidis, M. G. Ruddlesden-Popper Hybrid Lead Iodide Perovskite 2D Homologous Semiconductors. *Chem. Mater.* **2016**, *28* (8), 2852–2867.

(47) Du, K. Z.; Tu, Q.; Zhang, X.; Han, Q.; Liu, J.; Zauscher, S.; Mitzi, D. B. Two-Dimensional Lead(II) Halide-Based Hybrid Perovskites Templated by Acene Alkylamines: Crystal Structures, Optical Properties, and Piezoelectricity. *Inorg. Chem.* **2017**, *56* (15), 9291–9302.

(48) Mitzi, D. B. A Layered Solution Crystal Growth Technique and the Crystal Structure of (C 6 H 5 C 2 H 4 NH 3) 2 PbCl 4. *J. Solid State Chem.* **1999**, *145* (2), 694–704.

(49) Spanopoulos, I.; Hadar, I.; Ke, W.; Tu, Q.; Chen, M.; Tsai, H.; He, Y.; Shekhawat, G.; Dravid, V. P.; Wasielewski, M. R.; et al. Uniaxial Expansion of the 2D Ruddlesden-Popper Perovskite Family for Improved Environmental Stability. *J. Am. Chem. Soc.* **2019**, *141* (13), 5518–5534.

(50) Mitzi, D. B.; Brock, P. Structure and Optical Properties of Several Organic-Inorganic Hybrids Containing Corner-Sharing Chains of Bismuth Iodide Octahedra. *Inorg. Chem.* **2001**, *40* (9), 2096–2104.

(51) Hrizi, C.; Chaari, N.; Abid, Y.; Chniba-Boudjada, N.; Chaabouni, S. Structural Characterization, Vibrational and Optical Properties of a Novel One-Dimensional Organic-Inorganic Hybrid Based-Iodobismuthate(III) Material, [C 10H 7NH 3]BiI 4. *Polyhedron* **2012**, *46* (1), 41–46.

(52) Ma, C.; Shen, D.; Huang, B.; Li, X.; Chen, W. C.; Lo, M. F.; Wang, P.; Hon-Wah Lam, M.; Lu, Y.; Ma, B.; et al. High Performance Low-Dimensional Perovskite Solar Cells Based on a One Dimensional Lead Iodide Perovskite. *J. Mater. Chem. A* **2019**, *7* (15), 8811–8817.

(53) Zhang, W.; Liu, X.; Li, L.; Sun, Z.; Han, S.; Wu, Z.; Luo, J. Triiodide-Induced Band-Edge Reconstruction of a Lead-Free Perovskite-Derivative Hybrid for Strong Light Absorption. *Chem. Mater.* **2018**, *30* (12), 4081–4088.

(54)   Correa-Baena, J.-P.; Nienhaus, L.; Kurchin, R. C.; Shin, S. S.; Wieghold, S.; Putri Hartono, N. T.; Layurova, M.; Klein, N. D.; Poindexter, J. R.; Polizzotti, A.; et al. *A* -Site Cation in Inorganic *A* $_3$ Sb $_2$ I $_9$ Perovskite Influences Structural Dimensionality, Exciton Binding Energy, and Solar Cell Performance. *Chem. Mater.* **2018**, *30* (11), 3734–3742.

(55)   Kim, B.; Seok, S. Il. Molecular Aspects of Organic Cations Affecting the Humidity Stability of Perovskites. *Energy Environ. Sci.* **2020**, *13* (3), 805–820.

(56)   Zhang, X.; Li, L.; Sun, Z.; Luo, J. Rational Chemical Doping of Metal Halide Perovskites. *Chem. Soc. Rev.* **2019**, *48* (2), 517–539.

(57)   Huang, W.; Yue, S.; Liu, Y.; Zhu, L.; Jin, P.; Wu, Q.; Zhang, Y.; Chen, Y.; Liu, K.; Liang, P.; et al. Observation of Unusual Optical Band Structure of CH3NH3PbI3 Perovskite Single Crystal. *ACS Photonics* **2018**, *5* (4), 1583–1590.

(58)   Liu, Y.; Yang, Z.; Cui, D.; Ren, X.; Sun, J.; Liu, X.; Zhang, J.; Wei, Q.; Fan, H.; Yu, F.; et al. Two-Inch-Sized Perovskite CH $_3$ NH $_3$ PbX $_3$ (X = Cl, Br, I) Crystals: Growth and Characterization. *Adv. Mater.* **2015**, *27* (35), 5176–5183.

(59)   Stoumpos, C. C.; Malliakas, C. D.; Kanatzidis, M. G. Semiconducting Tin and Lead Iodide Perovskites with Organic Cations: Phase Transitions, High Mobilities, and near-Infrared Photoluminescent Properties. *Inorg. Chem.* **2013**, *52* (15), 9019–9038.

(60)   Weller, M. T.; Weber, O. J.; Frost, J. M.; Walsh, A. Cubic Perovskite Structure of Black Formamidinium Lead Iodide, α-[HC(NH $_2$) $_2$]PbI $_3$, at 298 K. *J. Phys. Chem. Lett.* **2015**, *6* (16), 3209–3212.

(61)   Hanusch, F. C.; Wiesenmayer, E.; Mankel, E.; Binek, A.; Angloher, P.; Fraunhofer, C.; Giesbrecht, N.; Feckl, J. M.; Jaegermann, W.; Johrendt, D.; et al. Efficient Planar Heterojunction Perovskite Solar Cells Based on Formamidinium Lead Bromide. *J. Phys. Chem. Lett.* **2014**, *5* (16), 2791–2795.

(62)   Tao, S.; Schmidt, I.; Brocks, G.; Jiang, J.; Tranca, I.; Meerholz, K.; Olthof, S. Absolute Energy Level Positions in Tin- and Lead-Based Halide Perovskites. *Nat. Commun.* **2019**, *10* (1), 1–10.

(63)   Stoumpos, C. C.; Mao, L.; Malliakas, C. D.; Kanatzidis, M. G. Structure-Band Gap Relationships in Hexagonal Polytypes and Low-Dimensional Structures of Hybrid Tin Iodide Perovskites. *Inorg. Chem.* **2017**, *56* (1), 56–73.

(64)	Mancini, A.; Quadrelli, P.; Amoroso, G.; Milanese, C.; Boiocchi, M.; Sironi, A.; Patrini, M.; Guizzetti, G.; Malavasi, L. Synthesis, Structural and Optical Characterization of APbX3 (A=methylammonium, Dimethylammonium, Trimethylammonium; X=I, Br, Cl) Hybrid Organic-Inorganic Materials. *J. Solid State Chem.* **2016**, *240*, 55–60.

(65)	Geselle, M.; Fuess, H. Crystal Structure of Dimethylammonium Tribromoplumbate(II), (CH 3)2NH2PbBr 3. *Zeitschrift für Krist. Cryst. Struct.* **1997**, *212*, 234–234.

(66)	Panetta, R.; Righini, G.; Colapietro, M.; Barba, L.; Tedeschi, D.; Polimeni, A.; Ciccioli, A.; Latini, A. Azetidinium Lead Iodide: Synthesis, Structural and Physico-Chemical Characterization. *J. Mater. Chem. A* **2018**, *6* (21), 10135–10148.

(67)	Billing, D. G.; Lemmerer, A. Synthesis, Characterization and Phase Transitions in the Inorganic-Organic Layered Perovskite-Type Hybrids [(Cn H2n + 1NH 3)2PbI4], n = 4, 5 and 6. *Acta Crystallogr. Sect. B Struct. Sci.* **2007**, *63* (5), 735–747.

(68)	Hua, X. N.; Liao, W. Q.; Tang, Y. Y.; Li, P. F.; Shi, P. P.; Zhao, D.; Xiong, R. G. A Room-Temperature Hybrid Lead Iodide Perovskite Ferroelectric. *J. Am. Chem. Soc.* **2018**, *140* (38), 12296–12302.

(69)	Ishihara, H.; Watanabe, K.; Iwata, A.; Yamada, K.; Kinoshita, Y.; Okuda, T.; Krishnan, V. G.; Dou, S. S.; Weiss, A. NQR and X-Ray Studies of [N(CH3)4]3M2X9 and (CH3NH3)3M2X9 (M = Sb, Bi; X = Cl, Br). *Zeitschrift fur Naturforsch. - Sect. A J. Phys. Sci.* **1992**, *47* (1–2), 65–74.

(70)	Dohner, E. R.; Hoke, E. T.; Karunadasa, H. I. Self-Assembly of Broadband White-Light Emitters. *J. Am. Chem. Soc.* **2014**, *136* (5), 1718–1721.

(71)	Elsenety, M. M.; Kaltzoglou, A.; Antoniadou, M.; Koutselas, I.; Kontos, A. G.; Falaras, P. Synthesis, Characterization and Use of Highly Stable Trimethyl Sulfonium Tin(IV) Halide Defect Perovskites in Dye Sensitized Solar Cells. *Polyhedron* **2018**, *150*, 83–91.

(72)	Yuan, Z.; Zhou, C.; Tian, Y.; Shu, Y.; Messier, J.; Wang, J. C.; van de Burgt, L. J.; Kountouriotis, K.; Xin, Y.; Holt, E.; et al. One-Dimensional Organic Lead Halide Perovskites with Efficient Bluish White-Light Emission. *Nat. Commun.* **2017**, *8* (1), 14051.

(73) Mousdis, G. A.; Papavassiliou, G. C.; Terzis, A.; Raptopoulou, C. P. Preparation, Structures and Optical Properties of [H3N (CH2) 6NH3] BiX5 (X= I, Cl) and [H3N (CH2) 6NH3] SbX5 (X= I, Br). *Zeitschrift für Naturforsch. B* **1998**, *53* (8), 927–932.

(74) Bersuker, I. B. On the Origin of Ferroelectricity in Perovskite-Type Crystals. *Phys. Lett.* **1966**, *20* (6), 589–590.

(75) Bersuker, I. B. Pseudo-Jahn-Teller Effect - A Two-State Paradigm in Formation, Deformation, and Transformation of Molecular Systems and Solids. *Chem. Rev.* **2013**, *113* (3), 1351–1390.

(76) Fabini, D. H.; Laurita, G.; Bechtel, J. S.; Stoumpos, C. C.; Evans, H. A.; Kontos, A. G.; Raptis, Y. S.; Falaras, P.; Van Der Ven, A.; Kanatzidis, M. G.; et al. Dynamic Stereochemical Activity of the Sn2+ Lone Pair in Perovskite CsSnBr3. *J. Am. Chem. Soc.* **2016**, *138* (36), 11820–11832.

(77) Laurita, G.; Fabini, D. H.; Stoumpos, C. C.; Kanatzidis, M. G.; Seshadri, R. Chemical Tuning of Dynamic Cation Off-Centering in the Cubic Phases of Hybrid Tin and Lead Halide Perovskites. *Chem. Sci.* **2017**, *8* (8), 5628–5635.

(78) Taylor, V. C. A.; Tiwari, D.; Duchi, M.; Donaldson, P. M.; Clark, I. P.; Fermin, D. J.; Oliver, T. A. A. Investigating the Role of the Organic Cation in Formamidinium Lead Iodide Perovskite Using Ultrafast Spectroscopy. *J. Phys. Chem. Lett.* **2018**, *9* (4), 895–901.

(79) Motta, C.; El-Mellouhi, F.; Kais, S.; Tabet, N.; Alharbi, F.; Sanvito, S. Revealing the Role of Organic Cations in Hybrid Halide Perovskite CH3NH3PbI3. *Nat. Commun.* **2015**, *6* (1), 7026.

(80) Whitfield, P. S.; Herron, N.; Guise, W. E.; Page, K.; Cheng, Y. Q.; Milas, I.; Crawford, M. K. Structures, Phase Transitions and Tricritical Behavior of the Hybrid Perovskite Methyl Ammonium Lead Iodide. *Sci. Rep.* **2016**, *6* (1), 1–16.

(81) Maheshwari, S.; Fridriksson, M. B.; Seal, S.; Meyer, J.; Grozema, F. C. The Relation between Rotational Dynamics of the Organic Cation and Phase Transitions in Hybrid Halide Perovskites. *J. Phys. Chem. C* **2019**, *123* (23), 14652–14661.

(82) Jaeger, G. The Ehrenfest Classification of Phase Transitions: Introduction and Evolution. *Arch. Hist. Exact Sci.* **1998**, *53* (1), 51–81.

(83) Blundell, S. J.; Blundell, K. M. *Concepts in Thermal Physics*; Oxford University Press, 2009; Vol. 9780199562.

(84) Yin, W.-J.; Yang, J.-H.; Kang, J.; Yan, Y.; Wei, S. Halide Perovskite Materials for Solar Cells: A Theoretical Review. *J. Mater. Chem. A* **2015**, *3* (17), 8926–8942.

(85) Thind, A. S.; Huang, X.; Sun, J.; Mishra, R. First-Principles Prediction of a Stable Hexagonal Phase of CH 3 NH 3 PbI 3. *Chem. Mater.* **2017**, *29* (14), 6003–6011.

(86) Yin, W. J.; Shi, T.; Yan, Y. Unique Properties of Halide Perovskites as Possible Origins of the Superior Solar Cell Performance. *Adv. Mater.* **2014**, *26* (27), 4653–4658.

(87) Liu, M.; Johnston, M. B.; Snaith, H. J. Efficient Planar Heterojunction Perovskite Solar Cells by Vapour Deposition. *Nature* **2013**, *501* (7467), 395–398.

(88) Xiao, M.; Huang, F.; Huang, W.; Dkhissi, Y.; Zhu, Y.; Etheridge, J.; Gray-Weale, A.; Bach, U.; Cheng, Y.-B.; Spiccia, L. A Fast Deposition-Crystallization Procedure for Highly Efficient Lead Iodide Perovskite Thin-Film Solar Cells. *Angew. Chemie Int. Ed.* **2014**, *53* (37), 9898–9903.

(89) Deng, Y.; Zheng, X.; Bai, Y.; Wang, Q.; Zhao, J.; Huang, J. Surfactant-Controlled Ink Drying Enables High-Speed Deposition of Perovskite Films for Efficient Photovoltaic Modules. *Nat. Energy* **2018**, *3* (7), 560–566.

(90) Noel, N. K.; Stranks, S. D.; Abate, A.; Wehrenfennig, C.; Guarnera, S.; Haghighirad, A. A.; Sadhanala, A.; Eperon, G. E.; Pathak, S. K.; Johnston, M. B.; et al. Lead-Free Organic-Inorganic Tin Halide Perovskites for Photovoltaic Applications. *Energy Environ. Sci.* **2014**, *7* (9), 3061–3068.

(91) Im, J. H.; Jang, I. H.; Pellet, N.; Grätzel, M.; Park, N. G. Growth of CH3 NH3 PbI3 Cuboids with Controlled Size for High-Efficiency Perovskite Solar Cells. *Nat. Nanotechnol.* **2014**, *9* (11), 927–932.

(92) Saidaminov, M. I.; Abdelhady, A. L.; Maculan, G.; Bakr, O. M. Retrograde Solubility of Formamidinium and Methylammonium Lead Halide Perovskites Enabling Rapid Single Crystal Growth. *Chem. Commun.* **2015**, *51* (100), 17658–17661.

(93) Poglitsch, A.; Weber, D. Dynamic Disorder in Methylammoniumtrihalogenoplumbates (II) Observed by Millimeter-Wave Spectroscopy. *J. Chem. Phys.* **1987**, *87* (6373).

(94)   Chouhan, L.; Ghimire, S.; Subrahmanyam, C.; Miyasaka, T.; Biju, V. Synthesis, Optoelectronic Properties and Applications of Halide Perovskites. *Chem. Soc. Rev.* **2020**, *49* (10), 2869–2885.

(95)   Akkerman, Q. A.; Rainò, G.; Kovalenko, M. V.; Manna, L. Genesis, Challenges and Opportunities for Colloidal Lead Halide Perovskite Nanocrystals. *Nat. Mater.* **2018**, *17* (5), 394–405.

(96)   Huang, H.; Zhao, F.; Liu, L.; Zhang, F.; Wu, X.; Shi, L.; Zou, B.; Pei, Q.; Zhong, H. Emulsion Synthesis of Size-Tunable CH$_3$NH$_3$PbBr$_3$ Quantum Dots: An Alternative Route toward Efficient Light-Emitting Diodes. *ACS Appl. Mater. Interfaces* **2015**, *7* (51), 28128–28133.

(97)   Liu, X.; Cao, L.; Guo, Z.; Li, Y.; Gao, W.; Zhou, L. A Review of Perovskite Photovoltaic Materials' Synthesis and Applications via Chemical Vapor Deposition Method. *Materials (Basel).* **2019**, *12* (20), 3304.

(98)   Liu, J.; Xue, Y.; Wang, Z.; Xu, Z. Q.; Zheng, C.; Weber, B.; Song, J.; Wang, Y.; Lu, Y.; Zhang, Y.; et al. Two-Dimensional CH3NH3PbI3 Perovskite: Synthesis and Optoelectronic Application. *ACS Nano* **2016**, *10* (3), 3536–3542.

(99)   Vidyasagar, C. C.; Muñoz Flores, B. M.; Jiménez Pérez, V. M. Recent Advances in Synthesis and Properties of Hybrid Halide Perovskites for Photovoltaics. *Nano-Micro Lett.* **2018**, *10* (4), 68.

(100) Protesescu, L.; Yakunin, S.; Nazarenko, O.; Dirin, D. N.; Kovalenko, M. V. Low-Cost Synthesis of Highly Luminescent Colloidal Lead Halide Perovskite Nanocrystals by Wet Ball Milling. *ACS Appl. Nano Mater.* **2018**, *1* (3), 1300–1308.

(101) Pal, P.; Saha, S.; Banik, A.; Sarkar, A.; Biswas, K. All-Solid-State Mechanochemical Synthesis and Post-Synthetic Transformation of Inorganic Perovskite-Type Halides. *Chem. - A Eur. J.* **2018**, *24* (8), 1811–1815.

(102) Hong, Z.; Tan, D.; John, R. A.; Tay, Y. K. E.; Ho, Y. K. T.; Zhao, X.; Sum, T. C.; Mathews, N.; García, F.; Soo, H. Sen. Completely Solvent-Free Protocols to Access Phase-Pure, Metastable Metal Halide Perovskites and Functional Photodetectors from the Precursor Salts. *iScience* **2019**, *16* (0), 312–325.

(103) Abdelhady, A. L.; Saidaminov, M. I.; Murali, B.; Adinolfi, V.; Voznyy, O.; Katsiev, K.; Alarousu, E.; Comin, R.; Dursun, I.; Sinatra, L.; et al. Heterovalent Dopant Incorporation for Bandgap and Type Engineering of Perovskite Crystals.

J. Phys. Chem. Lett. **2016**, *7* (2), 295–301.

(104) Zhang, Z.; Ren, L.; Yan, H.; Guo, S.; Wang, S.; Wang, M.; Jin, K. Bandgap Narrowing in Bi-Doped CH 3 NH 3 PbCl 3 Perovskite Single Crystals and Thin Films. *J. Phys. Chem. C* **2017**, *121* (32), 17436–17441.

(105) Ng, M.; Halpert, J. E. Single Crystals of Mixed Br/Cl and Sn-Doped Formamidinium Lead Halide Perovskites *via* Inverse Temperature Crystallization. *RSC Adv.* **2020**, *10* (7), 3832–3836.

(106) Nayak, P. K.; Sendner, M.; Wenger, B.; Wang, Z.; Sharma, K.; Ramadan, A. J.; Lovrinčić, R.; Pucci, A.; Madhu, P. K.; Snaith, H. J. Impact of Bi 3+ Heterovalent Doping in Organic–Inorganic Metal Halide Perovskite Crystals. *J. Am. Chem. Soc.* **2018**, *140* (2), 574–577.

(107) Prochowicz, D.; Yadav, P.; Saliba, M.; Saski, M.; Zakeeruddin, S. M.; Lewiński, J.; Grätzel, M. Mechanosynthesis of Pure Phase Mixed-Cation MA: XFA1- XPbI3 Hybrid Perovskites: Photovoltaic Performance and Electrochemical Properties. *Sustain. Energy Fuels* **2017**, *1* (4), 689–693.

(108) Kubicki, D. J.; Prochowicz, D.; Pinon, A.; Stevanato, G.; Hofstetter, A.; Zakeeruddin, S. M.; Grätzel, M.; Emsley, L. Doping and Phase Segregation in Mn 2+ - and Co 2+ -Doped Lead Halide Perovskites from 133 Cs and 1 H NMR Relaxation Enhancement. *J. Mater. Chem. A* **2019**, *7* (5), 2326–2333.

(109) Chen, D.; Li, J.; Chen, X.; Chen, J.; Zhong, J. Grinding Synthesis of APbX 3 (A = MA, FA, Cs; X = Cl, Br, I) Perovskite Nanocrystals. *ACS Appl. Mater. Interfaces* **2019**, *11* (10), 10059–10067.

(110) Yu, J. C.; Kim, D. Bin; Jung, E. D.; Lee, B. R.; Song, M. H. High-Performance Perovskite Light-Emitting Diodes via Morphological Control of Perovskite Films. *Nanoscale* **2016**, *8* (13), 7036–7042.

(111) Arya, S.; Mahajan, P.; Gupta, R.; Srivastava, R.; Tailor, N. kumar; Satapathi, S.; Sumathi, R. R.; Datt, R.; Gupta, V. A Comprehensive Review on Synthesis and Applications of Single Crystal Perovskite Halides. *Prog. Solid State Chem.* **2020**, *60*, 100286.

(112) Eperon, G. E.; Stranks, S. D.; Menelaou, C.; Johnston, M. B.; Herz, L. M.; Snaith, H. J. Formamidinium of Formamidinium Lead Trihalide: A Broadly Tunable Perovskite for Efficient Planar Heterojunction Solar Cells. *Energy Environ. Sci.*

2014, *7* (3), 982.

(113) Pellet, N.; Gao, P.; Gregori, G.; Yang, T. Y.; Nazeeruddin, M. K.; Maier, J.; Grätzel, M. Mixed-Organic-Cation Perovskite Photovoltaics for Enhanced Solar-Light Harvesting. *Angew. Chemie - Int. Ed.* **2014**, *53* (12), 3151–3157.

(114) Jodlowski, A. D.; Roldán-Carmona, C.; Grancini, G.; Salado, M.; Ralaiarisoa, M.; Ahmad, S.; Koch, N.; Camacho, L.; de Miguel, G.; Nazeeruddin, M. K. Large Guanidinium Cation Mixed with Methylammonium in Lead Iodide Perovskites for 19% Efficient Solar Cells. *Nat. Energy* **2017**, *2* (12), 972–979.

(115) Bi, C.; Chen, B.; Wei, H.; DeLuca, S.; Huang, J. Efficient Flexible Solar Cell Based on Composition-Tailored Hybrid Perovskite. *Adv. Mater.* **2017**, *29* (30), 1605900.

(116) Parobek, D.; Roman, B. J.; Dong, Y.; Jin, H.; Lee, E.; Sheldon, M.; Son, D. H. Exciton-to-Dopant Energy Transfer in Mn-Doped Cesium Lead Halide Perovskite Nanocrystals. *Nano Lett.* **2016**, *16* (12), 7376–7380.

(117) Das Adhikari, S.; Dutta, S. K.; Dutta, A.; Guria, A. K.; Pradhan, N. Chemically Tailoring the Dopant Emission in Manganese-Doped $CsPbCl_3$ Perovskite Nanocrystals. *Angew. Chemie Int. Ed.* **2017**, *56* (30), 8746–8750.

(118) Liu, H.; Wu, Z.; Shao, J.; Yao, D.; Gao, H.; Liu, Y.; Yu, W.; Zhang, H.; Yang, B. $CsPbxMn1-XCl3$ Perovskite Quantum Dots with High Mn Substitution Ratio. *ACS Nano* **2017**, *11* (2), 2239–2247.

(119) Miao, X.; Qiu, T.; Zhang, S.; Ma, H.; Hu, Y.; Bai, F.; Wu, Z. Air-Stable $CsPb1-XBixBr3$ ($0 \le x \ll 1$) Perovskite Crystals: Optoelectronic and Photostriction Properties. *J. Mater. Chem. C* **2017**, *5* (20), 4931–4939.

(120) Cho, H.; Jeong, S.-H.; Park, M.-H.; Kim, Y.-H.; Wolf, C.; Lee, C.-L.; Heo, J. H.; Sadhanala, A.; Myoung, N.; Yoo, S.; et al. Overcoming the Electroluminescence Efficiency Limitations of Perovskite Light-Emitting Diodes. *Science (80-.).* **2015**, *350* (6265), 1222–1225.

(121) Tan, H.; Jain, A.; Voznyy, O.; Lan, X.; García de Arquer, F. P.; Fan, J. Z.; Quintero-Bermudez, R.; Yuan, M.; Zhang, B.; Zhao, Y.; et al. Efficient and Stable Solution-Processed Planar Perovskite Solar Cells via Contact Passivation. *Science (80-.).* **2017**, *355* (6326), 722–726.

(122) Levchuk, I.; Osvet, A.; Tang, X.; Brandl, M.; Perea, J. D.; Hoegl, F.; Matt, G. J.;

Hock, R.; Batentschuk, M.; Brabec, C. J. Brightly Luminescent and Color-Tunable Formamidinium Lead Halide Perovskite FAPbX 3 (X = Cl, Br, I) Colloidal Nanocrystals. *Nano Lett.* **2017**, *17* (5), 2765–2770.

(123) Philippe, B.; Park, B. W.; Lindblad, R.; Oscarsson, J.; Ahmadi, S.; Johansson, E. M. J.; Rensmo, H. Chemical and Electronic Structure Characterization of Lead Halide Perovskites and Stability Behavior under Different Exposures-A Photoelectron Spectroscopy Investigation. *Chem. Mater.* **2015**, *27* (5), 1720–1731.

(124) Ito, S. Research Update: Overview of Progress about Efficiency and Stability on Perovskite Solar Cells. *APL Mater.* **2016**, *4* (9), 091504.

(125) Smith, I. C.; Hoke, E. T.; Solis-Ibarra, D.; McGehee, M. D.; Karunadasa, H. I. A Layered Hybrid Perovskite Solar-Cell Absorber with Enhanced Moisture Stability. *Angew. Chemie* **2014**, *126* (42), 11414–11417.

(126) Hassan, Y.; Song, Y.; Pensack, R. D.; Abdelrahman, A. I.; Kobayashi, Y.; Winnik, M. A.; Scholes, G. D. Structure-Tuned Lead Halide Perovskite Nanocrystals. *Adv. Mater.* **2016**, *28* (3), 566–573.

(127) Azam, M.; Yue, S.; Xu, R.; Liu, K.; Ren, K.; Sun, Y.; Liu, J.; Wang, Z.; Qu, S.; Lei, Y.; et al. Highly Efficient Solar Cells Based on Cl Incorporated Tri-Cation Perovskite Materials. *J. Mater. Chem. A* **2018**, *6* (28), 13725–13734.

(128) Milot, R. L.; Sutton, R. J.; Eperon, G. E.; Haghighirad, A. A.; Martinez Hardigree, J.; Miranda, L.; Snaith, H. J.; Johnston, M. B.; Herz, L. M. Charge-Carrier Dynamics in 2D Hybrid Metal-Halide Perovskites. *Nano Lett.* **2016**, *16* (11), 7001–7007.

(129) Abdelhady, A. L.; Saidaminov, M. I.; Murali, B.; Adinolfi, V.; Voznyy, O.; Katsiev, K.; Alarousu, E.; Comin, R.; Dursun, I.; Sinatra, L.; et al. Heterovalent Dopant Incorporation for Bandgap and Type Engineering of Perovskite Crystals. *J. Phys. Chem. Lett.* **2016**, *7* (2), 295–301.

(130) Gray, M. B.; McClure, E. T.; Woodward, P. M. Cs 2 AgBiBr 6−x Cl x Solid Solutions – Band Gap Engineering with Halide Double Perovskites. *J. Mater. Chem. C* **2019**, *7* (31), 9686–9689.

(131) Volonakis, G.; Filip, M. R.; Haghighirad, A. A.; Sakai, N.; Wenger, B.; Snaith, H. J.; Giustino, F. Lead-Free Halide Double Perovskites via Heterovalent Substitution of Noble Metals. *J. Phys. Chem. Lett.* **2016**, *7* (7), 1254–1259.

(132) Pandey, N.; Kumar, A.; Chakrabarti, S. Investigation of the Structural, Electronic, and Optical Properties of Mn-Doped CsPbCl3: Theory and Experiment. *RSC Adv.* **2019**, *9* (51), 29556–29565.

(133) Nakamura, Y.; Shibayama, N.; Hori, A.; Matsushita, T.; Segawa, H.; Kondo, T. Crystal Systems and Lattice Parameters of CH3NH3Pb(I1-XBrx)3 Determined Using Single Crystals: Validity of Vegard's Law. *Inorg. Chem.* **2020**, *59* (10), 6709–6716.

(134) Jang, D. M.; Park, K.; Kim, D. H.; Park, J.; Shojaei, F.; Kang, H. S.; Ahn, J. P.; Lee, J. W.; Song, J. K. Reversible Halide Exchange Reaction of Organometal Trihalide Perovskite Colloidal Nanocrystals for Full-Range Band Gap Tuning. *Nano Lett.* **2015**, *15* (8), 5191–5199.

(135) Noh, J. H.; Im, S. H.; Heo, J. H.; Mandal, T. N.; Seok, S. Il. Chemical Management for Colorful, Efficient, and Stable Inorganic-Organic Hybrid Nanostructured Solar Cells. *Nano Lett.* **2013**, *13* (4), 1764–1769.

(136) Jeon, N. J.; Noh, J. H.; Yang, W. S.; Kim, Y. C.; Ryu, S.; Seo, J.; Seok, S. Il. Compositional Engineering of Perovskite Materials for High-Performance Solar Cells. *Nature* **2015**, *517* (7535), 476–480.

(137) Madjet, M. E. A.; Akimov, A. V.; El-Mellouhi, F.; Berdiyorov, G. R.; Ashhab, S.; Tabet, N.; Kais, S. Enhancing the Carrier Thermalization Time in Organometallic Perovskites by Halide Mixing. *Phys. Chem. Chem. Phys.* **2016**, *18* (7), 5219–5231.

Chapter 2

Experimental Techniques and Synthesis

2.1 Experimental Techniques

2.1.1 Powder X-ray diffraction and analysis

In 1912, Max Von Laue discovered the diffraction of X-ray by crystals and was awarded the Noble prize in Physics in 1914.[1] The collimated X-ray strikes the sample and the electromagnetic waves are scattered by the atoms/ions. Most waves cancel each other out through destructive interference. The signals observed by diffractometer are constructive interference. Lawrence Bragg and Henry Bragg summarised the rule of the constructive interference as Bragg's law:

$$n\lambda = 2d\sin\theta \qquad \text{(Equation 2.1)}$$

which describes the relationship between the plane spacing d and the wavelength of the radiation λ. The intensity of XRD is determined by the electron density of the atoms in the cell, thus heavy metals and halides, such as Pb and Br/I, contribute the majority of the diffraction in OIHPs. With XRD, the organic cation atomic position and the orientation within the unit cell is hard to determine with a high degree of certainty.

Under ideal conditions, the diffraction peaks are sharp lines. However, the laboratory X-ray sources are not perfectly collimated and strictly monochromatic. In addition, the reflecting planes of crystals are not infinite. The broadening of diffraction width caused by microscale or nanoscale crystals is widely studied[2,3] and the particle size can be estimated by the Scherrer equation:[4]

$$p = \frac{K\lambda}{b\cos\theta} \qquad \text{(Equation 2.2)}$$

where p is the mean size of the ordered domain, K is Scherrer (shape) constant which has a typical value of 0.9, λ is the X-ray wavelength, b is the breadth at full width at half maximum intensity (FWHM) in radians, and θ is the Bragg angle.

2.1.1.1 Laboratory powder X-ray diffraction (PXRD)

PXRD was used to determine phase(s) formed and to check the structure of the materials. PXRD data were collected from powder (either solution precipitation or ball mill grinding) packed into a standard sample holder, or a PANalytical holder with zero-background Si substrate and an optional Kapton film cover. A PANalytical Empyrean diffractometer with Cu $K_{\alpha1}$ (λ = 1.5406 Å) or a Rigaku Miniflex 600 diffractometer with both Cu $K_{\alpha1}$ (λ = 1.5406 Å) and $K_{\alpha2}$ (λ = 1.5444 Å) were used to collect data. Low temperature PXRD between 88 K and 273 K was carried out in capillary mode using a Stoe STADIP diffractometer with Cu $K_{\alpha1}$ (λ = 1.5406 Å) and Cobra Plus non-liquid-nitrogen cryostream from Oxford Cryosystems. Data were typically collected over the range of 5-70° 2θ, with 1 hour collection time for PANalytical Empyrean diffractometer and Stoe STADIP diffractometer, and 15 minutes collection time for Rigaku Miniflex 600 diffractometer.

2.1.1.2 Laboratory single crystal X-ray diffraction (SCXRD)

All SCXRD data collection and analysis was carried out by Dr. David Cordes, University of St Andrews. SCXRD was carried out at 293 K, 173 K and 93 K using a Rigaku FR-X Ultrahigh Brilliance Microfocus RA generator/confocal optics with Rigaku XtaLAB P200 diffractometer [Mo K_{α} radiation (λ = 0.71075 Å)]. All data were corrected for Lorentz polarization effects, and a multi-scan absorption correction was applied by using CrystalClear.[5] Structures were solved by Patterson methods (PATTY)[6] and refined by full matrix least-squares against F^2 (SHELXL-2018/3).[7] Non-hydrogen atoms were refined anisotropically, and hydrogen atoms were refined using a riding model.

2.1.1.3 Rietveld refinement

Rietveld refinement was carried out with the program General Structure Analysis System (GSAS).[8] GSAS is used to process and analyse PXRD. It is also used to characterise mixture(s) of phases by refining the structural parameters of each phase and their weight fraction. Reference cif files were obtained either from single crystal diffraction measurements or from the Inorganic Crystal Structure Database.[9] The theoretical diffraction pattern was calculated from the reference cif files and compared to the

observed diffraction data. Zero point was refined in case the sample zero-point shifted. A shifted Chebyschev function with 13 background parameters was used to fit the background of the observed data.

Other than the background, the refinement of a calculated pattern contains structure information factors and profile function.[8] The structure information factors include lattice parameters, atomic positions, site occupancies and isotropic thermal displacement parameters (U_{iso}). Spherical harmonic preferred orientation is refined with 18 terms and cylindrical symmetry. The peak shape and asymmetry are also refined, and together with the structural parameters generates a calculated pattern by a least squares minimisation. The quality of fit is determined both by visual inspection of the profile and the goodness-of-fit parameters. The goodness-of-fit parameters are represented by R-factor, Rp, weighted R-factor wRp and 'reduced' weighted variance χ^2:

$$R_p = \frac{\sum |I_o - I_c|}{\sum I_o} \qquad \text{(Equation 2.3)}$$

$$wR_p = \left(\frac{\sum w(I_o - I_c)^2}{\sum I_o}\right)^{1/2} \qquad \text{(Equation 2.4)}$$

$$\chi^2 = \frac{w(I_o - I_c)^2}{N_o - N_{var}} \qquad \text{(Equation 2.5)}$$

I_o and I_c are the observed and calculated intensity respectively, w is the weighting factor, N_o is the total number of observations in all histograms, and N_{var} is the number of variables in the refinement.

2.1.2 Scanning Electron Microscopy (SEM)

SEM was used to image the surface morphology and microstructure of the materials. Electrons are generated with either a tungsten or lanthanum hexaboride (LaB_6) filament and then accelerated with high voltage. The image is obtained by analysing the signals from the beam-specimen interaction. A Jeol JSM-5600 SEM was used to obtain images of samples and accelerating voltage was set at 5 kV. The machine is equipped with a tungsten filament electron source and a secondary electron detector. Specimens were attached to carbon conductive adhesive on a Cu substrate.

2.1.2.1 Energy Dispersive X-ray spectroscopy (EDX)

EDX was used to identify the elemental composition of materials. It is an attachment to the SEM and analyses the X-rays emitted from the beam-specimen interactions. The electrons of the specimen are excited to high atomic levels by the incident high energy electron beams. When the excited electrons relax to their ground state, characteristic X-rays are generated since each element has a unique atomic structure. The target elements were chosen for fitting and the composition was decided by the relative signal intensities. An Oxford Inca EDX system was used to analyse samples with an accelerating voltage of 40 kV.

2.1.3 UV-Vis absorption spectroscopy

Solid-state UV-Vis absorption spectroscopy (UV) is a useful tool to study the optical properties of materials. As powdered solids are typically non-transparent, the solid-state UV measures the reflectance of samples. The light sources are a deuterium (D_2) lamp (190 to 350 nm) for use in the ultraviolet region and a halogen (WI) lamp (350 to 900 nm) for use in the Vis/Near-infrared region.[10] The light from the source is focused and enters the monochromator. The monochromatic light then travels to samples through an integrating sphere. Integrating spheres are provided with a light trap (Figure **2.1**) so that the reflectance of samples can be measured by the detector. Solid-state UV of all samples were recorded using a JASCO-V650 double beam spectrophotometer and an ISV-722 integrating sphere accessory, 60 mm diameter. The measurement wavelength ranges from 190 to 900 nm and the exact range depends on the visual color of the samples.
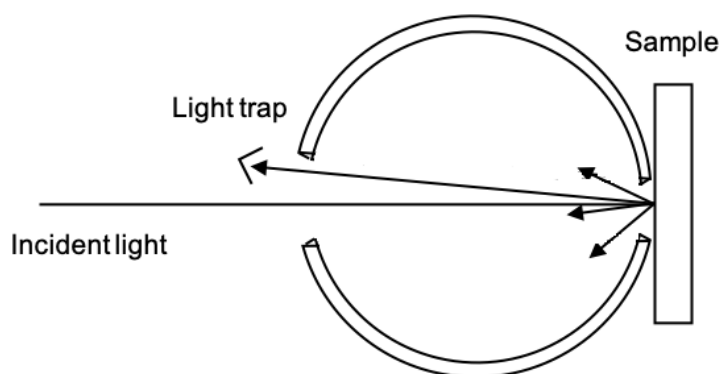

Figure 2.1. Representation of diffuse reflectance in an integrating sphere used in solid-state UV-Vis absorption spectroscopy.

2.1.3.1 Bandgap calculation

The bandgaps of the materials were calculated from the absorption spectra. The bandgap, i.e. the energy difference between the valence band and conduction band, was determined from the intersection point of the fitted baseline and the onset of the absorption spectrum. Figure **2.2** shows an illustration of this on an energy scale. The values of y-axis $f(\alpha)$ is a function of the absorption coefficient α, which can be defined as:

$$\alpha = \frac{\ln(Ref(\lambda))}{d} = -\frac{\ln(1-abs(\lambda))}{d} \qquad \text{(Equation 2.6)}$$

where $Ref(\lambda)$ and $abs(\lambda)$ are the reflection and the absorption of the sample respectively, and d is the sample thickness in centimetres, and $f(\alpha)$ depends on the band structure nature of the materials whether the optical transition is direct or indirect. The approach of Tauc *et al.*[11,12] is used to decide the bandgap E_g, of the materials:

Direct transition $\qquad\qquad f(\alpha) = \alpha^2 (\alpha^2 \propto (h\nu - E_g)) \qquad$ (Equation **2.7**)

Indirect transition $\qquad f(\alpha) = \sqrt{\alpha h\nu} \, (\sqrt{\alpha h\nu} \propto (h\nu - E_g)) \qquad$ (Equation **2.8**)

All bandgaps of the samples were determined by the Band-Gap Calculation program in Spectra Manager CFR of the spectrophotometer.
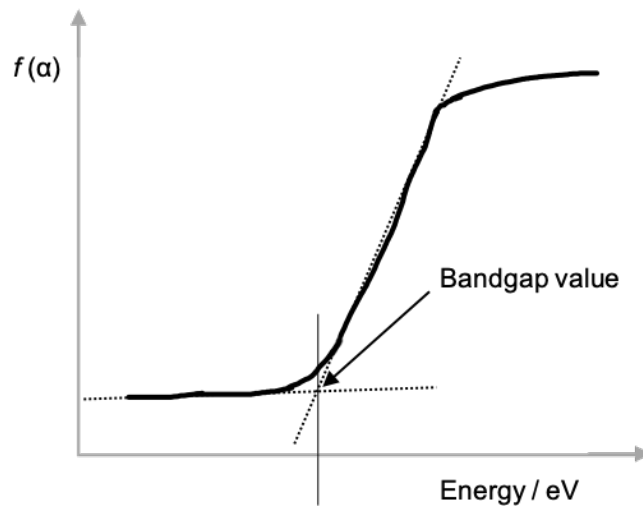

Figure 2.2. Illustration of bandgap calculation method – the bandgaps were determined from the intersection point of the fitted baseline and the onset of the absorption spectrum.

2.1.4 Grinding ball mill

Teflon ball mill pots were used for all mechanosyntheses. The diameter and depth of the pots were 38.6 mm and 45.9 mm, respectively. Nine high wear-resistant zirconia grinding media with diameter of 10 mm were added into each pot. The mixture was ground using a FRITSCH Pulverisette planetary ball mill. The rotational speed was set to 600 rpm and rotation time was set as 1 hour.

2.1.5 ^{1}H and ^{13}C NMR spectra

^{1}H and ^{13}C NMR spectra were recorded on a Bruker Advance spectrometer (400 MHz for ^{1}H, 101 MHz for ^{13}C). ^{1}H and ^{13}C NMR spectra were referenced against residual solvent peaks with respect to tetramethylsilane ($\delta = 0$ ppm). The samples were dissolved in either d-chloroform or d_6-DMSO for NMR analyses. The data were analysed using MestReNova software.

2.1.5.1 Determination of the molar ratio of A-cation using ^{1}H NMR spectra

^{1}H NMR spectroscopy was used to determine the molar ratio of the mixed-cation perovskite. The as-synthesised perovskite powder (ca. 60 mg) was dissolved in ca. 0.6 mL d_6-DMSO. The solutions were stirred at room temperature until the powder dissolved. The solutions from precipitation synthesis were transferred into NMR tubes while the solutions from mechanosynthesis were filtered to clear non-perovskite particles, such as polymer fibres or micro-particles from the ball mill before the transfer. A dichlorobenzene internal standard (20 μL) was added by micropipette. The solution was mixed before the analysis. Before integration, the baseline was corrected using Whittaker Smoother method and the phase was corrected using the whitening algorithm. The peaks of standard reagent dichlorobenzene were integrated first and normalised to 4.00 ($4 \times {}^1$H). Then the peaks of A$^+$ (A = MA or FA), Az$^+$ were integrated as I_{A+}, I_{Az+}, respectively. One example of this analysis on a mixed A-cation perovskite Az$_{0.1}$FA$_{0.9}$PbBr$_3$ is shown in Figure **2.3**. The molar ratios of organic A$^+$ cation were calculated by the equation:

$$\alpha_{A+} = \frac{I_{A+}}{I_{A+} + I_{Az+}/4} \qquad \text{(Equation } \mathbf{2.9})$$
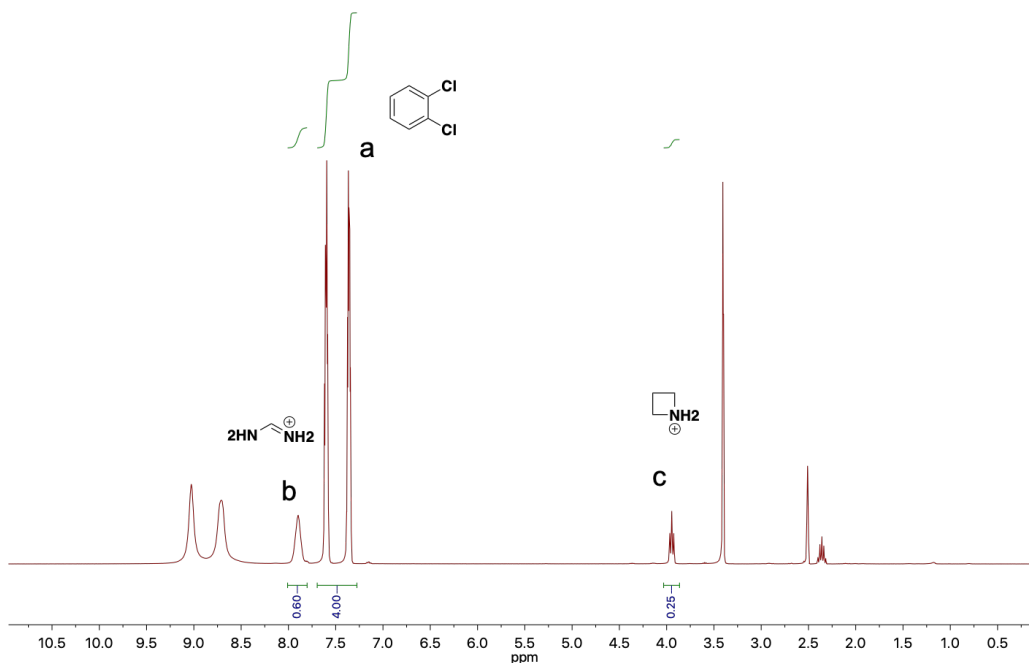
Figure 2.3. An example of the ^{1}H NMR analysis on a mixed A-cation perovskite Az$_{0.1}$FA$_{0.9}$PbBr$_3$ in d_6-DMSO. Dichlorobenzene (20 μL) was used as the internal standard.

2.1.6 Dielectric measurement

A dielectric is an electrical insulator or wide-bandgap semiconductor which can be polarised by the applied electric field. Capacitance, C, is the ratio of the electric charge (Q) that dielectric materials can store to the applied electric potential (U); $C = Q / U$. The capacitance can also be denoted as:

$$C = \varepsilon_r \varepsilon_0 \frac{A}{d}$$
(Equation **2.10**)

where ε_r is relative permittivity, ε_0 is the vacuum permittivity, and A and d are the area and the thickness of the dielectric, respectively. Relative permittivity is a useful parameter to indicate a phase transition within materials because of the polarisation changes induced by atom repositioning during the transition. The discussion above concerns the dielectric behaviour in a static electric field. However, in reality applied voltage may vary with time. The complex permittivity, ε_r^* is used to describe the dielectric in alternating field:

50

$$\varepsilon_r^* = \varepsilon_r' - j\varepsilon_r^{''} \qquad \text{(Equation 2.11)}$$

where real component ε_r' is the relative permittivity, and the imaginary component or absolute loss $\varepsilon_r^{''}$ indicates the energy loss in the dielectric in the alternating field. Dielectric loss is also expressed as a normalised loss or dissipation which is known as tan δ:

$$tan\delta = \varepsilon_r^{''} / \varepsilon_r' \qquad \text{(Equation 2.12)}$$

Besides the polarisation process and frequency, the relative permittivity of dielectrics depends on temperature.[13,14] Figure 2.4 shows a generic model of possible relative permittivity changes with temperature. In O to A, the sharp decrease while cooling may be due to the orientation (freezing) of permanent dipoles in the material; the gentle decrease at lower temperature is due to the diminishing motion of the dipoles and decreasing contribution to the polarisation of the material. The overall polarisation gained from electronic and ionic polarisation does not change significantly with the temperature. The gap between O and O' is due to the hysteresis of temperature response of the material and may either be related to the thermodynamics of any phase transition, or due to experimental factors such as thermal lag. In O to B, the average dipole alignment decreases as the activated random thermal motion hinders the collective charge displacement of the material in the electric field. In B to C, the sharp decrease happens when the material melts and the structure of it changes; the latter descent is due to the same process of the melted material as O to B.

Samples for electrical measurements were prepared by pressing powdered samples into a pellets of 10 mm diameter under a load of 1 ton. The opposing faces of the pellets were then coated with either gold or silver paste electrodes. For measurements below room temperature, the relative permittivity and loss were collected using an Agilent 4294A precision impedance analyser connected to a closed-cycle cryostat. The working temperature range is from 50 to 320 K. The sample was mounted next to a thermocouple in the sealed chamber which was evacuated to a pressure no greater than 6×10^{-2} mbar. In general, heating/cooling rates of 2 K/min were used and the temperature interval of data collection was 2 K. Data were collected over the frequency range of 100 Hz to 10 MHz.
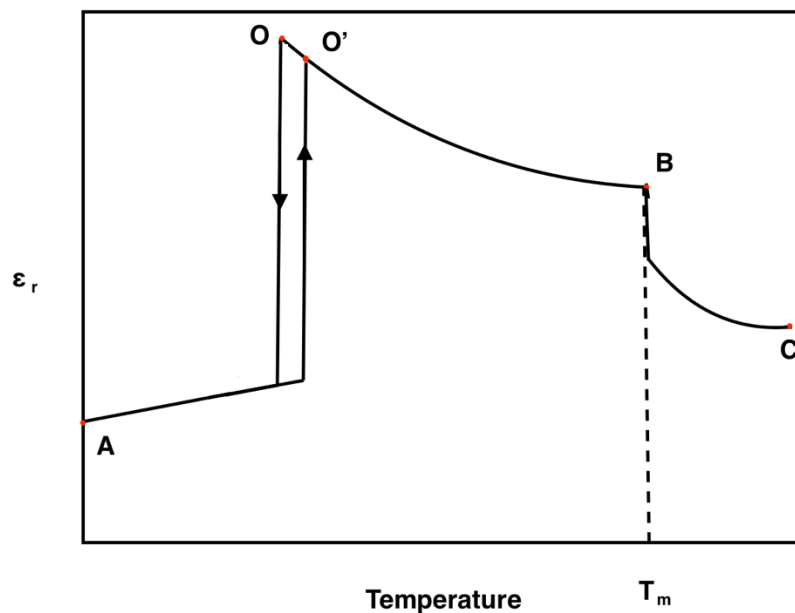
Figure 2.4. Temperature dependence of relative permittivity, adapted from Ref. 14 with permission under licence "Attribution-Non-Commercial-Share Alike 2.0 UK: England & Wales".

2.1.7 Thermo-gravimetric analysis (TGA)

TGA is used to analyse the sample mass change with changing temperatures over time. Around 5 mg of samples were weighted and put into a Al_2O_3 crucible for the analysis. Then the crucible was transferred to the balance in the Netzsch Thermogravimetric Analyzer TG 209, which was programmed to start heating from room temperature to 700 °C at a rate of 10 °C / min under N_2 flow.

2.2 Experimental details of synthesis

2.2.1 Precursor synthesis

2.2.1.1 Synthesis of azetidinium bromide

AzCl (0.47 g, 5 mmol, 1 equiv.) and NaBr (1.02g, 10 mmol, 2 equiv.) were dissolved in 50 mL EtOH. The reaction flask was sparged with N_2 for 10 min and then the mixture was stirred at 50 °C under N_2 for 18 h. The reaction mixture was filtered, and the solvent

of the filtrate was removed under reduced pressure. DCM was added to re-dissolve the product and a second filtration was carried out to remove the remaining sodium salts. The crude product was recrystallized twice from EtOH/diethyl ether. The recovered solid was dried under vacuum for 24 h before use. White needle-like crystals were obtained. **Yield:** 82 %. **Mp.:** 132 - 135 °C. **^{1}H NMR (400 MHz, CDCl$_3$) δ (ppm)** 9.37 (s, 2H), 4.24 – 4.12 (m, 4H), 2.61 (p, J = 8.4 Hz, 2H). **^{13}C NMR (101 MHz, CDCl$_3$) δ (ppm)** 46.16, 18.48. **Elemental Analysis.** Calculated: C, 26.11; H, 5.84; N, 10.15; Br, 57.90; Found: C, 26.24; H, 5.65; N, 9.99.

2.2.1.2 Synthesis of azetidinium iodide

Potassium hydroxide (1.30 g, 23 mmol, 1.5 equiv.) was dissolved in 3 mL deionised water and mixed with azetidinium chloride (1.45 g, 15 mmol, 1 equiv.) under stirring for 30 min. The intermediate azetidine was extracted at 80 ℃ under reduced pressure and condensed with liquid nitrogen. Hydroiodic acid (3 mL, 23 mmol, 1.5 equiv.) was then added into the condensed solution and reacted under stirring for 30 min at room temperature. The solvent was then removed under reduced pressure at 80 ℃. The crude products were dissolved in 3 mL EtOH and the product recrystallized from diethyl ether. The recovered solid was dried under vacuum for 24 h before use. White needle-like crystals were obtained. **Yield:** 86%. **Mp.:**137-138 °C **^{1}H NMR (500 MHz, DMSO-d_6) δ (ppm)** 8.42 (s, 2H), 3.98 – 3.89 (m, 4H), 2.37 (p, J = 8.3 Hz, 2H). **^{13}C NMR (126 MHz, DMSO-d_6) δ (ppm)** 46.53, 18.93. **Elemental Analysis**. Calculated: C, 19.48; H, 4.36; N, 7.57; I, 68.59; Found: C, 19.61; H, 4.24; N, 7.66.

2.2.1.3 Synthesis of methylammonium bromide/iodide

The synthesis protocol is a modification of that reported in the literature.[15,16] MABr/I was synthesised by reacting methylamine (20 mL, 0.1 mol, 1 equiv.) and hydrobromic acid (20 mL, 0.17 mol, 1.7 equiv.) / hydroiodic acid (24 mL, 0.12 mol, 1.2 equiv.), respectively, in a round-bottom flask at 0 °C for 2 h with stirring. The solvent was carefully removed under reduced pressure. The white crude products were recrystallized from EtOH/diethyl ether and dried under vacuum for 24 h. White needle-like crystals were obtained for both

products. MABr: **Yield:** 83 %. **^{1}H NMR (400 MHz, CDCl$_3$) δ (ppm)** 7.50 (s, 3H), 2.38 (s, 3H). MAI: **Yield:** 46 %. **^{1}H NMR (400 MHz, CDCl$_3$) δ (ppm)** 7.48 (s, 3H), 2.38 (d, J = 0.8 Hz, 3H). The characterisation matches that reported in the literature.[15,16]

2.2.1.4 Synthesis of formamidinium bromide/iodide

The synthesis protocol is a modification of that reported in the literature.[17] Formamidinium acetate (1.04 g, 10 mmol, 1 equiv.) and hydrobromic acid (2.3 mL, 20 mmol, 2.0 equiv.) / hydroiodic acid (2.4 mL, 12 mmol, 1.2 equiv.), respectively, were mixed and stirred at 50 °C for 20 min. The solvent was removed under reduced pressure. The white crude products were dissolved in EtOH and the product recrystallized from diethyl ether. The recovered solid was dried under vacuum for 24 h before use. White needle-like crystals were obtained for both products. FABr: **Yield:** 91 %. **Mp.:** 132 - 136 °C (reported[18] as 133 – 140 °C) **^{1}H NMR (400 MHz, DMSO-d_6) δ (ppm)** 8.75 (s, 4H), 7.86 (s, 1H). **^{13}C NMR (101 MHz, DMSO-d_6) δ (ppm)** 40.19. **Elemental Analysis.** Calculated: C, 9.61; H, 4.03; N, 22.42; Br, 63.94; Found: C, 9.42; H, 4.14; N, 22.30. FAI: **Yield:** 88 %. **Mp.:** 235 - 240 °C (reported[17] as 242 °C). **^{1}H NMR (400 MHz, DMSO-d_6) δ (ppm)** 8.84 (s, 4H), 7.86 (s, 1H). **^{13}C NMR (101 MHz, DMSO-d_6) δ (ppm)** 39.96. **Elemental Analysis.** Calculated: C, 6.98; H, 2.93; N, 16.29; Br, 73.80; Found: C, 6.97; H, 3.03; N, 16.25. The characterisation matches that reported in the literature.[19,20]

2.2.2 Synthesis of perovskite

2.2.2.1 Synthesis of AzPbCl$_3$, AzPbBr$_3$, and AzPbI$_3$

A solution precipitation method was adapted to synthesise azetidinium lead chloride (AzPbCl$_3$). A mechanical grinding method was adapted to synthesise azetidinium lead iodide (AzPbI$_3$). Both a solution precipitation method and a mechanical grinding method were adapted to synthesise azetidinium lead bromide (AzPbBr$_3$).

Precipitation synthesis: AzPbCl$_3$ samples were prepared by mixing AzCl (0.094 g, 1.0 mmol, 1 equiv.) and PbCl$_2$ (0.278 g, 1.00 mmol, 1 equiv.) in 2 mL DMSO solution at room temperature and in air. After stirring for 1 h, clear solutions were obtained. A controlled amount of DCM (8 mL) was added slowly into the solution and the solution

was shaken for 1 min and then left to stand for 10 min before vacuum filtration. The resulting powders were washed with 10 mL DCM twice and dried in vacuum for 24 h. The samples were obtained as white powder. Single crystals of $AzPbCl_3$ were obtained by slow diffusion of antisolvent DCM into the same concentration solution in a sealed vial. White needle-like crystals were obtained within 24 h. AzBr (0.138 g, 1.00 mmol, 1 equiv.) and $PbBr_2$ (0.367 g, 1.00 mmol, 1 equiv.) were stirred in 2 mL DMF for 10 min before 0.5 mL DMSO was added into the solution. The solution was stirred until it became homogenous. Acetonitrile (20 – 25 mL) was added slowly into the solution, whereupon a pale yellow precipitate formed immediately. The mixture was left to stand for 10 min before filtration. The resulting powders were washed with acetonitrile twice and dried under vacuum for 24 h. A pale yellow powder was obtained. The single crystal of $AzPbBr_3$ was obtained by placing the solution into a sealed chamber with low-boiling point antisolvent (DCM) to allow the single crystal to grow with antisolvent diffusion. The diffusion took 2 to 3 days until pale yellow needle-like crystals were obtained.

Mechanosynthesis: AzBr (0.138 g, 1.00 mmol, 1 equiv.) and $PbBr_2$ (0.367 g, 1.00 mmol, 1 equiv.) were mixed by gentle grinding for 5 min before the mixture was transferred into the ball mill and ground at 600 rpm for 1 h. A pale yellow powder was obtained. AzI (0.185 g, 1.00 mmol, 1 equiv.) and PbI_2 (0.461 g, 1.00 mmol, 1 equiv.) were mixed by gentle grinding for 3 min before the mixture was transferred into the ball mill and ground at 600 rpm for 1 h. An orange powder was obtained.

2.2.2.2 Synthesis of mixed-cation perovskite

Both an antisolvent precipitation method and a mechanical grinding method were adapted to synthesise mixed A-cation samples with general compositions: $Az_{1-x}FA_xPbBr_3$, $Az_{1-x}MA_xPbBr_3$ and $MA_{1-x}FA_xPbBr_3$ ($0 \leq x \leq 1$).

Mechanosynthesis: $Az_{1-x}FA_xPbBr_3$ ($0 \leq x \leq 1$) samples were prepared by mixing appropriate molar ratios of vacuum dried AzBr and FABr with $PbBr_2$ in a mortar and pestle and gently ground for 3 min. The mixture was then transferred into the ball mill and ground at 600 rpm for 1 h. The samples obtained ranged from pale yellow (low x) to red/orange (high x). $Az_{1-x}MA_xPbBr_3$ ($0 \leq x \leq 1$) were prepared by mixing appropriate molar ratios of vacuum dried AzBr and MABr with $PbBr_2$ in the ball mill and ground at

600 rpm for 1 h. $MA_{1-x}FA_xPbBr_3$ ($0 \leq x \leq 1$) samples were prepared by mixing appropriate molar ratios of vacuum dried MABr and FABr with $PbBr_2$ in the ball mill and ground at 600 rpm for 1 h.

Precipitation synthesis: $Az_{1-x}FA_xPbBr_3$ ($0 \leq x \leq 1$) samples were prepared by mixing appropriate molar ratios of AzBr and FABr with $PbBr_2$ in DMF/DMSO (4:1, 2.5 mL, 0.4 M) solution at room temperature in air. After stirring for 1 h, clear solutions were obtained. 20 mL acetonitrile was added slowly into the solution and the solution was shaken for 3 min and then left to stand for 15 min before filtration. The resulting powders were washed with 10 mL acetonitrile twice and dried in vacuum for 24 h. The samples obtained ranged from pale yellow (low x) to red/orange (high x).

$Az_{1-x}MA_xPbBr_3$ ($0 \leq x \leq 1$) were prepared by mixing appropriate molar ratios of AzBr and MABr with $PbBr_2$ in DMF/DMSO (4:1) solution (ca. 0.5 M) at room temperature and in air. After stirring for 2 h, clear solutions were obtained. Acetonitrile was added slowly into the solutions and these were left to stand for 10-30 min before filtration. The resulting powders were washed with acetonitrile and diethyl ether twice and dried in vacuum for 24 h. The samples obtained ranged from pale yellow (low x) to orange (high x).

$MA_{1-x}FA_xPbBr_3$ ($0 \leq x \leq 1$) samples were prepared by mixing appropriate molar ratios of MABr and FABr with $PbBr_2$ in DMF solution (ca. 0.5 M) at room temperature. After stirring for 1 h, clear solutions were obtained. 20 mL acetonitrile was added slowly into the solution and the solution was left to stand for 15 min before filtration. The resulting powders were washed with 10 mL acetonitrile twice and dried in vacuum for 24 h. The samples obtained were red/orange.

2.2.2.3 Step antisolvent precipitation synthesis of $Az_{0.5}FA_{0.5}PbBr_3$

Set 1: AzBr, FABr and $PbBr_2$ were dissolved in DMF/DMSO (4:1) – 0.4 M where the nominal composition was $Az_{0.5}FA_{0.5}PbBr_3$. The solution was divided evenly into 5 sample vials after stirring. The volume of antisolvent acetonitrile added into the solution ranged from 1 mL, 2 mL, 5 mL, 10 mL to 20 mL. The precipitates were dried in vacuum for 24 h before analysis.

Set 2: AzBr, FABr and $PbBr_2$ were dissolved in DMF/DMSO (4:1) – 0.4 M where the nominal composition was $Az_{0.5}FA_{0.5}PbBr_3$. The total amount of antisolvent added into the solution acetonitrile, including rinsing and washing, was recorded. To obtain enough powder for the analysis, the total amount of antisolvent ranged from 1 mL, 7 mL, 16 mL to ca. 30 mL. The extra volume of antisolvent was to compensate for the loss during vacuum filtration. The precipitates were dried in vacuum for 24 h before analysis.

2.2.2.4 Synthesis of azetidinium mixed-halide perovskite

A mechanical grinding method was adapted to synthesise $AzPbCl_xBr_{3-x}$ and $AzPbBr_xI_{3-x}$ $(0 \le x \le 3)$. $AzPbCl_xBr_{3-x}$ $(0 \le x \le 3)$ samples were prepared by mixing appropriate molar ratios of vacuum dried precipitation synthesised $AzPbCl_3$ or AzBr and $PbCl_2$ or $PbBr_2$ in a mortar and pestle and gently ground for 1 min. The mixture was then transferred into the ball mill and ground at 600 rpm for 1 h. The samples obtained ranged from white to pale yellow. $AzPbBr_xI_{3-x}$ $(0 \le x \le 3)$ samples were prepared by mixing appropriate molar ratios of vacuum dried AzBr or AzI and $PbBr_2$ or PbI_2 in the ball mill and ground at 600 rpm for 1 h. The samples obtained ranged from pale yellow to orange.

2.2.2.5 Synthesis of low dimensional structure with azetidinium

Az_2PbBr_4 can be obtained by either hand grinding or mechanosynthesis. AzBr (0.276 g, 2.00 mmol, 2 equiv.) and $PbBr_2$ (0.367 g, 1.00 mmol, 1 equiv.) were mixed in a mortar and pestle and ground for 30 min. For the mechanosynthesis, the same stoichiometric amount of AzBr and $PbBr_2$ were mixed in ball mill and ground at 600 rpm for 1 h. A yellow powder was obtained from both syntheses.

AzBr (0.150 g, 1.09 mmol, 3 equiv.) and $BiBr_3$ (0.325 g, 0.725 mmol, 2 equiv.) were stirred in 2 mL DMF solution at room temperature and in air. After stirring for 1 h, clear solutions were obtained. DCM (20 mL) was added into the solution, whereupon a yellow precipitate formed immediately. The resulting powders were washed with DCM twice and dried under vacuum for 24 h. A bright yellow powder was obtained. Single crystal of azetidinium bismuth bromide was obtained by placing the solution into a sealed chamber with DCM to allow the single crystal to grow with antisolvent diffusion. Bright yellow needle-like crystals were obtained.

References

(1)   The Nobel Prize in Physics 1914 - NobelPrize.org https://www.nobelprize.org/prizes/physics/1914/summary/ (accessed Jan 23, 2020).

(2)   Londoño-Restrepo, S. M.; Jeronimo-Cruz, R.; Millán-Malo, B. M.; Rivera-Muñoz, E. M.; Rodriguez-García, M. E. Effect of the Nano Crystal Size on the X-Ray Diffraction Patterns of Biogenic Hydroxyapatite from Human, Bovine, and Porcine Bones. *Sci. Rep.* **2019**, *9* (1).

(3)   Muniz, F. T. L.; Miranda, M. A. R.; Morilla Dos Santos, C.; Sasaki, J. M. The Scherrer Equation and the Dynamical Theory of X-Ray Diffraction. *Acta Crystallogr. Sect. A Found. Adv.* **2016**, *72* (3), 385–390.

(4)   Cullity, B. D.; Stock, S. R. Elements of X-Ray Diffraction, Third Edition. Prentice-Hall 2001, pp 92–102.

(5)   CrystalClear-SM Expert 2.1. Rigaku Americas, Rigaku Americas, The Woodlands, Texas, USA, and Rigaku Corporation;Tokyo, Japan. 2015.

(6)   DIRDIF-99. Beurskens, P. T.; Beurskens, G.; de Gelder, R.; Garcia-Granda, S.; Gould, R. O.; Israel, R.; Smits, J. M. *M.*; Crystallography Laboratory, University of Nijmegen, The Netherlands, 1999.

(7)   Sheldrick, G. M.; IUCr. Crystal Structure Refinement with *SHELXL*. *Acta Crystallogr. Sect. C Struct. Chem.* **2015**, *71* (1), 3–8.

(8)   A. C. Larson and R.B. V. Dreele. *Los Alamos National Laboratory Report LAUR*; 2004.

(9)   Startpage ICSD | ICSD https://icsd.products.fiz-karlsruhe.de/ (accessed Feb 19, 2021).

(10)   Model V-630/650/660/670 Spectrophotometer Hardware/Function Manual; 2010.

(11)   Tauc, J.; Grigorovici, R.; Vancu, A. Optical Properties and Electronic Structure of Amorphous Germanium. *Phys. status solidi* **1966**, *15* (2), 627–637.

(12)   Tauc, J. OPTICAL PROPERTIES AND ELECTRONIC STRUCTURE OF AMORPHOUS Ge AND Si. *Mat. Res. Bull.* **1968**, *3*, 1–21.

(13)   Waser, R.; Böttger, U.; Tiedke, S. *Polar Oxides : Properties, Characterization,*

and Imaging; Wiley-VCH, 2005.

(14)   DoITPoMS - TLP Library Dielectric materials - Effect of temperature on the dielectric constant https://www.doitpoms.ac.uk/tlplib/dielectrics/temperature.php (accessed Feb 3, 2020).

(15)   Cao, M.; Tian, J.; Cai, Z.; Peng, L.; Yang, L.; Wei, D. Perovskite Heterojunction Based on CH3NH3PbBr3 Single Crystal for High-Sensitive Self-Powered Photodetector. *Appl. Phys. Lett.* **2016**, *109* (23), 233303.

(16)   Shi, D.; Adinolfi, V.; Comin, R.; Yuan, M.; Alarousu, E.; Buin, A.; Chen, Y.; Hoogland, S.; Rothenberger, A.; Katsiev, K.; et al. Low Trap-State Density and Long Carrier Diffusion in Organolead Trihalide Perovskite Single Crystals. *Science (80-.).* **2015**, *347* (6221), 519–522.

(17)   FAI | Formamidinium Iodide | 879643-71-7 | Formamidine hydroiodide | Ossila https://www.ossila.com/products/formamidinium-iodide-fai?variant=21624890817 (accessed Feb 10, 2020).

(18)   Formamidinium Bromide, >99.5% Purity FABr | CAS 146958-06-7 | Ossila https://www.ossila.com/products/formamidinium-bromide-fabr?variant=21625455361 (accessed Feb 10, 2020).

(19)   Perumal, A.; Shendre, S.; Li, M.; Tay, Y. K. E.; Sharma, V. K.; Chen, S.; Wei, Z.; Liu, Q.; Gao, Y.; Buenconsejo, P. J. S.; et al. High Brightness Formamidinium Lead Bromide Perovskite Nanocrystal Light Emitting Devices. *Sci. Rep.* **2016**, *6* (June), 1–10.

(20)   Hanusch, F. C.; Wiesenmayer, E.; Mankel, E.; Binek, A.; Angloher, P.; Fraunhofer, C.; Giesbrecht, N.; Feckl, J. M.; Jaegermann, W.; Johrendt, D.; et al. Efficient Planar Heterojunction Perovskite Solar Cells Based on Formamidinium Lead Bromide. *J. Phys. Chem. Lett.* **2014**, *5* (16), 2791–2795.

Chapter 3

Organic-inorganic hybrid perovskite – azetidinium lead bromide
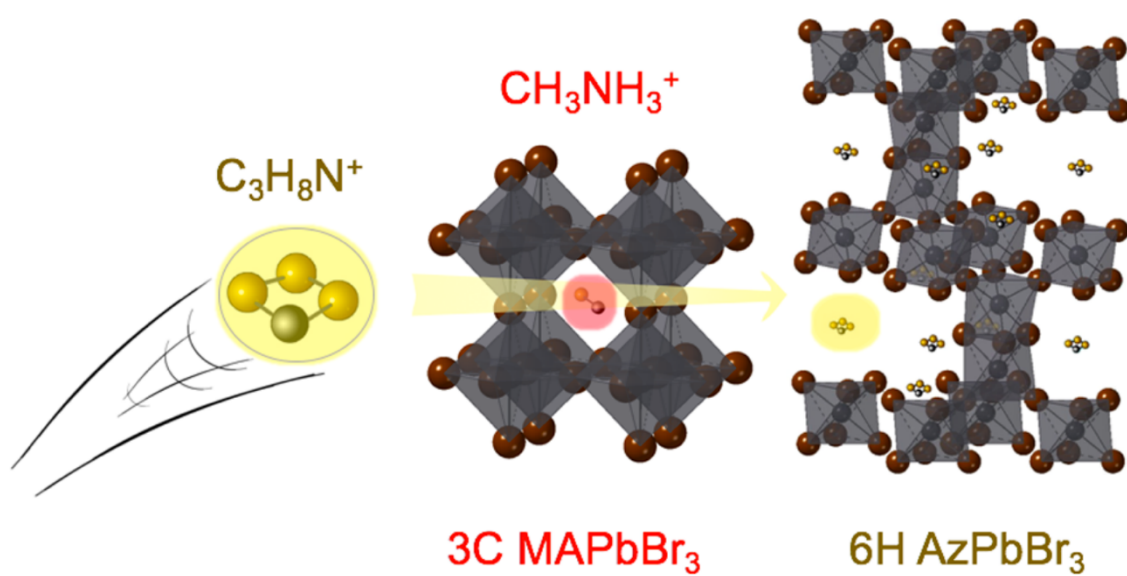
Cover picture: TOC graphic of publication arising from this chapter

3.1 Introduction

As discussed in Chapter 1, OIHPs are currently one of the fastest-growing areas of solid-state materials science. While much of the understanding of OIHPs borrows from the more mature area of oxide perovskites, there is still much to learn regarding the solid-state chemistry due to dynamic effects associated with the organic cations, their increased covalency relative to oxides, and also their chemical stability.

Azetidinium (Az^+), a four-member ring ammonium $(CH_2)_3NH_2^+$, is here proposed to be a potential A-cation candidate to form lead halide OIHPs with tolerance factors close to 1.00. Examples using Az as the A-cation in OIHPs are limited to triiodide analogues.[1,2] Pering *et al.*[1] reported the optical bandgap of $AzPbI_3$ to be 2.15 eV and the $AzPbI_3$ thin film was reported to better withstand exposure to moisture than $MAPbI_3$ without decomposing, although the exposure time was only a few seconds. Riccardo *et al.*[2] determined the structure of $AzPbI_3$ to be a 9R rhombohedral polytype within the space group $\bar{R}3$. The $AzPbI_3$ was synthesised by a two-step recrystallisation solution approach.

DFT calculations predicted that the 2H hexagonal (δ-H phase, yellow) is more thermodynamically stable for $APbI_3$ (A = MA and FA) than the black (pseudo-) cubic phase (tetragonal, orthorhombic).[3,4] This is supported by experimental observations of irreversible colour change of $APbI_3$ (A = MA and FA) thin film from black to yellow under ambient environment.[5,6] It is essential to study the formation of the hexagonal phase and prevent the cubic-hexagonal phase transition in the ambient environment. Thus, additional examples of hexagonal perovskite polytypes are needed.

Stoumpos *et al.*[7] found that hexagonal perovskite structures were common in tin-based OIHPs. For lead-based OIHPs, 2H and 4H hexagonal polytypes have been reported with cations such as $NH_2(CH_3)_2^+$ (DMA) and $NH(CH_3)_3^+$ (TMA).[8–11] Gratia *et al.*[12] also reported a crystallisation process with a structural change from 2H, 4H and 6H (hexagonal) to 3C (cubic) depending on x in the solid solution $(FAPbI_3)_x(MAPbBr_3)_{1-x}$; however, in that study DMSO solvent molecules were found to be present in the crystal lattice and it is unclear how their presence may affect the exact polymorph adopted, or its resulting stability.

The focus of this chapter is the detailed structural and optoelectronic characterisation of a new 6H OIHP – $AzPbBr_3$. The analyses include variable temperature PXRD, variable temperature SCXRD, dielectric spectroscopy and absorption spectra. The structure of $AzPbBr_3$ was determined to be a 6H polytype and the two possible phase transitions on cooling were analysed with variable temperature PXRD and dielectric spectroscopy. The octahedral distortion of $AzPbBr_3$ was analysed based on the Pb and Br coordination data from variable temperature SCXRD.

3.2 New stable 6H organic-inorganic hybrid lead perovskite - $AzPbBr_3$

3.2.1 Synthesis and structural analysis of $AzPbBr_3$

As AzBr is not commercially available, it was synthesised by ion-exchange using AzCl and NaBr and its purity verified by ^{1}H and ^{13}C NMR spectra and elemental analysis (Chapter 2). The $AzPbBr_3$ material was obtained both by solution precipitation synthesis and mechanosynthesis. For the former, stoichiometric dry AzBr was mixed with $PbBr_2$ in DMF/DMSO (4:1, by volume) and precipitated with anti-solvent (Table **3.1**).[13] In the mechanosynthesis, stoichiometric dry AzBr was mixed with $PbBr_2$ using a ball mill and ground at 600 rpm for 1 hour. Regardless of the synthetic approach, $AzPbBr_3$ with the 6H structure was obtained, suggesting that this phase is thermodynamically favoured for this composition. Experimental conditions with varied solvent, antisolvent and solution temperature, and corresponding PXRD of precipitation synthesised samples are shown in Table **3.1** and Figure **3.1a**, respectively.

In addition, $AzPbBr_3$ obtained from both synthetic methods were highly stable in the 6H form and showed no visual or structural degradation after storage in ambient air for 6 months (Figures **3.1b, 3.1c**). The PXRD of the mechanosynthesised $AzPbBr_3$ showed additional features in the base of the broad main peaks which were especially evident around 12 – 14°. Such features were not present in the precipitation synthesised samples. These features match well with the reported features from bimodal CdS particles[14] and indicate the presence of multiple subpopulations of different sizes of 6H perovskite particles.

Table 3.1. Experimental details of solution precipitation synthesis of AzPbBr$_3$ powder samples, adapted from Ref. 13 with permission. Copyright (2019) American Chemical Society.

Compound composition	Solvent	Stirring temperature / °C	Stirring time / h	Anti-solvent	Drying time / h	Pattern reference
0.0828 g AzBr (0.06 mmol) + 0.2202 g PbBr2 (0.06 mmol)	1 mL DMF + 0.5 mL DMSO	0	6	Acetonitrile	24	1
		20	6	Acetonitrile	24	2
		20	10	Toluene	7	3
		20	10	DCM	7	4
		60	6	Acetonitrile	48	5
		60	6	Toluene	48	6

SEM of both mechano- and precipitation synthesised AzPbBr$_3$ (Figures **3.2a, 3.2b**) indicates the presence of a large proportion of relatively smaller particles in mechanosynthesised AzPbBr$_3$ explaining the broad PXRD tails in Figure **3.1c**.

Crystals suitable for SCXRD of AzPbBr$_3$ perovskite were obtained by slow diffusion of the anti-solvent chloroform into the solution of perovskite in DMF. AzPbBr$_3$ appears as bright yellow needle-like crystals and SEM micrographs show the crystals to be "spear-like" (Figures **3.2c**) where the hexagonal cross-section ranges from 25 to 90 μm and overall length is about 1 mm. The data obtained at 293 K indicates AzPbBr$_3$ adopts the 6H perovskite structure in the space group $P6_3/mmc$ with lattice parameter a = 8.745 Å, c = 21.329 Å (Figure **3.2d**). The SCXRD data also indicate that the Az cations are situated over high-symmetry lattice sites, and show considerable disorder. As a result, they are represented by solid spheres and are located in the centre of electron density associated with the Az. For the discussion below, the Az, Pb and Br and atoms were classified as two categories (Az1, Az2, Pb1, Pb2, Br3 and Br4) according to their atomic positions in the unit cell under the symmetry operation.
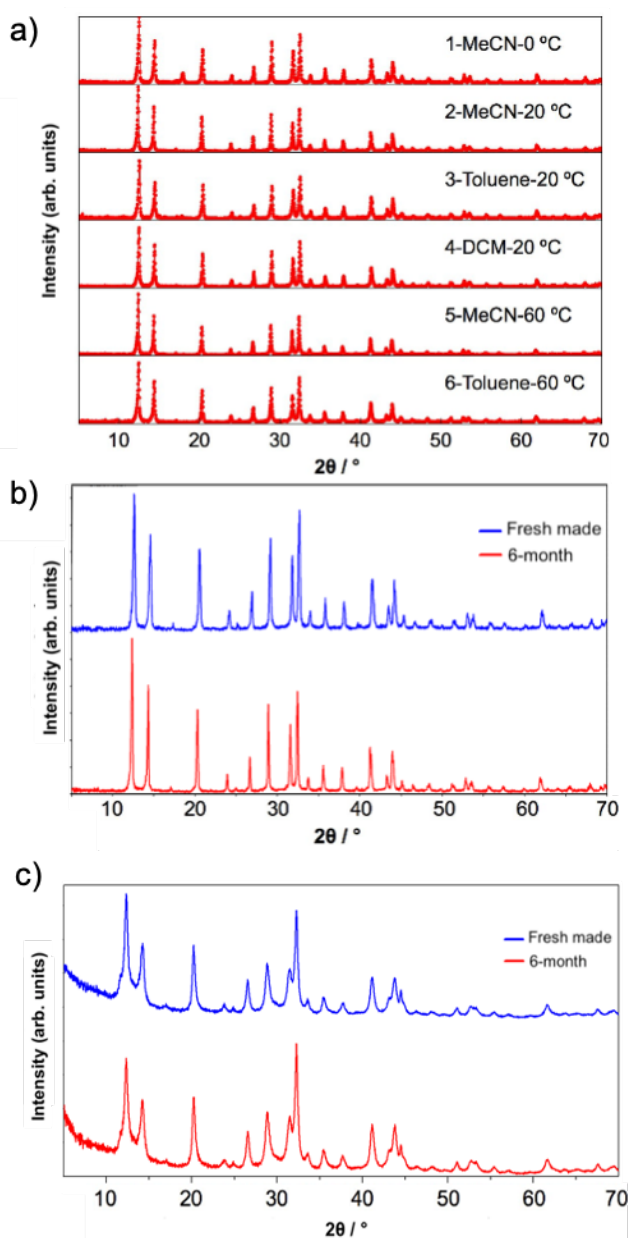
Figure 3.1. (a) Associated PXRD patterns with various synthetic conditions (Table **3.1**) of AzPbBr$_3$ (note that the peak at 17° is from the Teflon sample holder). Comparison of PXRD patterns of freshly made (blue, top) and after storage in ambient air for 6 months (red, bottom) of (b) precipitation synthesised (c) mechanosynthesised AzPbBr$_3$ samples. Figures (a, b) are adapted from Ref. 13 with permission. Copyright (2019) American Chemical Society.
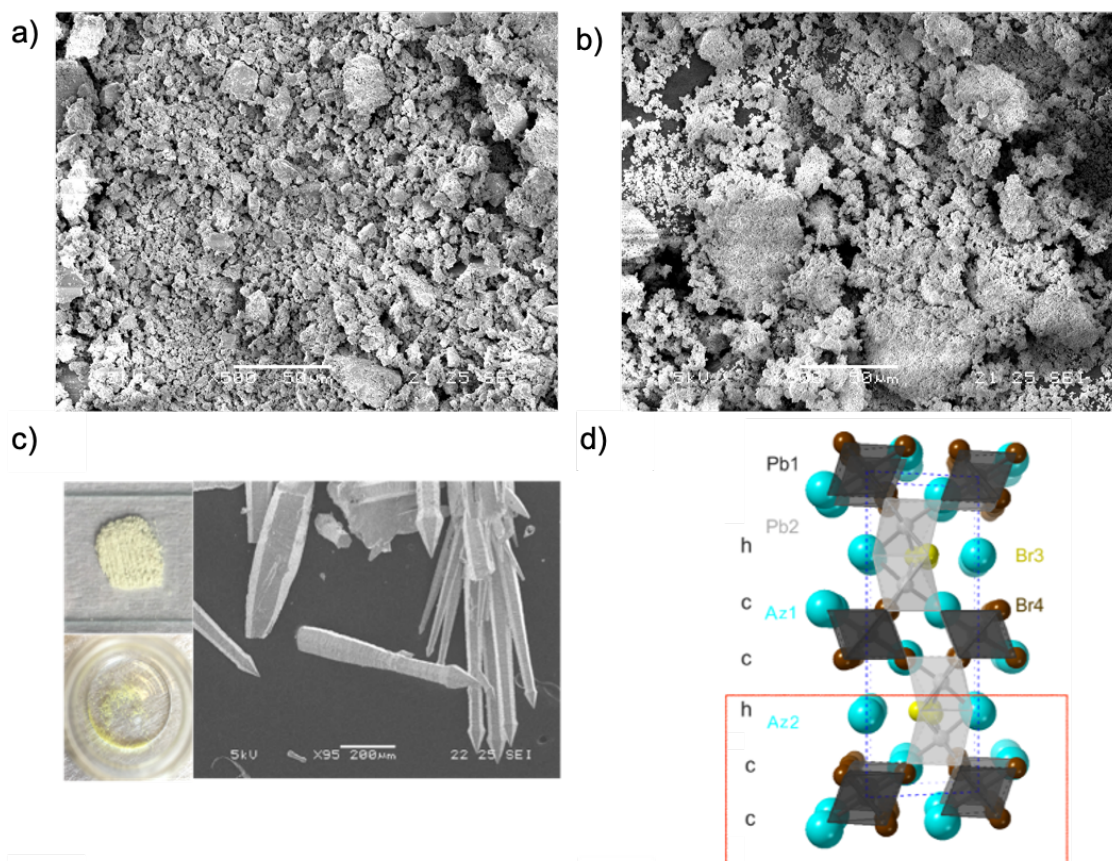
Figure 3.2. SEM images of AzPbBr$_3$ samples obtained from (a) mechanosynthesis (b) precipitation synthesis. The white scale bar in both images is 50 μm (c) optical images of powder and single crystal AzPbBr$_3$ sample (left), and SEM micrograph of single crystals (right – scale bar is 200 μm) (d) 6H hexagonal perovskite structure as determined from SCXRD at 293 K, indicating (*hcc*)$_2$ packing sequence and combination of face- and corner-sharing octahedra. Adapted from Ref. 13 with permission. Copyright (2019) American Chemical Society.

Rietveld refinement of PXRD data confirms that powder samples adopt the same structure (Figure **3.3**). The 6H perovskite structure is akin to the high temperature hexagonal polymorph of BaTiO$_3$[15,16] and has a (*hcc*)$_2$ stacking sequence in Jagodzinski notation (i.e. ABCBAC), resulting in pairs of face-sharing octahedra linked by corner-sharing ones. Single crystal and powder crystallographic data are shown in Table **3.2**.

Table 3.2. Crystallographic data of the $AzPbBr_3$ perovskite obtained from both SCXRD and PXRD at selected temperatures, reproduced from Ref. 13 with permission. Copyright (2019) American Chemical Society.

	Single crystal	Single crystal	Single crystal[a]	Powder (plate)	Powder (capillary)	Powder (capillary)
T / K	293	173	93	293	293	173
empirical formula	$C_3H_8Br_3NPb$	$C_3H_8Br_3NPb$	$C_3H_8Br_3NPb$	$C_3H_8Br_3NPb$	$C_3H_8Br_3NPb$	$C_3H_8Br_3NPb$
fw	505.02	505.02	505.02	505.02	505.02	505.02
description	yellow prism	yellow prism	yellow prism	pale yellow	pale yellow	pale yellow
space group	$P6_3/mmc$	$P6_3/mmc$		$P6_3/mmc$	$P6_3/mmc$	$P6_3/mmc$
a / Å	8.745(2)	8.6827(11)	8.608(2)	8.7441(8)	8.746(1)	8.671(7)
c / Å	21.329(4)	21.251(3)	21.345(6)	21.297(1)	21.33(1)	21.23(5)
vol / Å³	1412.6(7)	1387.5(3)	1369.7(7)	1410.2(3)	1413.1(5)	1382.(9)
ρ (calc) / g/cm³	3.562	3.626		3.840	3.832	3.916
reflns collected	16421	16176		3822	6499	6499
GOF on F²	1.176	1.093		4.697[b]	0.8995[b]	0.1860[b]
R_1 [$I > 2\sigma(I)$]	0.0213	0.0233		0.0893[c]	0.0933[c]	0.0688[c]
wR_2 (all data)	0.0559	0.0534		0.083[d]	0.1240[d]	0.0936[d]

[a] This data is provided as a representative example of obtained data from collections tried at 93 K. Goodness-of-fit parameters for Rietveld refinements of powder data: [b] χ^2 ; [c] R_p; [d] wR_p; see Figure **3.3** for refinement profile at 293 K. Note that χ^2 values < 1 for the PXRD (capillary) results at 293 and 173 K are due to the poor signal-to-noise ratio of the data obtained.
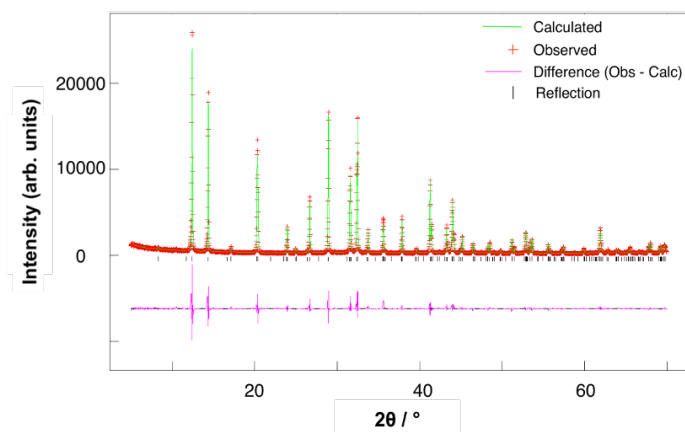
Figure 3.3. Rietveld refinement profile of AzPbBr$_3$ PXRD data at 293 K, refined in space group *P*6$_3$/*mmc*, lattice parameter a = 8.744(1) Å, c = 21.29(7) Å, R_{wp}=0.1195, χ^2 = 9.720, reproduced from Ref. 13 with permission. Copyright (2019) American Chemical Society.

Thermal stability of AzPbBr$_3$ was tested with TGA under N$_2$ atmosphere (Figure **3.4**). Weight loss of samples started at 220 ℃ and the decomposition temperature (T$_d$, 5% weight loss temperature) is 290 ℃. The weight fraction of sample mass dropped to 75% and remained unchanged from 400 to 510 ℃. The weight loss continued after the temperature was increased above 510 ℃ and the sample fully decomposed at 600 ℃ with 4% weight left which represents the carbon black formed during pyrolysis under N$_2$.[17] Considering the weight fraction of PbBr$_2$ to AzPbBr$_3$ is 73%, the pyrolysis product was mainly PbBr$_2$ in the range of 400 - 510 ℃, which then vaporised above 510 ℃.
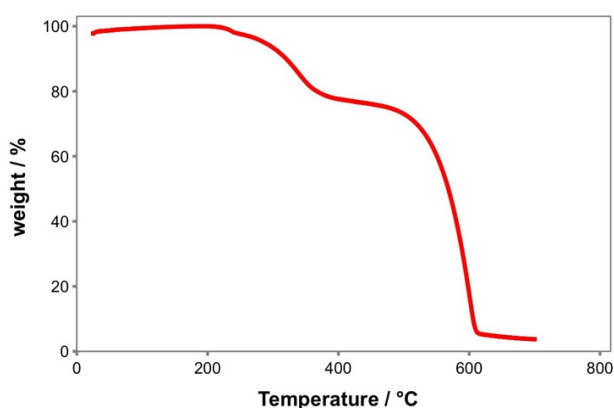

Figure 3.4. TGA data of AzPbBr$_3$ with a decomposition temperature (T$_d$, 5% weight loss temperature) at 290 ℃, reproduced from Ref. 13 with permission. Copyright (2019) American Chemical Society.

3.2.2 Variable temperature XRD

Both PXRD and SCXRD were collected at or below room temperature due to the relatively low decomposition temperature (T_d) of the samples. While cooling from 293 to 88 K, PXRD data were collected in 10-20 K increments. The samples were filled in capillary as the first attempt (Figures **3.5a, 3.5b**). Visual inspection of the diffraction patterns gives no clear indication of any symmetry breaking; no systematic peak broadening/splitting or additional reflections are observed with decreasing temperature. Although the data show clear ice peaks at around 25° (2θ) when the temperature went below 140 K, data at all temperatures were refined in space group $P6_3/mmc$. To further study the low-temperature structure of AzPbBr$_3$, a more detailed data collection was attempted. PXRD was collected with powders from an angular range of 5° to 70°, and temperature ranging from 12 to 160 K in 10 K steps, from 165 to 180 K in 1 K steps, and then from 180 to 300 K in 20 K steps (Figures **3.5c, 3.5d**). From these PXRD patterns, the thermal expansion of the unit cell can be divided into three stages. In the low temperature phase below 173 K (see examples at 130 K), there is systematic peak splitting clearly evidently in the (110) and (203) reflections. The intermediate phase from 174 K to ca. 180 K is characterised with additional peaks, *e.g.* at 17° and 31°. In the high temperature phase with temperatures higher than ca. 180 K, the structure is the high symmetry 6H structure with the $P6_3/mmc$ space group.

2D contour plots of the data (Figures **3.5b**, **3.5d**), highlight the obvious change in rate of thermal contraction around 173 K. PXRD data, collected from both capillary and powder, were refined in the space group $P6_3/mmc$, and the obtained lattice parameters are shown in Figure **3.6** as a function of temperature together with single crystal data collected at 293, 173, and 93 K. Both PXRD data sets indicate a clear change on cooling below ca. 173 K where the *a* parameter sharply decreases. The *c* parameter also decreases down to 173 K but then expands below this temperature. Overall the cell volume is dominated by the change in *a* and also shows a sudden decrease on cooling below 173 K. Note that lattice parameters obtained from SCXRD also shows a similar change and confirmed this anisotropic change in cell dimensions.
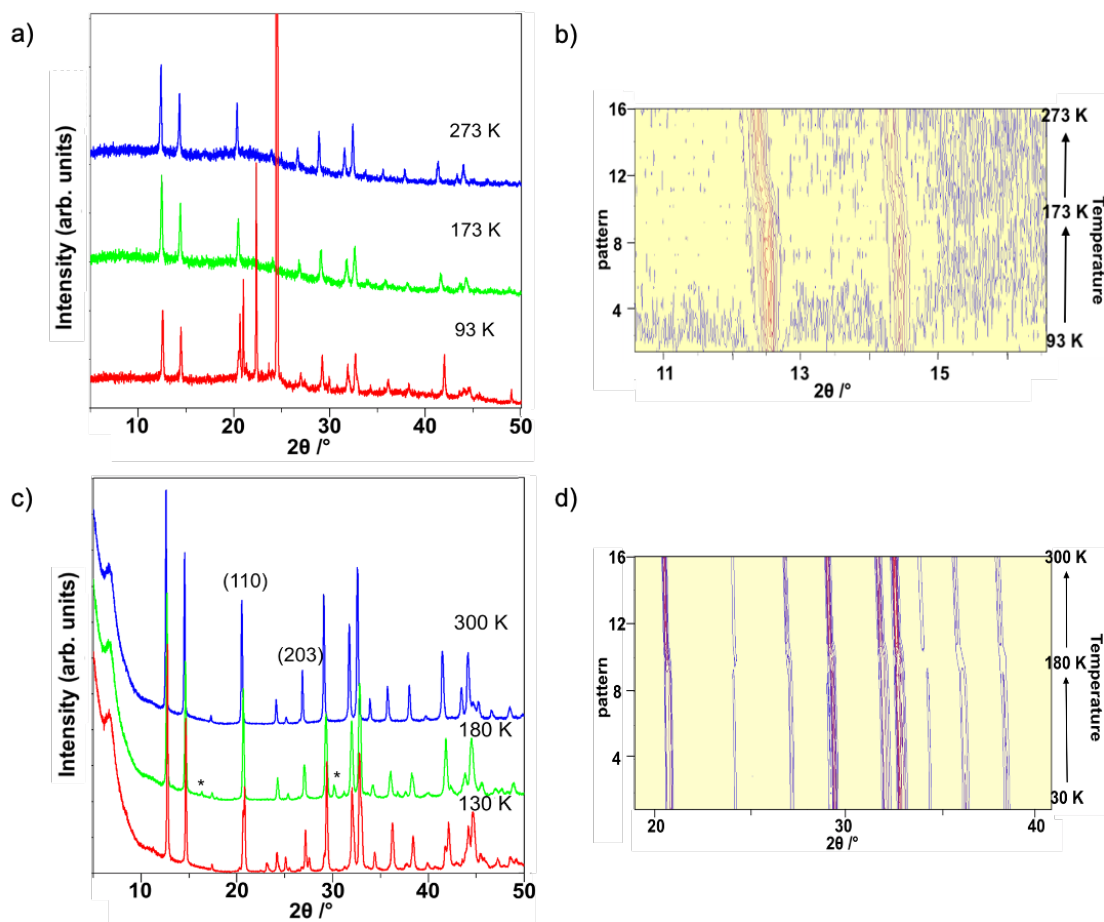
Figure 3.5. Low temperature PXRD patterns of AZPbBr$_3$ powders – 16 capillary and powder measurements between 12 and 300 K: Capillary measurement (a) 3 specific patterns at 93 K, 173 K and 273 K (b) 2D contour plot of 16 patterns (88 K to 273 K). Figures (a, b) are adapted from Ref. 13 with permission. Copyright (2019) American Chemical Society. Powder measurement: (c) 3 specific patterns at 130 K, 180 K and 300. The characteristic peaks of the intermediate phase are marked by *, (d) 2D contour plot of 16 patterns (30 K to 300 K).

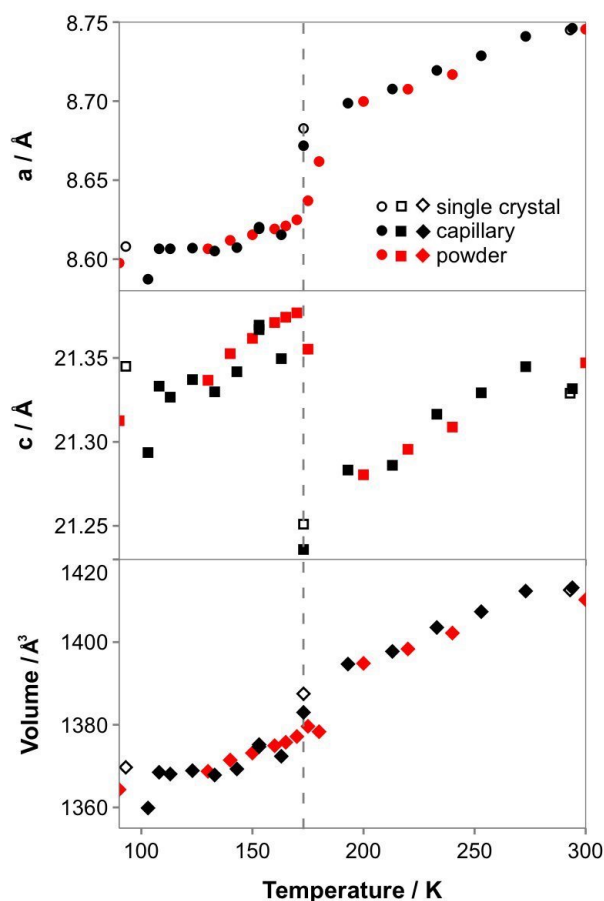**Figure 3.6.** Lattice parameters as a function of temperature for $AzPbBr_3$ obtained from Rietveld refinement of variable temperature PXRD, from both capillary and powder study; parameters obtained from SCXRD data are also included and are in good agreement.

To identify the possible low temperature and the intermediate phase of $AzPbBr_3$, ISODISTORT[18] analysis was performed. The organic moieties are simplified and modelled as Mn as it has similar electron density. The *Pnnm* space group in the orthorhombic system offers a reasonable match considering the bars and peak intensities in Rietveld refinement (Figure **3.7**). The refined lattice parameters are $a = 21.312$ Å, $b = 14.895$ Å and $c = 8.596$ Å with goodness-of-fit parameters $\chi^2 = 15.88$, $wR_p = 0.161$. Despite the multiple attempts to refine the intermediate phase, it was not possible to determine a satisfactory, unique space group with a plausible size of unit cell.
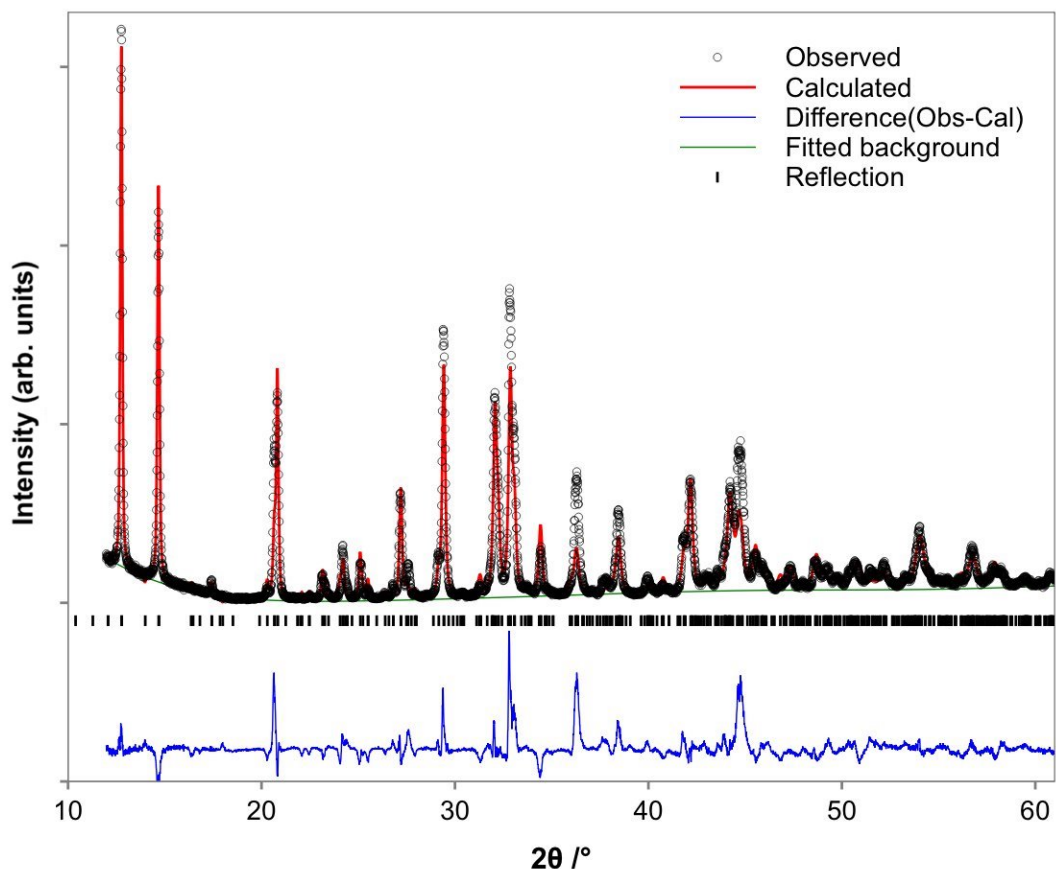
Figure 3.7. Rietveld refinement of PXRD data at 90 K in *Pnnm* space group with observed data (black dots), calculated data (red line), background (green line), reflection position (black bar) and difference plot (blue line). The refined lattice parameters are $a = 21.312$ Å, $b = 14.895$ Å and $c = 8.596$ Å with goodness-of-fit parameters of $\chi^2 = 15.88$, $wR_p = 0.161$.

Single crystal data were collected at 293, 173, and 93 K. Compared to the variable temperature PXRD, the 293 and 173 K SCXRD data show considerable disorder of the Az molecules at the A-site with no evidence of a symmetry-breaking phase transition in this range (Table **3.2**). Data collected from single crystals at 93 K was indexed in the primitive trigonal/orthorhombic crystal system. Neither a unique acceptable determination of the space group, nor refinement of the structure could be made, despite repeated attempts over several data-collections. Several plausible structure solutions (*P-31c, P6₃/m, Pnnm, Fmm2*, etc) were investigated, but all the refinements attempted

resulted in significant problems. These included high R-factors, and many non-positive atoms found near Pb-Br frameworks and in locations likely to be occupied by Az^+ cations. These issues are suspected to result from the incomplete phase transition, despite the crystals being held in cold-stream for extended periods of time. Regardless of the issue in the 93 K SCXRD data, the same crystals had data collected again at higher temperatures which proved agreeable to structure solution, so it was clearly a reversible factor. Although a unique satisfactory solution for the 93 K structure could not be made, it was possible to locate Pb and Br atoms in most plausible solutions. These solutions consistently gave rise to the same 6H Pb-Br framework obtained at higher temperatures, with some distortions which will be described in detail below. No apparent change in the Az^+ cation behavior was observed at low temperatures compared with room temperature data.

Although SCXRD is relatively insensitive to both the position and dynamics of the light atoms of Az^+, the Pb and Br positions could be determined with greater certainty, and with little variation with regard to the exact space group used. The behavior of the surrounding Pb-Br framework was studied in more detail in order to identify possible origins of the anisotropic distortion on cooling below *ca.* 173 K. The room temperature structure, as determined from the single crystal data, shows some interesting features. For instance, the distances between *c-h* and *c-c* packing layers are markedly different (Figure **3.8**), resulting in distortion of the octahedra. The elongation of the face-sharing Pb2-centred octahedra is particularly evident, and the Br⋯Br packing distance along the *c*-axis is 8% longer compared to that of the corner-sharing Pb1-centred octahedra. This is presumably driven by the Pb⋯Pb ionic repulsion as the Pb2 atoms are each displaced along the *c*-axis and away from the octahedral barycentre by 0.155 Å. This causes an elongation of the Pb2-Br3 bond lengths and reduction in the Pb2-Br3 bond angles to < 90° i.e. those at the point of face-sharing in the *h*-layer. There is an associated compression of the Pb2-Br4 bonds and increase in the Pb2-Br4 bond angles, which form the *c*-layers. This is also evident from the short Br3⋯Br3 (ca. 3.88 Å) and long Br4⋯Br4 (ca. 4.41 Å) bond lengths that form the opposing faces of the Pb2-Br octahedra in the *ab* plane (Figures **3.8c**, **3.8d**). The resulting effect is that the corner-sharing Pb1-octahedra are uniaxially compressed along the *c*-axis with equivalent Pb1-Br4 bond lengths.

Besides the Pb2···Pb2 ionic repulsion, it is assumed that this distortion is also caused in part by the steric effect of the Pb^{2+} lone pair and also the second-order Jahn-Teller effect.[19]

The origin of the anisotropic behaviour on cooling is particularly evident from the preliminary structure solutions of the single crystal diffraction data obtained at 93 K.
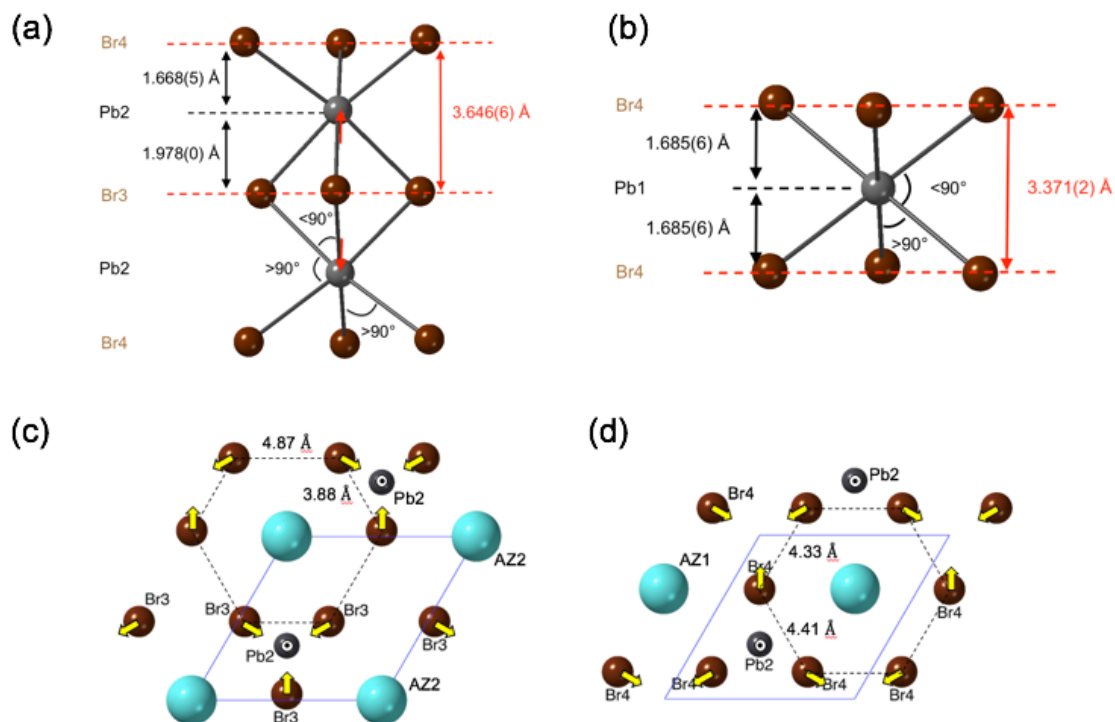
Figure 3.8. Structural features of 6H $AzPbBr_3$ as determined from single crystal data at 293K. (a) Face sharing Pb2 octahedra indicating Pb-Pb repulsion and increased close packing distance compared to Pb1-Br4 octahedra (b) in the *c*-layers (c) view along *c*-axis showing pinching of Br3 atoms (yellow arrows) which form one face of the Pb2 octahedra in the *h*-layer, and (d) associated "pushing out" of Br4 atoms in the c-layer as the Pb2 atom is displaced along the *c*-axis (in this case, out of the page, as denoted by the circled dot ⊙). Reproduced from Ref. 13 with permission. Copyright (2019) American Chemical Society.

Table 3.3. Variation in close packing interlayer distances, Pb2···Pb2 separation and Pb2 off-centring (Δz) as a function of temperature as determined from SCXRD, reproduced from Ref. 13 with permission. Copyright (2019) American Chemical Society.

Temp. /K	c-c distance /Å	c-h distance /Å	Pb2-Pb2 distance /Å	Δz /Å
293	3.373	3.646	3.956	0.155
173	3.343	3.641	3.918	0.139
93	3.193	3.740	3.979	0.120

Initially the crystal undergoes the expected contraction on cooling; however, at 93 K the disparity in the close packing interlayer spacing between c-c and c-h layers is dramatically increased. This results from a sudden expansion of the c-h interlayer distance while the c-c layers continue to contract (Table **3.3**), indicating that the net expansion in the c-axis on cooling (Figure **3.8**) is driven solely by the h-c spacing. As a result of this h-c expansion, although the face-sharing Pb2 octahedra are expanded in the c-axis, the Pb2 are less off-centred (Δz = 0.120 Å at 93 K compared to 0.155 Å at 293 K) despite the sudden increase in Pb2-Pb2 separation (Table **3.3**). This suggests the anisotropic behaviour and expansion of these octahedra in the c-axis is driven by the Pb···Pb repulsion. In addition to the expansion of the c-h interlayer spacing there is a significant increase in the distortion of the Az2-Br3 close packing in the h-layer. The pinching of the Br3 atoms that form the shared face of Pb2 octahedra (described for the 293 K structure in Figure **3.9**) is dramatically increased. The in-plane displacement of the Br ions in the h layer results in a rotation of the shared octahedral face around the c-axis. A cch stacking portion of the structure is shown at both 293 and 93 K in Figures **3.9a** and **3.9b** respectively, and clearly reveals the rotation of the shared octahedral face in the h-layer at 93 K while the close packing in the c-layers and corner sharing octahedra remain relatively regular.

Despite a lack of specific information regarding the position or orientation of the Az cations, this distortion in the h-layer significantly changes the coordination environment of the Az2 cation. In order to demonstrate this in more detail, an Az2 cation (represented in Figure **3.9c** by a sphere) was placed on the close packing position with fractional

coordinates $(0, 0, z)$ where z is the same as that of the Br3 anions. The resulting close-packed 12-coordination environment for the Az2 cation (Figure **3.9c**) clearly shows that the six in-plane Br3 anions bifurcate further into three alternating short (3.80 Å) and long (4.83 Å) bonds – denoted as Br3 (short) and Br3' (long) as shown in Figure **3.10**. The extent of bifurcation is evident by the comparison with the bond distances of 4.52 Å for Az2 to Br4 anions in the adjacent (c) layers. As the single crystal data do not appear to suggest any static orientation of the Az cations, this change in environment is unlikely to be driven by hydrogen bonding between Az and Br. Instead, the origin of this distortion is likely due to the Pb2$\cdots$Pb2 interaction in the face-sharing octahedra.
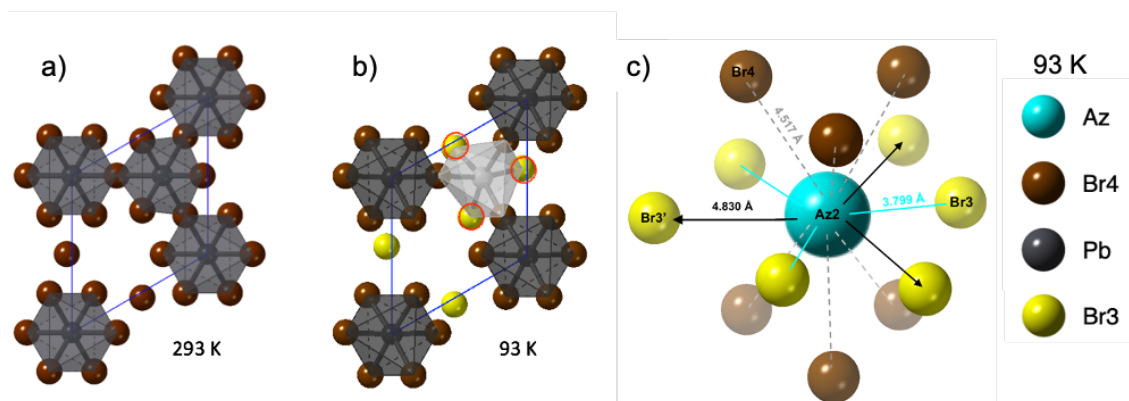
Figure 3.9. *cch*-fragment of the 6H AzPbBr$_3$ structure viewed down the *c*-axis at (a) 293 K and (b) 93 K, highlighting the distortion in the *h* layer (Br3 - yellow spheres) at 93 K compared to 293 K. (c) The resulting distortion of the dodecahedral environment occupied by the Az2 cation at 93 K. Az2-Br4 bonds (4.52 Å) are marked with dash lines and alternating short (3.80 Å) and long (4.83 Å) Az2-Br3 bonds are marked with solid lines and arrow, respectively. Adapted from Ref. 13 with permission. Copyright (2019) American Chemical Society.

Figure 3.10. The in-plane view of Az2-site in perovskite structure (refined in $P6_3/mmc$) at 93 K. Among the six Br3 in the hexagonal close-packing layer (Az2-Br3), there are three alternating short (3.80 Å) and long (4.83 Å) bonds with short bonds marked with dashed lines. Th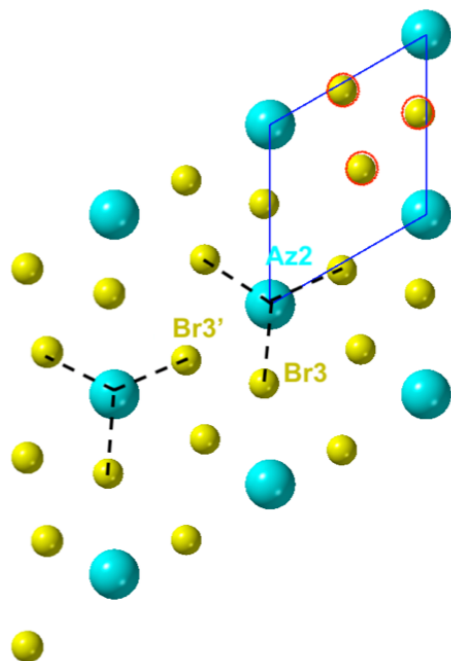e coresponding Br3 are denoted as Br3 (short) and Br3' (long). Reproduced from Ref. 13 with permission. Copyright (2019) American Chemical Society.

The degree of octahedral distortion may be determined quantitatively as the octahedral distortion parameter (Δ_1) and bond angle distortion (Δ_2) as defined by:[20]

$$\Delta_1 = \frac{1}{6}\sum |R_{av} - R_i| \qquad \text{(Equation 3.1)}$$

$$\Delta_2 = \frac{1}{12}\sum |90 - \varphi_i| \qquad \text{(Equation 3.2)}$$

where, R_i and φ_i are the respective individual bond lengths and bond angles, and R_{av} is the mean Pb-Br bond distance. Distortion indices for $AzPbBr_3$ obtained from SCXRD are given in Table **3.4**. Although the corner-sharing Pb1 octahedra remain regular in terms of their bonding (Δ_1), indicating that the Pb1 atoms are centred, the octahedra become increasingly compressed in the c-axis on cooling, resulting in an increased deviation in the bond angles from 90° (increasing Δ_2). In contrast, the extent of the distortion of the face-sharing Pb2 octahedra is relatively consistent at 293 and 173 K with similar values

76

for both Δ_1 and Δ_2 at each temperature. At 93 K, however, there is a clear change: Δ_1 decreases significantly as a result of the more centred Pb2 cations within the octahedra; Δ_2 increases significantly, reflecting the distortion within the h (Az, Br3) layer and torsion of the three Br3' atoms which form the shared face between octahedra.

In the absence of any evidence for loss of Az cation dynamics from variable temperature SCXRD, the unusual thermal expansion behaviour, structural distortion and large dielectric peak at 173 K is likely driven by a combination of Pb2$\cdots$Pb2 repulsion and increased steric effect of the Pb lone pair as the thermal motion decreases.

Table 3.4. Octahedral distortion parameters for $AzPbBr_3$ calculated from SCXRD data collected at 293, 173 and 93 K, reproduced from Ref. 13 with permission. Copyright (2019) American Chemical Society.

Temperature	293 K		173 K		93 K	
Octahedra	Pb1	Pb2	Pb1	Pb2	Pb1	Pb2
Δ_1 / Å	0	0.028	0	0.027	0	0.006
Δ_2 / °	1.782	4.369	1.968	4.192	4.204	6.506

3.2.3 Optical and electronic properties

The absorption spectrum for $AzPbBr_3$ is shown in Figure **3.11a**, and is compared to the well-studied 3C perovskite $MAPbBr_3$. The absorption edge for $AzPbBr_3$ is blued-shifted by 122 nm (4920 cm^{-1}, 0.61 eV) and shows a wider bandgap E_g, of 2.81 eV compared to 2.20 eV for $MAPbBr_3$. The increased bandgap is consistent with computational predictions that show larger bandgaps for face-sharing octahedral systems compared to structures based solely on corner- sharing octahedra.[21] Figure **3.11b** shows the dependence of the bandgap of lead bromide OIHPs as a function of tolerance factor t, including the present experimental data for $AzPbBr_3$ and $MAPbBr_3$ alongside those reported for 4H hexagonal $DMAPbBr_3$ (experimental) and 2H hexagonal $TMAPbBr_3$ (calculated).[8,9] As expected, the tolerance factor increases in line with the perovskite polymorph observed (3C < 6H < 4H < 2H), and the increased bandgap is consistent with

the observations of Stoumpos *et al.*[7] and Gratia *et al.*[12] for tin OIHPs and mixed-cation lead OIHPs. The linear trend found for the bandgap and tolerance factor (and hence observed polytype) can be attributed to the relative ratio of the cubic close-packing (corner-sharing octahedra) and hexagonal close-packing (face-sharing octahedra) as shown in Table **3.5**. This trend can be explained by the average B-X-B bond angle, which varies by (180° - ϕ) in ccp perovskites but in mixed *h-c* systems contains a contribution of ~90° bonds from the face-sharing octahedra.[22] There is a significant jump in the bandgap between 2H and 4H, which may be filled by 9R polytypes that have yet to be reported. From a simple tolerance factor projection, the bandgaps of 9R OIHP lead bromide perovskites might be expected to be of the order 3.0 – 3.2 eV.

To gain a better understanding of the electronic properties of the new 6H perovskite, DFT calculations and analyses were performed based on the crystalline model obtained from SCXRD at 173 K. Initially, the Az cations are substituted with Cs cations to avoid the complications related to the position and orientation of the organic moieties. This approximation is reasonable for the valence and conduction band calculation as these bands are usually dominated by the X and B orbitals.[24]
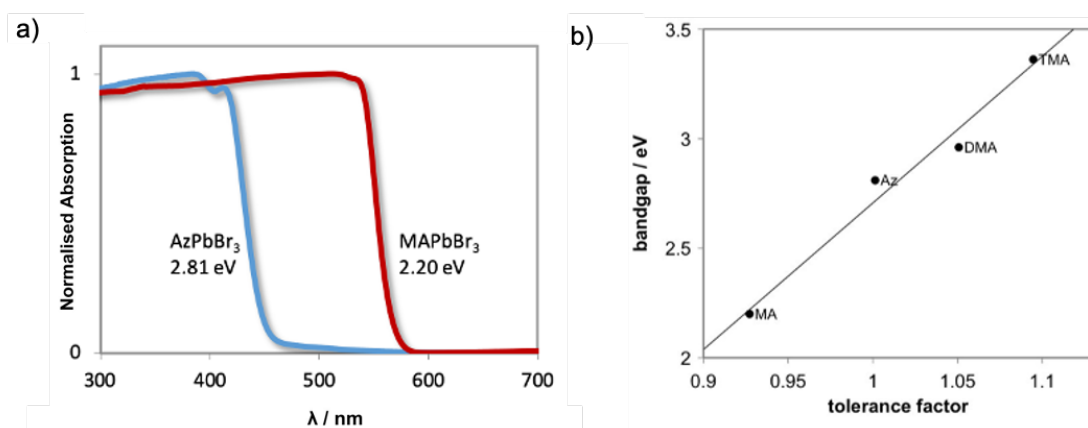
Figure 3.11. (a) Absorption spectra and associated bandgap obtained from AzPbBr$_3$ and MAPbBr$_3$ powders. (b) Dependence of bandgap on tolerance factors for lead OIHPs with different A-cations and resulting close packing of the perovskites. The corresponding cations of these OIHPs were MA$^+$(3C), Az$^+$(6H), DMA$^+$ (4H) and TMA$^+$ (2H).[9,10,23] Adapted from Ref. 13 with permission. Copyright (2019) American Chemical Society.

Table 3.5. The proportion of the cubic close-packing and hexagonal close-packing of perovskite polytypes and the stacking sequence of their AX_3 layers, adapted from Ref. 13 with permission. Copyright (2019) American Chemical Society.

Perovskite polytypes	Stacking sequence	Cubic close-packing /%	Hexagonal close-packing /%
3C	*c*	100	0
6H	*hcc*	66.7	33.3
4H	*hc*	50	50
9R	*hhc*	33.3	66.7
2H	*h*	0	100

The calculations adopt the PBE method,[25] either in the absence of or including spin-orbit coupling. The band structure of 6H, 'AzPbBr$_3$' perovskite, as reported in Figure **3.12a**, clearly indicates that this compound is a direct bandgap semiconductor. The partial density of states of 'AzPbBr$_3$' in Figure **3.12b** suggests that the valence band edge is dominated by the anti-bonding combination of 4p atomic orbitals of Br and 6s orbitals of Pb (Figure **3.12d**). In the meantime, the conduction band edge is dominated by 6p orbitals from Pb (Figure **3.12e**). The DFT electronic bandgap can be compared to the optical bandgap from UV-vis measurements in Figure **3.11**. In this respect, the 0.61 eV blue-shift in the optical absorption from the fully corner-sharing 3C MAPbBr$_3$ structure to the mixed face-/corner-sharing 6H AzPbBr$_3$ structure, is well reproduced by DFT calculations (0.47 eV), and even more so when spin-orbit coupling is taken into account (0.58 eV).[26]

The influence of the position and orientation of the organic cation was also investigated. As discussed in Chapter 1, the organic cations affected the band structure by introducing distortion of the octahedral packing.[27] This mechanism is adopted in the following calculations.
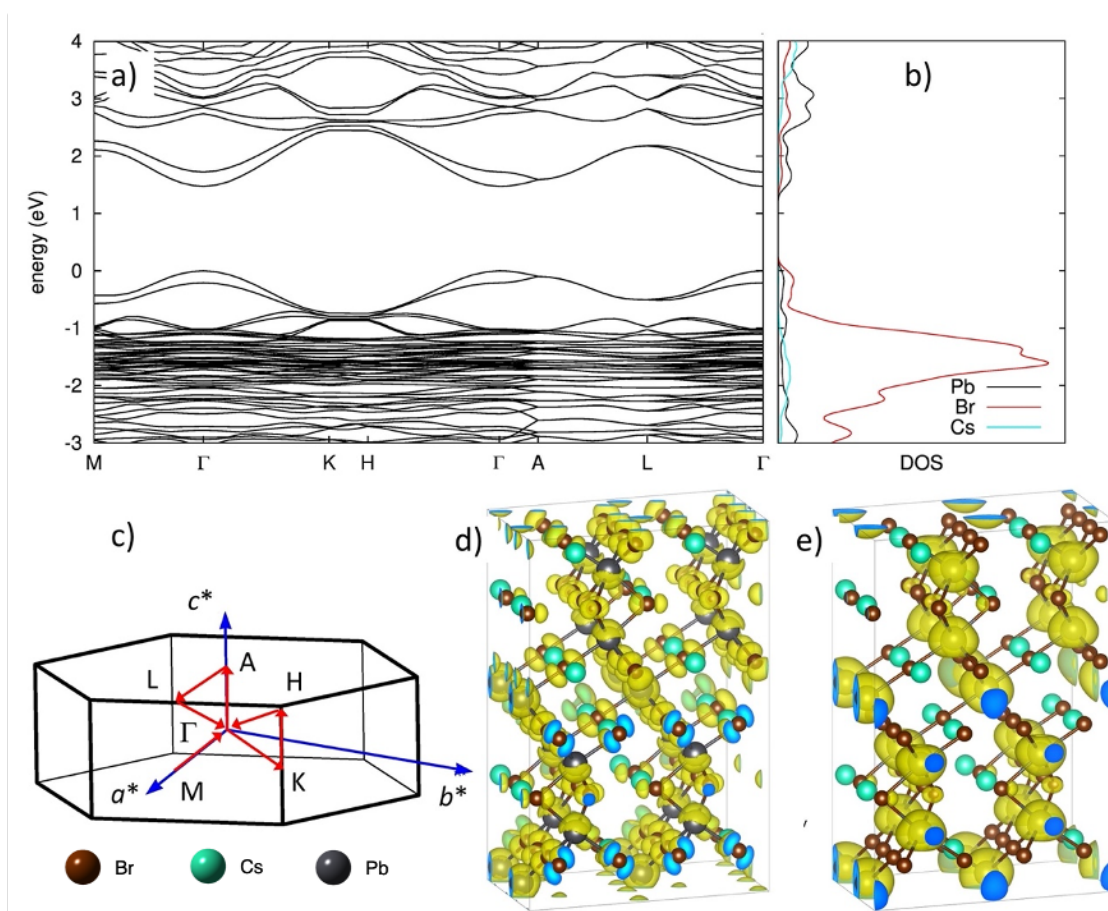
Figure 3.12. (a) Band structure of 6H 'APbBr$_3$' perovskite (calculation with PBE, including spin-orbit coupling, A = Cs). The valence band maximum is set to zero. (b) Corresponding partial density of states (c) first Brillouin zone for hexagonal primitive lattice. Wavefunction localization of the (d) valence band edge and (e) conduction band edge at Γ point. Reproduced from Ref. 13 with permission. Copyright (2019) American Chemical Society.

As the position and orientation was unclear in SCXRD data, three models were adopted to locate the Az$^+$, two with aligned Az$^+$ (model-1 and model-2, Figure **3.13**) and one with randomly chosen orientation (model-3), and all performed full atomic relaxation. The resulting relaxed AzPbBr$_3$ structures show tilting of the corner-shared octahedra within the range 162° to 178° and the resulting bandgap varies from 2.56 eV to 2.65 eV, which is very close to the one for the untilted Cs-substituted structure (2.55 eV). This further

supports the conclusion that the blue-shift of the absorption edge in the UV-vis measurements for AzPbBr$_3$ compared to MAPbBr$_3$ (Figure **3.11a**) is attributed to the change in the organisation of the octahedral linkages, from pure corner-sharing in MAPbBr$_3$ to mixed corner- and face-sharing octahedra in AzPbBr$_3$. Model-2 gives a very small relative stability energy while the other two models show little variation in such values. The similar energies suggest a negligible driving force for the cation ordering and helps explain the difficulty in determination of the position and orientation of the cations in low temperature SCXRD study.
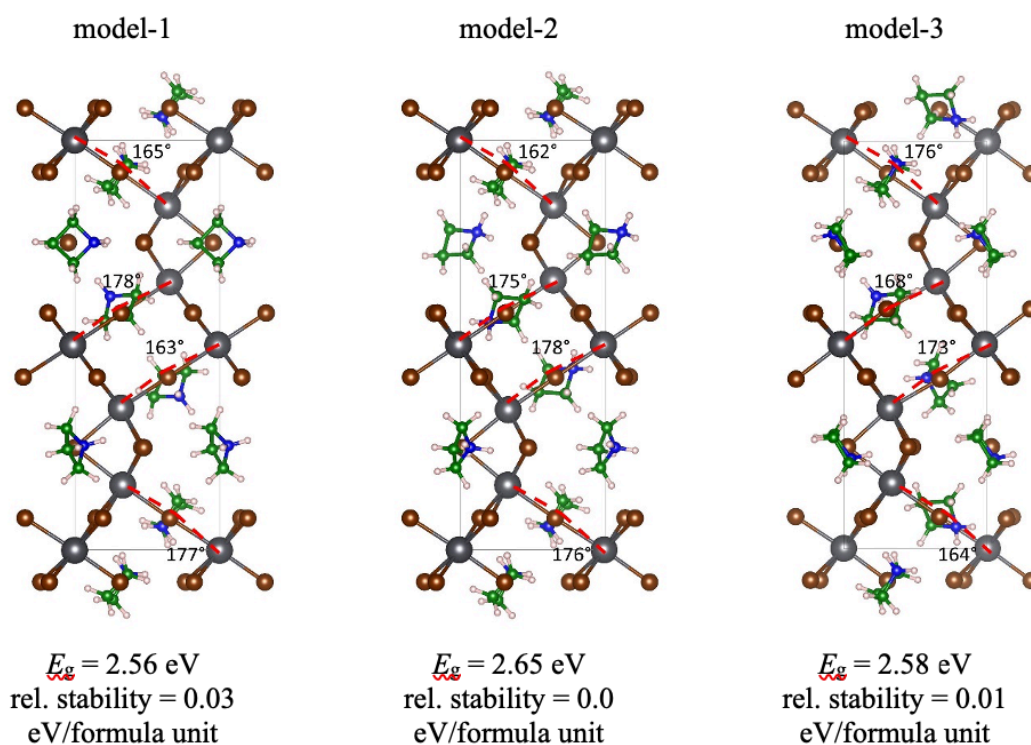
Figure 3.13. Different models for AzPbBr$_3$ 6H perovskites. The models differ in the orientation of the Az cation. Model-1 and model-2 have a certain degree of alignment of the cations as a start, while the original orientation of the Az cations in model-3 is fully random. The atomic positions of models 1-3 are fully relaxed, with valence Pb-Br-Pb angles for the corner-shared octahedra as indicated. The bandgap and the relative stability of the three models is also given, reproduced from Ref. 13 with permission. Copyright (2019) American Chemical Society.

3.2.4 Dielectric properties

Electrical characterisation of AzPbBr$_3$ using impedance spectroscopy indicated no appreciable conductivity at temperatures up to ca. 200 °C (473 K) with sample resistivity remaining in excess of 10^7 Ωcm. Figure **3.14** shows the dielectric data (relative permittivity ε_r, and dielectric loss tan δ) for AzPbBr$_3$ over the temperature range 50-300 K collected on both heating and cooling cycles at 1 K/min. The relative permittivity shows a sharp, frequency independent peak around 170-190 K on both cooling and heating suggestive of a phase transition. The peak position shows significant thermal hysteresis, which may indicate the transition is 1st order, but is also likely to have some contribution from thermal lag. The dielectric loss shows a frequency dependent peak but at slightly lower temperature ca. 100-120 K, again with some thermal hysteresis. The broad, frequency dependent dielectric loss peak at lower temperature could result from a change in Az dynamics. The peak in the permittivity is comparable to that observed in other lead OIHPs and is associated with structural phase transitions due to ordering of the A-cation.[28] However, as discussed previously, both low temperature XRD and DFT calculations suggest that this is not the case. The dielectric loss peak at lower temperature has no clearly-associated feature in the permittivity although there is also some evidence of frequency dependence in ε_r at the corresponding temperature (70 - 100 K).
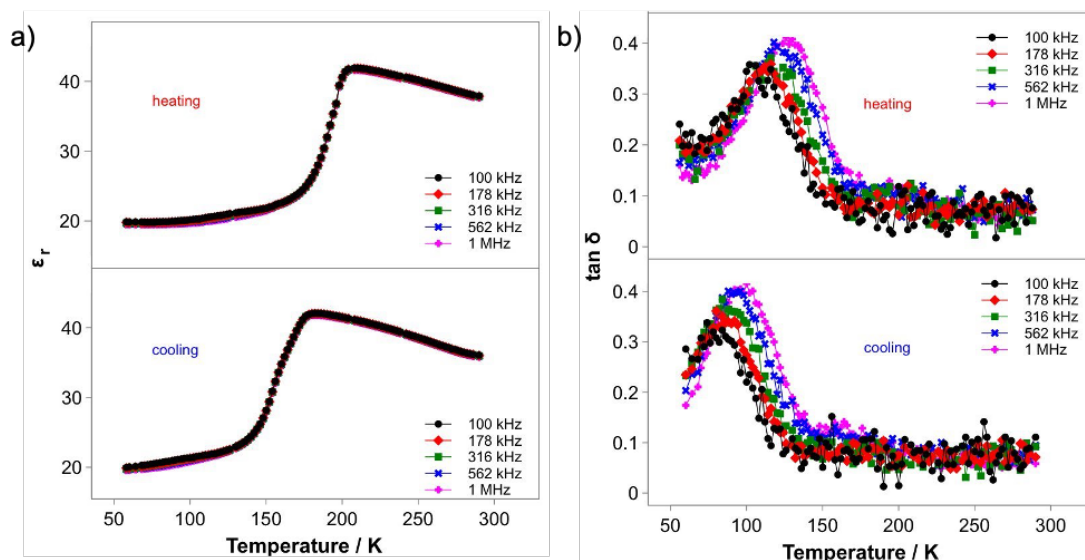

Figure 3.14. Temperature and frequency dependence of (a) relative permittivity ε_r and (b) dielectric loss tan δ of AzPbBr$_3$ at the heating/cooling rate of 1 K/min, adapted from Ref. 13 with permission. Copyright (2019) American Chemical Society.

The dielectric properties of AzPbBr$_3$ show a large dielectric anomaly in the real permittivity at ca. 173 K which is associated with a structural transition as discussed in the variable PXRD section. At lower temperatures, a clear dielectric loss peak is evident together with a frequency dependence of the relative (real) permittivity, Figure **3.15a** and **3.15b**. The possible phase transition associated with the frequency dispersion can be fitted to a constant phase element (CPE) which accounts for deviations from the ideal.[29,30] CPE can be represented as a circuit element with an complex admittance Y^*:

$$Y^*_{CPE}(\omega) = A_0(i\omega)^n \qquad \text{(Equation } \mathbf{3.3})$$

where A_0 is the reciprocal electrical impedance ($|Z^*|$) at 1 rad/s, i is the imaginary number, ω is the frequency dispersion, and where $0 \leq n \leq 1$, indicating a range of non-ideal behaviour ranging from $n = 1$ for $Y^*(\omega)$ for a perfect capacitor to $n = 0$ for that of a resistor. Using the relation $Y^*(\omega) = i\omega C_0\varepsilon^*(\omega)$, the complex permittivity $C_0\varepsilon^*(\omega)$ is given by:

$$C_0\varepsilon^*_{CPE}(\omega) = A_0\omega^{n-1} \qquad \text{(Equation } \mathbf{3.4})$$

This allows the frequency dispersion of the real permittivity to be quantitatively fitted as $\varepsilon_r \propto \omega^{n-1}$, where $n = 1$ indicates an ideal, non-dispersive dielectric response. Frequency dispersion fits to the real permittivity, indicating a minimum n of ca. 0.995 (maximum dissipation) in agreement with the dielectric loss data (Figure **3.15c**). The use of CPE elements is not unusual in impedance analyses of ferroelectrics[31,32] and ionic conductors,[33] but the origin in each case is typically unknown. In many cases it is a "fudge factor" yielding an exponent n that can represent multiple deviations from ideal behaviour, including electrical inhomogeneity. The value of approximately 0.995 obtained here is typical for crystalline solids.[31–33]
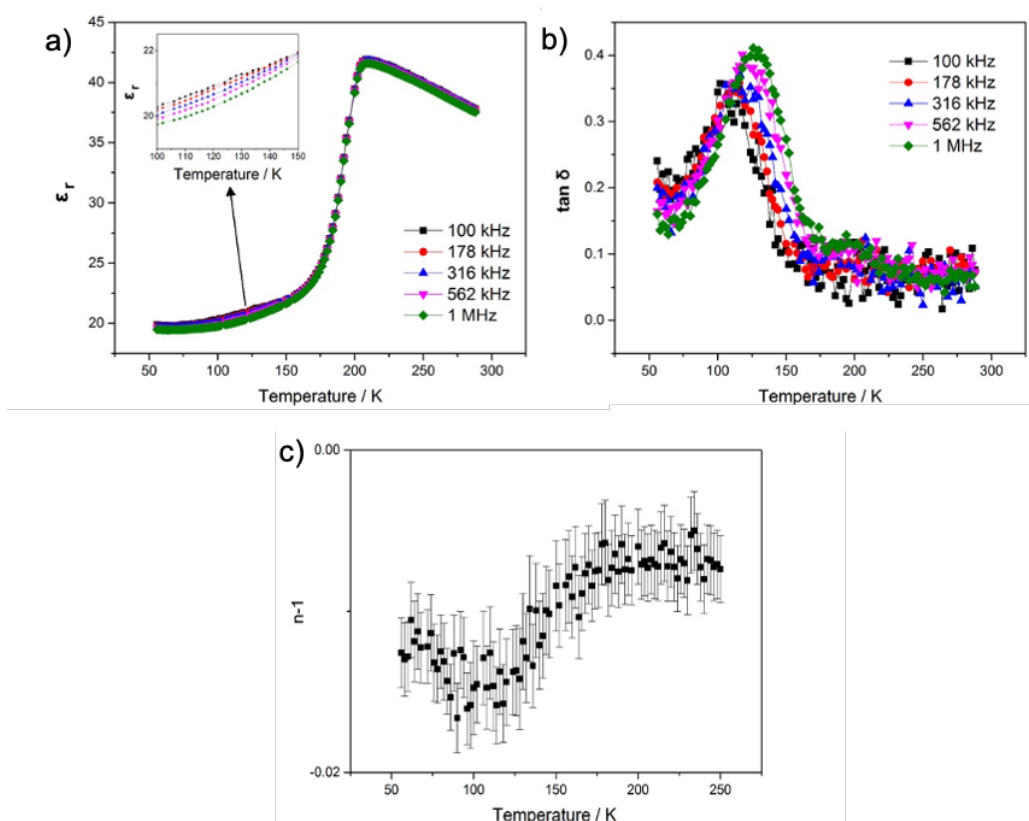
Figure 3.15. (a) Real and (b) imaginary permittivity as a function of temperature for AzPbBr$_3$, showing relaxer-like frequency dependence. (c) Fit of the real permittivity to a CPE element (exponent n) indicating the frequency dependence of $\varepsilon_r \propto \omega^{n-1}$.

3.3 Conclusion

A new OIHP perovskite AzPbBr$_3$, with the 6H-perovskite structure has been successfully synthesised. The material is stable in air for > 6 months and has an optical bandgap of 2.81 eV. DFT calculations are in good agreement with a calculated, direct bandgap of 2.55 eV; the larger bandgap when compared to that of cubic close packed (3C) perovskites is predominantly due to poorer connectivity of the Pb-X orbital overlap on introduction of face-sharing octahedra in the hexagonal structure. On cooling AzPbBr$_3$ undergoes a symmetry lowering distortion which was identified by variable temperature PXRD and dielectric spectroscopy. This transition is evident by an anisotropic change in the lattice parameters on cooling (expansion in c and contraction in a) that is most likely driven by the Pb$\cdots$Pb repulsion in the face sharing octahedra. However, it was not possible to satisfactorily determine a unique space group from SCXRD, despite multiple attempts.

References

(1)   Pering, S. R.; Deng, W.; Troughton, J. R.; Kubiak, P. S.; Ghosh, D.; Niemann, R. G.; Brivio, F.; Jeffrey, F. E.; Walker, A. B.; Islam, M. S.; et al. Azetidinium Lead Iodide for Perovskite Solar Cells. *J. Mater. Chem. A* **2017**, *5* (39), 20658–20665.

(2)   Panetta, R.; Righini, G.; Colapietro, M.; Barba, L.; Tedeschi, D.; Polimeni, A.; Ciccioli, A.; Latini, A. Azetidinium Lead Iodide: Synthesis, Structural and Physico-Chemical Characterization. *J. Mater. Chem. A* **2018**, *6* (21), 10135–10148.

(3)   Thind, A. S.; Huang, X.; Sun, J.; Mishra, R. First-Principles Prediction of a Stable Hexagonal Phase of CH 3 NH 3 PbI 3. *Chem. Mater.* **2017**, *29* (14), 6003–6011.

(4)   Li, Z.; Yang, M.; Park, J. S.; Wei, S. H.; Berry, J. J.; Zhu, K. Stabilizing Perovskite Structures by Tuning Tolerance Factor: Formation of Formamidinium and Cesium Lead Iodide Solid-State Alloys. *Chem. Mater.* **2016**, *28* (1), 284–292.

(5)   Koh, T. M.; Fu, K.; Fang, Y.; Chen, S.; Sum, T. C.; Mathews, N.; Mhaisalkar, S. G.; Boix, P. P.; Baikie, T. Formamidinium-Containing Metal-Halide: An Alternative Material for near-IR Absorption Perovskite Solar Cells. *J. Phys. Chem. C* **2014**, *118* (30), 16458–16462.

(6)   Stoumpos, C. C.; Malliakas, C. D.; Kanatzidis, M. G. Semiconducting Tin and Lead Iodide Perovskites with Organic Cations: Phase Transitions, High Mobilities, and near-Infrared Photoluminescent Properties. *Inorg. Chem.* **2013**, *52* (15), 9019–9038.

(7)   Stoumpos, C. C.; Mao, L.; Malliakas, C. D.; Kanatzidis, M. G. Structure-Band Gap Relationships in Hexagonal Polytypes and Low-Dimensional Structures of Hybrid Tin Iodide Perovskites. *Inorg. Chem.* **2017**, *56* (1), 56–73.

(8)   Geselle, M.; Fuess, H. Crystal Structure of Dimethylammonium Tribromoplumbate(II), (CH 3)2NH2PbBr 3. *Zeitschrift für Krist. Cryst. Struct.* **1997**, *212*, 234–234.

(9)   Zaleski, J.; Pietraszko, A. Structure at 200 and 298 K and X-Ray Investigations of the Phase Transition at 242 K of [NH 2 (CH 3) 2] 3 Sb 2 Cl 9 (DMACA). *Acta Crystallogr. Sect. B Struct. Sci.* **1996**, *52* (2), 287–295.

(10) Mancini, A.; Quadrelli, P.; Amoroso, G.; Milanese, C.; Boiocchi, M.; Sironi, A.; Patrini, M.; Guizzetti, G.; Malavasi, L. Synthesis, Structural and Optical Characterization of APbX3 (A=methylammonium, Dimethylammonium, Trimethylammonium; X=I, Br, Cl) Hybrid Organic-Inorganic Materials. *J. Solid State Chem.* **2016**, *240*, 55–60.

(11) Anelli, C.; Chierotti, M. R.; Bordignon, S.; Quadrelli, P.; Marongiu, D.; Bongiovanni, G.; Malavasi, L. Investigation of Dimethylammonium Solubility in MAPbBr 3 Hybrid Perovskite: Synthesis, Crystal Structure, and Optical Properties. *Inorg. Chem.* **2019**, *58* (1), 944–949.

(12) Gratia, P.; Zimmermann, I.; Schouwink, P.; Yum, J.-H.; Audinot, J.-N.; Sivula, K.; Wirtz, T.; Nazeeruddin, M. K. The Many Faces of Mixed Ion Perovskites: Unraveling and Understanding the Crystallization Process. *ACS Energy Lett.* **2017**, *2* (12), 2686–2693.

(13) Tian, J.; Cordes, D. B.; Quarti, C.; Beljonne, D.; Slawin, A. M. Z.; Zysman-Colman, E.; Morrison, F. D. Stable 6H Organic-Inorganic Hybrid Lead Perovskite and Competitive Formation of 6H and 3C Perovskite Structure with Mixed A Cations. *ACS Appl. Energy Mater.* **2019**, *2* (8), 5427–5437.

(14) Holder, C. F.; Schaak, R. E. Tutorial on Powder X-Ray Diffraction for Characterizing Nanoscale Materials. *ACS Nano* **2019**, *13* (7), 7359–7365.

(15) Akimoto, J.; Gotoh, Y.; Oosawa, Y.; IUCr. Refinement of Hexagonal BaTiO3. *Acta Crystallogr. Sect. C Cryst. Struct. Commun.* **1994**, *50* (2), 160–161.

(16) Sinclair, D. C.; Skakle, J. M. S.; Morrison, F. D.; Smith, R. I.; Beales, T. P. Structure and Electrical Properties of Oxygen-Deficient Hexagonal BaTiO₃. *J. Mater. Chem.* **1999**, *9* (2), 1327–1331.

(17) Widmann, G. *Interpreting TGA Curves: Information for Users of Mettler Toledo Thermal Analysis Systems*; 2001.

(18) Campbell, B. J.; Stokes, H. T.; Tanner, D. E.; Hatch, D. M. ISODISPLACE: A Web-Based Tool for Exploring Structural Distortions. *J. Appl. Crystallogr.* **2006**, *39* (4), 607–614.

(19)   Bersuker, I. B. Critical Review of Contributions to the Jahn-Teller Symposium JT2010 and Beyond. In *Vibronic Interactions and the Jahn-Teller Effect: Theory and Applications*; Atanasov, M., Daul, C., Tregenna-Piggott, P. L. W., Eds.; Springer Netherlands: Dordrecht, 2011; pp 1–22.

(20)   Cordrey, K. J.; Stanczyk, M.; Dixon, C. A. L.; Knight, K. S.; Gardner, J.; Morrison, F. D.; Lightfoot, P. Structural and Dielectric Studies of the Phase Behaviour of the Topological Ferroelectric La $_{1-x}$ Nd $_x$ TaO $_4$. *Dalt. Trans.* **2015**, *44* (23), 10673–10680.

(21)   Kamminga, M. E.; De Wijs, G. A.; Havenith, R. W. A.; Blake, G. R.; Palstra, T. T. M. The Role of Connectivity on Electronic Properties of Lead Iodide Perovskite-Derived Compounds. *Inorg. Chem.* **2017**, *56* (14), 8408–8414.

(22)   Goodenough, J. B.; Zhou, J.-S. Localized to Itinerant Electronic Transitions in Transition-Metal Oxides with the Perovskite Structure. *Chem. Mater.* **1998**, *10* (10), 2980–2993.

(23)   Geselle, M.; Fuess, H. Crystal Structure of Tetrakis(Ethylammonium) Decachlorotriplumbate(II), (C2H5NH3)4Pb3Cl10. *Zeitschrift fur Krist.* **1997**, *212* (1), 241–242.

(24)   Goodenough, J. B. Metallic Oxides. *Prog. Solid State Chem.* **1971**, *5* (C), 145–399.

(25)   Perdew, J. P.; Burke, K.; Ernzerhof, M. Generalized Gradient Approximation Made Simple. *Phys. Rev. Lett.* **1996**, *77* (18), 3865–3868.

(26)   Mosconi, E.; Umari, P.; De Angelis, F. Electronic and Optical Properties of MAPbX$_3$ Perovskites (X = I, Br, Cl): A Unified DFT and GW Theoretical Analysis. *Phys. Chem. Chem. Phys.* **2016**, *18* (39), 27158–27164.

(27)   Amat, A.; Mosconi, E.; Ronca, E.; Quarti, C.; Umari, P.; Nazeeruddin, M. K.; Grätzel, M.; De Angelis, F. Cation-Induced Band-Gap Tuning in Organohalide Perovskites: Interplay of Spin–Orbit Coupling and Octahedra Tilting. *Nano Lett.* **2014**, *14* (6), 3608–3616.

(28)   Maeda, M.; Hattori, M.; Hotta, A.; Suzuki, I. Dielectric Studies on CH $_3$NH $_3$PbX $_3$ (X = Cl and Br) Single Cystals. *J. Phy. Soc. Jpn* **1997**, *66* (5), 1508–1511.

(29)   Jonscher, A. K. The 'Universal' Dielectric Response. *Nature* **1977**, *267* (5613), 673–679.

(30)   Jonscher, A. K. Dielectric Relaxation in Solids. *J. Phys. D. Appl. Phys.* **1999**, *32* (14), R57–R70.

(31)   Morrison, F. D.; Jung, D. J.; Scott, J. F. Constant-Phase-Element (CPE) Modeling of Ferroelectric Random-Access Memory Lead Zirconate-Titanate (PZT) Capacitors. *J. Appl. Phys.* **2007**, *101* (9), 094112.

(32)   West, A. R.; Sinclair, D. C.; Hirose, N. Characterization of Electrical Materials, Especially Ferroelectrics, by Impedance Spectroscopy. *J. Electroceramics* **1997**, *1* (1), 65–71.

(33)   Abram, E. J.; Sinclair, D. C.; West, A. R. A Strategy for Analysis and Modelling of Impedance Spectroscopy Data of Electroceramics: Doped Lanthanum Gallate. *J. Electroceramics* **2003**, *10* (3), 165–177.

Chapter 4

Exploring the formation of 6H and 3C perovskite structures with mixed A-cation
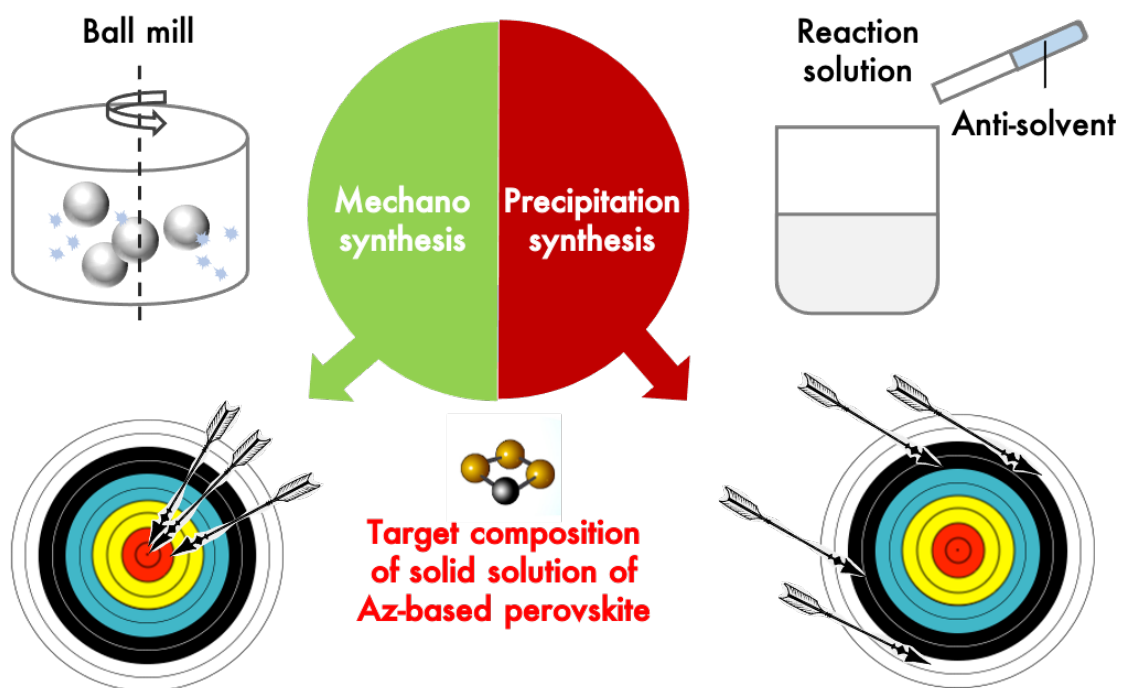
Cover picture: TOC graphic of publication arising from this chapter

4.1 Introduction

As discussed in Chapter 1, mixing A-cations in perovskites has been reported to be beneficial for bandgap tuning,[1] improving moisture resistance,[2] and power conversion efficiency of photovoltaic devices.[3,4] The bandgap of 6H AzPbBr$_3$ was found to be 2.81 eV (Chapter 3), which is much larger than the reported bandgap of the 3C perovskites FAPbBr$_3$ (2.16 eV)[5] and MAPbBr$_3$ (2.20 eV, Figure **3.11**). Although a complete solid solution is not possible due to non-isostructural end members, the degree of replacement of Az by FA or MA in the 6H structure, and similarly replacement of FA or MA by Az in the 3C structure, was investigated by preparing a series of compositions according to Az$_{1-x}$FA$_x$PbBr$_3$ and Az$_{1-x}$MA$_x$PbBr$_3$ ($0 \leq x \leq 1$) using both precipitation synthesis and mechanosynthesis. MA$_{1-x}$FA$_x$PbBr$_3$ was also prepared by both synthetic methods as a reference system. The cation composition was studied with ^{1}H NMR spectroscopy and bandgap progression as a function of cation composition was studied by absorption spectroscopy.

To obtain perovskite solid solutions (e.g. with mixed A-cations), synthetic methods including anti-solvent[6,7] and oversaturation[1,8] precipitation or mechanosynthesis (grinding)[9,10] are typically used. Principally, the choice of synthetic method has an impact on the morphology of the perovskite material. During precipitation synthesis, however, it is usually assumed that the actual sample composition retains the nominal initial molar ratio of ion sources of the precursor solution. Importantly, this assumes that the kinetics of precipitation are independent of the precursor species and nominal composition. The validity of this assumption is often not checked by compositional analysis but rather validated by the observation of a systematic change in properties. In contrast, during mechanosynthesis, all the precursor materials are retained, and the reaction product is obtained under thermodynamic control in a manner analogous to conventional high temperature solid-state routes. Under such conditions, the final product(s) must reflect the global starting composition and, therefore, if a single phase perovskite product is achieved then this must have the nominal starting composition.

Any mismatch between nominal and actual composition may reduce the reliability of the conclusions drawn from subsequent structural and photophysical studies. Examples of nominal and actual composition mismatch in mixed-metal[11–15] and mixed-halide[13]

perovskite systems have been studied using X-ray photoelectron spectroscopy (XPS) and flame atomic absorption spectroscopy. These studies demonstrated that the actual amount of Sn and Bi, incorporated in $FAPb_{1-x}Sn_xBr_3$[13] and Bi-doped $MAPbX_3$ (X = Cl, Br, I)[11,12,14] single crystals respectively, was significantly less than the nominal percentages of Sn and Bi in the initial respective solution. In another example, the actual Cl% in $FAPbBr_{3-x}Cl_x$[13] crystals was found to be larger than the nominal value for Cl-poor target compositions (< 50% Cl) but smaller for Cl-rich reactions. Similar instances were also found for A-cation substitutions.[16,17] For instance, Spanopoulos et al.[16] demonstrated by NMR analysis that the actual ethylenediammonium (en) incorporated in $(MA_{1-x}en_x)PbI_3$ was less than the nominal composition. To account for such mismatches, several explanations have been proposed,[11,14,18] including the difference between valence (and hence induced compensating defects) and ionic radii, and surface effects (especially for XPS) for mixed metal (M-site) solid solutions. Such explanations for mixed halide and mixed A-cation systems are absent as most studies overlooked the composition with respect to halide and organic A-cation content. Most compositional studies of nominal and actual compositions of solid solutions with substitutions at A, M, and X sites are carried out on samples prepared by precipitation methods and in systems that can support a complete solid solution due to isostructural endmembers. Beyond simple observation of lattice parameter variations (Vegard's law), a lack of structural contrast makes it challenging to determine if the system sustains solid solution formation or has phase separation.

Considering the compositional consistency of mechanosynthesis, the formation of 6H and 3C lead bromide perovskite with mixed organic A-cations is explored to study the relation between the nominal and actual composition using both NMR spectra and PXRD analyses.

4.2 Mixed A-cation perovskite

4.2.1 Synthesis and PXRD analysis

$Az_{1-x}FA_xPbBr_3$ and $Az_{1-x}MA_xPbBr_3$ ($0 \leq x \leq 1$) compositions were prepared by both mechanosynthesis and precipitation synthesis. For mechanosynthesis, samples of Az_{1-}

$_x$FA$_x$PbBr$_3$ and Az$_{1-x}$MA$_x$PbBr$_3$ ($0 \leq x \leq 1$) were prepared by mixing appropriate molar ratios of AzBr and FABr/MABr with PbBr$_2$ with a mortar and pestle, and the mixture was then transferred into the ball mill and ground at 600 rpm for 1 hour. For the antisolvent precipitation synthesis, samples of Az$_{1-x}$FA$_x$PbBr$_3$ and Az$_{1-x}$MA$_x$PbBr$_3$ ($0 \leq x \leq 1$) were prepared by mixing appropriate molar ratios of AzBr and FABr/MABr with PbBr$_2$ in a DMF/DMSO (4:1 by volume) solution. Acetonitrile was slowly added to the reaction mixture and the resulting precipitate was collected by filtration. Detailed procedures are given in Chapter 2. The SEM images of the single phase AzPbBr$_3$ and FAPbBr$_3$ samples obtained from both syntheses are shown in Figure **4.1**. As expected, the particle size of precipitation-synthesised samples is larger than that of mechanosynthesised ones.
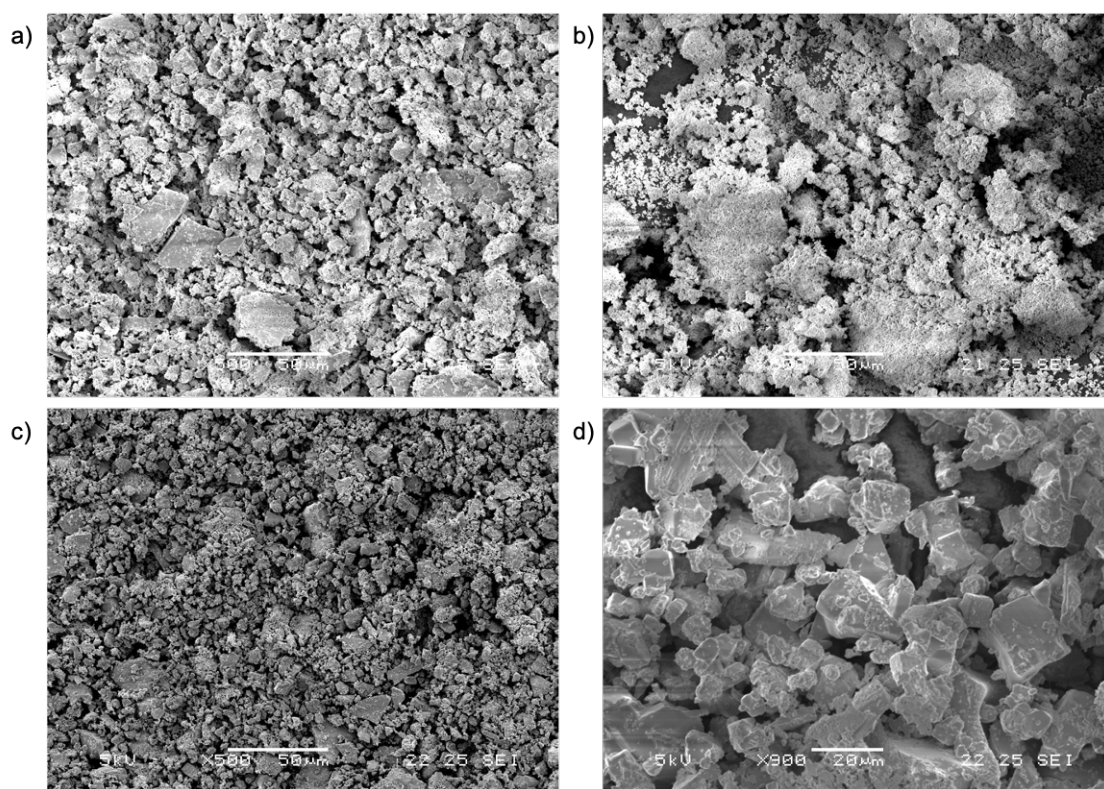

Figure 4.1. SEM images of AzPbBr$_3$ from (a) mechano- (b) precipitation synthesis and FAPbBr$_3$ from (c) mechano- and (d) precipitation synthesis. The white scale bar is 20 µm for image (d) while scale bar in other images is 50 µm. Reproduced from Ref. 19 with permission. Copyright (2021) American Chemical Society.

During the precipitation synthesis, gradual addition of the antisolvent produced a noticeable change in colour of the precipitate. Initially, the colour of the precipitate resembled more closely the colour of the perovskite with the richer cation source, ($AzPbBr_3$ is pale yellow and $MAPbBr_3$/$FAPbBr_3$ is red/orange) and in later stages of precipitation, the colour of the precipitate appeared to be midway between the pale yellow and red/orange colours of the end member compositions. The observation of colour progression is difficult during grinding due to the opaque chamber of the ball mill. However, the progress of mechanosynthesis of one sample ($Az_{0.5}FA_{0.5}PbBr_3$) was tracked by periodic interruption of the grinding process – the colour was orange in the early stage of mechanosynthesis and bright yellow in the late stage of grinding (Figure **4.2**).
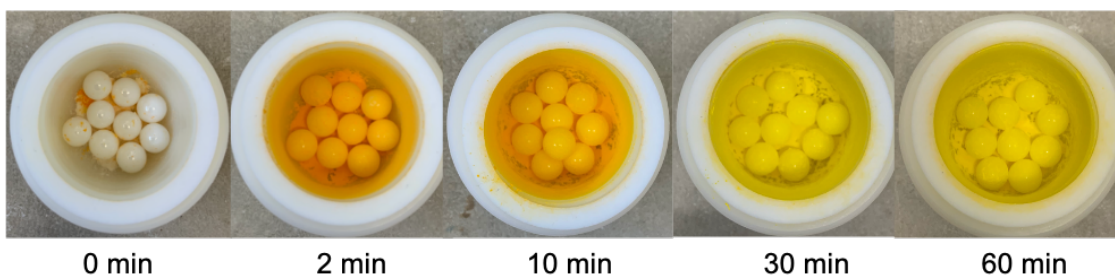

| 0 min | 2 min | 10 min | 30 min | 60 min |

Figure 4.2. Colour progression of $Az_{0.5}FA_{0.5}PbBr_3$ during mechanosynthesis, reproduced from Ref. 19 with permission. Copyright (2021) American Chemical Society.

In this chapter, x' and x are used to represent the nominal and actual FA^+ or MA^+ composition in the mixed cation perovskite, respectively. The systematic colour change with composition of $Az_{1-x'}FA_{x'}PbBr_3$ ($0 \leq x' \leq 1$) samples from both synthetic routes is shown in Figures **4.3a** and **4.3b**. Empirically, the transition from yellow to red/orange was observed at a smaller nominal composition ($x' = 0.4$) for the precipitation samples than mechanosynthesised ones ($x' = 0.6$). Comparisons of the PXRD data between mechano- and precipitation syntheses are shown in Figures **4.3c** and **4.3d**. Regions of solid solution formation (single phase regions) separated by a region of two-phase mixture at intermediate x' can be identified for both syntheses on $Az_{1-x'}FA_{x'}PbBr_3$, but the extent of solid solution formation is different. The PXRD of the mechanosynthesised samples indicates that for $x' \leq 0.4$ only peaks associated with the 6H polytype are

observed, and for $x' \geq 0.7$ only the 3C phase is present, while at intermediate x' values the PXRD indicates a two-phase mixture. The PXRD of the precipitation shows that for $x' \leq 0.2$ or for $x' \geq 0.8$ peaks associated with the 6H or 3C polytypes were observed.
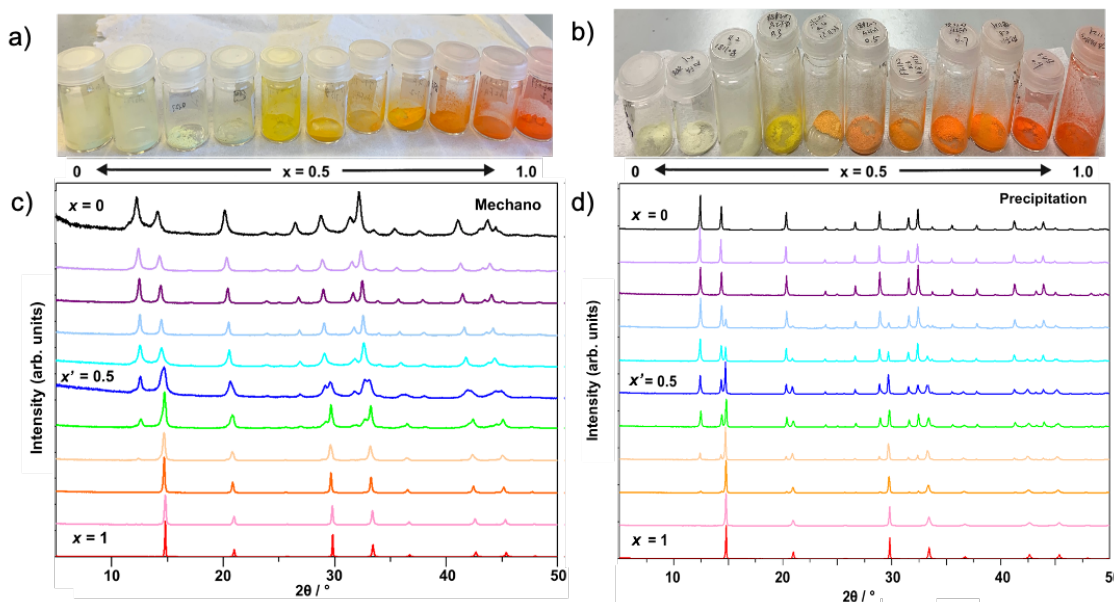

Figure 4.3. Photos and PXRD data of powders of $Az_{1-x'}FA_{x'}PbBr_3$ with nominal composition $0 \leq x' \leq 1$ (in $x' = 0.1$ increments) prepared by (a, c) mechanosynthesis and (b, d) precipitation synthesis. Reproduced from Ref. 19 with permission. Copyright (2021) American Chemical Society.

To ensure all starting materials were consumed during the grinding synthesis, one sample ($Az_{0.4}FA_{0.6}PbBr_3$) in the two-phase solid solution region was reground for an additional hour. The PXRD of the starting materials and samples before and after regrinding are shown in Figure **4.4**. No trace of starting materials, and no change in lattice parameters were observed in samples before and after regrinding. Reground samples showed no visual change in appearance and Rietveld refinement (discussed in section 4.2.3) indicated an insignificant change in both phase fraction (cubic phase ratio from 0.436 to 0.453) and lattice parameters of 6H (~1% change) and 3C (~2% change) phase. These analyses suggest all starting materials were consumed during mechanosynthesis.
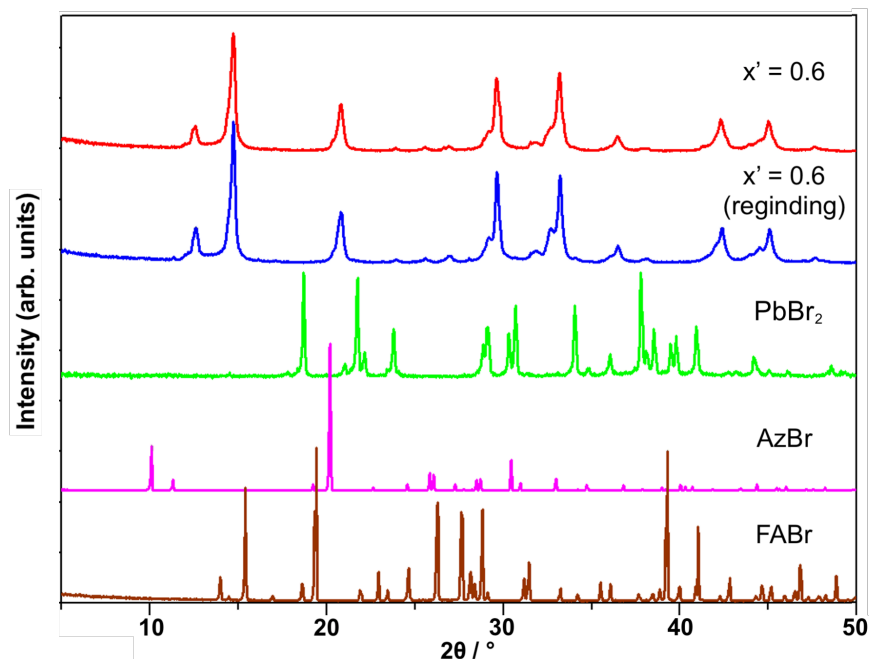
Figure 4.4. PXRD of mechanosynthesised $Az_{0.4}FA_{0.6}PbBr_3$ before and after regrinding for an additional hour, and PXRD of starting materials $PbBr_2$, AzBr and FABr, reproduced from Ref. 19 with permission. Copyright (2021) American Chemical Society.

The degree of replacement of Az by MA in the 6H structure, and similarly replacement of MA by Az in the 3C structure, was investigated by preparing a series of compositions according to $Az_{1-x'}MA_{x'}PbBr_3$, $0 \leq x' \leq 1$ in 0.1 increments for precipitation synthesis and in 0.2 increments for mechanosynthesis. The resulting powders obtained from precipitation synthesis show a gradual colour change from pale yellow in Az-rich compositions to orange with increasing amount of $MAPbBr_3$ (Figure **4.5a**). PXRD analysis of precipitation synthesised $Az_{1-x'}MA_{x'}PbBr_3$ shows more extensive solid solutions where for $x' \leq 0.3$ or for $x' \geq 0.8$ only the 6H or 3C polytypes were observed (Figure **4.5b**), in comparison to the previously described $Az_{1-x'}FA_{x'}PbBr_3$. The PXRD of the mechanosynthesised samples indicates that for $x' \leq 0.2$ only peaks associated with the 6H polytype are observed, and for $x' > 0.4$ only the 3C phase is present (Figure **4.5c**). As the intermediate x' associated with two-phase mixture is small ($0.2 < x' \leq 0.4$), $Az_{1-x'}MA_{x'}PbBr_3$ samples with 0.067 increments were prepared by mechanosynthesis in this composition range of two-phase mixture and the analysis is shown in the following section.
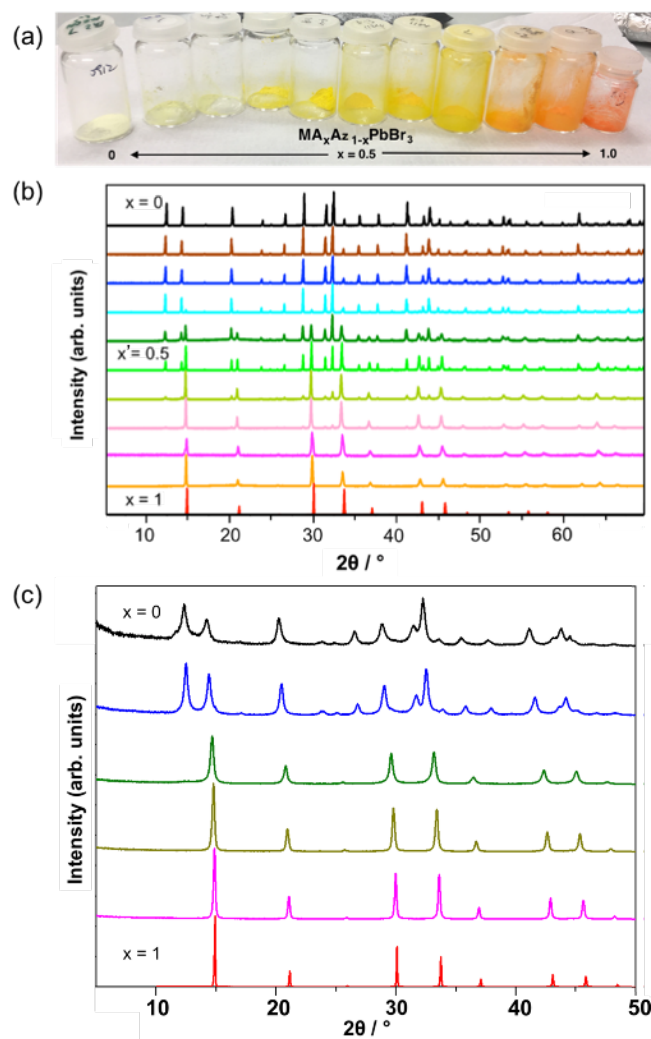
Figure 4.5. (a) Colour change of precipitation synthesised samples prepared according to composition $Az_{1-x'}MA_{x'}PbBr_3$ ($0 \leq x' \leq 1$); PXRD data of samples obtained from (b) precipitation synthesis (c) mechanosynthesis. Figures (a, b) are adapted from Ref. 6 with permission. Copyright (2019) American Chemical Society. Figure (c) is reproduced from Ref. 19 with permission. Copyright (2021) American Chemical Society.

The PXRD peaks for $Az_{1-x'}MA_{x'}PbBr_3$ and $Az_{1-x'}FA_{x'}PbBr_3$ prepared by mechanosynthesis are generally wider than that of the precipitation synthesis, presumably due to the smaller crystallite size. The crystallite size of the 6H phase in $Az_{1-x'}FA_{x'}PbBr_3$ ($x' \leq 0.8$) and 3C phase for $x' \geq 0.8$ was estimated from the Scherrer equation:[20]

$$p = \frac{K\lambda}{b\cos\theta} \hspace{4cm} \text{(Equation } \textbf{4.1}\text{)}$$

where p is the mean crystallite size, K is Scherrer (shape) constant, λ is the X-ray wavelength (1.5406 Å), b is the breadth at full width at half maximum intensity (FWHM) in radians, and θ is the Bragg angle. The Scherrer equation analysis on 6H and 3C phase is shown in Table **4.1**. The FWHM of the high intensity (011) and (001) peak was chosen for the analysis on 6H and 3C phase respectively. The shape constant was set to the typical value 0.9. [20] The crystallite size of the 6H phase from the precipitation synthesis is more than twice as large as that from mechanosynthesis, which was confirmed by SEM (Figure **4.6**). However, the crystallite size of 3C phase was hard to determine in the two-phase mixture region, due to the presence of overlapping major peaks from the 6H phase. The crystallite size of $FAPbBr_3$ from the precipitation synthesis was also estimated to be slightly larger than that from the mechanosynthesis with the Scherrer equation, which is in agreement with the SEM images in Figure **4.1**.
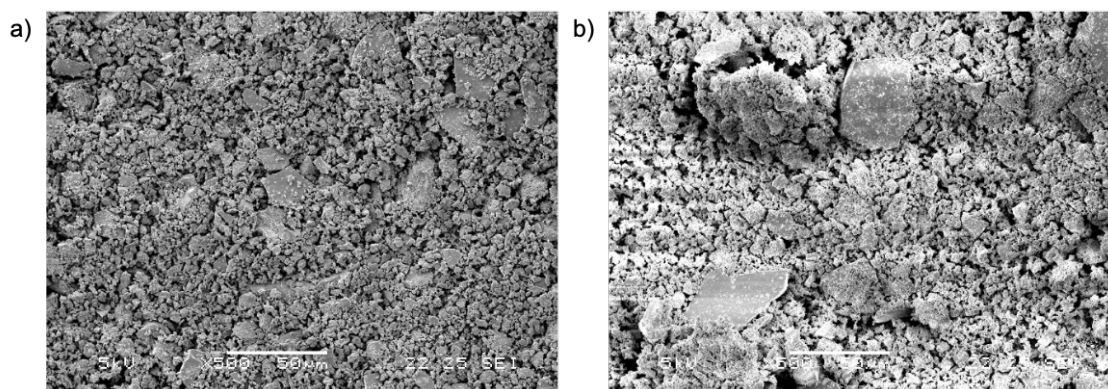

Figure 4.6. Examples of SEM images of $Az_{0.6}FA_{0.4}PbBr_3$ from (a) mechano- (b) precipitation synthesis. The white scale bar is 50 μm in both images. Reproduced from Ref. 19 with permission. Copyright (2021) American Chemical Society.

Table 4.1. Calculation of crystallite size of 6H phase in the mixed-cation perovskite $Az_{1-x'}FA_{x'}PbBr_3$ ($x' \leq 0.8$) and 3C phase for $x' \geqslant 0.8$ in both mechano- and precipitation synthesis using the Scherrer equation, adapted from Ref. 19 with permission. Copyright (2021) American Chemical Society.

Grinding				Precipitation			
x'	Peak position (2θ)/ °	FWHM / °	p / nm	x'	Peak position (2θ)/ °	FWHM / °	p / nm
0	12.398	0.185	43.2	0	12.417	0.107	74.7
0.1	12.367	0.332	24.1	0.1	12.376	0.091	87.8
0.2	12.452	0.264	30.3	0.2	12.423	0.092	86.9
0.3	12.504	0.224	35.7	0.3	12.385	0.101	79.1
0.4	12.520	0.382	20.9	0.4	12.442	0.098	81.5
0.5	12.544	0.316	25.3	0.5	12.401	0.115	69.5
0.6	12.595	0.357	22.4	0.6	12.416	0.114	70.1
0.7	12.376	0.236	33.9	0.7	12.390	0.102	78.3
				0.8	12.456	0.121	66.0
Average			28.8 ± 7.7	Average			77.1 ± 7.7
0.8	14.689	0.151	53.0	0.9	14.776	0.104	77.0
0.9	14.787	0.151	53.1	1	14.760	0.072	111
1	14.736	0.080	100				
Average			68.7 ± 27	Average			94.0 ± 24

4.2.2 Cation composition analysis

Using o-dichlorobenzene as an internal standard, solution-state ^{1}H NMR analysis (details included in section 2.1.5.1) was carried out on the as-synthesised samples to determine the actual FA^+/MA^+ composition, x, and compare it with nominal x', in $Az_{1-x'}FA_{x'}PbBr_3$ and $Az_{1-x'}MA_{x'}PbBr_3$ prepared by both synthetic methods. The comparison between actual x and nominal x' is shown in Figure **4.7**. As expected, the actual x obtained by ^{1}H NMR spectra closely matches with nominal x' in both sets of mechanosynthesis samples as all starting materials are retained during the ball milling reaction. To ensure that this analysis represented the as-synthesised perovskite, ^{1}H NMR analysis of both the isolated bulk powder and the residue left in the ball mill was carried out for $Az_{1-x}FA_xPbBr_3$, with both samples revealing similar compositions (Table **4.2**). By contrast, the ^{1}H NMR analysis of samples from the precipitation synthesis indicated that the actual FA/MA content (x) is consistently lower than the nominal value in the precursor solution (x') for both $Az_{1-x}FA_xPbBr_3$ and $Az_{1-x}MA_xPbBr_3$ (Figure **4.7b** and **4.7d**). The cation composition mismatch is apparent for $x' < 0.8$ in $Az_{1-x}FA_xPbBr_3$, which suggests the mixed cation perovskite precipitation is affected by the relative cation concentration of the precursor solution. The reason behind the composition mismatch is discussed in the section below.

Table 4.2. Comparison of actual x in mechanosynthesis of $Az_{1-x}FA_xPbBr_3$ between the powder removed from ball mill (actual x) and powder left in ball mill (actual $x_{residue}$), adapted from Ref. 19 with permission. Copyright (2021) American Chemical Society.

Nominal x'	Actual x	Actual $x_{residue}$	Nominal x'	Actual x	Actual $x_{residue}$
0.1	0.142	0.158	0.8	0.799	0.800
0.2	0.268	0.265	0.9	0.906	0.900
0.6	0.634	0.597			
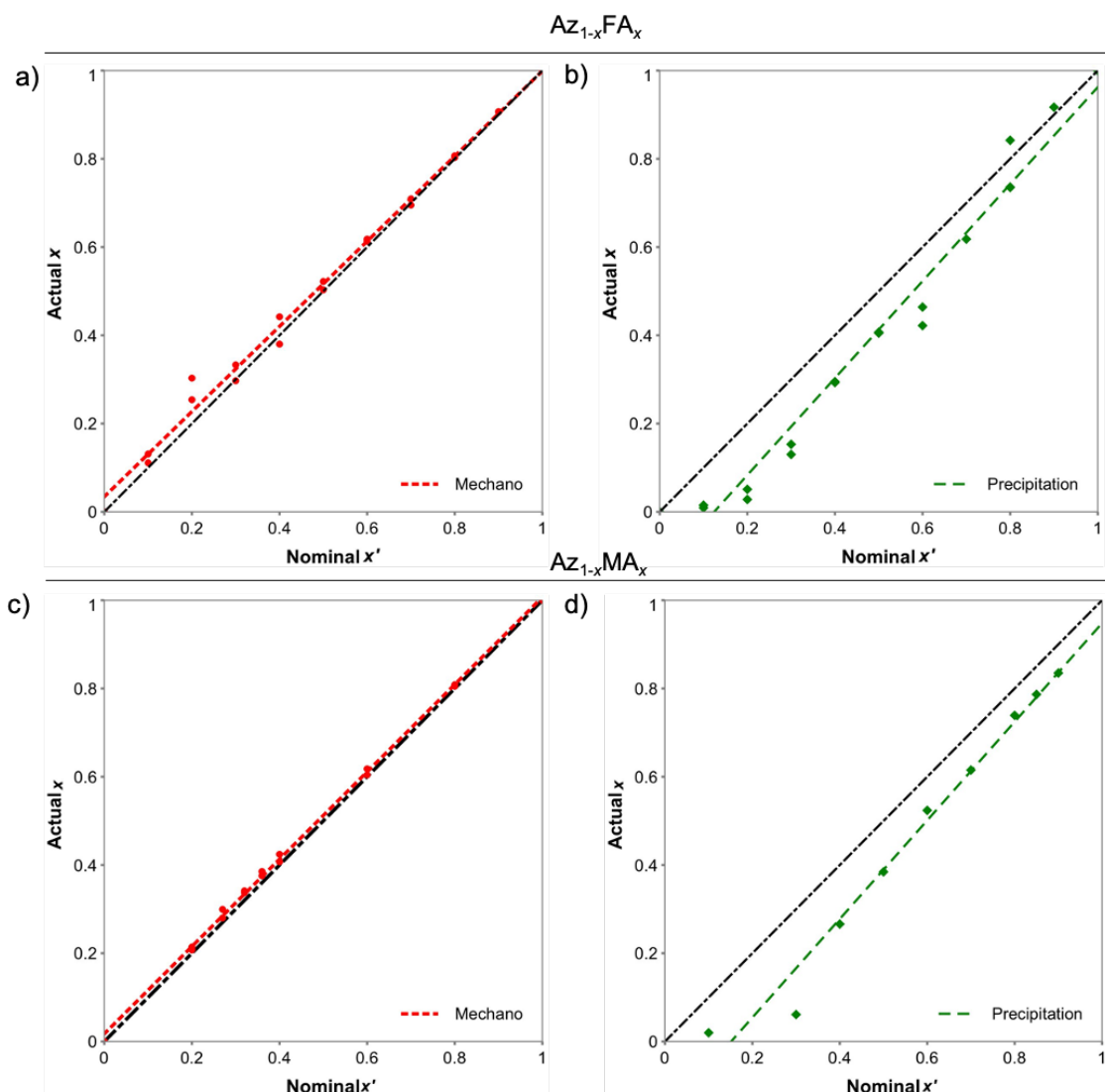
Figure 4.7. The comparison of nominal (x') and actual (x) FA$^+$/MA$^+$ cation content determined by ^{1}H NMR analysis on Az$_{1-x}$FA$_x$PbBr$_3$ and Az$_{1-x}$MA$_x$PbBr$_3$ samples prepared by (a, c) mechanosynthesis and (b, d) precipitation synthesis. Dash lines are a linear fit to the actual values and black dot-dash lines indicate the instance for $x = x'$ composition for comparison Adapted from Ref. 19 with permission. Copyright (2021) American Chemical Society.

4.2.3 Rietveld refinement of PXRD of $Az_{1-x}FA_xPbBr_3$

Rietveld refinement of the PXRD data of $Az_{1-x}FA_xPbBr_3$ samples from both syntheses was carried out to study the phase mixture and the solid solution regions. Examples of refinement of $AzPbBr_3$, $FAPbBr_3$ and $Az_{0.4}FA_{0.6}PbBr_3$ are shown in Figure **4.8**. The weight fraction of both 6H and 3C phase was determined from the refinements and are shown in terms of mol fraction versus actual x (obtained by ^{1}H NMR analysis on $Az_{1-x}FA_xPbBr_3$) in Figures **4.9a** and **4.9b**. For $Az_{1-x}FA_xPbBr_3$ samples obtained by mechanosynthesis, an intermediate two-phase region appears for $0.42 \leq x \leq 0.79$. This contrasts with samples obtained from the precipitation synthesis, where the region is much larger $0.10 \leq x \leq 0.94$. A rise in temperature of the milling beaker was observed and thus the temperature inside the beaker was measured with a hand-held pyrometer immediately after the grinding. The temperature was found to be 50.4 ± 3.9 °C. It was hypothesised that the increase in temperature could provide sufficient thermal energy to aid FA^+ and Az^+ diffusion into 6H and 3C phases during grinding, however this was discounted based on post-synthesis annealing experiments which showed no change on heating as discussed in section 4.2.5.

The observation of the colour change of the precipitate mentioned in the beginning of section 4.2.1 indicates that the precipitation of 6H and 3C phases tend to progress at different rates, which is related to their cation concentration in the precursor solution. In order to investigate the A-cation stoichiometry of samples as precipitation progressed, a stepwise antisolvent addition experiment was performed (experimental details in section 2.2.2.3). Based on the observed colour change during precipitation, the initial assumption was that the 6H phase precipitates first and the 3C phase follows with increasing volume of antisolvent.
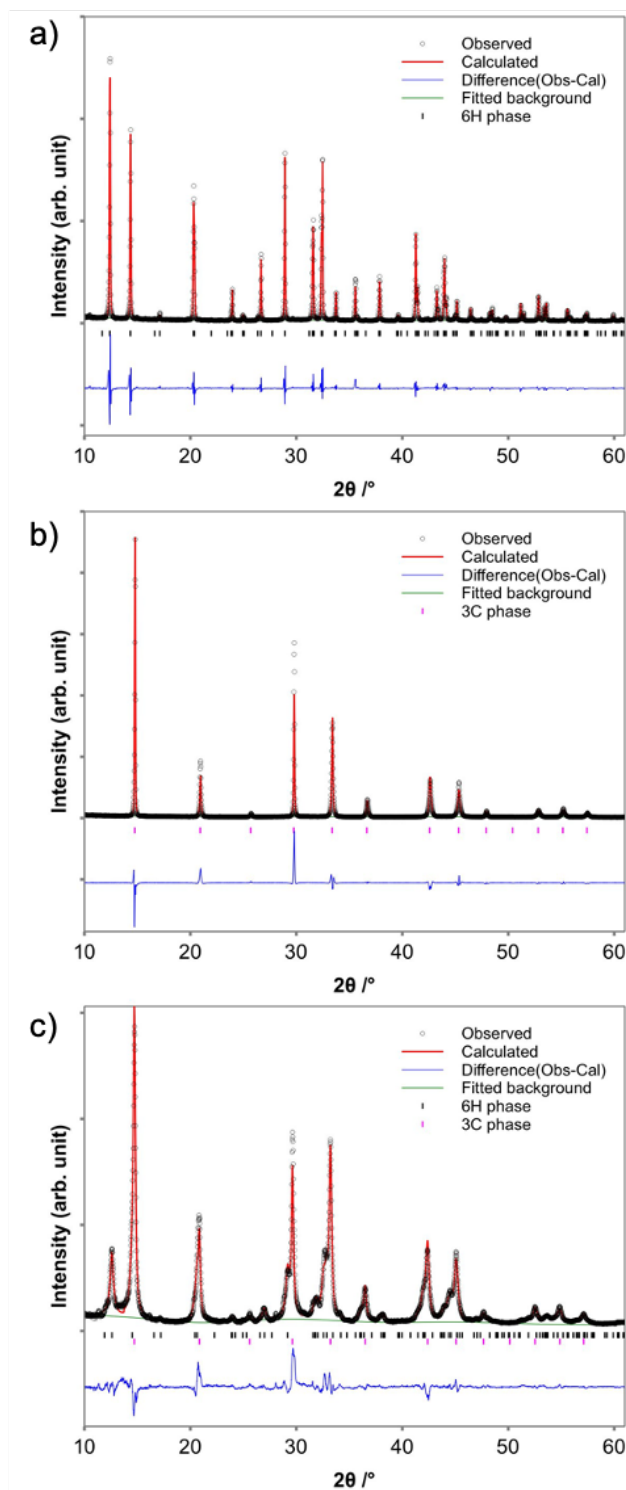
Figure 4.8. Example of Rietveld refinement profile of PXRD data for (a) $AzPbBr_3$ (b) $FAPbBr_3$ and (c) $Az_{0.4}FA_{0.6}PbBr_3$ with observed intensity (open circles), calculated intensity (red line), background (green line), reflection position (black bar for 6H phase and magenta bar for 3C phase) and difference curve (blue line). Reproduced from Ref. 19 with permission. Copyright (2021) American Chemical Society.

Figure 4.9. Mole fraction and cell volume (per formula unit) of hexagonal (6H) and cubic (3C) perovskite phases as determined by Rietveld refinement of PXRD data for $Az_{1-x}FA_xPbBr_3$ samples prepared by (a, c) mechano- and (b, d) precipitation synthesis. Values are shown as a function of overall, actual x as determined by NMR spectra. The vertical dashed lines indicate the boundaries between the single-phase solid solution and intermediate two-phase regions. Reproduced from Ref. 19 with permission. Copyright (2021) American Chemical Society.

The actual x obtained by ^{1}H NMR analysis (Table **4.3**) of the precipitated samples shows that they are deficient in FA^+ in the early stages of addition of the antisolvent. In set 1, different amounts of antisolvent were added into parallel batches of perovskite solution,

while the overall amount of antisolvent added into one perovskite solution was recorded in set 2. The details of the two sets of synthesis are in Section **2.2.2.3**. The incorporation of such a small amount (ca. 6%) of FA^+ in the early stages of precipitation is evident from the colour of the powders, which appeared close in colour to $AzPbBr_3$ (Figure **4.10**). Similarly, there is no 3C phase detected by PXRD in these precipitated samples, the actual x of which is less than 0.07. This result is consistent with the solid solution/two phase regions indicated in Figure **4.9**. These stepwise antisolvent experiments show that the 6H phase is more likely to precipitate first with antisolvent present under a similar cation concentration, while the 3C phase only precipitates with lower Az^+ cation concentrations. This kinetic difference accounts for both the composition mismatch found in Figure **4.9b** and the small solid solution region observed in $Az_{1-x}FA_xPbBr_3$ samples obtained by precipitation.

Table 4.3. Actual x and unit cell volume of 6H phase of two trials (set 1 and set 2) of stepwise antisolvent precipitation synthesis of $Az_{0.5}FA_{0.5}PbBr_3$, adapted from Ref. 19 with permission. Copyright (2021) American Chemical Society.

Set 1			Set 2		
Volume of acetonitrile / mL	Actual x	Unit cell volume / Å^3	Volume of acetonitrile / mL	Actual x	Unit cell volume / Å^3
1	0.025	1420.308	1	0.024	-
2	0.044	1419.838	7	0.060	-
5	0.063	1418.322	16	0.294	-
10	0.171	1410.823	30 (ex.)	0.803	-
20 (ex.)	0.298	1419.055			

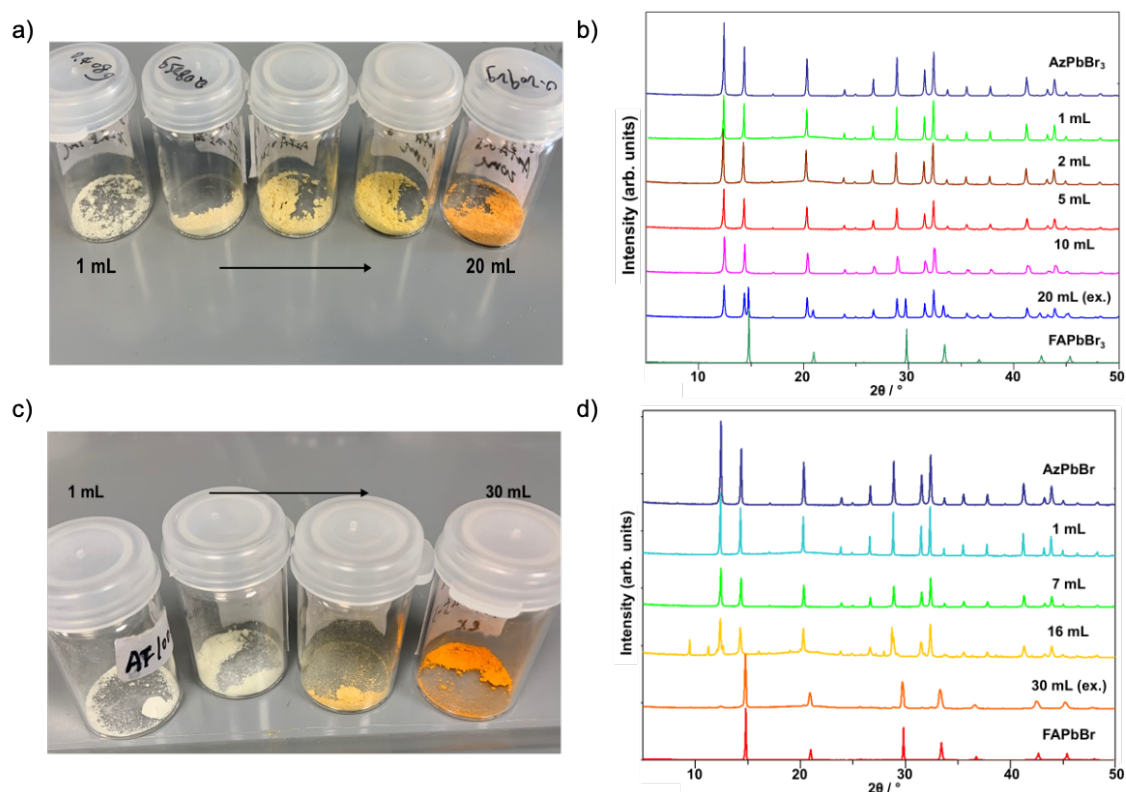**Figure 4.10.** Stepwise antisolvent precipitation synthesis of $Az_{0.5}FA_{0.5}PbBr_3$: (a, c) visualisation of the colour of the powders (b, d) PXRD analysis. (a, b) are from set 1 and (c, d) are from set 2. Reproduced from Ref. 19 with permission. Copyright (2021) American Chemical Society.

In the mixed-cation system $Az_{1-x}FA_xPbBr_3$, a complete solid solution is impossible as the end members are not isostructural (6H and 3C perovskite), although partial solid solutions may form at either end given the similar A-cation size from calculation.[21,22] In the single phase (solid solution) regions (as determined by PXRD, Figures **4.9c** and **4.9d**), the actual x values as determined from ^1H NMR analysis correspond to the actual FA^+ composition of the solid solution. A more conventional expression of solid solution general formulae is needed; $Az_{1-y}FA_yPbBr_3$ (6H, Az-rich) and $Az_zFA_{1-z}PbBr_3$ (3C, FA-rich), where y and z denote the degree of substitution of FA and Az at the A-site from the parent structure. This also allows us to distinguish them from $Az_{1-x}FA_xPbBr_3$ especially for mixed phase samples; in the two-phase region, x corresponds to the global FA content with an unknown distribution over the two phases.

The lattice parameters of each polytype as a function of x were determined by Rietveld refinement, including two-phase refinement for intermediate x. The cell volume (Figure **4.9c** and **4.9d**) of $Az_{1-x}FA_xPbBr_3$ as a function of composition shows a close resemblance to the reported $BaTiO_3$–$CaTiO_3$ solid solution system,[23] in which the lattice parameter progression changes from decreasing to essentially invariant as the composition extends from the single phase region into the two-phase region. In the single phase 6H solid solution region, the lattice constant and cell volume show a systematic decrease with increasing FA content. This is more evident in samples obtained via mechanosynthesis. For the 3C region of those samples, the solid solution shows an increase in cell volume with increasing Az content. These volume-composition dependencies suggest that FA^+ is smaller than Az^+ in contrast to computational studies which suggest FA is marginally larger.[21,22] The suggestion that FA^+ is smaller than Az^+ is also consistent with the experimental results that $AzPbBr_3$ forms a 6H structure and $FAPbBr_3$ forms a cubic structure while their tolerance factors, using computed cation sizes, are both 1.0. However, the size effect of organic cations in extended structures is largely based on a hard sphere approximation, which implies their free rotation. This may not be true for either FA^+ or Az^+ in these structures at room temperature and requires further study.

For samples obtained from the precipitation synthesis, the cell volume in the Az-rich region is invariant as a function of x, which suggests a relatively small degree of substitution by FA when compared to mechanosynthesised samples of the same composition. Presumably, this is due to the phase separation between 3C and 6H phases during the precipitation as a result of the different precipitation rates. The sharp decrease of the volume at $x = 0.84$ is possibly due to the error of the refinement as the fraction of the 6H phase in these samples is very low. For precipitation synthesised samples in the FA-rich region, the slight increase in cell volume indicates a relatively small degree of substitution by Az. Overall, there is limited solid solution formation during the precipitation synthesis.

4.2.4 Rietveld refinement of $Az_{1-x}MA_xPbBr_3$

The lattice parameters of each polymorph (6H, 3C) as a function of x were determined by Rietveld refinement, including two phase refinement for intermediate x. Rietveld

refinements for the $Az_{1-x}MA_x$ system shows the presence of limited solid solutions of $Az_{1-y}MA_yPbBr_3$ (6H) and $Az_zMA_{1-z}PbBr_3$ (3C) for both syntheses (Figure **4.11**). For samples obtained from the mechanosynthesis, an intermediate two-phase region appears for $0.27 \leq x \leq 0.49$, compared to precipitation synthesised samples, where the two-phase region is larger ($0.07 \leq x \leq 0.71$). The cell volume expansion as a function of increasing Az content (fitted lines, Figure **4.11**) in the 3C solid solution region is similar for both mechano- and precipitation syntheses. The unit cell volume of the 6H phase in precipitation synthesised samples is invariant as a function of x (Figure **4.11d**), presumably due to the incompressibility of the face-sharing Pb-Br octahedra in the 6H-structure due to the Pb$^{...}$Pb repulsion, which does not allow collapse of the unit cell volume on insertion of the smaller MA cation.

4.2.5 Comparison between $Az_{1-x}MA_x$ and $Az_{1-x}FA_x$ solid solutions

The solid solution ranges of the $Az_{1-x}MA_x$ and $Az_{1-x}FA_x$ systems are included in Table **4.4**. Experimental results suggest that the size of Az^+ is larger than that of FA^+, and both cations are larger than MA^+. The relative size relationship between FA^+ and MA^+ can be confirmed from the lattice parameters of the reported (cubic) $FAPbBr_3$ and $MAPbBr_3$, where $a(FAPbBr_3) = 5.98$ Å and $a(MAPbBr_3) = 5.92$ Å.[6,24] In oxide perovskites, it is generally acknowledged that solid solution formation follows Hume–Rothery rules,[25] which describe the empirical observation that the size difference between the solute and solvent atoms should be within 15% for substitutional solid solutions. This is because too large a size mismatch generates local strain. In the (Ba, Sr, Ca)TiO_3 system, for example, all three end members form (pseudo-)cubic perovskites. The cation radii for Ba^{2+}, Sr^{2+} and Ca^{2+} are 1.61, 1.44 and 1.34 Å, respectively[26], and complete solid solutions form for $Ba_{1-x}Sr_xTiO_3$ and $Sr_{1-x}Ca_xTiO_3$, indicating this full range of A-cation size can be accommodated in the crystal structure (the average A-cation size varies continuously across the combined solid solutions). However, for $Ba_{1-x}Ca_xTiO_3$ only < 30% Ca substitution can be tolerated due to the large size mismatch and resulting local strain.[27–30] Similarly, it is expected to be easier for relatively larger Az^+ to replace the cations in the larger A-site interspace in $FAPbBr_3$ than $MAPbBr_3$ independent of the synthetic method and for a more extensive solid solution to form.
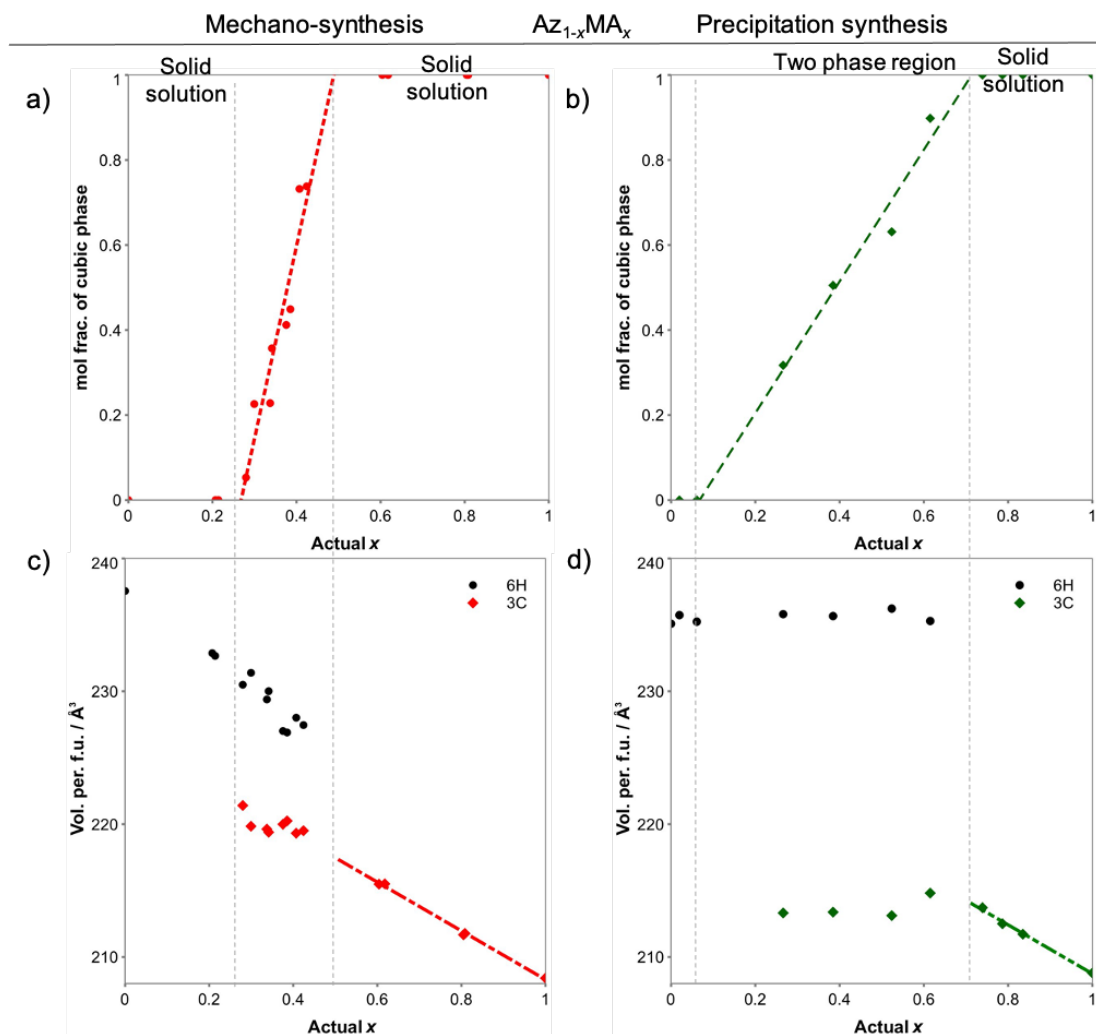
Figure 4.11. Mole fraction and cell volume (per formula unit) of 6H and 3C phases determined by Rietveld refinement of PXRD data for $Az_{1-x}MA_xPbBr_3$ samples prepared by (a, c) mechano- and (b, d) precipitation synthesis. Values are shown as a function of actual x determined by NMR spectra. Vertical dashed lines indicate the boundaries between the single-phase solid solution and intermediate two-phase regions. Dash-dot lines and dash-dot-dot lines are linear fits to the cell volume as a function of actual x for samples in the 3C solid solution region. Reproduced from Ref. 19 with permission. Copyright (2021) American Chemical Society.

However, the observations here are contrary to this notion. For mechanosynthesis of the 3C solid solutions, in $Az_zFA_{1-z}PbBr_3$, the degree of Az substitution extends to $z = 0.21$ compared to $z = 0.51$ for $Az_zMA_{1-z}PbBr_3$. Synthesised samples by precipitation show

similar results where the solid solution range of $Az_zFA_{1-z}PbBr_3$ is smaller than that of $Az_zMA_{1-z}PbBr_3$, but this observation does not take into account any possible kinetically-limited aspects.

A possible explanation for this observation is that the extent of solid solution formation observed here is dependent only on the global average A-cation size and that local strain due to size mismatch plays a less significant role. In other words, mixed A-cation halide perovskite would not tolerate the single phase 3C solid solution if the average A-cation size is larger than a certain value. This can be estimated by examining the maximum unit cell volume of the 3C phase in each system (Figure **4.12a**). Under the assumption that Vegard's law holds for all these solid solutions, a linear relationship between the average A-cation radius and cell volume can be fitted to the results from $MA_{1-x}FA_xPbBr_3$ samples with $r_{FA} = 253$ pm and $r_{MA} = 217$ pm (Figure **4.12b**).[21]

Table 4.4. Solid solution ranges for $Az_{1-x}FA_x$ and $Az_{1-x}MA_x$ samples prepared by mechano- and precipitation syntheses, reproduced from Ref. 19 with permission. Copyright (2021) American Chemical Society.

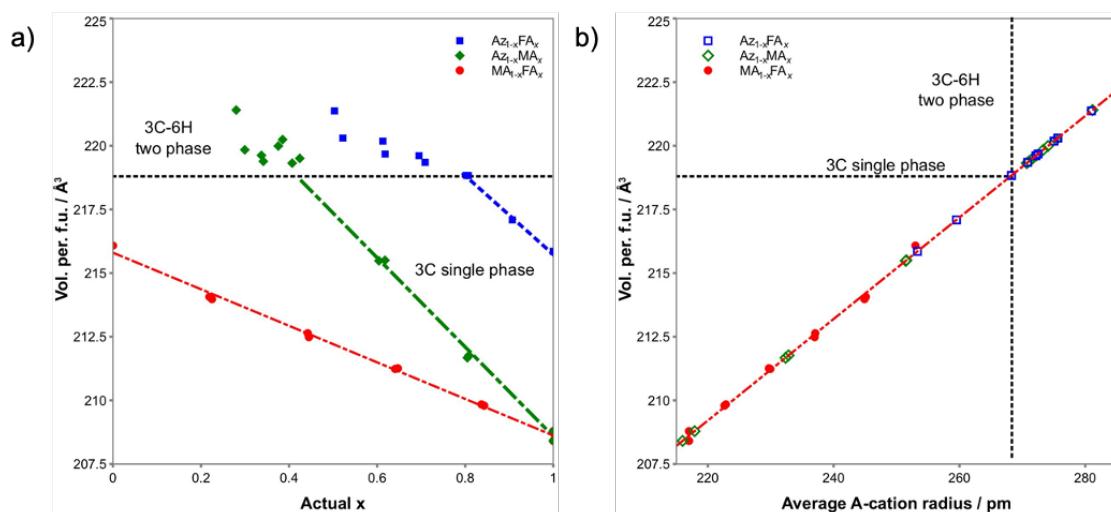|	Solid solution range	Mechano-synthesis	Precipitation synthesis
6H	$Az_{1-y}FA_yPbBr_3$	$y \leq 0.42$	$y \leq 0.10$
	$Az_{1-y}MA_yPbBr_3$	$y \leq 0.27$	$y \leq 0.07$
3C	$Az_zFA_{1-z}PbBr_3$	$z \leq 0.21$	$z \leq 0.06$
	$Az_zMA_{1-z}PbBr_3$	$z \leq 0.51$	$z \leq 0.29$

Figure 4.12. (a) Unit cell volume of 3C perovskite phases determined by Rietveld refinement of PXRD data for $MA_{1-x}FA_xPbBr_3$, $Az_{1-x}FA_xPbBr_3$ and $Az_{1-x}MA_xPbBr_3$ samples prepared by mechanosynthesis (b) unit cell volume of 3C FA/MA perovskite samples plotted with average A-cation radius under the assumption of Vegard's law with $r_{FA} = 253$ pm and $r_{MA} = 217$ pm.[21] The line is fitted with the results from $MA_{1-x}FA_xPbBr_3$ and the hollow points from $Az_{1-x}FA_xPbBr_3$ and $Az_{1-x}MA_xPbBr_3$ samples are added in according to their unit cell volume. Black dotted lines indicate the upper limit cell volume (ca. 219 $Å^3$ per formula unit) of cubic single-phase solid solution and corresponding average A-cation radius (ca. 268 pm), which separates the 3C single phase and 3C-6H two-phase region. Reproduced from Ref. 19 with permission. Copyright (2021) American Chemical Society.

By extrapolation, the cation radius of Az is estimated to be 315 ± 11 pm (from $Az_{1-x}FA_x$ data) or 304 ± 6 pm (from $Az_{1-x}MA_x$ data). These crude estimations for the Az^+ cation radius are significantly larger than the computed cation radius ($r_{Az} = 250$ pm) reported by Kieslich *et al.*[21] and clearly requires further study. The tolerance factor of $AzPbBr_3$ calculated with $r_{Az} = 310$ pm (average of the two values above) is 1.14, which is in agreement with the fact that it forms 6H hexagonal structure rather than cubic (Chapter 3). The reason behind the differing influence of local strain on the extent of solid solution formation between oxide and halide perovskites might result from the strong M-O bonds and resulting rigid framework in comparison to the M-X framework in halides. The Young's moduli of halide perovskites are of the order 10 – 20 GPa (for $MAPbX_3$, X = Cl,

Br, I),[31] which are approximately an order of magnitude lower than for oxide perovskites (> 100 GPa).[32]

The 6H solid solution ranges described by $Az_{1-y}FA_yPbBr_3$ and $Az_{1-y}MA_yPbBr_3$ are both extremely limited in the precipitation synthesised samples. For the mechanosynthesised 6H solid solution $Az_{1-y}FA_yPbBr_3$, the degree of FA substitution extends to $y \leq 0.42$ and to $y \leq 0.27$ for $Az_{1-y}MA_yPbBr_3$, which are consistent with size predictions. In other words, the replacement of Az^+ in the 6H-structured solid solutions favours the cation of similar size (FA^+) rather than the smaller cation (MA^+).

Annealing is reported to be a common method in perovskite device fabrication, which initiates and accelerates perovskite formation, removes residual solvent, and improves crystal growth.[33] These benefits result from interdiffusion and reorganization induced by the temperature. Samples in the two-phase region obtained by both mechano- and precipitation syntheses were kept in 100 °C (a commonly used annealing temperature[33,34]) for 5 hours. These heated samples were analysed by ^1H NMR spectra and PXRD and the results are shown in Figure **4.13**. The composition (actual x), phase fraction and lattice parameters of mechanosynthesised AzFA and AzMA perovskite samples in the two-phase region showed no significant change after heating. Similarly, the actual x, phase fraction and lattice parameters of the corresponding precipitation synthesised AzFA- and AzMA-containing perovskite samples did not vary (within error). Presumably, these perovskite samples are stable at 100 °C and no interdiffusion was observed after 5 hours of heating.
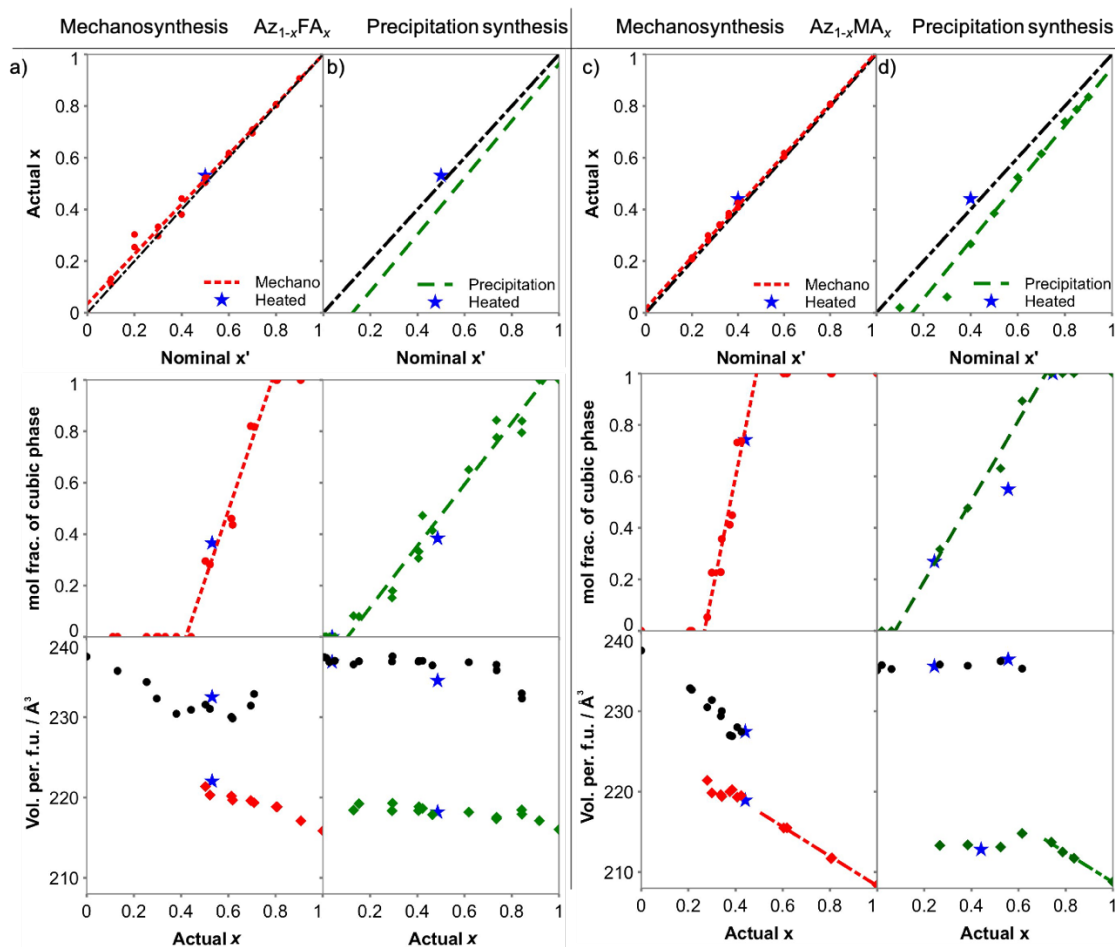
Figure 4.13. Nominal (x') and actual (x) MA^+/FA^+ cation content determined by ^1H NMR analysis, and mole fraction and cell volume (per formula unit) of hexagonal (6H) and cubic (3C) perovskite phases as determined by Rietveld refinement of PXRD data for heated (a, b) $Az_{1-x}FA_xPbBr_3$ and (c, d) $Az_{1-x}MA_xPbBr_3$ samples, prepared by (a, c) mechano- and (b, d) precipitation synthesis. The results from heated samples are marked with stars. Reproduced from Ref. 19 with permission. Copyright (2021) American Chemical Society.

4.2.6 $MA_{1-x}FA_xPbBr_3$ as a reference system

Both $MAPbBr_3$ and $FAPbBr_3$ adopt the cubic (3C) perovskite structure[6,24] and have been shown to form a complete solid solution and so can be used as a reference system for the synthesis routes described above. $MA_{1-x}FA_xPbBr_3$ has been studied by solution synthetic methods such as solution deposition[35] and LARP.[36] For instance, Slimi et al.[35] dissolved

MABr/FABr in DMF solution and synthesised $MA_{1-x}FA_xPbBr_3$ by spin-coating these solutions onto ITO substrates; the lattice parameters of the $MA_{1-x}FA_xPbBr_3$ thin films showed a systematic linear decrease with increasing nominal MA content (Figure **4.14**), although A-cation compositions were not studied. A complete solid solution of cubic phase was found for $MA_{1-x}FA_xPbBr_3$, however, the presence of a very small amount of $PbBr_2$ was found in PXRD for nearly equimolar fraction composition ($x = 0.4 – 0.6$) and its presence was explained with competitive formation of MA/FA perovskite. The influence of the presence of $PbBr_2$ on perovskite cation composition is unclear.
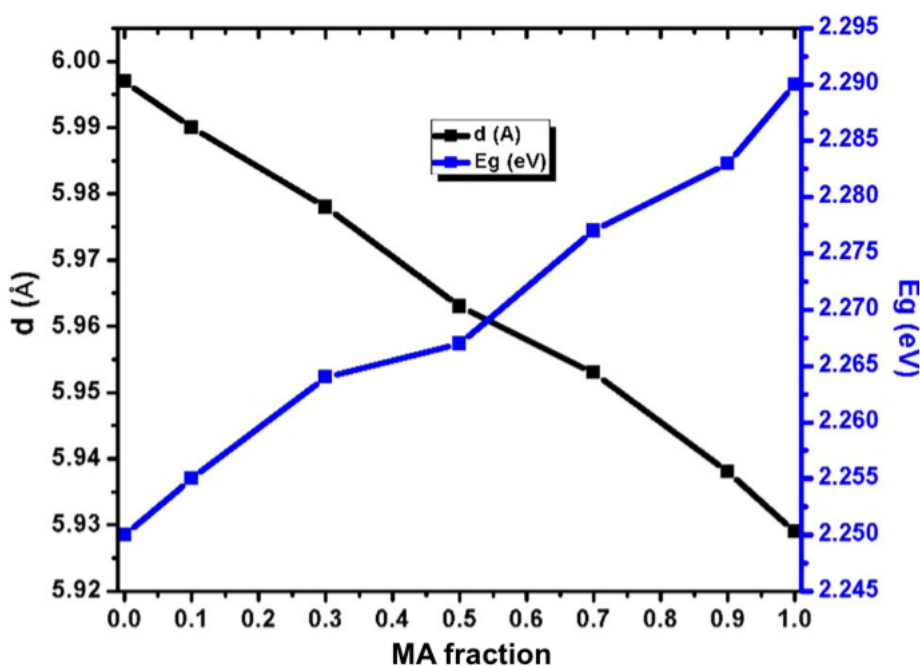

Figure 4.14. Interplanar *d*-spacing (lattice parameter *a*) and bandgap as a function of (nominal) MA content of $MA_{1-x}FA_xPbBr_3$ thin films. Adapted from Ref. 35 with permission.

To further study the competitive solid solution formation and actual cation composition of products, similar synthesis protocols were applied (precipitation and grinding) to the $MA_{1-x}FA_x$ system ($0 \leq x \leq 1$). The compositional analysis of $MA_{1-x}FA_xPbBr_3$, shows $x \approx x'$ for both synthetic routes (Figure **4.15a** and **4.15b**). As shown in Figure **4.16**, no presence of $PbBr_2$ was observed in the PXRD of $MA_{1-x}FA_xPbBr_3$, even at the composition with nearly equimolar fraction ($x = 0.4, 0.6$). Rietveld refinement of PXRD data shows

that the cell volume varies linearly as a function of actual x (Figure **4.15c**). The linear fit of lattice parameters as a function of FA cation content shows a similar dependence for samples obtained from both synthetic routes. These results suggest a complete solid solution of $MA_{1-x}FA_xPbBr_3$, which is presumably due to the reasonably similar size of A-site cations ($r_{FA} = 253$ pm and $r_{MA} = 217$ pm[21]) and isostructural (3C) end members. Importantly, no compositional mismatch was observed regardless of synthetic route.

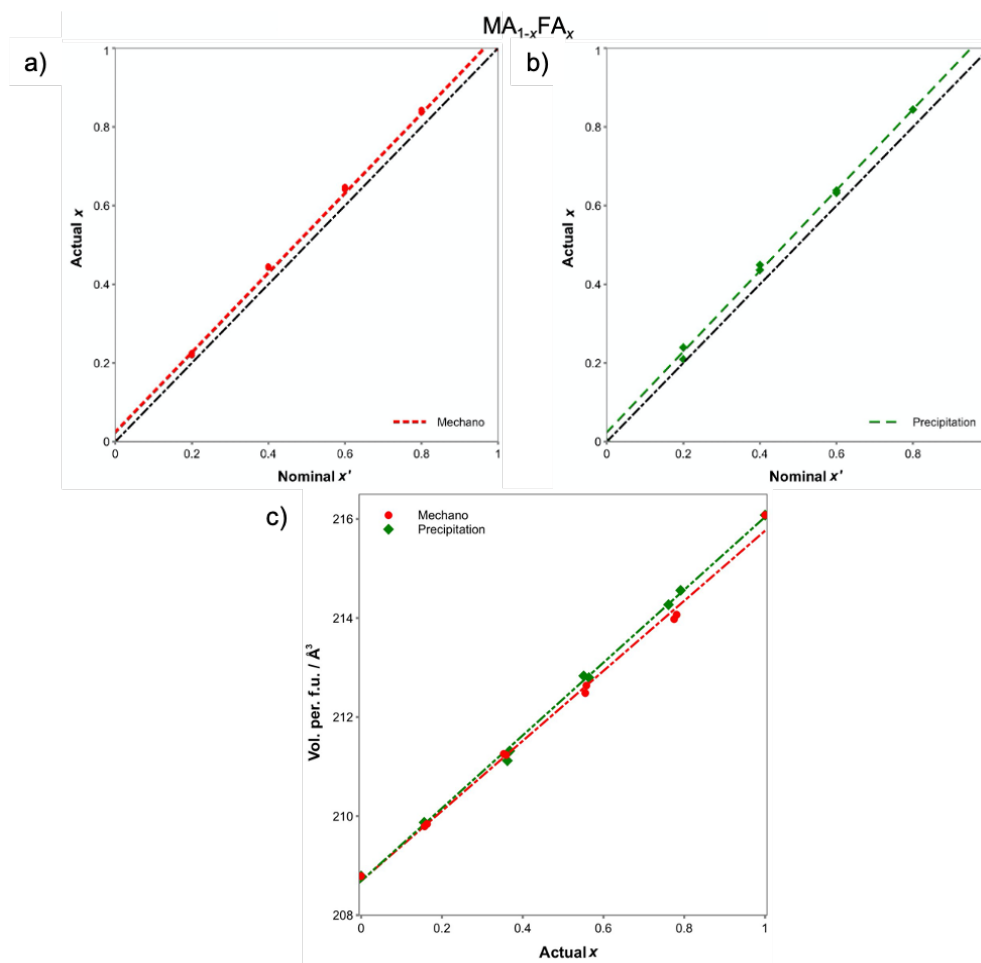**Figure 4.15.** The comparison of nominal (x') and actual (x) FA^+ content determined by NMR in $MA_{1-x}FA_xPbBr_3$ prepared by (a) mechanosynthesis (b) precipitation synthesis. Dash lines are linear fit to the actual values and black dot-dash lines represent $x' = x$ composition for comparison (c) unit cell volume of 3C perovskite phase as determined by Rietveld refinement of PXRD data for $MA_{1-x}FA_xPbBr_3$ samples prepared by mechano- (circles) and precipitation synthesis (diamonds). The dash-dot lines and dash-dot-dot lines are fit of unit cell volume with actual x of mechano- and precipitation samples. Adapted from Ref. 19 with permission. Copyright (2021) American Chemical Society.
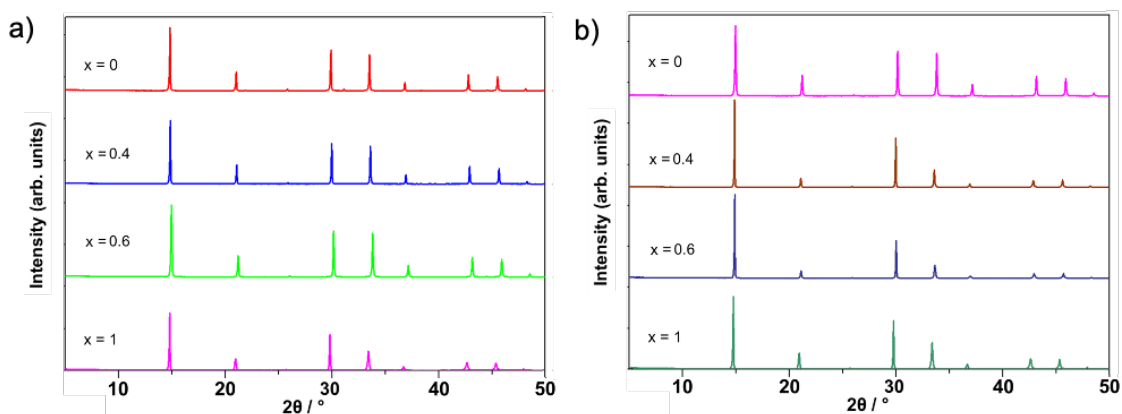
Figure 4.16. PXRD data of $MA_{1-x}FA_xPbBr_3$ samples obtained from (a) mechanosynthesis and (b) precipitation synthesis.

4.3 Optical properties of mixed cation perovskite

The optical properties of the solid solutions/two-phase mixtures of $Az_{1-x}FA_xPbBr_3$ and $Az_{1-x}MA_xPbBr_3$ samples were studied by absorption spectroscopy (Figure **4.17**). Regardless of how the $Az_{1-x}FA_xPbBr_3$ samples were synthesised (Figure **4.17a** and **4.17b**), the absorption onsets are systematically red-shifted with increasing FA^+. Optical measurements indicate that the absorption edge for the 6H solid solution samples $Az_{1-y}FA_yPbBr_3$, obtained from the mechanosynthesis is red-shifted from ca. 440 nm ($AzPbBr_3$) to ca. 540 nm ($y = 0.38$). The absorption edge of $Az_{0.62}FA_{0.38}PbBr_3$ is relatively close to that of $FAPbBr_3$ (585 nm). As the solid-state absorption spectra is surface sensitive, the shifted absorption edge at such composition may be due to the presence of some 3C crystallites formed at the surface, the amount of which is insufficient to be detected by PXRD. Moreover, the absorption edge for the 6H solid solution samples obtained from the precipitation synthesis remains invariant at ca. 440 nm ($0 \leq y \leq 0.051$). By contrast, the 3C solid solution, $Az_zFA_{1-z}PbBr_3$, from both syntheses shows a blue-shift from ca. 585 nm ($FAPbBr_3$) to ca. 565 nm ($z = 0.20$, mechanosynthesis) and ca. 576 nm ($z = 0.08$, precipitation synthesis), respectively. In the two-phase region ($0.10 \leq x \leq 0.94$) of the precipitation synthesised samples, the low volume fraction of the 6H phase for $0.62 \leq x \leq 0.74$ (Figure **4.9b**) means that the absorption is dominated by the 3C component and the absorption edge remains around 560 nm. For the $0.14 \leq x < 0.62$ compositions, which

have a significant phase fraction of both 6H and 3C, two absorption edges were observed corresponding to each phase (6H ~470 nm; 3C ~ 560 nm).
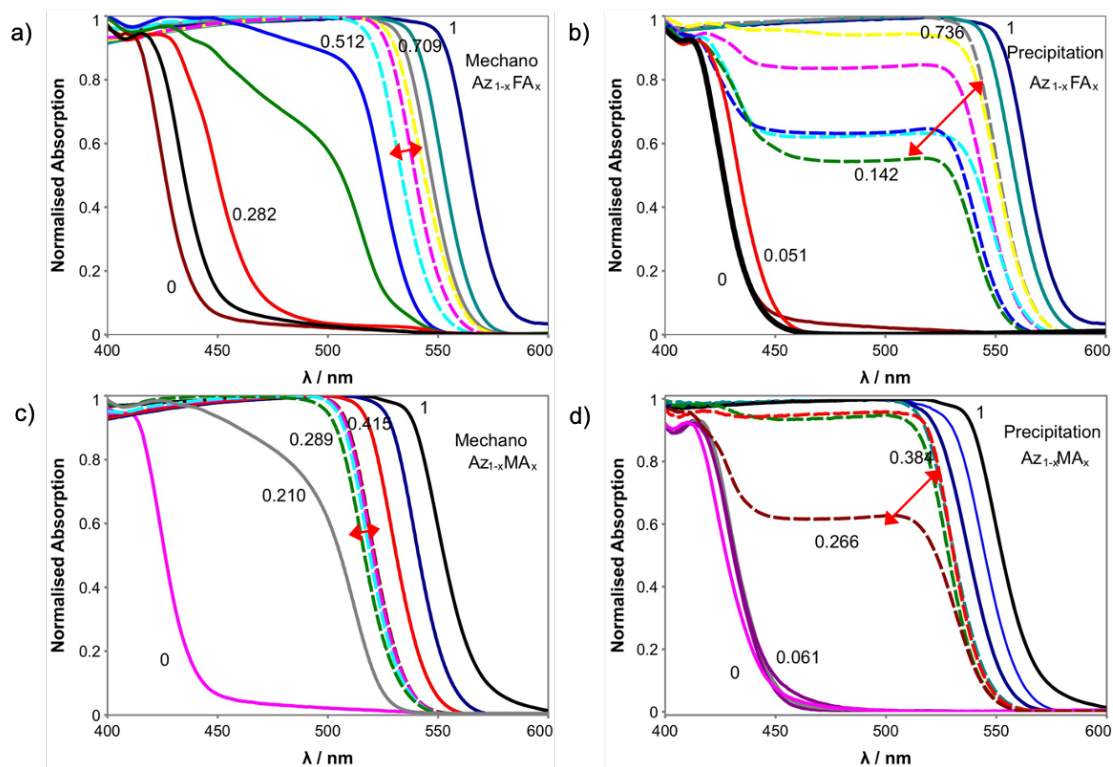

Figure 4.17. Absorption spectra of $Az_{1-x}FA_xPbBr_3$ samples prepared by (a) mechanosynthesis and (b) precipitation synthesis. Absorption spectra of $Az_{1-x}MA_xPbBr_3$ samples prepared by (c) mechanosynthesis and (d) precipitation synthesis. Spectra from single phase (solid solution) compositions as determined by PXRD are plotted with solid lines. Multi-phase samples are plotted with dashed lines and are also marked with arrows. Adapted from Ref. 19 with permission. Copyright (2021) American Chemical Society.

The absorption spectra of the corresponding $Az_{1-x}MA_x$ samples are shown in Figures **4.17c** and **4.17d** as a comparison, and show a similar absorption edge shift as a function of x. For precipitation synthesised samples, optical measurements (Figure **4.17d**) indicate that the absorption edge for the 6H solid solution $Az_{1-y}MA_yPbBr_3$ ($0 \leq y \leq 0.061$) is rather invariant at around 450 nm. By contrast, the 3C solid solution $Az_zMA_{1-z}PbBr_3$ from both syntheses, shows a blue-shift from ca. 575 nm (MAPbBr₃) to ca. 550 nm ($z = 0.51$,

mechanosynthesis) and ca. 560 nm ($z = 0.29$, precipitation synthesis), respectively. In the two-phase region ($0.07 \leq x \leq 0.71$) of the precipitation synthesised samples, the absorption is dominated by the 3C component and the absorption edge remains around 540 nm, even for the two-phase mixture. For the $x = 0.27$ composition, which has a significant phase fraction of both 6H and 3C, a similar feature to $Az_{1-x}FA_xPbBr_3$ was observed where two absorption edges appear, which correspond to each phase (6H ~450 nm; 3C ~ 540 nm).

4.3.1 Bandgap variation in mixed cation perovskites

The bandgap (E_g) values calculated from the onset of the absorption spectra from both $Az_{1-x}FA_x$ and $Az_{1-x}MA_x$ samples are shown in Figures **4.18a and 4.18b**. The bandgap of the $Az_{1-x}FA_x$ samples in the 6H solid solution region shows a nonlinear character which can be rationalised in terms of the bowing effect,[23,37] where a smaller bandgap was obtained for the intermediate composition of solid solutions than expected from linear interpolation of the end member values. Bandgap bowing is often fitted to a second order polynomial to account for the divergence from linearity, with a bowing parameter b as the binominal coefficient of the fitting equation:[37]

$$E_g(x) = (1 - x)E_{g|(x=0)} + xE_{g|(x=1)} - bx(1 - x) \qquad \text{(Equation 4.2)}$$

The bowing parameters of the mechanosynthesised mixed cation $Az_{1-x}FA_xPbBr_3$ is 0.94 with a goodness-of-fit R^2 value of 0.944. The bandgaps of $Az_{1-x}MA_x$ samples and the precipitation synthesised $Az_{1-x}FA_x$ samples show a linearly progressive increase with increasing Az content (decreasing x) in both the 3C solid solution and two-phase region. Bandgaps of $MA_{1-x}FA_x$ samples are also included in Figure **4.18c** for comparison. Both precipitation and mechanosynthesised samples display a similar trend of slightly decreasing bandgap with increasing MA substitution. This trend is due to the unit cell expansion as a result of variation of the Pb-Br bond, with varying A-cation size as discussed in Chapter 3. The bandgap of $MA_{1-x}FA_xPbBr_3$ has been reported with a nearly linear relationship with MA composition within a short range (2.25 – 2.29 eV, Figure **4.14**).[35] A slightly larger bandgap variation is observed here (2.14 – 2.20 eV).
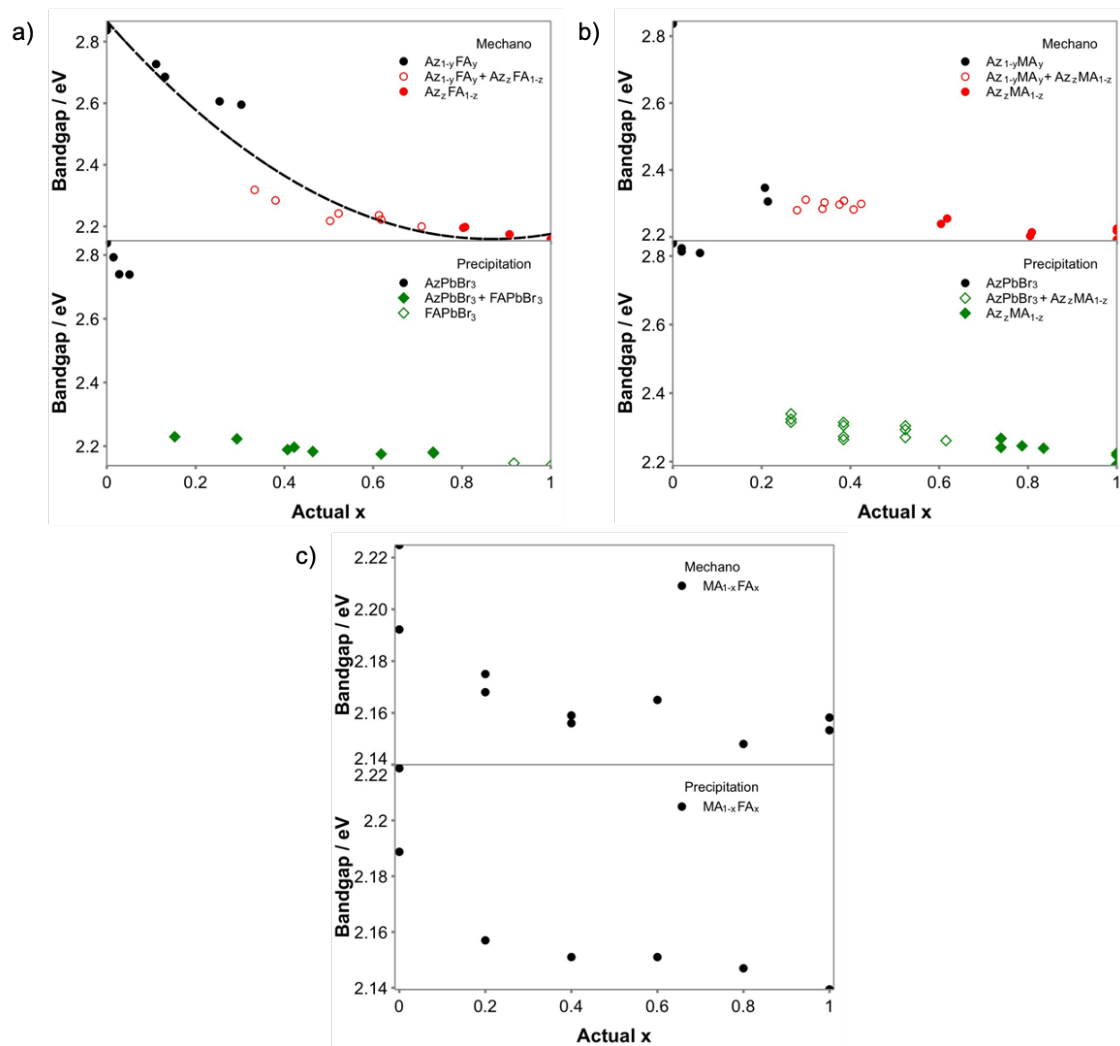
Figure 4.18. Bandgap determined from the absorption spectra of (a) $Az_{1-x}FA_xPbBr_3$ (b) $Az_{1-x}MA_xPbBr_3$ and (c) $MA_{1-x}FA_xPbBr_3$ synthesised from both mechano- and precipitation synthesis. Adapted from Ref. 19 with permission. Copyright (2021) American Chemical Society.

4.4 Conclusion

Solid solution formation in the systems $Az_{1-x}FA_xPbBr_3$ and $Az_{1-x}MA_xPbBr_3$ ($0 \leq x \leq 1$) was explored using both mechano- and precipitation syntheses. For samples obtained from the precipitation synthesis, the actual FA% or MA% in the precipitate was found to be less than the nominal composition in the reaction solution as a result of different precipitation rates of 3C and 6H perovskite polytypes. No such composition mismatch

was found for mechanosynthesised samples. A 3C-6H two-phase region was found to be present for $0.42 \leq x \leq 0.79$ and $0.10 \leq x \leq 0.94$, for mechano- and precipitation synthesis of $Az_{1-x}FA_xPbBr_3$, respectively; the two-phase region for mechanosynthesised and precipitation synthesised $Az_{1-x}MA_xPbBr_3$ appeared for $0.27 \leq x \leq 0.49$ and $0.07 \leq x \leq 0.71$. The cell volume as a function of the composition (volume increases with increasing Az^+ content) in both 6H (Az-rich) and 3C (FA-rich) solid solution regions suggests the Az^+ cation is actually larger than FA^+, which is incongruent to the cation size reported in the literature.[21,22] Under the assumption of Vegard's law, the cation radius of Az^+ is estimated to be ~310 pm and therefore the tolerance factor of $AzPbBr_3$ is 1.14, which is consistent with the fact that it forms a 6H hexagonal perovskite rather than a cubic perovskite. By comparison, in the 3C solid solution regions (Az-poor), the solid solution range in $Az_zFA_{1-z}PbBr_3$ is surprisingly smaller than in $Az_zMA_{1-z}PbBr_3$, given that MA^+ is much smaller than FA^+. This suggests that the extent of the single-phase solid solution of halide perovskites is dependent only on the average A-cation size, while the size mismatch is less of an influence, in contrast to solid solution formation observed in oxide perovskites. Overall, the work in this chapter reveals the importance of cross-checking the nominal (reaction) with the actual (product) composition, especially when the synthetic method may be under kinetic control or multi-phases can be formed in the system. When doping larger A-site organic cations in OIHPs, the average A-cation radius might be used as a guide to prevent unwanted phase separation. The computed size of organic cations and the presence of any dynamic/preferential bonding effects should be re-examined and considered during study of OIHP systems.

References

(1)   Stoumpos, C. C.; Malliakas, C. D.; Kanatzidis, M. G. Semiconducting Tin and Lead Iodide Perovskites with Organic Cations: Phase Transitions, High Mobilities, and near-Infrared Photoluminescent Properties. *Inorg. Chem.* **2013**, *52* (15), 9019–9038.

(2)   Prochowicz, D.; Yadav, P.; Saliba, M.; Saski, M.; Zakeeruddin, S. M.; Lewiński, J.; Grätzel, M. Mechanosynthesis of Pure Phase Mixed-Cation MA: XFA1- XPbI3 Hybrid Perovskites: Photovoltaic Performance and Electrochemical Properties. *Sustain. Energy Fuels* **2017**, *1* (4), 689–693.

(3)   Azam, M.; Yue, S.; Xu, R.; Liu, K.; Ren, K.; Sun, Y.; Liu, J.; Wang, Z.; Qu, S.; Lei, Y.; et al. Highly Efficient Solar Cells Based on Cl Incorporated Tri-Cation Perovskite Materials. *J. Mater. Chem. A* **2018**, *6* (28), 13725–13734.

(4)   Saliba, M.; Matsui, T.; Domanski, K.; Seo, J.-Y.; Ummadisingu, A.; Zakeeruddin, S. M.; Correa-Baena, J.-P.; Tress, W. R.; Abate, A.; Hagfeldt, A.; et al. Incorporation of Rubidium Cations into Perovskite Solar Cells Improves Photovoltaic Performance. *Science (80-.).* **2016**, *354* (6309), 206–209.

(5)   Hanusch, F. C.; Wiesenmayer, E.; Mankel, E.; Binek, A.; Angloher, P.; Fraunhofer, C.; Giesbrecht, N.; Feckl, J. M.; Jaegermann, W.; Johrendt, D.; et al. Efficient Planar Heterojunction Perovskite Solar Cells Based on Formamidinium Lead Bromide. *J. Phys. Chem. Lett.* **2014**, *5* (16), 2791–2795.

(6)   Tian, J.; Cordes, D. B.; Quarti, C.; Beljonne, D.; Slawin, A. M. Z.; Zysman-Colman, E.; Morrison, F. D. Stable 6H Organic-Inorganic Hybrid Lead Perovskite and Competitive Formation of 6H and 3C Perovskite Structure with Mixed A Cations. *ACS Appl. Energy Mater.* **2019**, *2* (8), 5427–5437.

(7)   Shi, D.; Adinolfi, V.; Comin, R.; Yuan, M.; Alarousu, E.; Buin, A.; Chen, Y.; Hoogland, S.; Rothenberger, A.; Katsiev, K.; et al. Solar Cells. Low Trap-State Density and Long Carrier Diffusion in Organolead Trihalide Perovskite Single Crystals. *Science* **2015**, *347* (6221), 519–522.

(8)   Liu, J.; Han, Q.; Bai, Y.; Du, K. Z.; Li, T.; Ji, D.; Zhou, Y.; Cao, C.; Shin, D.; Ding, J.; et al. Additive Engineering for High-Performance Room-Temperature-

Processed Perovskite Absorbers with Micron-Size Grains and Microsecond-Range Carrier Lifetimes. *Energy Environ. Sci.* **2017**, *10* (11), 2365–2371.

(9)   Martínez-Sarti, L.; Palazon, F.; Sessolo, M.; Bolink, H. J. Dry Mechanochemical Synthesis of Highly Luminescent, Blue and Green Hybrid Perovskite Solids. *Adv. Opt. Mater.* **2020**, *8* (4), 1901494.

(10)   Chen, D.; Li, J.; Chen, X.; Chen, J.; Zhong, J. Grinding Synthesis of APbX$_3$ (A = MA, FA, Cs; X = Cl, Br, I) Perovskite Nanocrystals. *ACS Appl. Mater. Interfaces* **2019**, *11* (10), 10059–10067.

(11)   Abdelhady, A. L.; Saidaminov, M. I.; Murali, B.; Adinolfi, V.; Voznyy, O.; Katsiev, K.; Alarousu, E.; Comin, R.; Dursun, I.; Sinatra, L.; et al. Heterovalent Dopant Incorporation for Bandgap and Type Engineering of Perovskite Crystals. *J. Phys. Chem. Lett.* **2016**, *7* (2), 295–301.

(12)   Zhang, Z.; Ren, L.; Yan, H.; Guo, S.; Wang, S.; Wang, M.; Jin, K. Bandgap Narrowing in Bi-Doped CH$_3$NH$_3$PbCl$_3$ Perovskite Single Crystals and Thin Films. *J. Phys. Chem. C* **2017**, *121* (32), 17436–17441.

(13)   Ng, M.; Halpert, J. E. Single Crystals of Mixed Br/Cl and Sn-Doped Formamidinium Lead Halide Perovskites *via* Inverse Temperature Crystallization. *RSC Adv.* **2020**, *10* (7), 3832–3836.

(14)   Nayak, P. K.; Sendner, M.; Wenger, B.; Wang, Z.; Sharma, K.; Ramadan, A. J.; Lovrinčić, R.; Pucci, A.; Madhu, P. K.; Snaith, H. J. Impact of Bi^{3+} Heterovalent Doping in Organic–Inorganic Metal Halide Perovskite Crystals. *J. Am. Chem. Soc.* **2018**, *140* (2), 574–577.

(15)   van der Stam, W.; Geuchies, J. J.; Altantzis, T.; van den Bos, K. H. W.; Meeldijk, J. D.; Van Aert, S.; Bals, S.; Vanmaekelbergh, D.; de Mello Donega, C. Highly Emissive Divalent-Ion-Doped Colloidal CsPb$_{1–x}$M$_x$Br$_3$ Perovskite Nanocrystals through Cation Exchange. *J. Am. Chem. Soc.* **2017**, *139* (11), 4087–4097.

(16)   Spanopoulos, I.; Ke, W.; Stoumpos, C. C.; Schueller, E. C.; Kontsevoi, O. Y.; Seshadri, R.; Kanatzidis, M. G. Unraveling the Chemical Nature of the 3D "Hollow" Hybrid Halide Perovskites. *J. Am. Chem. Soc.* **2018**, *140* (17), 5728–5742.

(17) Weber, O. J.; Charles, B.; Weller, M. T. Phase Behaviour and Composition in the Formamidinium-Methylammonium Hybrid Lead Iodide Perovskite Solid Solution. *J. Mater. Chem. A* **2016**, *4* (40), 15375–15382.

(18) Ito, N.; Kamarudin, M. A.; Hirotani, D.; Zhang, Y.; Shen, Q.; Ogomi, Y.; Iikubo, S.; Minemoto, T.; Yoshino, K.; Hayase, S. Mixed Sn–Ge Perovskite for Enhanced Perovskite Solar Cell Performance in Air. *J. Phys. Chem. Lett.* **2018**, *9* (7), 1682–1688.

(19) Tian, J.; Zysman-Colman, E.; Morrison, F. D. Compositional Variation in Hybrid Organic–Inorganic Lead Halide Perovskites: Kinetically versus Thermodynamically Controlled Synthesis. *Chem. Mater.* **2021**, acs.chemmater.1c00470.

(20) Langford, J. I.; Wilson, A. J. C. Scherrer after Sixty Years: A Survey and Some New Results in the Determination of Crystallite Size. *J. Appl. Crystallogr.* **1978**, *11* (2), 102–113.

(21) Kieslich, G.; Sun, S.; Cheetham, A. K.; Cheetham, T.; Gregor, K.; Shijing, S.; Anthony, K. C. Solid-State Principles Applied to Organic-Inorganic Perovskites: New Tricks for an Old Dog. *Chem. Sci.* **2014**, *5* (12), 4712–4715.

(22) Becker, M.; Klüner, T.; Wark, M. Formation of Hybrid ABX_3 Perovskite Compounds for Solar Cell Application: First-Principles Calculations of Effective Ionic Radii and Determination of Tolerance Factors. *Dalt. Trans.* **2017**, *46* (11), 3500–3509.

(23) Lee, S.; Levi, R. D.; Qu, W.; Lee, S. C.; Randall, C. A. Band-Gap Nonlinearity in Perovskite Structured Solid Solutions. *J. Appl. Phys.* **2010**, *107* (2), 1–6.

(24) Schueller, E. C.; Laurita, G.; Fabini, D. H.; Stoumpos, C. C.; Kanatzidis, M. G.; Seshadri, R. Crystal Structure Evolution and Notable Thermal Expansion in Hybrid Perovskites Formamidinium Tin Iodide and Formamidinium Lead Bromide. *Inorg. Chem.* **2018**, *57* (2), 695–701.

(25) Janghorban, K.; Kirkaldy, J. S.; Weatherly, G. C. The Hume-Rothery Size Rule and Double-Well Microstructures in Gold-Nickel. *J. Phys. Condens. Matter* **2001**, *13* (38), 8661–8676.

(26) Shannon, R. D. Revised Effective Ionic Radii and Systematic Studies of Interatomic Distances in Halides and Chalcogenides. *Acta Crystallogr. Sect. A* **1976**, *32* (5), 751–767.

(27) Mitsui, T.; Westphal, W. B. Dielectric and X-Ray Studies of $Ca_xBa_{1-x}TiO_3$ and $Ca_xSr_{1-x}TiO_3$. *Phys. Rev.* **1961**, *124* (5), 1354–1359.

(28) Basmajian, J. A.; DeVries, R. C. Phase Equilibria in the System $BaTiO_3$–$SrTiO_3$. *J. Am. Ceram. Soc.* **1957**, *40* (11), 373–376.

(29) Sinclair, D. C.; Paul Attfield, J. The Influence of A-Cation Disorder on the Curie Temperature of Ferroelectric $ATiO_3$ Perovskites. *Chem. Commun.* **1999**, No. 16, 1497–1498.

(30) DeVRIES, R. C.; ROY, R. Phase Equilibria in the System $BaTiO_3$-$CaTiO_3$. *J. Am. Ceram. Soc.* **1955**, *38* (4), 142–146.

(31) Li, W.; Wang, Z.; Deschler, F.; Gao, S.; Friend, R. H.; Cheetham, A. K. Chemically Diverse and Multifunctional Hybrid Organic-Inorganic Perovskites. *Nat. Rev. Mater.* **2017**, *2* (3), 1–18.

(32) Yang, H.; Ohishi, Y.; Kurosaki, K.; Muta, H.; Yamanaka, S. Thermomechanical Properties of Calcium Series Perovskite-Type Oxides. *J. Alloys Compd.* **2010**, *504* (1), 201–204.

(33) Mohd Yusoff, A. R. Bin; Gao, P.; Nazeeruddin, M. K. Recent Progress in Organohalide Lead Perovskites for Photovoltaic and Optoelectronic Applications. *Coord. Chem. Rev.* **2018**, *373*, 258–294.

(34) Cao, M.; Tian, J.; Cai, Z.; Peng, L.; Yang, L.; Wei, D. Perovskite Heterojunction Based on $CH_3NH_3PbBr_3$ Single Crystal for High-Sensitive Self-Powered Photodetector. *Appl. Phys. Lett.* **2016**, *109* (23), 233303.

(35) Slimi, B.; Mollar, M.; Marí, B.; Chtourou, R. Thin Film of Perovskite (Mixed-Cation of Lead Bromide $FA_{1-x}MA_xPbBr$) Obtained by One-Step Method. *J. Electron. Mater.* **2019**, *48* (12), 8014–8023.

(36) Mei, G.; Zhang, Y.; Xu, B.; Liu, H.; Zhong, J.; Shi, K.; Sun, X. W.; Wang, K. Bright and Efficient Light-Emitting Diodes Based on Perovskite Quantum Dots with Formamidine-Methylamine Hybrid Cations. *J. Phys. D. Appl. Phys.* **2018**, *51*

(45), 454003.

(37) Chatterjee, S.; Payne, J.; Irvine, J. T. S.; Pal, A. J. Bandgap Bowing in a Zero-Dimensional Hybrid Halide Perovskite Derivative: Spin-Orbit Coupling: Versus Lattice Strain. *J. Mater. Chem. A* **2020**, *8* (8), 4416–4427.

Chapter 5

Exploring mixed-halide perovskite with azetidinium
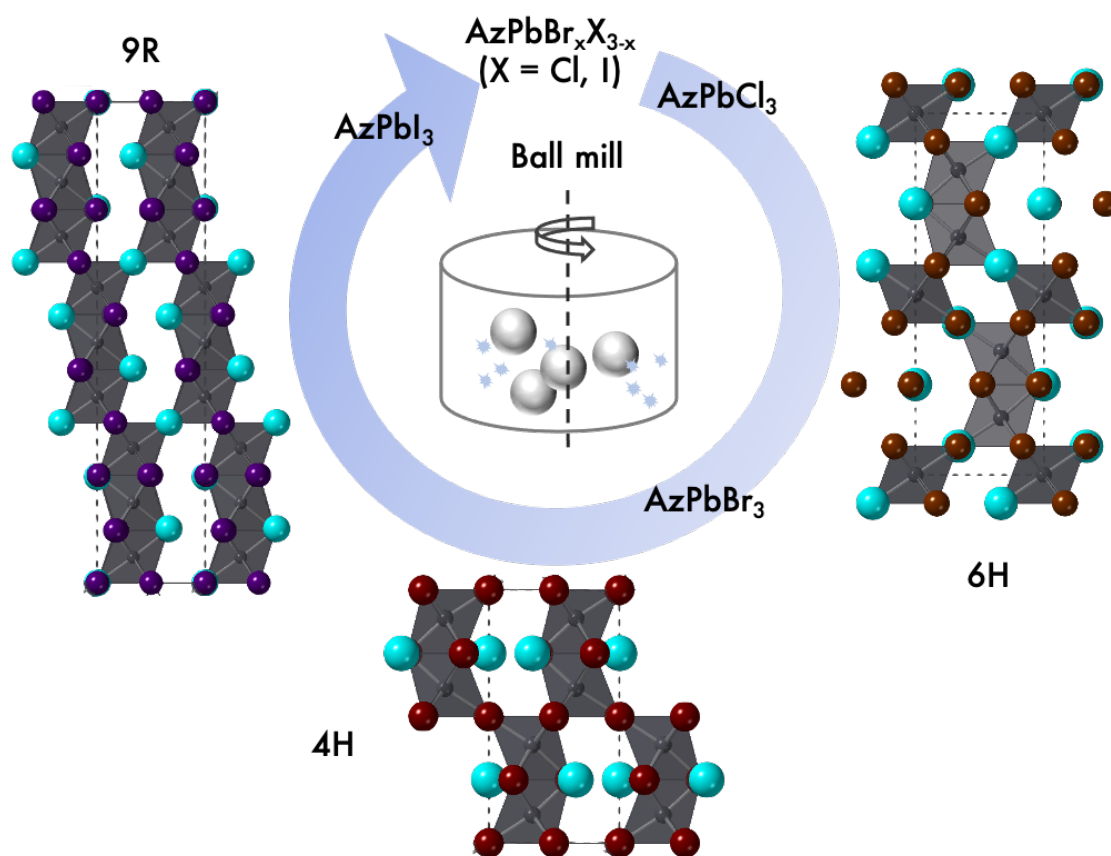
Cover picture: TOC graphic of publication arising from this chapter

5.1 Introduction

In Chapter 4, the bandgaps of Az-based OIHPs were tuned using mixed cations at the A-site - $Az_{1-x}FA_xPbBr_3$ and $Az_{1-x}MA_xPbBr_3$ ($0 \leq x \leq 1$). Due to partial solid solution formation, the scope for bandgap tuning with A-site substitution is limited, especially in the 6H-rich single-phase region (Figure **4.18**). Mixing halide is likely much more effective for bandgap tuning due to the changes in Pb-X orbital interactions.[1–4] Noh *et al.*[4] reported a linear relationship between Br content, and the lattice parameters and corresponding bandgap in the $MAPbBr_xI_{3-x}$ perovskite. Chen *et al.*[2] reported a grinding synthesis of $APbX_3$ (A = MA or FA, X = Cl, Br, I) nanocrystals, the emission maxima of which shifted from 400 nm (3.10 eV) to 780 nm (1.59 eV) with the halide changing from I to Cl, as the band structure of $APbX_3$ has a strong dependence on halide electronic energies.

The 6H $AzPbBr_3$ has been discussed in Chapter 3 and Panetta *et al.*[5] determined the structure of $AzPbI_3$ as the 9R rhombohedral perovskite polytype. The assumption is that the formation of either solid solutions or different structures are feasible in Az mixed halide perovskites considering the reported mixed halide perovskite compounds in other systems. For example, Gratia *et al.*[3] reported a mixed halide/cation composition with a progressive structural change from 2H, 4H and 6H to 3C depending on x in $(FAPbI_3)_x(MAPbBr_3)_{1-x}$. They reported the halide exchange drives the polytypic transformation. By comparison, a two-phase solid solutions region is reported for $MAPbBr_xI_{3-x}$ mixed halide perovskite while the crystal systems of the end members are cubic ($MAPbBr_3$) and tetragonal ($MAPbI_3$).[6] Mechanosynthesis is a solvent-free, environmentally friendly synthetic method, which has been reported as a simple and effective way to synthesise OIHPs.[7,8] In this chapter, mixed halide perovskites $AzPbBr_{3-x}X_x$ (X = Cl or I) were prepared by mechanosynthesis and their lattice parameters and optical absorption were analysed by PXRD and absorption spectra, respectively.

5.2 Mixed halide perovskites

5.2.1 Synthesis and PXRD analysis

The crystallisations of $AzPbCl_3$, $AzPbBr_{1.5}I_{1.5}$ and $AzPbI_3$ were carried out by slow diffusion of antisolvent DCM/acetonitrile/acetonitrile into DMSO, DMF/DSMO (4:1) and DMF/GBA (1:1) solution, respectively. $AzPbCl_3$ appears as white needle-like crystals, $AzPbBr_{1.5}I_{1.5}$ is bright yellow, and $AzPbI_3$ crystals are dark red. Stoichiometric amounts of dry AzCl and $PbCl_2$ were dissolved in DMSO and the anti-solvent DCM was slowly diffused into the perovskite/DMSO solution to obtain crystals suitable for SCXRD. $AzPbCl_3$ appears as white needle-like crystals. As AzI is not commercially available, AzI was synthesised by a two-step method: AzCl was deprotonated into azetidine, which was then reacted with HI. The crystals of AzI were white and needle-like, with a yield of 86 %. $AzPbCl_3$ powder was obtained by precipitation synthesis - stoichiometric AzCl was mixed with $PbCl_2$ in DMSO and precipitated with anti-solvent DCM. The precipitation synthesised $AzPbCl_3$ (confirmed by PXRD) was then used as the Cl source in the mechanosynthesis, as the purity of commercial AzCl was found to be < 90% (discussed below). The mechanosynthesis of $AzPbCl_xBr_{3-x}$ and $AzPbBr_xI_{3-x}$ ($0 \leq x \leq 3$) was carried out by mixing appropriate molar ratios of Az/halide source ($AzPbCl_3$, AzBr or AzI) and lead/halide source ($PbCl_2$, $PbBr_2$ or PbI_2) in the ball mill and grinding at 600 rpm for 1 hour. Detailed procedures are provided in Chapter 2.

While $AzPbCl_3$ was obtained by precipitation synthesis, $AzPbCl_xBr_{3-x}$ ($0 \leq x < 3$) samples were prepared by mechanosynthesis. The mechanosynthesis of Cl-containing samples was complicated by the purity of commercial AzCl, which is labelled by the manufacturer as below 95%. ^{1}H NMR analysis of the commercial AzCl is shown in Figure **5.1** and indicates it is not pure; elemental analysis indicated that the purity was actually below 90% (Calculated: C, 38.52; H, 8.62; N, 14.97; Cl, 37.89; Found: trial 1 - C, 34.30; H, 7.59; N, 12.23; trial 2 - 35.13; H, 8.05; N, 12.79). The purity issue of commercial AzCl was significant in mechanosynthesis and extra $PbCl_2$ peaks were found in the PXRD of the mechanosynthesised $AzPbCl_3$, which was obtained by mixing the stochiometric amounts of AzCl and $PbCl_2$ (Figure **5.2**). Excess AzCl ($PbCl_2$:AzCl = 1:1.3) was required for the mechanosynthesis of the single phase $AzPbCl_3$ as determined by PXRD; it cannot be excluded, however, that excess AzCl may remain but is not detectable by PXRD.

Recrystallisation of commercial AzCl was carried out by preparing a highly concentrated solution of AzCl in ethanol at 70 °C and slowly cooling it down to 0 °C, during which the crystals of AzCl precipitate. ^{1}H NMR spectra of the recrystallised AzCl samples (Figure **5.1**) indicated that it is possible to largely remove the impurities. However, the poor solubility of the samples in polar solvent (e.g. ethanol, acetone, methanol) and the similar solubility between samples and impurities in the solvent resulted in a low yield (< 10 %). Due to the difficulty in obtaining sufficient amounts (ca. 3 g) of recrystallised AzCl, it was not used as a precursor for the mechanosynthesis. Instead, $AzPbCl_3$ prepared by precipitation synthesis was used as the Cl source in the mechanosynthesis.
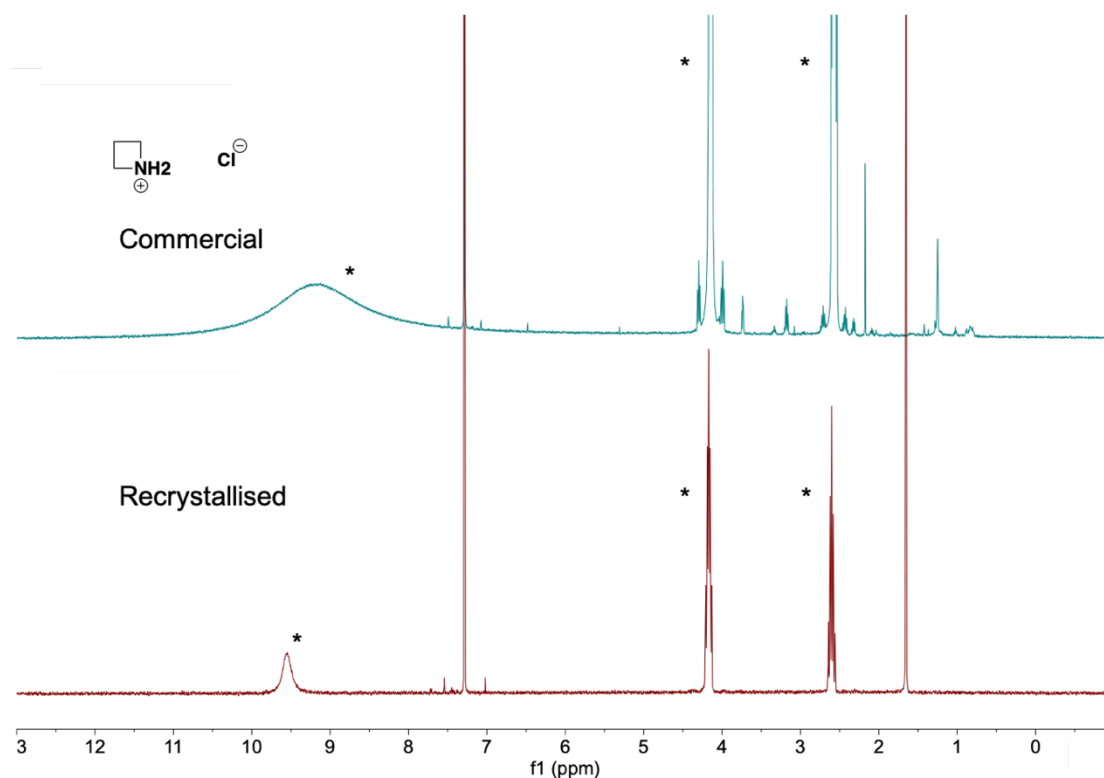

Figure 5.1. ^{1}H NMR spectra of commercial AzCl (top), and after recrystallisation (bottom) in *d*-chloroform. Characteristic peaks of Az are marked by *.
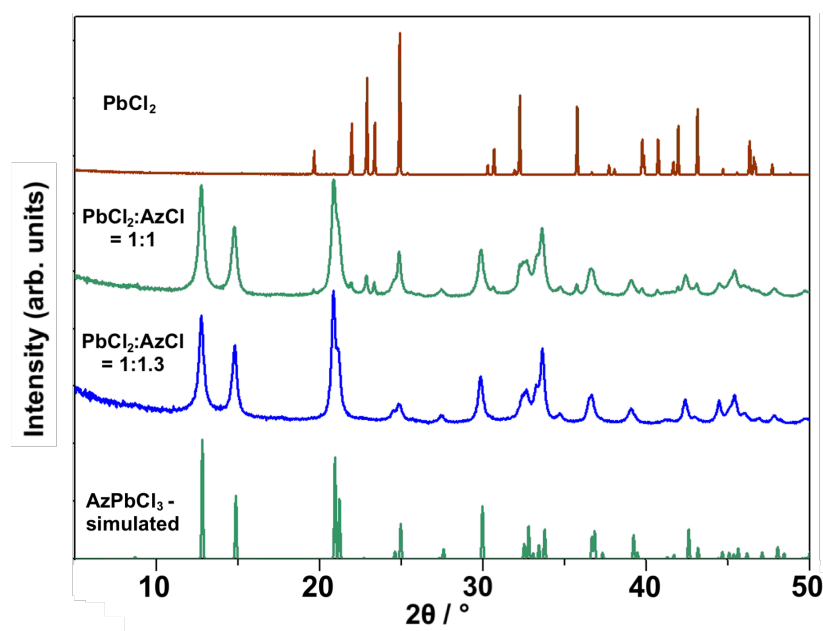
Figure 5.2. PXRD data of the commercial $PbCl_2$, mechanosynthesised $AzPbCl_3$ with $PbCl_2$:AzCl = 1:1 and 1:1.3, and the simulated reference patterns of $AzPbCl_3$ (determined by SCXRD). $PbCl_2$ peaks are clearly evident in $PbCl_2$:AzCl = 1:1 composition.

The colour progression (Figure **5.3a**) of the as-synthesised $AzPbCl_xBr_{3-x}$ is subtle and ranges from white ($AzPbCl_3$) to pale yellow ($AzPbBr_3$). The colours of the $AzPbBr_xI_{3-x}$ series show a clear systematic change from pale yellow ($AzPbBr_3$) to red-orange ($AzPbI_3$). The PXRD of the mixed halide perovskites are shown in Figures **5.3b** and **5.3c**. The PXRD of $AzPbCl_3$ shows the same 6H hexagonal structure as $AzPbBr_3$ (Chapter 3) while SCXRD confirms this 6H polytype (Figure **5.4**) with same $P6_3/mmc$ space group [PXRD: $a = 8.515(6)$ Å, $c = 20.44(9)$; SCRXD (293 K): $a = 8.5166(2)$ Å, $c = 20.4424(6)$ Å]. The PXRD of the Br-rich region show additional broad features in the base of the main peaks which are especially evident around $12 - 14°$. These features are similar to the PXRD of the mechanosynthesised $AzPbBr_3$ (Figure **3.1c**), which indicate the presence of multiple subpopulations of different sizes of 6H perovskite particles in those samples.

$AzPbI_3$ is reported as the 9R polytype[5] and the Rietveld refinement of the PXRD data for $AzPbI_3$ with the reported space group $R\bar{3}c$ results in a good fit of the peak positions and intensities (goodness-of-fit parameters: $\chi^2 = 1.545$, $wR_p = 0.056$), as shown in Figure **5.4**.
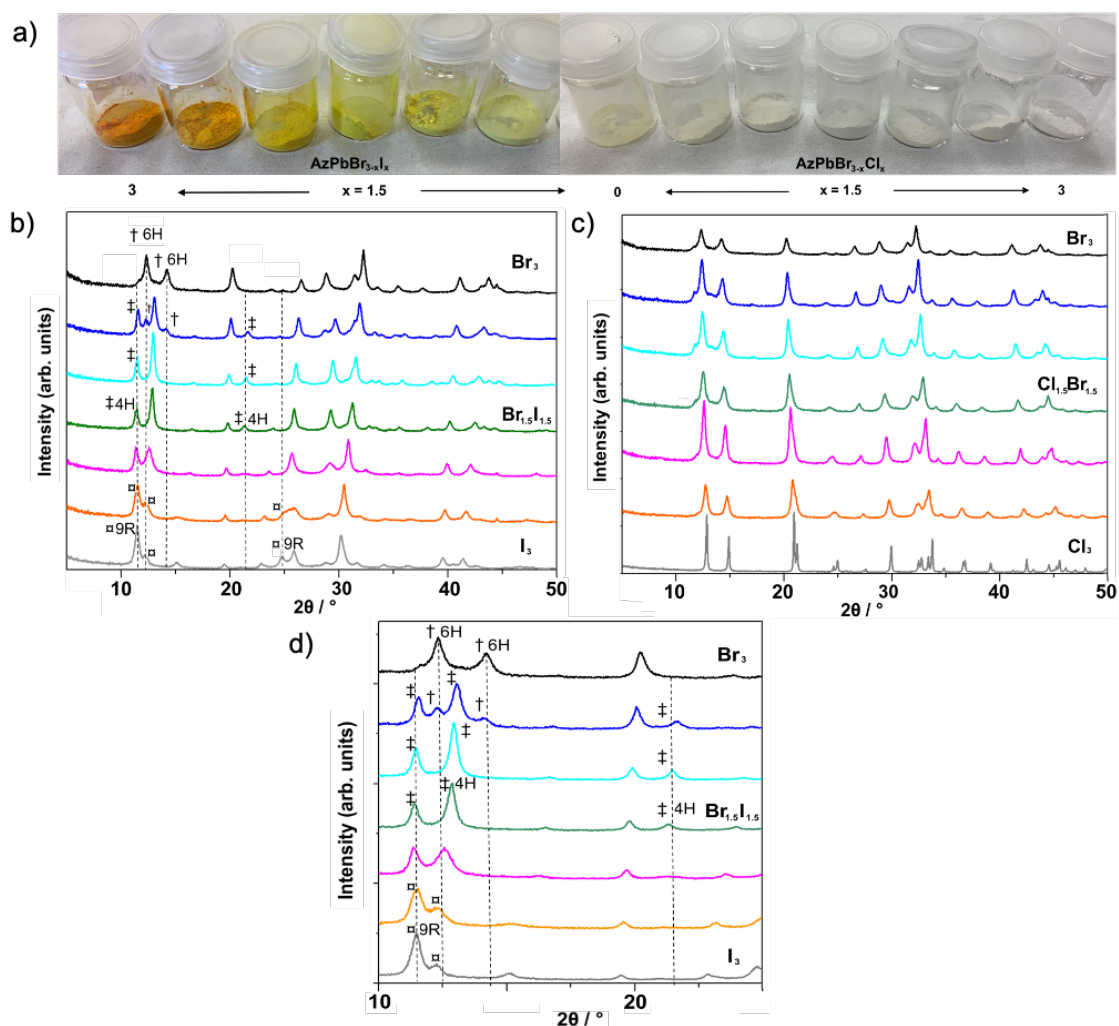
Figure 5.3. (a) Photos and (b, c, d) PXRD patterns of mixed halide perovskite: AzPbBr$_{3-x}$X$_x$ (X = Cl or I) with composition $0 \leq x \leq 3$ (in x = 0.5 increments) were prepared by mechanosynthesis, except AzPbCl$_3$ which was prepared by precipitation synthesis. ‡6H, †4H, ¤9R marks the peaks from the corresponding phases in the patterns.

This confirms that the 9R AzPbI$_3$ perovskite can also be obtained easily by mechanosynthesis compared with the reported two-step recrystallisation solution method.[5] This is also confirmed by SCXRD with lattice parameters being close to those seen in the refined PXRD data [SCXRD (293 K): a = 9.0835(5) Å, c = 35.104(3) Å; PXRD a = 9.101(1) Å, c = 35.00(2) Å]. Single phase perovskite samples (AzPbI$_3$ and AzPbCl$_3$) were re-examined by PXRD after being stored in air for 6 months and no visual or structural decomposition was observed (Figure **5.5**, PXRD of AzPbBr3 is in Figure **3.1**).
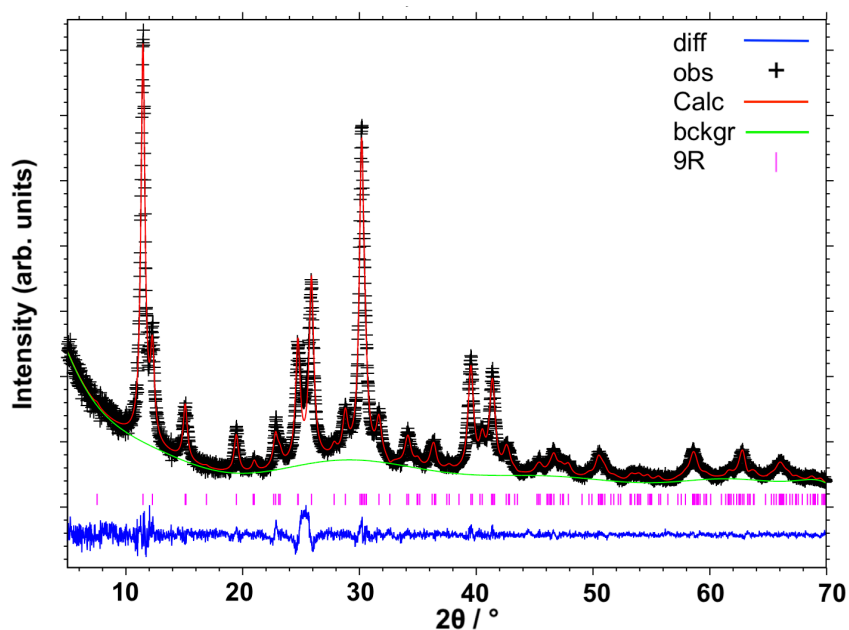
Figure 5.4. Rietveld refinement profile of PXRD data for AzPbI$_3$ refined in the 9R structure with observed data (cross), calculated data (red line), background (green line), reflection position (magenta bar) and difference plot (blue line). Goodness-of-fit parameters: $\chi^2 = 1.545$, $wR_p = 0.056$.
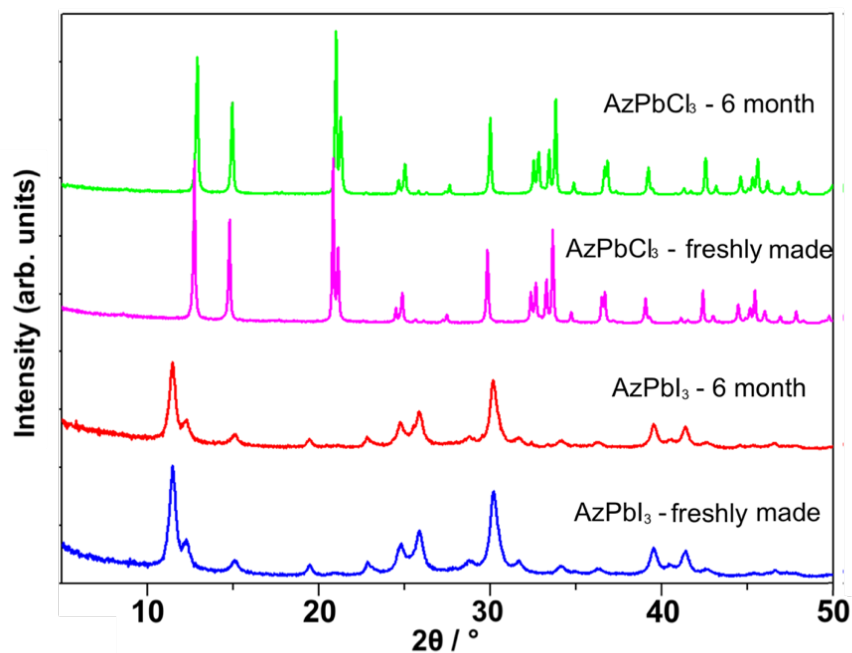

Figure 5.5. Comparison of PXRD patterns of freshly made mechanosynthesised AzPbCl$_3$ and AzPbI$_3$ samples, and again after storage in ambient air for 6 months.

5.2.1.1 Determination of the intermediate structure of AzPbBr$_x$I$_{3-x}$

The PXRD data of AzPbBr$_x$I$_{3-x}$ ($x \leq 2$) in Figure **5.3b** seem to indicate a structure that was neither 6H, 9R nor a two-phase mixture of these two polytypes. From the visual similarity of the PXRD patterns, it is assumed that the intermediate structure is also a perovskite polytype. The two most intense peaks, in the range 12° to 15°, are characteristic of both 6H (AzPbBr$_3$) and 9R (AzPbI$_3$) structures and have Miller indices (011)(012) and (01$\bar{1}$)(012), respectively. Assuming the Miller indices of two major peaks of the unknown intermediate phase might also be (010)(011) or (011)(012), analysis of the PXRD of AzPbBr$_{1.5}$I$_{1.5}$, and in particular the d-spacing of the two major peaks at 11.41° and 12.86°, is shown in Table **5.1**. Under the assumption of the intermediate structure being a hexagonal perovskite polytype, the average distance $\bar{c}$ between close packed layers of this phase should lie between those of AzPbBr$_3$ and AzPbI$_3$. While no reasonable factor could be found for $\bar{c}_{cal}$ using (011)(012) indexing, the average layer distance $\bar{c}_{cal}$ using (010)(011) indices when divided by 4, sits in the correct range: $\bar{c}_{cal} = c_{cal}/4 = 15.18 / 4 = 3.796$ Å compared with $\bar{c}$(AzPbBr$_3$) = 3.555 Å and $\bar{c}$(AzPbI$_3$) = 3.897 Å. Using the same (010)(011) indexing, a_{cal} = 8.956 Å also lies between a(AzPbBr$_3$) = 8.743 Å and a(AzPbI$_3$) = 9.085 Å. Thus, a 4H structure[9] with $P6_3/mmc$ space group is a likely candidate because the factor found for $\bar{c}_{cal}$ is 4.

Table 5.1. Lattice parameter calculation (c_{cal} and a_{cal}) using the two major peaks from the PXRD of AzPbBr$_{1.5}$I$_{1.5}$ and the lattice parameter from AzPbBr$_3$ and AzPbI$_3$ single crystals.

2θ (°)	d-spacing / Å	$(hkl)_1$	$(hkl)_2$	c_{cal} / Å	a_{cal} / Å		c / Å	a / Å	packing layer distance $\bar{c}$ / Å
11.41	7.756	011	012	26.30	9.373	AzPbBr$_3$	21.33	8.743	3.555
12.86	6.907	010	011	15.18	8.956	AzPbI$_3$	35.07	9.805	3.897

Note: d-spacing is calculated with the Bragg equation (Equation **2.1**), where X-ray wavelength is 1.5406 Å. $(hkl)_1$ and $(hkl)_2$ are the assumed Miller indices of the two major peaks from the PXRD of AzPbBr$_{1.5}$I$_{1.5}$.

A 4H structural MnPbBr$_{1.5}$I$_{1.5}$ model was constructed for Rietveld refinement, where Mn is used as a proxy for the Az cation as it has similar electron density. The different halide anions are randomly distributed across the anion sites. The goodness-of-fit parameters from the Rietveld refinement of AzPbBr$_{1.5}$I$_{1.5}$ to an adapted 4H model (Figure **5.6**) indicate a good fit: $\chi^2 = 3.509$, $wR_p = 0.075$.

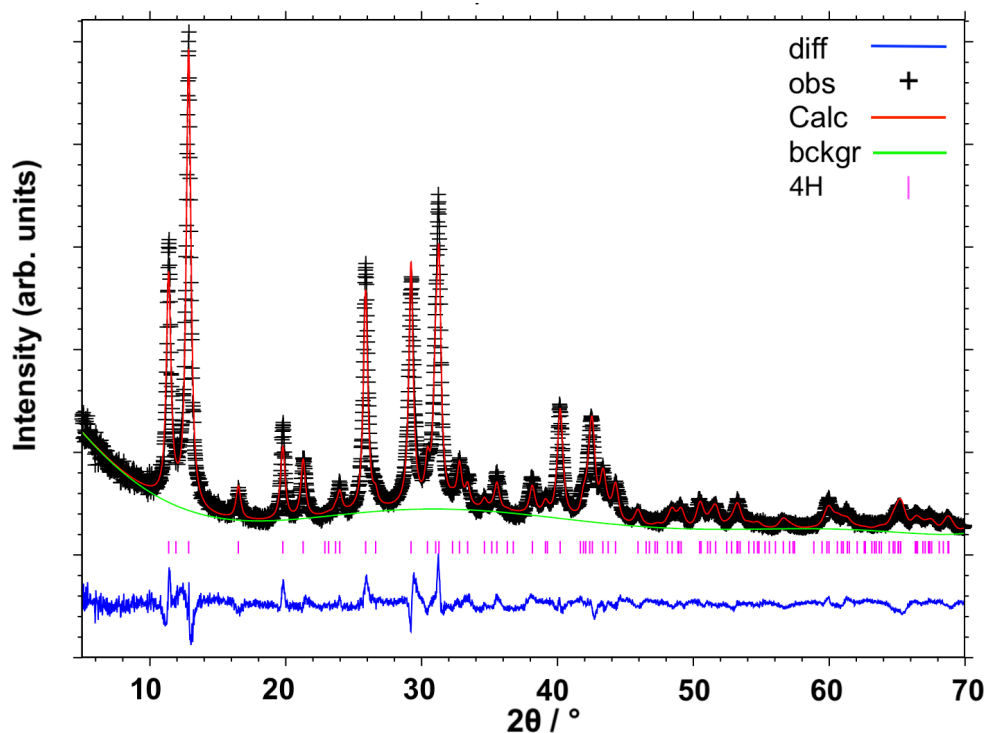**Figure 5.6**. The Rietveld refinement profile of PXRD data for AzPbBr$_{1.5}$I$_{1.5}$ with observed (cross), calculated data (red line), background (green line), reflection position (magenta bar) and difference plot (blue line) which adapted 4H structure[9] with *P*6$_3$/*mmc* space group. Goodness-of-fit parameters: $\chi^2 = 3.509$, $wR_p = 0.075$.

The 4H perovskite structure has a (*hc*)$_2$ stacking sequence in Jagodzinski notation, resulting in alternating face-sharing and corner-sharing octahedra (Figure **5.7**). With varying halide composition from Cl to Br to I, the structure progresses from 6H (Cl through Br) to 4H (Br-rich Br/I solid solution) to 9R (I-rich) polytypes. This is in accordance with the corresponding change in ratio of corner-sharing to face-sharing octahedra (Table **3.5**). The positions of 4H characteristic peak at around 22° shift to lower

diffraction angles with increasing I ratio in the composition, which indicates cell volume expansion (Figure **5.3d**). SCXRD of the $AzPbBr_{1.5}I_{1.5}$ suggests that a mixture of phases exists in the precipitation-prepared single crystals. Potentially, $AzPbX_3$ single-halide materials were included in the crystals, however no evidence of mixed phase was evident in the same compositions prepared by mechanosynthesis, again highlighting the need for caution with samples prepared using the kinetically-controlled precipitation route compared to the thermodynamically-controlled mechanosynthesis as discussed in Chapter 4. However, it was possible to isolate and structurally characterise $AzPbBr_{1.5}I_{1.5}$ by SCXRD. No major difference was found in lattice parameters of SCXRD (Table **5.2**) and the refined PXRD data [SCXRD (293 K): $a = 8.958(4)$ Å, $c= 14.846(6)$ Å; PXRD (ambient): $a = 8.964(3)$Å, $c = 14.82(9)$ Å]. Due to the high-symmetry of the SCXRD structural model, both Br and I are placed equally on the same halide sites with half-occupancy in the refinement of SCXRD.
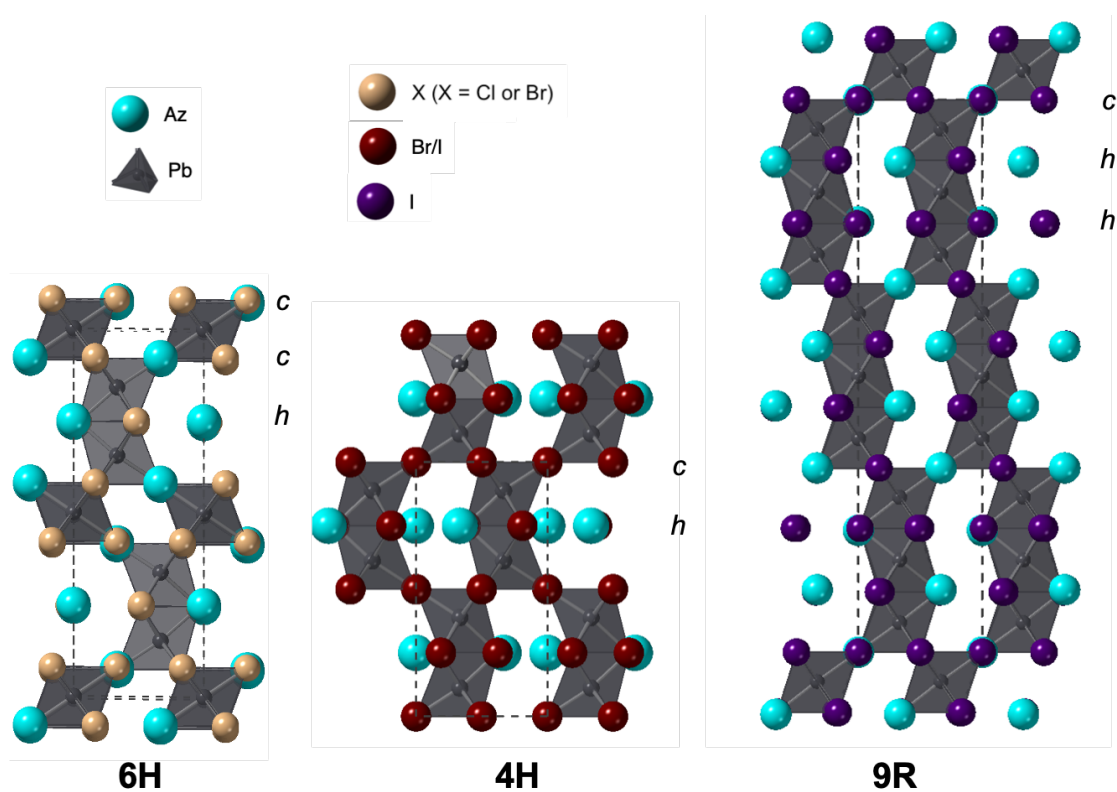

Figure 5.7. Crystal structure of different hexagonal/rhombohedral azetidinium lead halide perovskite polytypes: 6H ($AzPbX_3$, X = Br, Cl), 4H ($AzPbBr_{1.5}I_{1.5}$) and 9R ($AzPbI_3$) viewed along *a*-axis, where the AX_3 stacking sequence is denoted with *h*- and *c*- for hexagonal and cubic close packed layers.

Table 5.2. Selected crystallographic data obtained by single crystal X-ray diffraction of samples prepared by precipitation.

	AzPbCl$_3$	AzPbCl$_3$	AzPbBr$_{1.5}$I$_{1.5}$	AzPbBr$_{1.5}$I$_{1.5}$	AzPbI$_3$	AzPbI$_3$
temperature [K]	293	173	293	93	293	173
empirical formula	C$_3$H$_8$Cl$_3$NPb	C$_3$H$_8$Cl$_3$NPb	C$_3$H$_8$Br$_{1.5}$I$_{1.5}$NPb	C$_3$H$_8$Br$_{1.5}$I$_{1.5}$NPb	C$_3$H$_8$I$_3$NPb	C$_3$H$_8$I$_3$NPb
fw	371.64	371.64	575.51	575.51	645.99	645.99
crystal description	Colorless prism	Colorless prism	Yellow prism	Yellow prism	Red prism	Red prism
crystal size [mm^3]	0.06×0.03×0.02	0.12×0.09×0.04	0.05×0.03×0.03	0.05×0.03×0.03	0.14×0.04×0.03	0.14×0.04×0.03
space group	$P6_3/mmc$	$P6_3/mmc$	$P6_3/mmc$	$P6_3/mmc$	$R\bar{3}m$	$R\bar{3}m$
a [Å]	8.5166(2)	8.47 63(2)	8.958(4)	8.851(5)	9.0835(5)	8.983(2)
c [Å]	20.4424(6)	20.3303(6)	14.846(6)	14.760(8)	35.104(3)	35.130(10)
vol [Å]^3	1284.09(7)	1264.99(7)	1031.7(11)	1001.4(13)	2508.4(3)	2454.9(14)
Z	6	6	4	4	9	9
ρ (calc) [g/cm^3]	2.884	2.927	3.705	3.817	3.849	3.933
μ [mm^{-1}]	20.556	20.866	26.578	27.382	23.375	23.885
F(000)	996	996	988	988	2466	2466
reflections collected	15836	15651	10667	3027	9911	9671
independent reflections (R_{int})	669 (0.0307)	661 (0. 0324)	399 (0.1002)	390 (0.0875)	616 (0.2150)	611 (0.0924)
parameters, restraints	48, 12	48, 8	12, 0	12, 0	17, 0	17, 0
GOF on F^2	1.123	1.085	1.226	1.177	1.154	1.116
R_1 [$I > 2\sigma(I)$]	0.0217	0.0225	0.0545	0.0684	0.0842	0.0422
wR_2 (all data)	0.0562	0.0602	0.1829	0.2038	0.2370	0.1230
largest diff. peak/hole [e/Å^3]	1.214, -1.045	1.550, -0.983	2.760, -1.033	3.118, -2.028	4.546, -5.568	2.719, -2.686

To study the transition between these polytypes, the lattice parameters of each were determined by Rietveld refinement. The lattice parameters of the single halide perovskites $AzPbX_3$ (X = Cl, Br, I) and the mixed halide composition $4H\text{-}AzPbBr_{1.5}I_{1.5}$ are shown in Table **5.3**. The average interlayer distance along the c-axis ($\bar{c}$) and lattice parameter a increase with the transition sequence from 6H to 4H to 9R. The cell volume of those polytypes (normalised to the number of formula units per unit cell) varies linearly as a function of average anion radius. In Figure **5.8a**, the average anion radius was calculated using r_I = 220 pm, r_{Br} = 196 pm and r_{Cl} = 181 pm according to Shannon.[10] While this linear variation within each polytype solid solution is expected in accordance with Vegard's law, it is interesting to note that the linear relationship extends continuously across all three polytypes. Presumably this reflects the AX_3 close packing volume, and it also suggests that the polytype adopted is largely driven by the degree of Pb$\cdots$Pb interactions, which is emphasised in face-sharing (*h)* layers. The substitution of increasingly large, and less electronegative, halide anions result in an expansion of MX_6 octahedra, which decreases the electrostatic energy (Madelung energy) of the ionic crystals and allows for more face sharing octahedral layers and Pb$\cdots$Pb proximity.

Table 5.3. Lattice parameters and goodness-of-fit parameters for Rietveld refinement of PXRD data for trihalide and mixed halide perovskite compositions.

	$AzPbCl_3$	$AzPbBr_3$	$AzPbBr_{1.5}I_{1.5}$	$AzPbI_3$
Space group	$P6_3/mmc$	$P6_3/mmc$	$P6_3/mmc$	$R\bar{3}$
Polytype	6H	6H	4H	9R
a / Å	8.515(6)	8.758(2)	8.964(3)	9.101(1)
c / Å	20.44(9)	21.42(5)	14.82(9)	35.00(2)
volume / Å^3	1284.2(6)	1423.3(0)	1032.0(4)	2510.8(3)
$\bar{c}$ / Å *	3.408	3.570	3.707	3.889
χ^2	3.066	4.697	3.509	1.545
wR_p	0.069	0.083	0.075	0.056

* The average interlayer distance along c-axis.

In addition to the 4H, 6H and 9R single phase solid solutions, intermediate two-phase regions of 6H-4H and 4H-9R were also identified by PXRD, as shown in Figure **5.8a**. For the 6H-4H two phase-region, the peaks of both phases could be readily identified, but the boundary of the 4H-9R two-phase region was difficult to ascertain due to the overlap of the major peaks (Figures **5.3b, 5.3d**). Attempts at a two-phase refinement of the PXRD data of both two-phase regions were unsuccessful due to the overall breadth of peaks, overlap of major peaks and relatively low peak intensities of non-overlapping peaks. As a result, no lattice parameters are provided for the 6H-4H two-phase region. For the 4H-9R two-phase region, the data for compositions $AzPbBrI_2$ and $AzPbBr_{0.6}I_{2.4}$ were refined as single-phase approximations 4H and 9R respectively, and the resulting lattice parameters matched quite well with the linear fit as a function of average anion radius. All the refined lattice parameters of Az mixed halide perovskite were plotted as a function of average halide ionic radius and the data show a linear variation. As a general comparison, the cell volumes as a function of average anion radius for 3C $FAPbX_3$ and $MAPbX_3$ mixed halide perovskites[11–13] are shown in Figure **5.9** and display similar linear behaviour. Unlike the $AzPbX_3$ compositions of the current study, all MA- and FA-compositions adopt a single (3C) polytype.
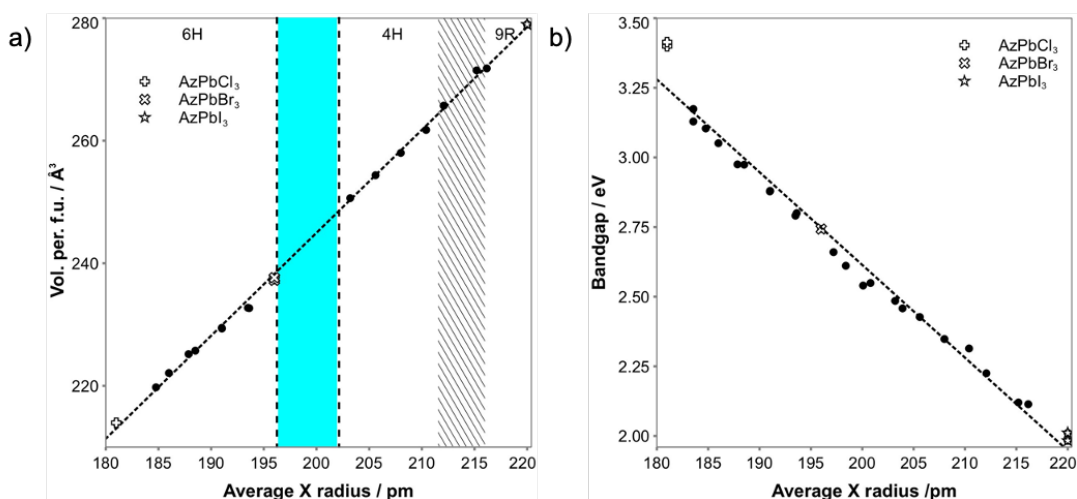

Figure 5.8. (a) Cell volume (per formula unit) of mixed halide perovskite determined by Rietveld refinement of PXRD data and (b) the bandgap determined from absorption spectra of samples $AzPbBr_{3-x}X_x$ (X = Cl or I) with composition $0 \leq x \leq 3$ plotted as a function of average halide anion radius. Intermediate 6H-4H (shaded) and 4H-9R (hatched) two phase-regions are indicated.
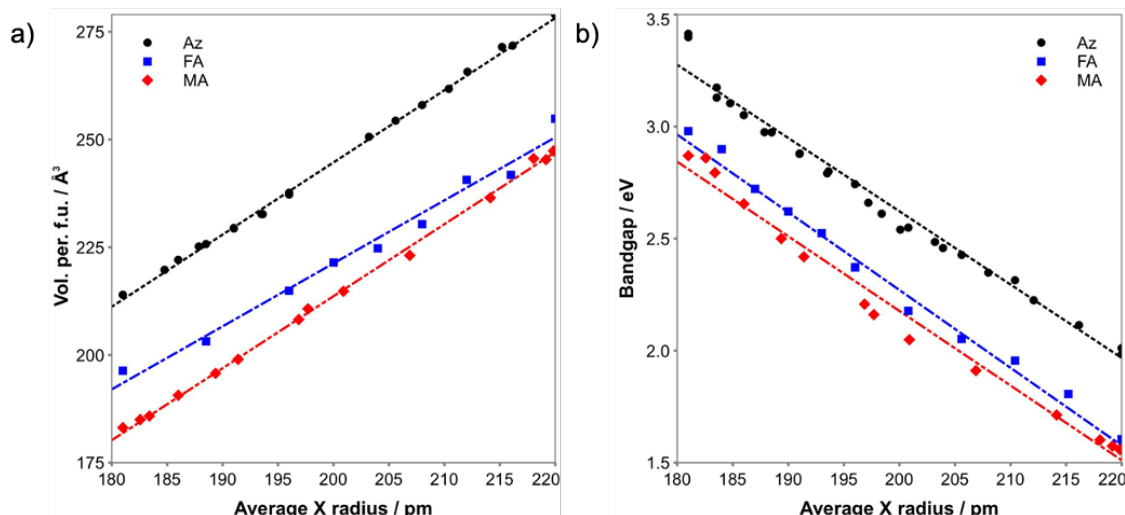
Figure 5.9. (a) Perovskite cell volume (per formula unit) and (b) bandgap determined from absorption spectra of samples $APbCl_xBr_{3-x}$ and $APbBr_xI_{3-x}$ (A = Az, FA,[12,13] MA,[11] $0 \leq x \leq 3$) plotted as a function of average halide anion radius.

5.2.2 Optical properties of mixed halide perovskites

The optical properties of the hexagonal/rhombohedral samples were studied by absorption spectroscopy (Figure **5.10**). The absorption onsets are systematically red-shifted with increasing average anion size (from Cl to I). The absorption onset of $AzPbBr_{3-x}X_x$ (X = Cl or I, $0 \leq x \leq 3$) samples are red-shifted from ca. 360 nm (3.44 eV, $AzPbCl_3$) to ca. 450 nm (2.76 eV, $AzPbBr_3$) to ca. 615 nm (2.02 eV, $AzPbI_3$). The background absorption of intermediate compositions in $AzPbCl_xBr_{3-x}$ samples lies above the normalised zero baseline, especially for $x = 2.5$. This might result from a small number of Br-rich crystallites on the sample surface, the amount of which is too small to be detected in PXRD. The absorption spectrum of $AzPbI_3$ bore close resemblance to the reported spectrum,[5] where three well defined transitions could be detected. The peak maxima of the three well defined transitions are at 551, 506, 470 nm while the reported transitions peak at 554, 503, 462 nm.

The bandgap as a function of halide composition for the mixed halide perovskites is shown in Figure **5.8b**. The bandgap of $AzPbCl_3$ and $AzPbI_3$ were calculated to be 3.41 ± 0.01 eV and 2.00 ± 0.02 eV, respectively. The errors were determined with the multiple

bandgap values measured from multiple samples (>3). The latter is in good agreement with the previously reported value of 1.97 eV.[5]
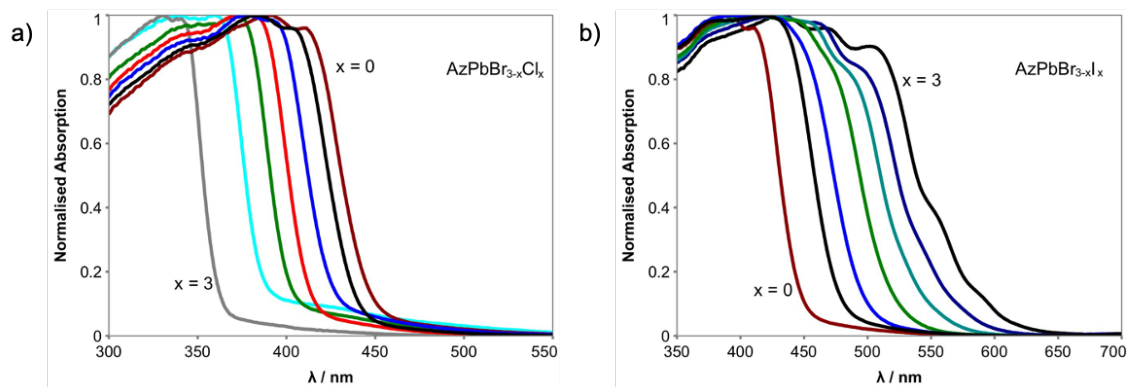

Figure 5.10. Absorption spectra of (a) $AzPbBr_{3-x}Cl_x$ (b) $AzPbBr_{3-x}I_x$ ($0 \leq x \leq 3$, in $x = 0.5$ increments) samples prepared by mechanosynthesis.

The bandgap varies linearly as a function of average anion radius, despite the change of halide composition and octahedral connectivity. As discussed in Chapter 3, the varying ratio of corner-sharing to face-sharing octahedral connectivity changes the efficiency of Pb-X orbital overlap; in conjunction with the change in Pb-X bond length, average bond angles and covalency, this gives rise to the bandgap variation. Comparison of the behaviour of the Az-based perovskites with corresponding MA-, and FA-based mixed halide perovskites shows that the lattice parameter progression as a function of halide composition is linear in all cases. However, the reported relation of bandgap versus halide composition is not consistent across these studies. Some studies have reported a nonlinear relationship, which is described as a bowing effect,[4,11,14] while other studies have documented a linear progression[15,16] as observed here. Bandgap bowing is often fitted to a second order polynomial, with a bowing parameter b as the binominal coefficient of the fitting equation. The bowing parameters of $MAPbBr_{3-x}X_x$ (X = Cl or I) are relatively small (7×10^{-4} to 0.33)[4,11] compared to the bowing parameters found for other mixed metal perovskite systems (0.5 to 1.33).[17–20] The work in this Chapter illustrates a good example of a linear variation between bandgap and halide composition, and it is yet unclear why both linear and non-linear relationships have been reported for mixed halide perovskites

with the same organic cation and metal. This may related to anion segregation when prepared using kinetically-controlled precipitation routes as discussed in Chapter 4.[6]

5.3 Conclusion

Following the studies on $AzPbBr_3$ and mixed A-cation Az-containing perovskites, mixed halide compositions $AzPbBr_{3-x}X_x$ (X = Cl or I) were successfully synthesised using a mechanosynthesis grinding method. The single phase trihalide materials $AzPbX_3$ (X = Cl, Br or I) were shown to be stable in air for > 6 months. In addition to the 6H polytype adopted by $AzPbBr_3$, as shown in Chapter 3, and 9R polytype reported for $AzPbI_3$,[5] $AzPbCl_3$ was also shown to form in the 6H polytype and an additional 4H polytype was found for $AzPbBr_{3-x}I_x$ (ca. $0 < x \leq 2$) compositions. With varying halide composition, the structure progresses from 6H to 4H to 9R perovskite polytype. A complete and continuous solid solution is formed for compositions with the 6H structure and partial solid solutions form between the 6H and 4H and 4H and 9R polytypes. A linear variation in unit cell volume (scaled per formula unit) as a function of anion average radius is observed not only within the solid solution of each polytype (according to Vegard's law) but continuously across all three polytypes. This appears to be the first time that Vegard's law-type behaviour has been observed across several polytypes. This linear relationship, extending across all compositions, is accompanied by a linearly tuneable bandgap ranging from 2.00 to 3.41 eV as a function of average anion radius without any observations of the bowing effect. The linear variation of bandgap across all $AzPbX_3$ compositions and polytypes is comparable to that observed in $APbBr_{3-x}X_x$ (A = MA, or FA, X = Cl or I) but they all adopt a single (3C) polytype.[11-13]

References

(1) Nakamura, Y.; Shibayama, N.; Hori, A.; Matsushita, T.; Segawa, H.; Kondo, T. Crystal Systems and Lattice Parameters of $CH_3NH_3Pb(I_{1-x}Br_x)_3$ Determined Using Single Crystals: Validity of Vegard's Law. *Inorg. Chem.* **2020**, *59* (10), 6709–6716.

(2) Chen, D.; Li, J.; Chen, X.; Chen, J.; Zhong, J. Grinding Synthesis of $APbX_3$ (A = MA, FA, Cs; X = Cl, Br, I) Perovskite Nanocrystals. *ACS Appl. Mater. Interfaces* **2019**, *11* (10), 10059–10067.

(3) Gratia, P.; Zimmermann, I.; Schouwink, P.; Yum, J.-H.; Audinot, J.-N.; Sivula, K.; Wirtz, T.; Nazeeruddin, M. K. The Many Faces of Mixed Ion Perovskites: Unraveling and Understanding the Crystallization Process. *ACS Energy Lett.* **2017**, *2* (12), 2686–2693.

(4) Noh, J. H.; Im, S. H.; Heo, J. H.; Mandal, T. N.; Seok, S. Il. Chemical Management for Colorful, Efficient, and Stable Inorganic-Organic Hybrid Nanostructured Solar Cells. *Nano Lett.* **2013**, *13* (4), 1764–1769.

(5) Panetta, R.; Righini, G.; Colapietro, M.; Barba, L.; Tedeschi, D.; Polimeni, A.; Ciccioli, A.; Latini, A. Azetidinium Lead Iodide: Synthesis, Structural and Physico-Chemical Characterization. *J. Mater. Chem. A* **2018**, *6* (21), 10135–10148.

(6) Lehmann, F.; Franz, A.; Többens, D. M.; Levcenco, S.; Unold, T.; Taubert, A.; Schorr, S. The Phase Diagram of a Mixed Halide (Br, I) Hybrid Perovskite Obtained by Synchrotron X-Ray Diffraction. *RSC Adv.* **2019**, *9* (20), 11151–11159.

(7) Protesescu, L.; Yakunin, S.; Nazarenko, O.; Dirin, D. N.; Kovalenko, M. V. Low-Cost Synthesis of Highly Luminescent Colloidal Lead Halide Perovskite Nanocrystals by Wet Ball Milling. *ACS Appl. Nano Mater.* **2018**, *1* (3), 1300–1308.

(8) Pal, P.; Saha, S.; Banik, A.; Sarkar, A.; Biswas, K. All-Solid-State Mechanochemical Synthesis and Post-Synthetic Transformation of Inorganic Perovskite-Type Halides. *Chem. - A Eur. J.* **2018**, *24* (8), 1811–1815.

(9) García-Fernández, A.; Juarez-Perez, E. J.; Bermúdez-García, J. M.; Llamas-Saiz, A. L.; Artiaga, R.; López-Beceiro, J. J.; Señarís-Rodríguez, M. A.; Sánchez-Andújar, M.; Castro-García, S. Hybrid Lead Halide $[(CH_3)_2NH_2]PbX_3$ (X = Cl$^-$ and Br$^-$) Hexagonal Perovskites with Multiple Functional Properties. *J. Mater.*

Chem. C **2019**, *7* (32), 10008–10018.

(10) Shannon, R. D. Revised Effective Ionic Radii and Systematic Studies of Interatomic Distances in Halides and Chalcogenides. *Acta Crystallogr. Sect. A* **1976**, *32* (5), 751–767.

(11) Wang, W.; Su, J.; Zhang, L.; Lei, Y.; Wang, D.; Lu, D.; Bai, Y. Growth of Mixed-Halide Perovskite Single Crystals. *CrystEngComm* **2018**, *20* (12), 1635–1643.

(12) Jesper Jacobsson, T.; Correa-Baena, J. P.; Pazoki, M.; Saliba, M.; Schenk, K.; Grätzel, M.; Hagfeldt, A. Exploration of the Compositional Space for Mixed Lead Halogen Perovskites for High Efficiency Solar Cells. *Energy Environ. Sci.* **2016**, *9* (5), 1706–1724.

(13) Levchuk, I.; Osvet, A.; Tang, X.; Brandl, M.; Perea, J. D.; Hoegl, F.; Matt, G. J.; Hock, R.; Batentschuk, M.; Brabec, C. J. Brightly Luminescent and Color-Tunable Formamidinium Lead Halide Perovskite $FAPbX_3$ (X = Cl, Br, I) Colloidal Nanocrystals. *Nano Lett.* **2017**, *17* (5), 2765–2770.

(14) Kumawat, N. K.; Dey, A.; Kumar, A.; Gopinathan, S. P.; Narasimhan, K. L.; Kabra, D. Band Gap Tuning of $CH_3NH_3Pb(Br_{1-x}Cl_x)_3$ Hybrid Perovskite for Blue Electroluminescence. *ACS Appl. Mater. Interfaces* **2015**, *7* (24), 13119–13124.

(15) Park, B.; Philippe, B.; Jain, S. M.; Zhang, X.; Edvinsson, T.; Rensmo, H.; Zietz, B.; Boschloo, G. Chemical Engineering of Methylammonium Lead Iodide/Bromide Perovskites: Tuning of Opto-Electronic Properties and Photovoltaic Performance. *J. Mater. Chem. A* **2015**, *3* (43), 21760–21771.

(16) Wang, L.; Yuan, G. D.; Duan, R. F.; Huang, F.; Wei, T. B.; Liu, Z. Q.; Wang, J. X.; Li, J. M. Tunable Bandgap in Hybrid Perovskite $CH_3NH_3Pb(Br_{3-y}X_y)$ Single Crystals and Photodetector Applications. *AIP Adv.* **2016**, *6* (4).

(17) Lee, S.; Levi, R. D.; Qu, W.; Lee, S. C.; Randall, C. A. Band-Gap Nonlinearity in Perovskite Structured Solid Solutions. *J. Appl. Phys.* **2010**, *107* (2), 1–6.

(18) Chatterjee, S.; Payne, J.; Irvine, J. T. S.; Pal, A. J. Bandgap Bowing in a Zero-Dimensional Hybrid Halide Perovskite Derivative: Spin-Orbit Coupling: Versus Lattice Strain. *J. Mater. Chem. A* **2020**, *8* (8), 4416–4427.

(19) Goyal, A.; McKechnie, S.; Pashov, D.; Tumas, W.; Schilfgaarde, M. Van;

Stevanović, V. Origin of Pronounced Nonlinear Band Gap Behavior in Lead-Tin Hybrid Perovskite Alloys. *Chem. Mater.* **2018**, *30* (11), 3920–3928.

(20)   Hu, Z.; Lin, Z.; Su, J.; Zhang, J.; Chang, J.; Hao, Y. A Review on Energy Band-Gap Engineering for Perovskite Photovoltaics. *Sol. RRL* **2019**, *3* (12), 1–9.

Chapter 6

Exploring low dimensional perovskite-like structures with azetidinium – preliminary results

6.1 Introduction

Ruddlesden-Popper-like (R-P-like) layered phases have demonstrated higher moisture stability compared to 3D perovskite analogues.[1,2] R-P-like layered phases involve single or multiple inorganic sheets of MX_6 octahedra sandwiched between large organic cations. Although these look visually similar to R-P phases they often do not have the required rocksalt-structured interlayer between the 2D perovskite layers. Examples of organic cations commonly used for these R-P-like 2D layered structures are included in Table **1.1**. A wider range of A-cations is available for layered phases because the cations are able to be positioned in between the 2D inorganic sheets of interconnected M-X octahedra, compared to the choice of A-cation in 3D perovskite which is limited by the size of cuboctahedral cavities. For example, PMA_2PbI_4 was reported to be a R-P-like layered structure with a space group of *Pbca*.[3]

As mentioned in Chapter 1, 1D chain structures have also been reported. They have the advantage of large surface-to-volume ratios, which improves the light harvesting by reducing Rayleigh scattering.[4,5] However, the bandgaps of reported 1D materials are typically large (>2.2 eV). Although these large bandgaps limit their use in the visible range for photovoltaics,[6] it is reported that 1D materials can be used as white light emitters.[7] The remarkable optoelectrical properties of lead halide perovskite can be attributed to the $6s^26p^0$ electronic configuration of Pb^{2+}. The valence band of OIHPs has most contribution from the hybridisation of the halide p orbitals and Pb 6s orbitals, and the conduction band from the Pb 6p orbitals. The high density states of the hybridisation of halide p orbitals and Pb 6s orbitals allow the large absorption coefficient of the materials.[8,9] The ionic radius of Bi^{3+} is similar to that of Pb^{2+},[10] and both metal cations have $6s^26p^0$ electronic configuration. Therefore, Bi^{3+} is a suitable candidate for Pb substitution.

In this chapter, a $n = 1$ R-P phase Az_2PbBr_4 and a 1D corner-sharing chain structure azetidinium bismuth bromide, '$Az_3Bi_2Br_9$' were synthesised. The lattice parameters and optical absorption of Az_2PbBr_4 were analysed by PXRD and absorption spectra respectively. Although SCXRD of azetidinium bismuth bromide suggests a structure consisting of 1D zig-zag chains of corner sharing $BiBr_6$ octahedra, the location of the Az cations could not be ascertained, and the inclusion of solvent molecules could not be ruled out. PXRD of powder samples gave different diffraction patterns than expected from the single crystal results. Nevertheless, these intriguing results indicate an opportunity for further study in this system.

6.2 Synthesis and structural analysis of Az_2PbBr_4

Chapter 3 focuses on the precipitation synthesised $AzPbBr_3$. For solvent-free green chemistry purposes, mechanosynthesis of $AzPbBr_3$ ($AzBr:PbBr_2 = 1:1$) with hand grinding and ball mill was carried out. During grinding synthesis carried out by hand, a clear colour change from white to yellow was observed as grinding progressed. PXRD data of hand ground samples indicated they were highly crystalline (Figure **6.1**), although the PXRD pattern was found not to match that of the expected 6H hexagonal $AzPbBr_3$ product (Figure **3.1**). When compared to the PXRD pattern of $PbBr_2$, the presence of $PbBr_2$ peaks and other, sharp, unidentified peaks were observed in the hand ground samples ($AzBr:PbBr_2 = 1:1$), which indicated that these might be a mixture of $PbBr_2$ and a new Az-rich perovskite-related compound. Single A-cation layered perovskite-like structures have been reported with a general formula A_2MX_4 (such as BA_2PbI_4).[11] Thus mechanosynthesis of samples with composition of $AzBr:PbBr_2 = 2:1$ was attempted.

6.2.1 Synthesis of Az_2PbBr_4

Az_2PbBr_4 samples were obtained by mechanosynthesis by both ball mill and hand grinding. Stoichiometric dry AzBr was mixed with $PbBr_2$ ($AzBr:PbBr_2 = 2:1$) in the ball mill and ground at 600 rpm for 1 hour, or the mixtures were ground by hand in a mortar pestle for 25 minutes. Both methods produced yellow powders.
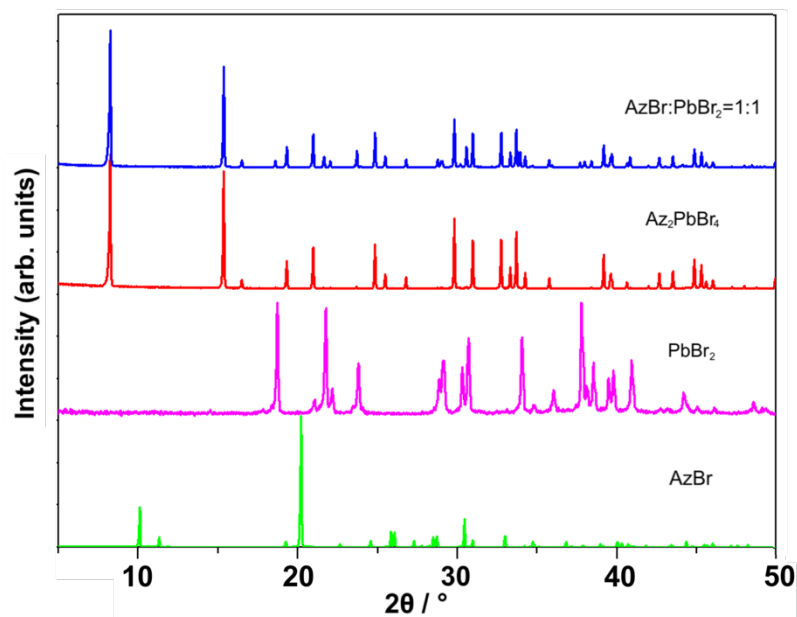
Figure 6.1. PXRD patterns of samples obtained from hand grinding mechanosynthesis with composition of patterns from top to bottom: $AzBr:PbBr_2 = 1:1$, $AzBr:PbBr_2 = 2:1$ (Az_2PbBr_4) and reference starting material $PbBr_2$ and AzBr.

6.2.2 Analysis of Az_2PbBr_4

Az_2PbBr_4 powder samples synthesised by both ball mill and hand grinding were analysed by PXRD and comparable patterns were obtained from both syntheses. PXRD of these samples indicated that the additional peaks due to $PbBr_2$ were no longer present (Figure **6.1**). The structure of these samples was determined to be a R-P $n = 1$ phase with $I4/mmm$ space group (Figure **6.2a**).[12,13] The Az cations, which are represented as solid spheres situated at the centre of electron density (corresponding to the Mn positions from refinements), form rocksalt layers with the Br anions. Ganguli[12] reported an empirical prediction that possible R-P phase structures are associated with a ratio of A-site and metal cation radius (r_A/r_M) in the range of 1.7 to 2.4. As discussed in Chapter 4, estimation of the cation radius of Az (~310 pm) is different from that calculated (250 pm).[14] The r_{Az}/r_{Pb} calculated with this estimation equals 2.60, and that from the literature[14] equals 2.10. The fact that it is possible to obtain the tetragonal R-P phase $n=1$ structure with Az_2PbBr_4 needs further study to check if the empirical prediction for the R-P phase is suitable for organic-inorganic hybrid systems.

For simplicity, Rietveld refinements were carried out by replacing the organic Az cation with Mn, as they have a similar electron density. Figure **6.2b** shows an example of PXRD data refinement of samples obtained from ball mill mechanosynthesis. The refined lattice parameters were $a = 5.993(6)$ Å and $c = 21.501(1)$ Å, with goodness-of-fit parameters $\chi^2 = 10.21$ and $wR_p = 0.115$. The difference between the organic moieties and Mn, which is associated with their actual atomic position and thermal motion, is one possible reason for such a high χ^2 value for the refinement and might lead to the differences in the peak shape and intensities shown.
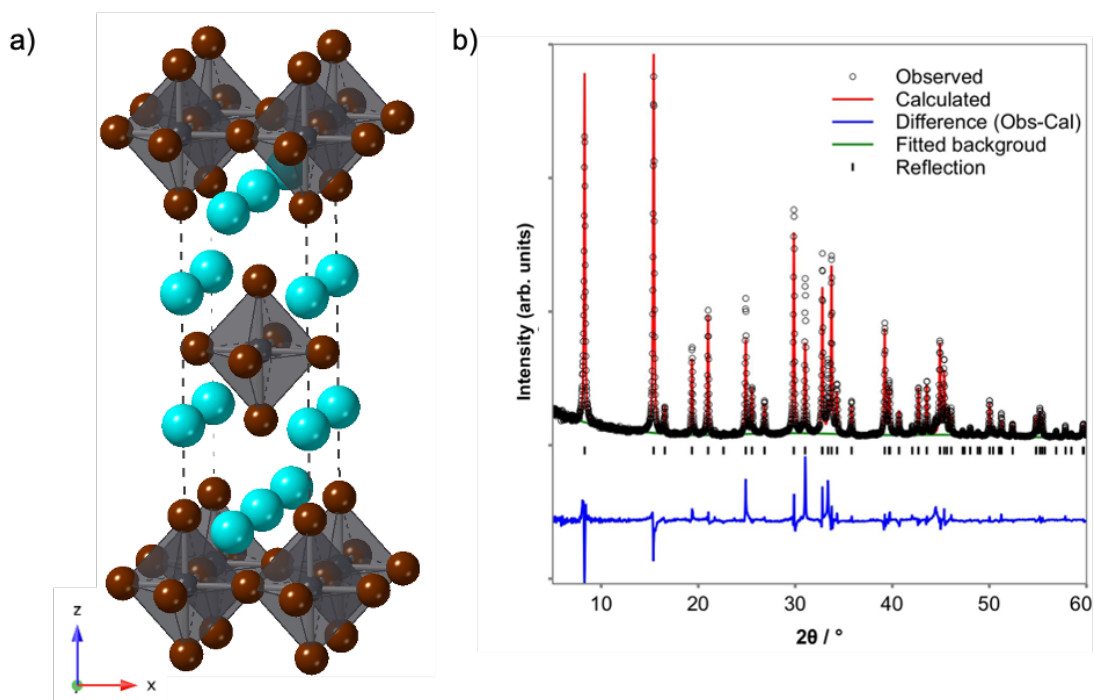

Figure 6.2. (a) R-P phase ($n = 1$) layered structure of Az_2PbBr_4 showing alternating layers of $AzPbBr_3$ perovskite and $AzBr$ rocksalt along the c-axis (b) Rietveld refinement of PXRD data of Az_2PbBr_4 obtained from ball mill mechanosynthesis in $I4/mmm$ space group with observed data (open circles), calculated data (red line), background (green line), reflection position (black bar) and difference plot (blue line). The refined lattice parameters are $a = 5.993$ Å, and $c = 21.501$ Å with goodness-of-fit parameters $\chi^2 = 10.21$ and $wR_p = 0.115$.

The absorption spectrum of Az_2PbBr_4 samples synthesised by ball milling is shown in Figure **6.3**. The absorption onset is at ca. 450 nm and the calculated bandgap is 2.74 eV, which is very similar to the calculated bandgap of $AzPbBr_3$ (2.81 eV, Figure **3.11**). It is worth exploring if azetidinium lead trichloride and triiodide counterparts possess similar layered structures and similarly if other members of the R-P homologous series with varying *n* exist.
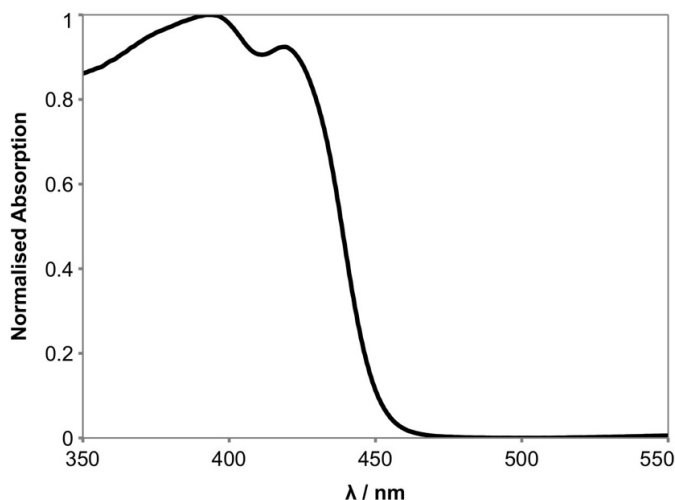

Figure 6.3. Absorption spectrum of Az_2PbBr_4 obtained from ball milling.

6.3 Synthesis and structural analysis of azetidinium bismuth bromide

The ionic radii of Bi^{3+} is similar to that of Pb^{2+},[10] and they both have $6s^26p^0$ electronic configuration. These features make Bi^{3+} an appropriate candidate for Pb substitution in halide perovskites. For instance, Kamminga *et al.*[15] reported $MA_3Bi_2I_9$ adopts a hexagonal structure with *P*6$_3$/*mmc* space group at 300 K and goes through two phase transition at 223 K and 143 K when cooling. The crystal structure and the simulated powder pattern of $MA_3Bi_2I_9$ at 300 K are shown in Figure **6.4**. As a result, the attempt to synthesise azetidinium bismuth bromide was carried out with a target composition of $Az_3Bi_2Br_9$.
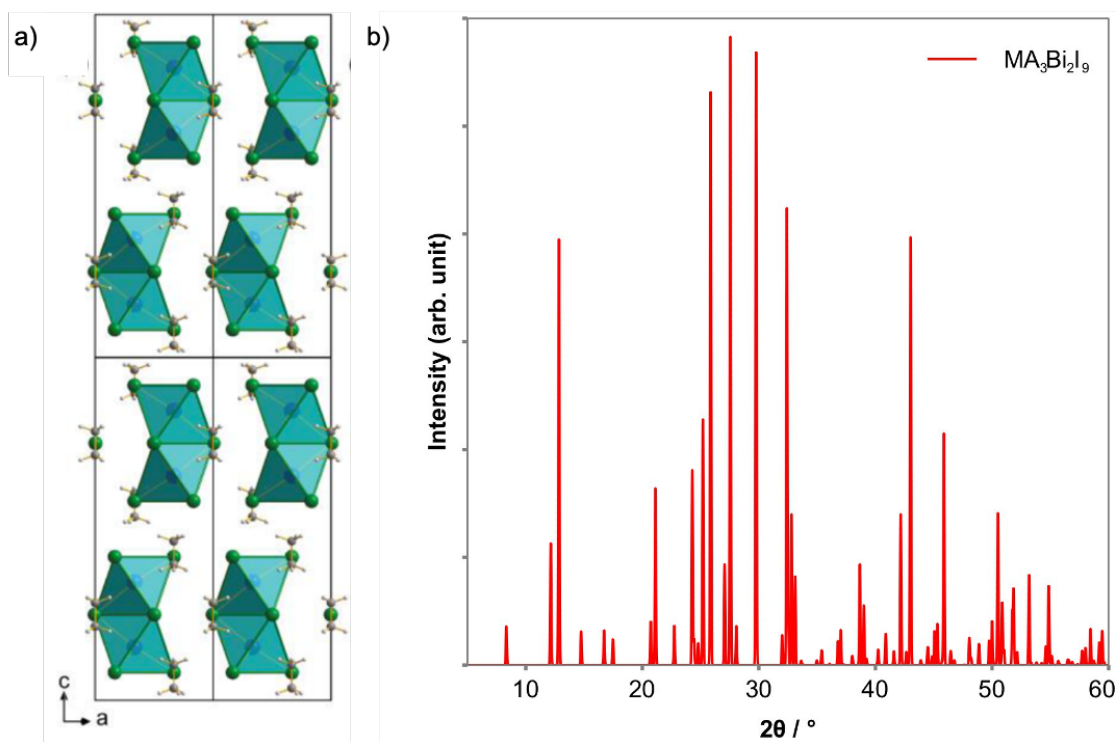
Figure 6.4. (a) Crystal structure of $MA_3Bi_2I_9$ at 300 K with $P6_3/mmc$ space group, reproduced from Ref. 15 with permission. Copyright (2017) American Chemistry Society. (b) Simulated powder pattern with the crystallographic file at 300 K from Ref. 15.

6.3.1 Synthesis of azetidinium bismuth bromide

For precipitation synthesis stoichiometric amounts of dry AzBr and $BiBr_3$ (AzBr:$BiBr_3$ = 3:2) were dissolved in DMF and the anti-solvent DCM was slowly diffused into the perovskite/DMF solution to obtain the crystals suitable for SCXRD. Powder samples of azetidinium bismuth bromide were prepared by mixing appropriate molar ratios of AzBr and $BiBr_3$ (AzBr:$BiBr_3$ = 3:2) in a DMF solution. DCM was slowly added to the reaction mixture and the resulting precipitate was collected by filtration. Mechanosynthesis was carried out by placing stoichiometric amounts of dry AzBr and $BiBr_3$ (AzBr:$BiBr_3$ = 3:2) in a ball mill and grinding at 600 rpm for 1 hour. Detailed procedures are given in Chapter 2.

6.3.2 Analysis of azetidinium bismuth bromide

Single crystals of azetidinium bismuth bromide were analysed by SCXRD and the structure was determined to contain 1D chains of corner-sharing $BiBr_6$ octahedra in a zig-zag formation (Figure **6.5**), although it was difficult to identify the position of the Az cations with certainty. 1D chains of $BiBr_6$ octahedra run along the *c*-axis and located at the centre and cell edges. Initial data collection at low temperature (173 K) indicated the crystals had *Pbcm* symmetry, however on heating to room temperature a base centred (*Cmcm*) orthorhombic unit cell was found with the same 1D $BiBr_6$ octahedral framework. This *Cmcm* symmetry was preserved on re-cooling to 173 K for a second time. This indicates these crystals went through irreversible change and reduced in crystallinity when they were not kept in the cold stream. A possible reason for this change may be loss of solvent; this also implies incorporation of solvent molecules even in the *Cmcm* phase cannot be discounted. However, given the sensitivity of X-rays to the Bi and Br positions, the nature of the octahedral framework is considered reliable. The lattice parameters of the orthorhombic azetidinium bismuth bromide were determined to be a = 13.11 Å, b =17.54 Å and c = 8.315 Å at 293 K with *Cmcm* space group. Despite the crystallographic information of the azetidinium bismuth bromide, the composition of the single crystal has not been determined yet due to the difficulty in determining the position of organic ions/molecules within the structure.
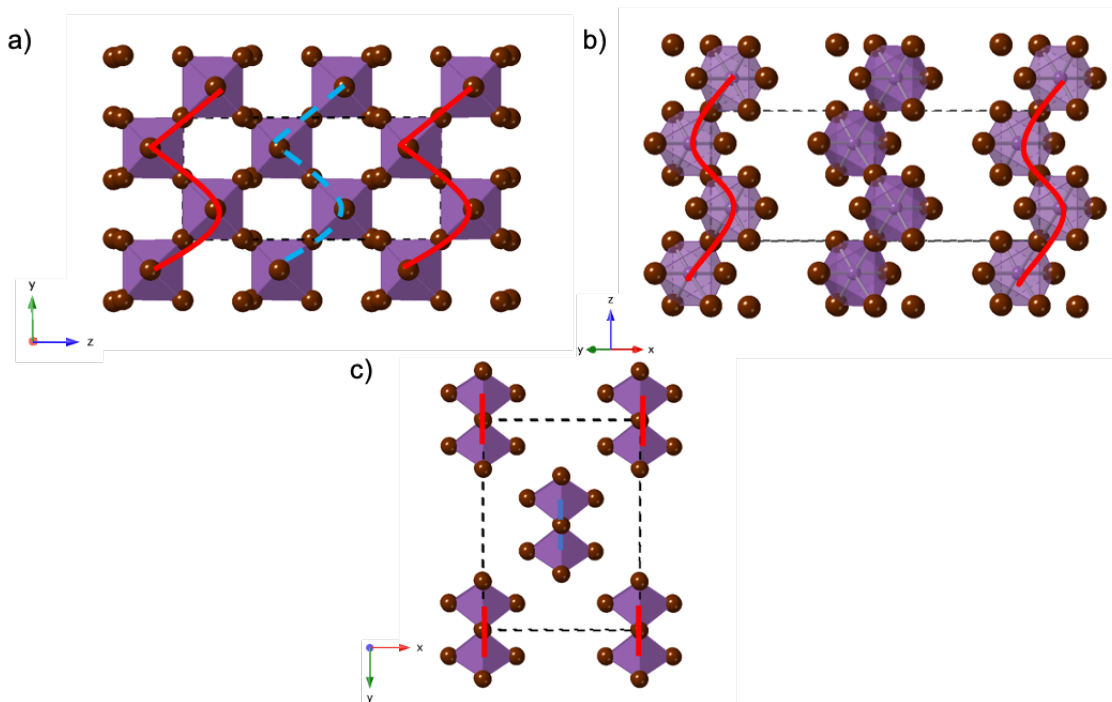
Figure 6.5. Cystal structure of azetidinium bismuth bromide at 293 K viewed along (a) *a*-axis (b) [110] direction (c) *c*-axis. The structure contains 1D chains of BiBr$_6$ octahedra in a zig-zag formation. Solid lines and dashed lines connecting Bi are drawn to guide visualisation of the structure.

PXRD patterns were obtained from powders from the antisolvent precipitation synthesis and from crushing single crystals (Figure **6.6**). These two patterns were found to be comparable. The PXRD of the mechanosynthesised samples indicates they are mixtures of different phases. One of the phases is observed in the precipitation synthesised powders but other phases are yet to be determined. There is no evidence of peaks from the starting materials (AzBr and BiBr$_3$), which suggests these starting materials were consumed during the synthesis. All three PXRD patterns were found to be contain a different phase(s) to the diffraction pattern simulated from the single crystal structure with space group *Cmcm*. One possible explanation for the structural disparity between powder and crystals is that the antisolvent DCM remains in the crystals and changes the structure. This explanation is unlikely as the same PXRD pattern was obtained from powder which was soaked in DCM and sealed in the sample holder. The reason behind the structural difference between the powder and crystals requires further study.
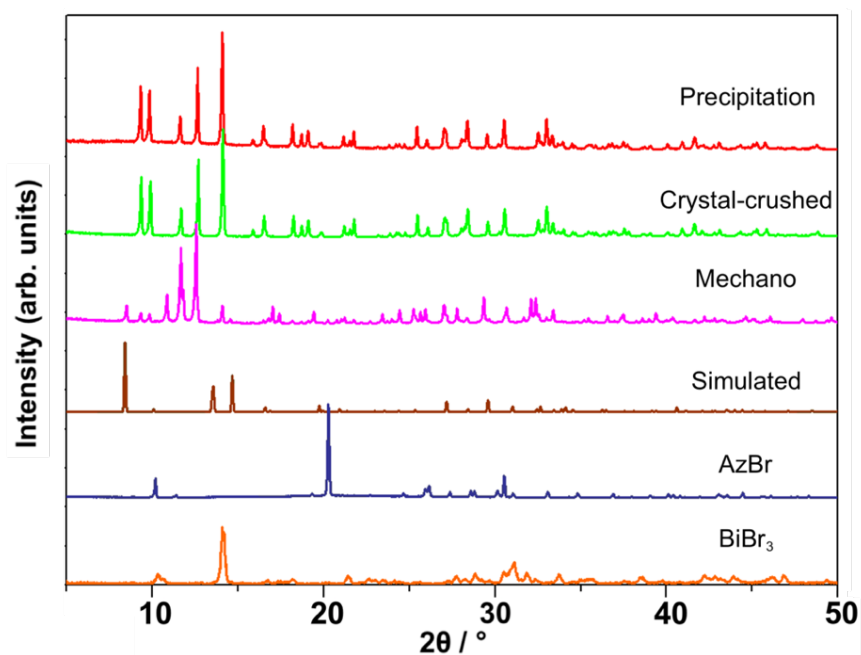
151

Figure 6.6. PXRD patterns of azetidinium bismuth bromide prepared by precipitation synthesis, crushing single crystals, and mechanosynthesis. PXRD pattern of simulation from single crystal with *Cmcm* space group, and reference patterns of raw materials AzBr and BiBr$_3$.

The absorption spectrum of azetidinium bismuth bromide powder samples synthesised by anti-solvent precipitation is shown in Figure **6.7**. The absorption onset is at ca. 468 nm and the calculated bandgap is 2.61 eV, which is smaller than the calculated bandgap of AzPbBr$_3$ (2.81 eV, Figure **3.11**) and larger than the reported organic-inorganic hybrid Bi-I compounds such as NPABiI$_5$ and BDABiI$_4$ etc. (2.29 – 2.53 eV, Table **1.1**).[6,16] As phase mixtures were found for the azetidinium bismuth bromide prepared by mechanosynthesis, the corresponding absorption was not measured until further determination of the phases.
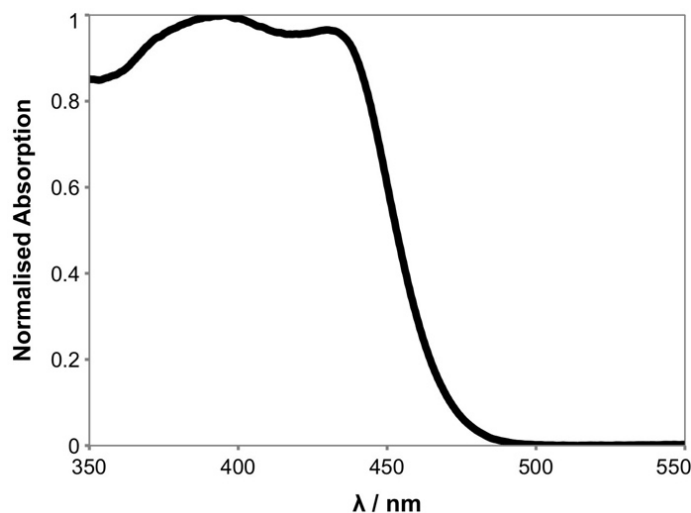
Figure 6.7. Absorption spectrum of azetidinium bismuth bromide samples obtained from antisolvent precipitation synthesis.

6.4 Conclusion

Two organic-inorganic hybrid compounds based on Az were synthesised and analysed - Az_2PbBr_4 and azetidinium bismuth bromide. Az_2PbBr_4 was determined to be a R-P phase (n = 1) layered structure with a space group of $I4/mmm$. Its bandgap (2.74 V) is comparable to that of $AzPbBr_3$ (2.81 eV). The single crystal structure of azetidinium bismuth bromide was determined to be 1D chain structure with $Cmcm$ space group. A phase transition from base centred ($Cmcm$, 293 K) to simple ($Pbcm$, 173 K) orthorhombic unit cell was found with SCXRD. PXRD analysis of azetidinium bismuth bromide powders, prepared by both precipitation synthesis and mechanosynthesis, found several phases different from the structure determined by single crystal. These phases have yet to be determined.

References

(1)   Tsai, H.; Nie, W.; Blancon, J. C.; Stoumpos, C. C.; Asadpour, R.; Harutyunyan, B.; Neukirch, A. J.; Verduzco, R.; Crochet, J. J.; Tretiak, S.; et al. High-Efficiency Two-Dimensional Ruddlesden-Popper Perovskite Solar Cells. *Nature* **2016**, *536* (7616), 312–317.

(2)   Leng, K.; Abdelwahab, I.; Verzhbitskiy, I.; Telychko, M.; Chu, L.; Fu, W.; Chi, X.; Guo, N.; Chen, Z.; Chen, Z.; et al. Molecularly Thin Two-Dimensional Hybrid Perovskites with Tunable Optoelectronic Properties Due to Reversible Surface Relaxation. *Nat. Mater.* **2018**, *17* (10), 908–914.

(3)   Mitzi, D. B.; Chondroudis, K.; Kagan, C. R. Design, Structure, and Optical Properties of Organic-Inorganic Perovskites Containing an Oligothiophene Chromophore. *Inorg. Chem.* **1999**, *38* (26), 6246–6256.

(4)   Mitzi, D. B.; Wang, S.; Feild, C. A.; Chess, C. A.; Guloy, A. M. Conducting Layered Organic-Inorganic Halides Containing 〈110〉-Oriented Perovskite Sheets. *Science (80-.).* **1995**, *267* (5203), 1473–1476.

(5)   Dohner, E. R.; Hoke, E. T.; Karunadasa, H. I. Self-Assembly of Broadband White-Light Emitters. *J. Am. Chem. Soc.* **2014**, *136* (5), 1718–1721.

(6)   Ma, C.; Shen, D.; Huang, B.; Li, X.; Chen, W. C.; Lo, M. F.; Wang, P.; Hon-Wah Lam, M.; Lu, Y.; Ma, B.; et al. High Performance Low-Dimensional Perovskite Solar Cells Based on a One Dimensional Lead Iodide Perovskite. *J. Mater. Chem. A* **2019**, *7* (15), 8811–8817.

(7)   Yuan, Z.; Zhou, C.; Tian, Y.; Shu, Y.; Messier, J.; Wang, J. C.; van de Burgt, L. J.; Kountouriotis, K.; Xin, Y.; Holt, E.; et al. One-Dimensional Organic Lead Halide Perovskites with Efficient Bluish White-Light Emission. *Nat. Commun.* **2017**, *8* (1), 14051.

(8)   Jin, Z.; Zhang, Z.; Xiu, J.; Song, H.; Gatti, T.; He, Z. A Critical Review on Bismuth and Antimony Halide Based Perovskites and Their Derivatives for Photovoltaic Applications: Recent Advances and Challenges. *J. Mater. Chem. A* **2020**, *8* (32), 16166–16188.

(9)   Shi, D.; Adinolfi, V.; Comin, R.; Yuan, M.; Alarousu, E.; Buin, A.; Chen, Y.;

Hoogland, S.; Rothenberger, A.; Katsiev, K.; et al. Low Trap-State Density and Long Carrier Diffusion in Organolead Trihalide Perovskite Single Crystals. *Science (80-.).* **2015**, *347* (6221), 519–522.

(10) Shannon, R. D. Revised Effective Ionic Radii and Systematic Studies of Interatomic Distances in Halides and Chalcogenides. *Acta Crystallogr. Sect. A* **1976**, *32* (5), 751–767.

(11) Stoumpos, C. C.; Cao, D. H.; Clark, D. J.; Young, J.; Rondinelli, J. M.; Jang, J. I.; Hupp, J. T.; Kanatzidis, M. G. Ruddlesden-Popper Hybrid Lead Iodide Perovskite 2D Homologous Semiconductors. *Chem. Mater.* **2016**, *28* (8), 2852–2867.

(12) Ganguli, D. Cationic Radius Ratio and Formation of K2NiF4-Type Compounds. *J. Solid State Chem.* **1979**, *30* (3), 353–356.

(13) Ganguly, P.; Rao, C. N. R. Crystal Chemistry and Magnetic Properties of Layered Metal Oxides Possessing the K2NiF4 or Related Structures. *J. Solid State Chem.* **1984**, *53* (2), 193–216.

(14) Kieslich, G.; Sun, S.; Cheetham, A. K.; Cheetham, T.; Gregor, K.; Shijing, S.; Anthony, K. C. Solid-State Principles Applied to Organic-Inorganic Perovskites: New Tricks for an Old Dog. *Chem. Sci.* **2014**, *5* (12), 4712–4715.

(15) Kamminga, M. E.; Stroppa, A.; Picozzi, S.; Chislov, M.; Zvereva, I. A.; Baas, J.; Meetsma, A.; Blake, G. R.; Palstra, T. T. M. Polar Nature of $(CH_3NH_3)_3Bi_2I_9$ Perovskite-Like Hybrids. *Inorg. Chem.* **2017**, *56* (1), 33–41.

(16) Hrizi, C.; Chaari, N.; Abid, Y.; Chniba-Boudjada, N.; Chaabouni, S. Structural Characterization, Vibrational and Optical Properties of a Novel One-Dimensional Organic-Inorganic Hybrid Based-Iodobismuthate(III) Material, [C 10H 7NH 3]BiI 4. *Polyhedron* **2012**, *46* (1), 41–46.

Chapter 7

Summary, conclusion and further work

7.1 Summary and Conclusion

OIHPs have attracted great interest for their structural diversity and optoelectronic properties. The aim of this thesis was to explore Az as an A-site cation in OIHPs. A detailed structure study of $AzPbBr_3$ was undertaken at room temperature and low temperature, which is presented in Chapter 3. Two follow-up studies on mixed A-cation and mixed halide perovskites based on Az are presented in Chapter 4 and Chapter 5. Some preliminary results of a layered structure Az_2PbBr_4 and a 1D chain structure azetidinium bismuth bromide are presented in Chapter 6. Characterisation of Az-based OIHPs was performed using powder and single crystal XRD, ^{1}H NMR spectra, absorption spectroscopies and SEM.

With the organic cation radius reported by Kieslich *et al*,[1] $AzPbBr_3$ was identified as a promising OIHP candidate, the tolerance factor of which was calculated to be 1.00. $AzPbBr_3$ was synthesised from solution using various anti-solvents at three temperatures (0 °C, 20 °C and 60 °C) and the structure of $AzPbBr_3$ was determined to be a 6H hexagonal perovskite with space group $P6_3/mmc$. A detailed structure analysis was carried out at ambient temperature and low temperature, and octahedral distortion was found at both temperatures. Two potential phase transitions were identified from the PXRD and dielectric spectra. The low temperature phase is proposed to be *Pnnm* while the space group of the intermediate phase is yet to be ascertained. Using absorption spectroscopy, the bandgap of $AzPbBr_3$ was found to be 2.81 eV.

$AzPbBr_3$ was proven to be stable in ambient environment for >6 months with no decomposition, and its bandgap (2.81 eV) is larger than that of $MAPbBr_3$ (2.20 eV) and $FAPbBr_3$ (2.16 eV). The mixed cation perovskite with Az and MA or FA should display a tuneable bandgap between those of the end members. In the mixed cation study, $Az_{1-x}FA_xPbBr_3$ and $Az_{1-x}MA_xPbBr_3$ ($0 \leq x \leq 1$) were explored using both mechano- and precipitation syntheses. For samples obtained from the precipitation synthesis, the actual

FA% or MA% in the precipitated product was found to be less than the nominal composition in the reaction solution as a result of different precipitation rates of 3C and 6H perovskite polytypes. Such composition mismatch was not found for mechanosynthesised samples. A 3C-6H two-phase region was found to be present for $0.42 \leq x \leq 0.79$ and $0.10 \leq x \leq 0.94$, for mechano- and precipitation synthesis of $Az_{1-x}FA_xPbBr_3$, respectively; the two-phase region for mechanosynthesised and precipitation synthesised $Az_{1-x}MA_xPbBr_3$ appeared for $0.27 \leq x \leq 0.49$ and $0.07 \leq x \leq 0.71$. The cell volume as a function of the composition (volume increases with increasing Az^+ content) in both 6H (Az-rich) and 3C (FA-rich) solid solution regions suggests the Az^+ cation is actually larger than FA^+, which is distinct to the cation size reported in the literature.[1,2] Under the assumption of Vegard's law, the cation radius of Az^+ is estimated to be ~310 pm and therefore the tolerance factor of $AzPbBr_3$ is 1.14, which is consistent with the fact that it forms a 6H hexagonal perovskite rather than a cubic perovskite. By comparison, in the 3C solid solution regions (Az-poor), the solid solution range in $Az_zFA_{1-z}PbBr_3$ is surprisingly smaller than in $Az_zMA_{1-z}PbBr_3$, given that MA^+ is much smaller than FA^+. This suggests that the extent of the single-phase solid solution of halide perovskites is dependent only on the average A-cation size, while the size mismatch is less of an influence, in contradiction to the solid solution formation observed in oxide perovskites. The work in this thesis reveals the importance of cross-checking the nominal (reaction) with the actual (product) composition, especially when the synthetic method may be under kinetic control or multiple phases can be formed in the system. When doping larger A-site organic cations in OIHPs, the average A-cation radius might be used as a guide to prevent unwanted phase separation. The computed size of organic cations and the presence of any dynamic/preferential bonding effects should be re-examined and considered during study of OIHPs.

With different anion radii, different structures are possible for Az mixed halide perovskite. In the mixed halide study, $AzPbBr_{3-x}X_x$ (X = Cl or I) were obtained by mechanosynthesis. The single-phase mono-halide materials ($AzPbX_3$ (X = Cl, Br or I) were shown to be stable in air for > 6 months. In addition to the 6H $AzPbBr_3$, hexagonal 6H and 4H, and rhombohedral 9R polytypes were found in the composition of $AzPbCl_3$, $AzPbBr_{3-x}I_x$ (ca. $0 < x \leq 2$) and $AzPbI_3$, respectively. A linear variation in unit cell volume as a function of anion average radius was observed not only within each solid solution in agreement

with Vegard's law, but extending linearly across all polytypes when cell volume is scaled per formula unit. A tuneable bandgap was achieved ranging from 2.00 to 3.41 eV, which also varies linearly across all three polytypes as a function of average anion radius.

During the hand grinding synthesis of $AzPbBr_3$, Az_2PbBr_4 was isolated and determined to be a R-P phase ($n = 1$) structure with an optical bandgap of 2.74 eV. The single crystal structure of azetidinium bismuth bromide was determined to be a 1D chain structure with *Cmcm* space group. However, the PXRD analysis on the azetidinium bismuth bromide powder, prepared by both precipitation synthesis and mechanosynthesis, indicated several structures different from the structure determined by single crystal. These structures have yet to be determined.

The structure and properties of all the Az-based OIHPs investigated are generally consistent with previous reported OIHP systems and follow empirical, size-based rules such as tolerance factor and Vegard's law. Two synthetic methods of OIHPs – mechanosynthesis and precipitation synthesis - were compared. Mechanosynthesis consistently resulted in the target composition, while composition mismatch was found for samples prepared by precipitation synthesis, especially for systems that allow multi phases. This composition mismatch is due to the formation of perovskite under kinetic control in the solution method.

7.2 Further work

Despite the effort spent on the low temperature SCXRD and PXRD of $AzPbBr_3$, the intermediate phase could not be identified. Higher quality crystals are required to determine the intermediate phase. Other crystal growth methods are worth trying to obtain these, such as solvothermal growth and top-seeded solution growth methods.[3,4]

In the mixed halide perovskite chapter, only samples from mechanosynthesis were explored. Samples synthesised using solution precipitation are worth exploring as the solution method is the most common method to synthesise OIHPs, as mentioned in Chapter 1. However, in the literature on mixed halide perovskites, it has been reported that the halide composition in other OIHP systems prepared by solution precipitation routes did not match that of the precursor solution.[5,6] This compositional mismatch

hinders the intention to achieve a full range of bandgap tunability. For example, the actual Cl% in $FAPbBr_{3-x}Cl_x$ crystals was found to be larger than the nominal value for Cl-poor target compositions (< 50% Cl) but smaller for Cl-rich reactions.[5] Similarly, $MAPbCl_{3-x}I_x$ compositions cannot be extensively tuned by merely altering the Cl/I ratio of the reaction solution, and only 3% - 4% of Cl was found in the spin coated thin film when the Cl/I ratio in the precursor solution was 1:3.[6] It would be interesting to study the halide composition, lattice parameters and phase ratios of the Az-based precipitation synthesised mixed-halide perovskites to assess if composition mismatch is also observed in these OIHP systems.

Az_2PbBr_4 has been successfully synthesised and determined to be R-P phase ($n = 1$). Further synthesis of other layered members ($n > 1$) can be carried out for the potential bandgap tunability. In the literature,[7] BA_2PbI_4 has been reported and it is the $n = 1$ case of the mixed cation layered structure $BA_2MA_{n-1}Pb_nI_{3n+1}$ ($n = 1, 2, 3…$), which adopt R-P-like structures and are used as the key functional layer in high-efficiency solar cells[8] and red LEDs.[9] Azetidinium lead perovskite may therefore have the potential to obtain similar layered structure compounds $Az_2MA_{n-1}Pb_nX_{3n+1}$ (X = Br, I), the bandgap of which should be tuneable by changing the number of inorganic layers (n). As discussed in Chapter 1, the optoelectronic properties of OIHPs are mainly determined by the band structure, which is related to the structure and connectivity of Pb-X framework. Az-based layered structure compounds $Az_2MA_{n-1}Pb_nX_{3n+1}$ (X = Br, I), if successfully synthesised, are expected to have similar band structure as $BA_2MA_{n-1}Pb_nI_{3n+1}$, which has potential for application in solar cells and LEDs.

Studies of mixed A-cation and mixed halide Az-based perovskites are reported in this thesis, so mixed metal (M-cation) Az-perovskite systems would be an obvious avenue for further studies. As discussed in Chapter 1, the appealing optoelectrical properties of OIHPs can be attributed to the $6s^26p^0$ electronic configuration of Pb^{2+}.[10,11] The ionic radii of Bi^{3+} and Sn^{2+} are similar to that of Pb^{2+},[12] and Bi^{3+} and Sn^{2+} have $6s^26p^0$ and $5s^26p^0$ electronic configuration, respectively. Sn-doped and Bi-doped OIHPs have been reported in the literature. Hao *et al.*[13] reported $MASn_{1-x}Pb_xI_3$ mixed metal perovskite with a tuneable bandgap, and a bandgap of 1.17 eV could be achieved. These studies suggest Sn-doped and Bi-doped azetidinium lead halide OIHPs are materials that can potentially lead to further bandgap tuning. The synthesis and brief investigation of '$Az_2Bi_3Br_9$' is

presented in Chapter 6. However, the PXRD of powders from precipitation synthesis and mechanosynthesis were different from the calculated powder pattern from the structure determined by SCXRD. The reason behind this difference needs to be explored.

References

(1)   Kieslich, G.; Sun, S.; Cheetham, A. K.; Cheetham, T.; Gregor, K.; Shijing, S.; Anthony, K. C. Solid-State Principles Applied to Organic-Inorganic Perovskites: New Tricks for an Old Dog. *Chem. Sci.* **2014**, *5* (12), 4712–4715.

(2)   Becker, M.; Klüner, T.; Wark, M. Formation of Hybrid ABX_3 Perovskite Compounds for Solar Cell Application: First-Principles Calculations of Effective Ionic Radii and Determination of Tolerance Factors. *Dalt. Trans.* **2017**, *46* (11), 3500–3509.

(3)   Cao, M.; Tian, J.; Cai, Z.; Peng, L.; Yang, L.; Wei, D. Perovskite Heterojunction Based on $CH_3NH_3PbBr_3$ Single Crystal for High-Sensitive Self-Powered Photodetector. *Appl. Phys. Lett.* **2016**, *109* (23), 233303.

(4)   Dong, Q.; Fang, Y.; Shao, Y.; Mulligan, P.; Qiu, J.; Cao, L.; Huang, J. Electron-Hole Diffusion Lengths > 175 Um in Solution-Grown $CH_3NH_3PbI_3$ Single Crystals. *Science* **2015**, *347* (6225), 967–970.

(5)   Ng, M.; Halpert, J. E. Single Crystals of Mixed Br/Cl and Sn-Doped Formamidinium Lead Halide Perovskites *via* Inverse Temperature Crystallization. *RSC Adv.* **2020**, *10* (7), 3832–3836.

(6)   Sanchez, R. S.; de la Fuente, M. S.; Suarez, I.; Munoz-Matutano, G.; Martinez-Pastor, J. P.; Mora-Sero, I.; Muñoz-Matutano, G.; Martinez-Pastor, J. P.; Mora-Sero, I. Tunable Light Emission by Exciplex State Formation between Hybrid Halide Perovskite and Core/Shell Quantum Dots: Implications in Advanced LEDs and Photovoltaics. *Sci. Adv.* **2016**, *2* (1), e1501104.

(7)   Stoumpos, C. C.; Cao, D. H.; Clark, D. J.; Young, J.; Rondinelli, J. M.; Jang, J. I.; Hupp, J. T.; Kanatzidis, M. G. Ruddlesden-Popper Hybrid Lead Iodide Perovskite 2D Homologous Semiconductors. *Chem. Mater.* **2016**, *28* (8), 2852–2867.

(8)   Tsai, H.; Nie, W.; Blancon, J. C.; Stoumpos, C. C.; Asadpour, R.; Harutyunyan, B.; Neukirch, A. J.; Verduzco, R.; Crochet, J. J.; Tretiak, S.; et al. High-Efficiency Two-Dimensional Ruddlesden-Popper Perovskite Solar Cells. *Nature* **2016**, *536* (7616), 312–317.

(9)   Tsai, H.; Nie, W.; Blancon, J.-C.; Stoumpos, C. C.; Soe, C. M. M.; Yoo, J.; Crochet,

J.; Tretiak, S.; Even, J.; Sadhanala, A.; et al. Stable Light-Emitting Diodes Using Phase-Pure Ruddlesden-Popper Layered Perovskites. *Adv. Mater.* **2018**, *30* (6), 1704217.

(10)   Jin, Z.; Zhang, Z.; Xiu, J.; Song, H.; Gatti, T.; He, Z. A Critical Review on Bismuth and Antimony Halide Based Perovskites and Their Derivatives for Photovoltaic Applications: Recent Advances and Challenges. *J. Mater. Chem. A* **2020**, *8* (32), 16166–16188.

(11)   Shi, D.; Adinolfi, V.; Comin, R.; Yuan, M.; Alarousu, E.; Buin, A.; Chen, Y.; Hoogland, S.; Rothenberger, A.; Katsiev, K.; et al. Low Trap-State Density and Long Carrier Diffusion in Organolead Trihalide Perovskite Single Crystals. *Science (80-.).* **2015**, *347* (6221), 519–522.

(12)   Shannon, R. D. Revised Effective Ionic Radii and Systematic Studies of Interatomic Distances in Halides and Chalcogenides. *Acta Crystallogr. Sect. A* **1976**, *32* (5), 751–767.

(13)   Hao, F.; Stoumpos, C. C.; Cao, D. H.; Chang, R. P. H.; Kanatzidis, M. G. Lead-Free Solid-State Organic-Inorganic Halide Perovskite Solar Cells. *Nat. Photonics* **2014**, *8* (6), 489–494.